

Spin Qubits in Double and Triple Quantum Dots

A dissertation presented

by

James Redding Medford

to

The Department of Physics

in partial fulfillment of the requirements

for the degree of

Doctor of Philosophy

in the subject of

Physics

Harvard University

Cambridge, Massachusetts

2013

©2013 - James Redding Medford

All rights reserved.

Dissertation Advisor
Professor Charles M. Marcus

Author
James Redding Medford

Spin Qubits in Double and Triple Quantum Dots

Abstract

This thesis presents research on the initialization, control, and readout of electron spin states in gate defined GaAs quantum dots. The first three experiments were performed with Singlet-Triplet spin qubits in double quantum dots, while the remaining two experiments were performed with an Exchange-Only spin qubit in a triple quantum dot.

The first experiment examines the relationship between a dynamic nuclear polarization (DNP) process and the increase in measured singlet return probability in a Singlet-Triplet qubit. We find that the DNP process creates an Overhauser field difference, ΔB_z , between dots, which enhances the relaxation of triplet states during the measurement. We propose a model which explains this relaxation mechanism, and find it in good agreement with the data.

The second and third experiments investigate the effects of dynamical decoupling sequences on the Singlet-Triplet qubit. We demonstrate the preservation of singlet-triplet superpositions by interlacing qubit rotations with Carr-Purcell (CP) sequences. We test the preservation of a singlet state with different dynamical decoupling schemes, finding a maximum coherence time of $T_2 \sim 80 \mu\text{s}$ for the CP sequence. The coherence time is studied for a number of π -pulses in the CP sequence, yielding an exponential dependence on even numbers of π -pulses. This allowed us to estimate the functional form of the noise spectrum influencing the qubit.

The fourth experiment studied the initialization, complete electrical control, and readout of an Exchange-only spin qubit in a triple quantum dot. We demonstrate over 75 qubit rotations at 47 GHz and create a method of measurement and state tomography,

enabling a quantification of the leakage from the qubit subspace.

In the final experiment, we bias the triple quantum dot in a regime that is protected from charge noise and leakage from the qubit subspace. In this regime we demonstrate a resonant two-axis control using microwaves, which offer superior control capabilities over the pulsed interactions used in the rest of this thesis. A 64 π -pulse dynamical decoupling sequence yields a coherence time of $\sim 19 \mu\text{s}$ and a noise power spectrum that is heavily dominated by low frequency noise.

Contents

Title Page	i
Abstract	iii
Table of Contents	v
List of Figures	viii
List of Tables	x
Acknowledgments	xi
Dedication	xii
1 Introduction	1
2 Qubits	3
2.1 The Bloch Sphere	3
2.2 The Rotating Frame	6
2.3 Statistical Ensembles	9
2.4 Generalized Measurements	10
2.5 Dephasing, Decoherence, and Relaxation	11
3 Semiconductor Quantum Dots and Spin Qubits	14
3.1 Gate Defined GaAs Heterostructures	14
3.2 Quantum Dots	17
3.3 Overhauser Fields and Nuclear Pumping	20
3.4 Phonons	22
3.5 Loss-DiVincenzo Qubits	23
3.6 Singlet-Triplet Qubits	25
3.7 Exchange-only Qubits	28
4 Singlet-Triplet Relaxation and Readout Visibility in an Overhauser Field Gradient	31
4.1 Introduction	32
4.2 System	34
4.3 Theory, relaxation model	35
4.4 Experimental Results	44
4.5 Conclusions	52
5 Interlaced Dynamical Decoupling and Coherent Operation of a Singlet-Triplet Qubit	54
5.1 Introduction	55
5.2 System	57
5.3 Decoherence and Dynamical Decoupling	58
5.4 Interlaced Operations	60

6 Scaling of Dynamical Decoupling for Spin Qubits	65
6.1 Introduction	66
6.2 Device and Qubit System	68
6.3 Dynamical Decoupling	69
6.4 CPMG scalings as Noise Spectrometer	69
6.5 CDD sequences	74
6.6 Conclusions	74
7 Self-Consistent Measurement and State Tomography of an Exchange-Only Spin Qubit	77
7.1 Introduction	78
7.2 Device and System	78
7.3 Two Exchange Interactions	80
7.4 Coherent Rotations	81
7.5 Exchange Noise	83
7.6 Dynamical Decoupling	85
7.7 Tomographic Characterization of the System	86
7.8 Measurement Tomography	88
7.9 State Tomography	89
7.10 Methods	92
8 Resonant Microwave Control of a Symmetric Exchange-Only Spin Qubit	94
8.1 Introduction	95
8.2 Device and System	96
8.3 Spectroscopy	98
8.4 Rabi Oscillations	99
8.5 Dynamical Decoupling	102
A Triple Dot Fabrication Recipe	105
A.1 Overview	105
A.2 Repeated actions	106
A.3 Mesa Patterning	107
A.4 Mesa Etch	108
A.5 Ohmic Pattern	110
A.6 Ohmic Deposition	111
A.7 Anneal Recipe	112
A.8 Fine Gates Pattern	113
A.9 Fine Gates Deposit	115
A.10 Outer Connection Layer Pattern	115
A.11 Outer Connection Layer Deposit	116
B Catalogue of Devices and Design Tips	118

C Cryogenic Measurement	122
C.1 Configuration of DC lines	123
C.2 Configuration of High Bandwidth Lines	125
C.3 High Frequency Control Circuits	126
C.4 Reflectometry	126
D Supplemental Material for Self- Consistent Measurement and State Tomography of an Exchange-Only Spin Qubit	133
D.1 Device	133
D.2 Measurement and Normalization	134
D.3 Figure 4b Theory Curves	138
D.4 Figure 5d Echo with Hyperfine Dephasing and Leakage, without Electrical Noise	141
D.5 Measurement Tomography for the Exchange Only Qubit	142
D.6 Theory Curves in All Panels of Figure 6	149
E Supplementary Information for Resonant Microwave Control of a Symmetric Exchange-Only Spin Qubit	153
E.1 Measurement and Normalization	153
E.2 Model of the exchange interactions	155
E.3 Model in Figure 8.2(c)	156
E.4 Model and Power Broadening in Figure 8.2(d)	156
E.5 Model in Figure 8.2(f)	158
E.6 Model in Figure 8.3 insets	161
E.7 Model in Figure 8.4	162
F Dipole Moment of the Symmetric Exchange Only Qubit	163
F.1 Static Dipole Moment of a Bloch Sphere State	163
F.2 Dipole Transition Matrix Element	166
Bibliography	168

List of Figures

2.1	Bloch Sphere Coordinates	4
2.2	Projective Measurement on a Bloch Sphere	6
2.3	Rotation Axis in the Rotating Frame	8
2.4	Dephasing and Relaxation	12
3.1	GaAs-AlGaAs Heterostructure	16
3.2	A gated quantum dot charge density	17
3.3	A quantum dot	18
3.4	Overhauser Fields	21
3.5	A Loss-DiVincenzo Qubit	24
3.6	A Singlet-Triplet Qubit	26
3.7	A Exchange-Only Qubit	29
4.1	Double Dot device and charge stability diagram	34
4.2	Energy levels and relaxation mechanisms as a function of detuning	37
4.3	Dynamic Nuclear Polarization	43
4.4	T_1 as a function of ΔB_z and ϵ	46
4.5	The affects of adiabaticity in loading into (1,1)	50
4.6	Visibility and measurement relaxation as a function of ΔB_z	52
5.1	Double Dot System	56
5.2	Interlaced X and Z rotations	59
5.3	Dynamical Decoupling Sequences	61
6.1	Double dot device and charge stability diagram	67
6.2	Energy level diagram and dynamical decoupling schematic	70
6.3	CPMG sequence spectroscopy	71
6.4	Full theory of $S(\omega)$	72
6.5	CDD with full theory	75
7.1	Device, qubit Bloch sphere and spectrum	79
7.2	Charge stability diagram and rotations around two axes	82
7.3	Fast rotation and visibility model	83
7.4	Effects of electrical and nuclear noise	85
7.5	Dynamical decoupling	87
7.6	Measurement and State Tomography	90
8.1	Device and Charge Stability Diagram	95
8.2	Qubit Spectroscopy	97
8.3	Frequency and Amplitude Control	100
8.4	Two-Axis Phase Control	101
8.5	Dynamical Decoupling and Noise Spectroscopy	103

B.1	ALD and Device Noise Reduction	121
C.1	Fridge Wiring	124
C.2	Control Wiring	127
C.3	Readout Wiring	128
C.4	rf Demodulation Circuit	129
C.5	PC Board with Tank Circuit	130
D.1	Single-shot histogram	135
D.2	Measurement relaxation and confirmation of 120° axis separation	137
D.3	Measurement tomography pulse sequences	145
D.4	Measurements of ρ_j	149
D.5	Tomography with and without bandwidth effects	150
E.1	Power Broadening	157
E.2	Spectroscopy with initialization in the upper Zeeman Manifold	161

List of Tables

B.1	Wafer Catalogue	119
B.2	Device Catalogue	120

Acknowledgments

Thank you to Charlie, Amir, Bert, and Emmanuel! More detailed acknowledgements to come...

To my parents and my sister

Chapter 1

Introduction

Your infinite capacity for patience will be rewarded sooner or later.

-a fortune from my takeout, 2011

The last sixty years have seen a rapid advancement in computing power through the miniaturization of electronic and photonic components. This push towards nanotechnology has led to devices whose properties can only be understood with quantum mechanics. These increasingly non-classical components are the backbone of classical computing, but they represent just a tiny fraction of the potential that quantum components have to process information.

Qubits, a shorthand for quantum bit [134], are the fundamental building block of quantum information processing. A qubit is a mathematical abstraction representing an ideal isolated quantum mechanical two level system. We have yet to realize a “perfect” qubit, one which is isolated from a noisy environment while remaining easy to manipulate, as these traits tend to be in opposition. In searching for a system that is both easy to control and hard to corrupt, researchers have examined a large number of physical systems including ion traps [30, 128], Nitrogen Vacancy (NV) centers in diamonds [68, 64], superconducting circuits involving Josephson Junctions [101, 91, 26, 74], nuclear spins excited with Nuclear Magnetic Resonance (NMR) techniques [34, 52, 33, 35], and electron spins [88, 114, 75] to name just a few.

In the remainder of this thesis, I will discuss a range of topics centered around the work I performed on electron spin qubits in lateral semiconductor quantum dots. Chapter 2

is devoted to laying out a brief foundation of single qubit properties, while chapter 3 covers background material from the broader community to provide the necessary framework for these results. Chapter 4 covers the measurement relaxation mechanisms associated with nuclear polarizations in double quantum dots whose characteristics were previously attributed to nuclear dark states and the “Zamboni” phenomena [125]. Chapter 5 investigates various dynamical decoupling techniques and their ability to preserve superpositions of quantum states. Chapter 6 focuses on using these dynamical decoupling schemes to perform spectroscopy of the noise sources incident on the qubit.

Chapters 7 and 8 shift from double quantum dot systems to triple quantum dot systems with a new form of qubit that does not require magnetic field gradients to operate. Chapter 7 demonstrates the initialization, control, and generalized measurement of a qubit formed from the three electron system. Chapter 8 refines the three electron qubit to one that is protected from charge noise and leakage, and which can be controlled using resonant excitations similar to those found in most other qubit systems.

Appendices A and B cover the design, fabrication and testing of devices in the course of the triple quantum dot project. Appendix C explains the wiring and control of the experiment, including an explanation of the reflectometry circuit used for the high bandwidth sensing. Appendix D provides the supplementary material for chapter 7, detailing the readout and calibration of the triple quantum dot, as well as more details in the calculations of POVM elements. Appendix E details the models used in chapter 8. Appendix F gives a back of the envelope calculation for the dipole moment of the symmetric exchange only spin qubit.

Chapter 2

Qubits

The quantum mechanical nature of the qubit is, roughly speaking, the source of the advantage that a quantum computer has over a classical computer. The quantum mechanical nature contributes in two significant ways. The first and most spectacular is that qubits can become entangled with one another, allowing among other things for the encoding of vast amounts of information in a relatively modest number of qubits and quantum teleportation [104]. Entanglement fundamentally requires more than one qubit, and as such is beyond the scope of the work described here. The second advantage is that a single qubit state can always be described as the superposition of two other quantum states, an effect which allows for an intrinsically quantum parallelism during logical operations. Clever quantum algorithms such as those in Refs. [135] and Refs. [55, 56] utilize these advantages to allow for speed ups in prime factorization and sorting which are thought to be impossible using only classical computers, motivating the study of qubit systems.

2.1 The Bloch Sphere

Mathematically, we describe the qubit state, $|\psi\rangle$, a superposition of “computational states” $|0\rangle$ and $|1\rangle$ as

$$|\psi\rangle = \alpha|0\rangle + \beta|1\rangle, \quad (2.1)$$

where α and β are complex numbers that satisfy the relation $|\alpha|^2 + |\beta|^2 = 1$, and the computational states $|0\rangle$ and $|1\rangle$ are an orthonormal basis that spans the qubit subspace. The normalization of α and β make it natural to think of $|\psi\rangle$ as a point on a sphere of

radius 1. This sphere is referred to as the Bloch sphere, and following Ref. [104], we can re-write $|\psi\rangle$ in terms of the spherical angles (θ, ϕ) as

$$|\psi\rangle = \cos(\theta/2)|0\rangle + e^{i\phi}\sin(\theta/2)|1\rangle. \quad (2.2)$$

This geometrical picture is extremely handy at the single qubit level, and will be referenced repeatedly.

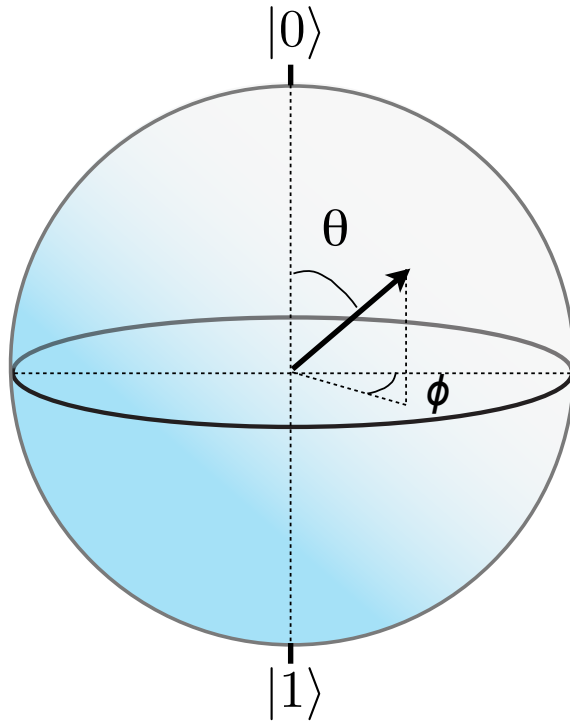


Figure 2.1: The wavefunction parameters θ and ϕ from eq. (2.2), mapped onto a Bloch Sphere.

The fact that qubits are two level systems makes the Pauli matrices

$$\begin{aligned} \mathbb{I} = \sigma_0 &= \begin{pmatrix} 1 & 0 \\ 0 & 1 \end{pmatrix} & \sigma_x = \sigma_1 &= \begin{pmatrix} 0 & 1 \\ 1 & 0 \end{pmatrix} \\ \sigma_y = \sigma_2 &= \begin{pmatrix} 0 & -i \\ i & 0 \end{pmatrix} & \sigma_z = \sigma_3 &= \begin{pmatrix} 1 & 0 \\ 0 & -1 \end{pmatrix} \end{aligned} \quad (2.3)$$

an intuitive representation for operators, where the Bloch sphere axes \hat{x} , \hat{y} , and \hat{z} relate to the corresponding Pauli matrices. The computational basis states which sit at the poles of the Bloch sphere, $|0\rangle$ and $|1\rangle$, are the eigenstates of σ_z , with eigenvalues of +1 and -1 respectively. The eigenstates of σ_x , $|X\pm\rangle = \frac{1}{\sqrt{2}}(|0\rangle \pm |1\rangle)$, lie in the equator of the Bloch sphere, along what we define as the \hat{x} -axis. Similarly, the eigenstates of σ_y lie along the \hat{y} -axis.

Manipulation of the qubit from one state to another is achieved by turning on and off terms in the Hamiltonian, \mathcal{H} . The qubit evolution is governed by the Schrödinger equation, $i\hbar \frac{d|\psi\rangle}{dt} = \mathcal{H}|\psi\rangle$. In the case of a time independent Hamiltonian, the solution is simply $|\psi(t)\rangle = \exp(-i\mathcal{H}t/\hbar)|\psi(0)\rangle$. We can represent the time evolution operator as

$$\exp(-i\gamma\mathcal{H}) = \cos(\gamma|\vec{n}|)\mathbb{I} - i\sin(\gamma|\vec{n}|)(n_x\sigma_x + n_y\sigma_y + n_z\sigma_z)/|n|, \quad (2.4)$$

where $n_i = \text{Tr}[\mathcal{H}\sigma_i]/2$ is the projection of the Hamiltonian onto the i^{th} Pauli matrix and $|\vec{n}| = \sqrt{n_x^2 + n_y^2 + n_z^2}$, which is the form of a rotation matrix for a two level system. The direction of \vec{n} is the axis around which the qubit state rotates while its length $|\vec{n}|$ indicates the speed or “strength” of the rotation.

Measurement or “readout” of the qubit state is also critical for computation applications. The simplest possible picture of readout is the binary projective measurement, where the qubit state is collapsed onto one of two orthogonal basis states¹ [143] which we will call $|+\rangle$ and $|-\rangle$. An individual measurement reveals nothing about the qubit state; only by repeating this measurement on an ensemble of identically prepared qubits can we determine the probability of collapsing onto one of the measurement states, $P_+ = |\langle +|\psi\rangle|^2$ and $P_- = |\langle -|\psi\rangle|^2$. If the measurement basis was chosen to be the computational basis, with $|+\rangle = |0\rangle$ and $|-\rangle = |1\rangle$, than P_+ and P_- reveal the magnitudes of α and β from

¹These basis states do not need to be the computational basis states $|0\rangle$ and $|1\rangle$

Eq (2.1), but nothing of the phase between them.

On a Bloch sphere, these probabilities represent the projection of the qubit state onto a line running from $|+\rangle$ to $|-\rangle$. If three unique measurement bases are chosen, defining three coordinate axes on the Bloch sphere, the state of the qubit can be reconstructed.² These three measurements compose state tomography, which is the full identification of a qubit state, up to a trivial global phase.

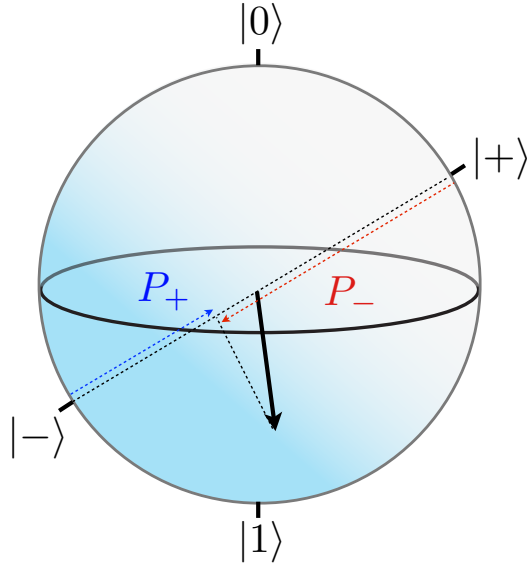


Figure 2.2: The probabilities $P_+ = |\langle +|\psi\rangle|^2$ and $P_- = |\langle -|\psi\rangle|^2$ of being in either $|+\rangle$ or $|-\rangle$ for a state indicated by the arrow.

2.2 The Rotating Frame

There is a special set of Hamiltonians that appear often in the context of qubits, where the Hamiltonian \mathcal{H} is dominated by one large term that is constant in time, and subject to small, oscillatory perturbations. This scenario was first studied in depth in the

²An argument could be made that since the qubit lies on the surface of the Bloch sphere, only two coordinates are necessary to define the qubit state, θ and ϕ from Eq (2.2). In practice this is true only for a “pure” state, one where there is no dephasing or state leakage, which I will discuss shortly in section 2.3 (see Eq (2.10)). The effect of these processes on the Bloch sphere though is to move the state inwards from the surface, necessitating a radius coordinate as well.

context of Nuclear Magnetic Resonance (NMR) [120, 13, 58] to understand the effects of a small transverse oscillating magnetic field B_1 on a nuclear species in the presence of a large longitudinal field B_0 . For convenience, we'll adopt the language of NMR, and map all qubit problems onto the spin-1/2 particle in these magnetic fields.

We can write the Hamiltonian as $\mathcal{H} = \hbar\gamma B_0\sigma_z/2 = \hbar\omega_{01}\sigma_z/2$, where $\gamma = g^*\mu/\hbar$ is the gyromagnetic ratio of the particle or qubit, g^* is the effective g-factor, μ is the magnetic dipole moment, and ω_{01} is the splitting between the ground and excited states, $|0\rangle$ and $|1\rangle$ respectively. In the absence of other terms, the spin precesses in the field, which is a rotation about the \hat{z} -axis of the Bloch sphere at a frequency ω_{01} . If we apply a small static transverse field $B_1\hat{x}$, where $B_1 \ll B_0$, the spatial axis of rotation shifts a small angle $\theta = \tan^{-1}(B_1/B_0)$ towards \hat{x} , and on the Bloch sphere rotations continue about the \hat{z} -axis at a new speed $\omega_{01} = \gamma\sqrt{B_0^2 + B_1^2} \approx \gamma B_0$.

Interesting dynamics occur when the small transverse field B_1 oscillates at a frequency $\omega \approx \omega_{01}$, with an interaction $\mathcal{H}_B = \hbar\gamma b_1 \cos(\omega t + \phi)\sigma_x$. It is more convenient to picture this field that oscillates along the \hat{x} -axis in real space as the sum of two fields, B_1^+ and B_1^- , which rotate about the \hat{z} -axis in opposite directions: $\mathcal{H}_B^+ = \hbar\gamma \frac{b_1}{2} [\cos(\omega t + \phi)\sigma_x + \sin(\omega t + \phi)\sigma_y]$ and $\mathcal{H}_B^- = \hbar\gamma \frac{b_1}{2} [\cos(\omega t + \phi)\sigma_x - \sin(\omega t + \phi)\sigma_y]$. We transform into a frame that is rotating with B_1^+ by

$$|\psi\rangle_{\text{rf}} = \exp[i\omega t\sigma_z/\hbar] |\psi\rangle \quad (2.5)$$

$$\frac{d|\psi\rangle_{\text{rf}}}{dt} = -\frac{i}{\hbar} \mathcal{H}_{\text{rf}} |\psi\rangle_{\text{rf}} \quad (2.6)$$

$$\mathcal{H}_{\text{rf}} = \exp[i\omega t\sigma_z/\hbar](\mathcal{H}_B^+ + \mathcal{H}_B^-) \exp[-i\omega t\sigma_z/\hbar] + \hbar\Delta\sigma_z, \quad (2.7)$$

where $|\psi\rangle_{\text{rf}}$ is the qubit state in a frame rotating with B_1^+ , and $\Delta \equiv \omega_{01} - \omega$ is the detuning between the oscillation frequency and the qubit splitting.

In this rotating frame, B_1^+ is static while B_1^- is rotating at twice the frequency of

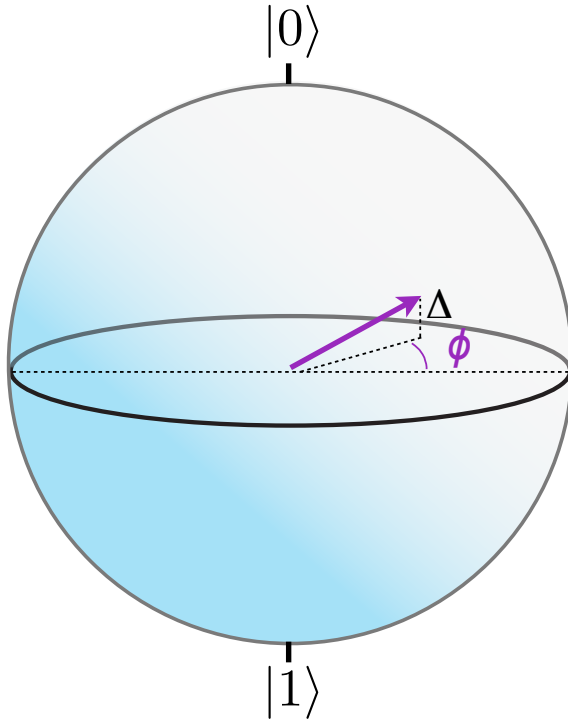


Figure 2.3: A rotation axis from an excitation with phase ϕ and detuning Δ is depicted with the purple arrow. The detuning lifts the rotation axis up out of the x - y plane.

the frame. If B_1 is much smaller than B_0 , we can apply the rotating wave approximation, throwing out B_1^- on the grounds that the highly oscillatory terms average to zero³. The final rotating frame Hamiltonian can then be expressed as

$$\mathcal{H}_{\text{rf}}/\hbar = \Omega[\cos(\phi)\sigma_x + \sin(\phi)\sigma_y] + \Delta\sigma_z \quad (2.8)$$

where $\Omega = \frac{1}{2}b_1\gamma$ is the nutation frequency⁴. We now see that if $\Omega \ll \omega_{01}$ it is possible to generate a rotation about an arbitrary axis in the Bloch sphere. In practice, experimentalists often operate at $\Delta = 0$, “on resonance” with the qubit, and control the qubit only through

³If the rotating wave approximation is insufficient, the Magnus expansion can be used to derive corrections in powers of $\frac{B_1}{B_0}$ [140], the first of which is a term along the \hat{z} -axis of the Bloch sphere.

⁴A nutation is a rotation from the top of the Bloch sphere to the bottom, that simultaneously spirals around the \hat{z} -axis. The name comes from the motion of a top.

the two-axis control provided by the phase of the oscillation.⁵

2.3 Statistical Ensembles

When considering ensembles of states for measurements, Eq (2.1) is no longer the most useful description of the qubit state. In its place, we turn to density matrices [31], $\rho = |\psi\rangle\langle\psi|$, which are 2x2 matrices formed from the outer product of Eq (2.1) and its complex conjugate. Explicitly, we can re-write Eq (2.1) and Eq (2.2) as

$$\rho = |\psi\rangle\langle\psi| = \begin{pmatrix} |\alpha|^2 & \alpha\beta^* \\ \alpha^*\beta & |\beta|^2 \end{pmatrix} = \begin{pmatrix} \cos^2(\theta/2) & \frac{1}{2}\sin(\theta)e^{-i\phi} \\ \frac{1}{2}\sin(\theta)e^{i\phi} & \sin^2(\theta/2) \end{pmatrix}. \quad (2.9)$$

In this last form it is easy to see that $\text{Tr}[\rho] = \cos^2(\theta/2) + \sin^2(\theta/2) = 1$ for any possible qubit state, a requirement that satisfies the conservation of probability.

To describe an ensemble of states, we add the density matrices for each state, weighted by their population in the ensemble $p_i = n_i/n_{total}$, $\rho = \sum_i p_i |\psi_i\rangle\langle\psi_i|$, where $\sum_i p_i = 1$. Since the probability of finding state i in the ensemble, p_i , sums to one, the trace of ρ is still one, regardless of whether every state in the ensemble is identical. To determine whether every state is identical, which would form a “pure” state, we look to $\text{Tr}[\rho^2]$, which equals one only for pure states. All other ensembles are referred to as “mixed” states, with the situation $\text{Tr}[\rho^2] = \frac{1}{2}$ being a completely mixed state. These mixed states are incoherent ensembles which often result from noise that causes variations between qubits in the ensemble.

The density matrix ρ is directly related to the Bloch vector \vec{r} as

$$\rho = \frac{\mathbb{I} + r_x\sigma_x + r_y\sigma_y + r_z\sigma_z}{2} \quad (2.10)$$

where $r_i = 2\text{Tr}[\rho\sigma_i]$ is the Bloch vector component. From Eq (2.10), we can see that $\text{Tr}[\rho^2] = \frac{1}{2}(1 + r_x^2 + r_y^2 + r_z^2)$, which confirms that $\frac{1}{2} \leq \text{Tr}[\rho^2] \leq 1$ in the absence of leakage.

⁵The phase ϕ is the phase *relative* to the phase of the first pulse that interacted with the qubit.

The Bloch vector length $|\vec{r}| = \sqrt{r_x^2 + r_y^2 + r_z^2}$ is then a direct measure of the purity of the ensemble.

2.4 Generalized Measurements

As mentioned above, a projective measurement is the simplest picture of qubit readout. In practice, it is too simplistic to capture the measurement process in an actual experiment. Actual measurements contain assignment errors due to noise and relaxation during the measurement, where an outcome that should have registered as $|+\rangle$ is recorded as $|-\rangle$. Actual measurements can also contain ambiguity as to which qubit state the $|+\rangle$ and $|-\rangle$ measurement basis states correspond to, an error which arises from small unintended single qubit rotations. For these reasons, we are interested in using the more sophisticated framework of Positive Operator-Valued Measure (POVM) elements and generalized measurements⁶ to quantify and correct the errors in our qubit measurement.

The POVM formalism consists of assigning all probabilities based on POVM elements, where the probability of an outcome “+” for state ρ is described as $P_+(\rho) = \text{Tr}[E_+\rho]$. Here E_+ is a POVM element, a 2×2 matrix with the probability conserving constraints that it is positive semi-definite, all of its eigenvalues are less than or equal to one, and $E_- \equiv \mathbb{I} - E_+$. E_+ and E_- are measured quantities that are determined experimentally by recording the probability that a set of known states $\{\rho_j\}$ will trigger a “+” outcome,

$$P_j \equiv P_+(\rho_j) = \text{Tr}[E_+\rho_j], \quad (2.11)$$

and inverting the system of equations (2.11) to solve for E_+ . The set of states ρ_j must span the qubit subspace, such as $\{|X_+\rangle\langle X_+|, |Y_+\rangle\langle Y_+|, |Z_+\rangle\langle Z_+|, \mathbb{I}/2\}$ ⁷, where $\mathbb{I}/2$ is the com-

⁶There are other reasons for using generalized measurements to discuss an experiment, such as superior state discrimination. The interested reader should consult Ref. [104], Section 2.2.6 for a more thorough background on the subject of POVMs and generalized measurements.

⁷Four states are required in $\{\rho_j\}$ because as a 2×2 Hermitian matrix, E_+ has four independent quantities.

pletely mixed state. If the qubit is composed of two levels which are coupled to additional states, and the qubit can leak from the qubit subspace into these states, the set of $\{\rho_j\}$ must be large enough to span the entire space⁸. This technique only works if $\{\rho_j\}$ is known with a very high degree of accuracy. The work in chapter 7 and appendix D describe how to handle the case of leakage into a large subspace when $\{\rho_j\}$ is only partially known.

Performing this calibration for the POVM elements of each of the measurement axes, E_{x+} , E_{y+} , and E_{z+} , allows for robust measurement of the qubit state, and accurate state tomography. The eigenvectors of E_+ are the states that the qubit was projected onto, hopefully some states close to the originally intended ones, while the eigenvalues represent the fidelities of those measurements.

2.5 Dephasing, Decoherence, and Relaxation

Physical realizations of qubits are described by a set of physical parameters that evaluate a qubit’s interaction with the environment. In NMR style qubits (sec 2.2), there is an applied field which splits the computational basis states at all times, separating interactions with the environment into two categories. The first is phase noise, which is described by T_2^* and T_2 . As the name implies, this is noise that affects the phase between the computational basis states (longitudinal coordinate on the Bloch sphere), but does not change the relative populations of those states. Since the phase of the qubit does not affect the energy, every state with the same population of $|0\rangle$ and $|1\rangle$ (constant latitude on the Bloch sphere) is degenerate, allowing for easy mixing between states of different phases.

The second type of interaction with the environment is one which changes the population of $|0\rangle$ and $|1\rangle$, through either the emission or absorption of energy, and is described by the T_1 or “lifetime” of the qubit. The emission and absorption of energy through phonon

⁸The dimensions of E_+ also grow as well. The POVM elements are as large as the number of states the quantum system can inhabit.

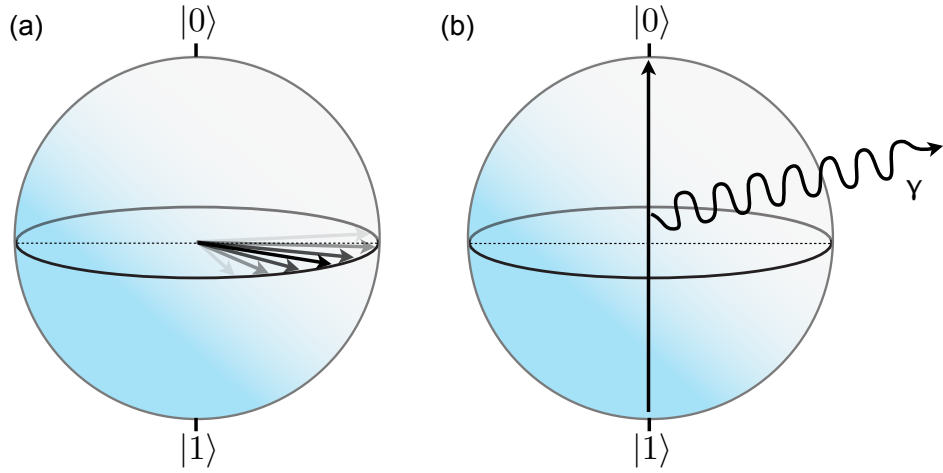


Figure 2.4: The effects of (a) dephasing and (b) relaxation on a Bloch sphere representation of a qubit state, where the arrow darkness in (a) indicates the proportion of the ensemble at that phase position. The relaxation process in (b) does not conserve the energy of the qubit, resulting in the emission of a phonon or photon γ to carry away the excess energy. See section 3.4 and chapter 4 for more details about phonon mediated relaxation

interactions is covered in section 3.4. It is worth noting here that with double quantum dot style qubits, $|0\rangle$ and $|1\rangle$ are often separated by only a small gap, making the distinction between relaxation and decoherence complicated.

Phase noise can be separated into two types, dephasing and decoherence. Dephasing is a measure of how rapidly an *ensemble* of qubits loses phase information, and is described by the timescale T_2^* . Dephasing occurs when members of the ensemble experience different conditions, such as local magnetic or electric environments, which cause the members to evolve under slightly different Hamiltonians, resulting in a distribution of phases across the ensemble. Unlike relaxation or decoherence, dephasing can be mitigated through clever qubit manipulation using dynamical decoupling techniques, which cancel out static or slow variations in the Hamiltonians across the ensemble, restoring coherence. The simplest and most familiar of these techniques is the Hahn Echo [58].

Decoherence is a measure of how rapidly an *individual* qubit loses its phase infor-

mation, with lower bound measured experimentally by the longest coherence time T_2 that is achievable with dynamical decoupling techniques. This information can be lost due to entanglement with the environment, or classical noise that occurs too rapidly to be corrected by dynamical decoupling sequence [36]. This sets a bound on the dephasing time that $T_2 \geq T_2^*$, while the relaxation rate limits the coherence time to be $T_2 \leq 2T_1$.

Chapter 3

Semiconductor Quantum Dots and Spin Qubits

The spin degree of freedom in a spin-1/2 particle is a natural realization of a potential qubit; an intrinsically two-level system that is relatively weakly coupled to its environment ($\mu_B \sim 58 \text{ }\mu\text{eV}/T$). This weak coupling to the environment allows, in principle, for long lived quantum states, while the lack of additional levels prevents leakage out of the qubit subspace. Though it is relatively challenging to address a single nuclear spin in bulk samples [63], work with high mobility semiconductor heterostructures has allowed for the relatively easy confinement and control of individual electrons in solid-state chips [29], making the electron spin a prime candidate for a qubit. Finally, the same technology that has made the high quality heterostructures and confinement lithography possible also produces today's cutting edge classical circuitry, potentially allowing for the semiconductor spin qubit to experience the same benefits in scaling and large scale wafer processing.

3.1 Gate Defined GaAs Heterostructures

The spins in the qubit devices discussed in this work are confined at the GaAs-Al_{0.3}Ga_{0.7}As interface of an extremely clean wafer grown with Molecular Beam Epitaxy (MBE). These wafers are chosen for two reasons. The first is that they provide a way to confine single electrons in a quantum well. The difference in band gaps between GaAs and Al_{0.3}Ga_{0.7}As results in a conduction band discontinuity of $\Delta E_c \sim 0.3 \text{ eV}$ [44, 38], providing

one wall of a quantum well. A layer of partially ionized silicon donors provides an electric field in the growth direction, \hat{z} , which serves as the other wall of the well. Some of the ionized electrons from the silicon layer populate the well, and eventually our qubits, while the majority fill surface states [38]. A gold-germanium eutectic¹ is annealed down from a bond pad to electrically contact the well, allowing the electro-chemical potential of the well to be manipulated. This connection is referred to as an “ohmic”². Appendix A details the recipe used to make the triple quantum dot device in chapters 7 and 8. For the fabrication of the device used in chapters 4, 5, and 6, please consult Ref. [4].

Confinement in the \hat{x} and \hat{y} directions is provided through voltages on lithographic gates. Metallic gates placed on the surface of this wafer form Schottky barriers that allow them to maintain a voltage with respect to the quantum well. If these gates are biased negative with respect to the ohmic connections they are capable of pushing away some or all of the electrons in the well directly underneath, as shown in Fig. 3.3. These empty regions formed electrostatic barriers between puddles of electrons in the well. The gates can also be used to capacitively shift the energy of the electron puddles in the well that have been isolated by the electrostatic barriers. Both of these effects become important for forming quantum dots.

The second reason these MBE wafers are chosen to contain the electrons is the smooth potential the electrons see while confined inside these wells. The electrons in this well form an electron gas at low temperatures ($T \sim 1$ K), characterized by a long mean free path and high mobility that arises from the separation between donors and quantum well. With the donors out of the way, there are far fewer scattering sites, and those sites are better screened by the electrons in the well, allowing these electrons to behave like

¹An alloy of gold and germanium, $\sim 88\%$ gold, $\sim 12\%$ germanium by weight, has a markedly lower melting point than either gold or germanium separately.

²See Ref. [65] for details as to the origin of the name.

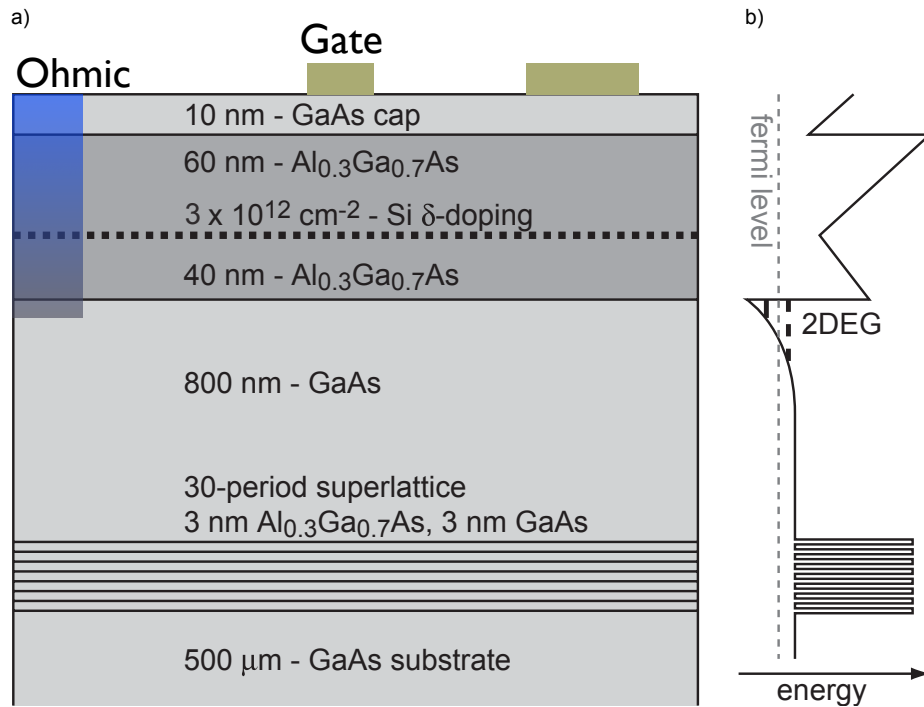


Figure 3.1: (a) A schematic of the GaAs-Al_{0.3}Ga_{0.7}As heterostructure used to form the device in chapters 7 and 8. The superlattice near the bottom of the heterostructure is grown to relieve stress between the bulk substrate and the MBE grown material, and to catch any impurities that percolate upwards from the substrate during the annealing part of the growth. (b) A schematic of the conduction band as a function of depth below the surface of the wafer. The electrons are confined in the triangular well labeled 2DEG. Adapted with permission from reference [4].

free two-dimensional particles with a reduced electron mass, $m_e^* \sim 0.067 m_e$ ³. This small effective mass plays an important role in determining the length scales of the lithographic features, allowing for single electrons to be confined in larger lithographic areas.

While removing the donors from the well results in a relatively smooth potential, it does not always result in a perfectly stable one. The origins of the fluctuations are not perfectly understood, though electrons tunneling from the Schottky barriers to the donors

³The fact that the particles in the well behave like free electrons is due to the band structure of GaAs near the γ point, which is parabolic in wave vector, $E \sim (\hbar k)^2$. If this dispersion relationship had been linear for instance, as is found in graphene, there would be a gas of relativistic particles instead.

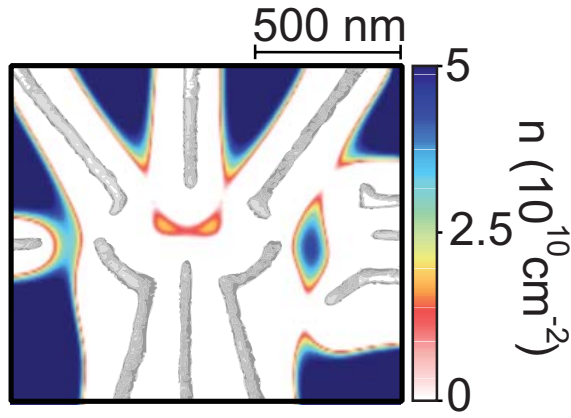


Figure 3.2: A simulation of the depletion of the 2DEG to create the double quantum dot device used in chapters 4, 5, and 6. The micrograph of the metal gates that are overlaid on top of the simulation are located 110 nm above the surface of the 2DEG. The electron density n is plotted on a truncated color scale, to allow the charge density in the dots to be seen. Adapted with permission from Ref. [5]

is a leading suspect [117, 21]. As examined in Refs. [117, 21], applying a small (~ 300 mV) positive voltage to the gates while cooling the device results in a significantly more stable device. This technique, referred to as bias cooling, or positive bias, was applied to all devices in this thesis. In addition to quieting the samples, the technique freezes in a negative charge under the gates that depends on the applied positive bias. This freezing of charge was used to help fine tune the device in chapters 4, 5, and 6, while a single voltage was used for all gates in the device in chapters 7 and 8.

3.2 Quantum Dots

Quantum dots are structures that bind a small number of conduction electrons to regions of the order of their de Broglie wavelength, $\lambda = h/2m_e^*E$, where E is the kinetic energy of the electrons in question. At these length scales the confinement causes discrete energy levels to form, much like the orbitals in a free atom. These artificial atoms are a useful testbed for probing quantum mechanics and studying the dynamics of isolated

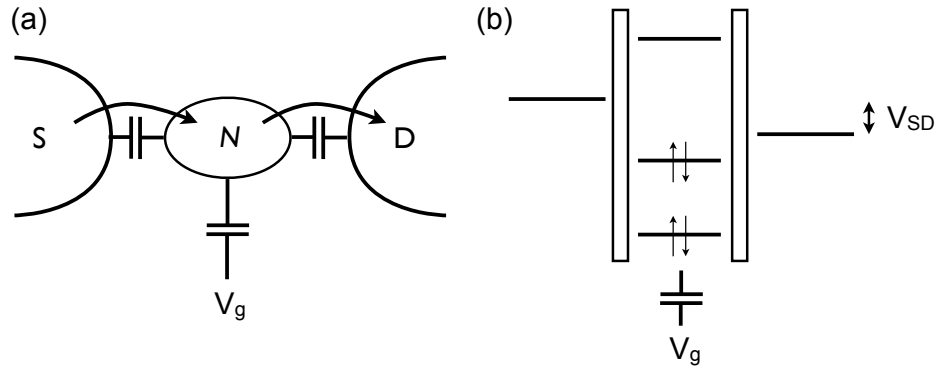


Figure 3.3: (a) A schematic of the capacitive network that describes the classical behavior a single quantum dot with N electrons. Tunneling is indicated schematically by arrows. Metallic reservoirs are marked source (S) and drain (D). (b) A level diagram of a quantum dot. The levels below the Fermi energy of the leads are filled, while the levels above the leads are empty. The voltage V_{SD} is the voltage applied between the source and drain reservoirs, which will drive a current when a dot level passes into that window. The tunnel barriers between the dot and the reservoirs are schematically represented by the rectangular walls.

electron systems, and they have been studied in a variety of materials, including semiconductor nanoparticles [45], superconducting islands [121], self-assembled semiconductor structures [73], and lateral [80] and vertical [79] semiconductor heterostructures.

The small size of the quantum dot has two main consequences. The first is the existence of orbitals at discrete energies. The quantum dot confines the electrons in an electrostatic potential which permits many bound states, each of which has a spin degeneracy allowing for two electrons of opposite spin to occupy it. The constant interaction model [148, 80] is used to describe the many-bodied states in a dot with many electrons. This model lumps all of the electron-electron interactions into a small correction to a constant capacitance C , and proceeds to treat the electrons as a group of non-interacting electrons occupying single particle states $|\psi_j\rangle$ with energies E_j .

The second consequence of the small dot size is that the self-capacitance, C , is very small, making the electrostatic charging energy associated with adding an electron, $E_C =$

Q^2/C , one of the largest energy scales associated with this system. As shown in Refs. [147, 59], this energy scale creates a regular structure in the energy spectrum corresponding to the addition of electrons from external reservoirs or “leads”. This structure is well described by the constant interaction model [153], which in single quantum dots creates the “Coulomb Diamond” structure, and in double quantum dots leads to the formation of a “honeycomb” structure.

In the constant capacitance model, the energy of a single quantum dot with N electrons is, up to a constant,

$$U(N) = \frac{(-|e|N + \sum_i C_i V_i)^2}{2C} + \sum_j^N E_j, \quad (3.1)$$

where C_i is the capacitance between the i^{th} metallic gate or lead at voltage V_i , $C \simeq \sum_i C_i$, and E_j is the energy of the occupied single particle state $|\psi_j\rangle$. The electrochemical potential of the dot, or the ground state energy level of the N^{th} electron, is given by $\mu \equiv U(N) - U(N-1)$ [147]. Excited orbitals are available at an energy $\Delta E = E_{N+1} - E_N$ above μ . When μ is equal to or less than the electrochemical potential of the lead, an electron can tunnel onto the dot. This capacitance model can be easily extended to include additional dots, as demonstrated for double dots in Ref. [59] and for triple dots in Refs. [150, 133].

The energy required to add an additional electron, $E_{\text{add}}(N) = \mu(N+1) - \mu(N) = E_C + \Delta E$, sets the maximum temperature at which the structure has a resolvable electron number. In practice, the quantum dots investigated in this work have discernible electron numbers at temperatures between 1 and 2 K, giving capacitances $C \sim e^2/4k_B T = 0.1 - 0.5$ aF. The charging energy is in general approximately an order of magnitude larger than the energy level spacing ΔE .

3.3 Overhauser Fields and Nuclear Pumping

The nuclei of gallium, arsenic, and aluminum all possess non-zero spins. The nuclei⁴⁵ of the two isotopes of gallium, Ga⁶⁹ and Ga⁷¹, are spin-3/2, as is the nuclei⁶ of As⁷⁵. The nuclei⁷ of Al²⁷ is spin-5/2. Since these nuclei have spins that are greater than 1/2, they all possess nuclear quadrupole moments as well.

These nuclear spins interact with the electron spin primarily through the contact hyperfine interaction⁸, which we write following Ref. [108] as

$$\mathcal{H}_{HF} = \frac{2\mu_0}{3} g_0 \mu_B \hbar \sum_j \gamma_{n,j} (\vec{I}_j \cdot \vec{S}) |\Psi(\vec{r}_j)|^2, \quad (3.2)$$

where μ_0 is the vacuum permeability, g_0 is the free electron g-factor, $\gamma_{n,j}$ is gyromagnetic ratio of nuclear spin j at position \vec{r}_j with operator \vec{I}_j , \vec{S} is the electron spin operator, and Ψ is the electron wave function.

Following Refs. [69, 141], we re-write this interaction as

$$\mathcal{H}_{hf} = g^* \mu_B \vec{B}_{nuc} \cdot \vec{S}, \quad (3.3)$$

where g^* is the effective electron g-factor, and \vec{B}_{nuc} is an effective magnetic field

$$\vec{B}_{nuc} = \frac{2\mu_0}{3} \frac{g_0}{g^*} \hbar \sum_j \gamma_{n,j} \langle \vec{I}_j \rangle_\alpha |\Psi(\vec{r}_j)|^2, \quad (3.4)$$

where $\langle \vec{I}_j \rangle_\alpha$ is the average polarization of nuclear species α , ie if spin j is Ga⁶⁹, then $\langle \vec{I}_j \rangle_\alpha$ is the average polarization of Ga⁶⁹. This contact hyperfine term from the Ga and

⁴Ga⁶⁹: gyromagnetic ratio $\gamma_n/2\pi = 10.25$ MHz/T, natural abundance $\sim 60\%$ [54]

⁵Ga⁷¹: gyromagnetic ratio $\gamma_n/2\pi = 13.02$ MHz/T, natural abundance $\sim 40\%$ [54]

⁶As⁷⁵: gyromagnetic ratio $\gamma_n/2\pi = 7.32$ MHz/T, natural abundance $\sim 100\%$ [54]

⁷Al²⁷: gyromagnetic ratio $\gamma_n/2\pi = 11.10$ MHz/T, natural abundance $\sim 100\%$ [54]

⁸The contact hyperfine interaction comes from the *s*-like orbital nature of the bands that contribute to the quantum well [38]. If the quantum well were formed from *p*-like orbitals, as is the case in some hole-gasses [25], the electron wavefunction would avoid the nuclei, drastically decreasing the contact hyperfine term. The *p*-like orbitals from the valence band do experience a dipole-dipole couplings between nuclei and electron spin [142] which is absent for *s*-like orbitals.

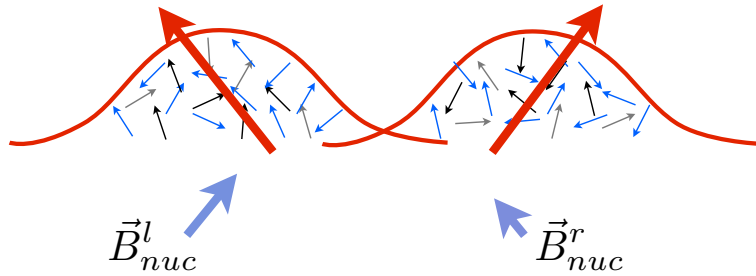


Figure 3.4: The contact hyperfine interaction can be approximated by an effective field \vec{B}_{nuc} , where the field strength depends on the alignment of the nuclear spins with the electron spin, weighted by the probability of the electron overlapping with that nuclei. The g -factor of the electron is approximately 1000 times that of the nuclei, indicated in the cartoon by the difference in arrow sizes.

As has been shown⁹ to cause dephasing and decoherence in spin qubits confined in GaAs-Al_{0.3}Ga_{0.7}As heterostructures [114]. The effective magnetic field \vec{B}_{nuc} is referred to as the Overhauser field, and as is clear in eq. (3.2), its interaction with the electron spin depends only on the total spin of the nuclear species, \vec{I}_j , and the overlap between the electronic wavefunction and the nuclei. While manipulating g^* would make \vec{B}_{nuc} change, it would not change the strength of the hyperfine interaction \mathcal{H}_{HF} .

The splitting between energy levels for each nuclear spin is approximately 40 neV/T of applied external field \vec{B}_{ext} , or a temperature of $\sim 500\mu\text{K}/\text{T}$. With lattice temperatures of $\sim 30 \text{ mK}$, electron temperatures typically $\sim 100 \text{ mK}$, and applied fields of less than 1 T, the spins are comfortably in a high temperature regime, where their polarization fluctuates easily.¹⁰ This allows us to treat the Overhauser field as a classical random variable which is Gaussian distributed about zero net polarization in the absence of Dynamic Nuclear Polarization (DNP). We can model the RMS fluctuations of \vec{B}_{nuc} as $\sigma_B = \frac{4.0 \text{ T}}{\sqrt{N}}$, where $N \sim 10^6$ is the number of nuclei that an electron in a single dot overlaps with [141].

⁹The aluminum atoms are only found in one boundary wall of the quantum well, where the electrons have a small ($\ll 10\%$) probability density [38], so we will ignore them.

¹⁰The low temperature regime is more accessible in Fractional Quantum Hall experiments, where lattice and electron temperatures can be $\sim 10 \text{ mK}$ and external fields reach $\sim 10 \text{ T}$.

At high fields, $\vec{B}_{ext} \gg \vec{B}_{nuc}$, the fluctuations of the longitudinal polarizations are somewhat inhibited, resulting in a slow evolution of \vec{B}_{nuc} and the dephasing of the spin qubits [141, 8], with a dephasing time in a single dot of $T_2^* = \hbar/g^*m\mu_B\sigma_B$. Fluctuations of the transverse polarizations remain rapid even at high magnetic fields [8]. References [16, 102] demonstrated the surprising result that the Larmor frequencies of all three nuclear species can affect the coherence of a double dot qubit at low external magnetic fields.

The mean value of \vec{B}_{nuc} can be shifted in a double quantum dot using DNP¹¹, as demonstrated in Refs. [116, 125], where a singlet state, $|S\rangle = \frac{1}{\sqrt{2}}(|\uparrow\downarrow\rangle - |\downarrow\uparrow\rangle)$, is passed adiabatically through a nuclear mediated anti-crossing to transition into $|T_+\rangle = |\uparrow\uparrow\rangle$. This anti-crossing is created by the transverse (flip-flop) terms in eq. (3.3), $B_{nuc}^+S^- + B_{nuc}^-S^+$, which flips one electron spin and flops a nuclear spin to conserve angular momentum. Since the state is transitioning from $|S\rangle$ to $|T_+\rangle$, a nuclear spin is always flipped downwards. Resetting this cycle without passing adiabatically through the anti-crossing leaves a net change of one unit of angular momentum, and repeating this cycle a large number of times ($\sim 10^6$) can result in sum polarizations in the tens of mT. As shown in chapter 4, the polarizations are not created evenly in each dot, which can result in polarization differences between dots to be as large as a few hundred mT [14]. Reference [14] uses a variation of this technique to control the random fluctuations in \vec{B}_{nuc} , resulting in longer dephasing times and opening the way to full two axis control in the double dot system [47].

3.4 Phonons

The relaxation processes discussed in section 2.5 require the qubit to shed the energy difference between states. In our solid state system, the most common way to shed energy at these energy scales (1-100 μ eV) is to emit a phonon, much like atomic states relax

¹¹Reference [151] also demonstrates DNP by applying an oscillating magnetic field. This method does not directly relate to the work in this thesis, so it will not be discussed in the remainder of this chapter.

through the emission of a photon. Phonons play an important role in the relaxation we see in chapter 4.

The probability of spontaneously emitting a phonon scales with the electron-phonon coupling strength and the density of states for phonons. The strongest coupling between phonons and the qubit occur when the phonon wavelength is similar to the size of the qubit, $\sim 50\text{-}500 \text{ nm}$. The phonon speed of different polarizations and directions of phonons in GaAs is of order $\sim 4000 \text{ m/s}$ [48, 99], which means that at our qubit length scales the phonon energies are $\omega \sim 10 \text{ GHz} \sim 40 \mu\text{eV}$. In this energy regime, 2D and 3D acoustic piezoelectric phonons have the strongest coupling to electrons [99]¹². The phonon density of states scales as ω^{D-1} , where D is the dimension of the phonon in question [48], indicating that the transition rate picks up an enhancement at high frequencies even as the phonon wavelength becomes incommensurate with the qubit.

To evaluate the possibility of stimulated emission, we need to consider the expected phonon occupation. At our base temperatures, $T \sim 50 \text{ mK}$, the occupation is given as $\langle n \rangle = 1/(\exp(\hbar\omega/kT) - 1) \sim 1 \times 10^{-4}$ for phonons with frequencies around 10 GHz, allowing us to only consider spontaneous emission. For phonons with frequencies around 1 GHz, the energy scale of the qubit in chapter 8, the expected occupation is ~ 0.5 , making effect associated with stimulated emission much harder to disregard.

3.5 Loss-DiVincenzo Qubits

In 1998, Daniel Loss and David DiVincenzo kicked off the field of spin qubits in semiconductor quantum dots with the publication of Ref. [88], where they described the Loss-DiVincenzo (LD) qubit. They proposed creating a quantum bit using the spin of an electron confined in a semiconductor quantum dot, where the basis states $|0\rangle$ and $|1\rangle$ were

¹²Deformation potential phonons become relevant at energy scales above $\sim 600 \mu\text{eV}$ [99].

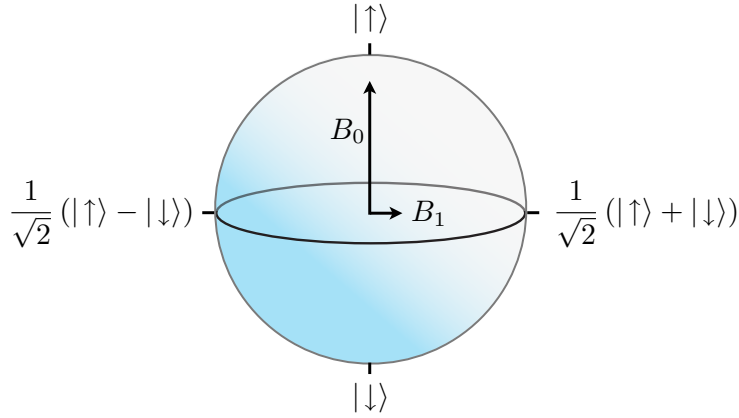


Figure 3.5: The Bloch sphere for an LD qubit in the lab frame. In the rotating frame, the term B_0 drops out, and the phase of B_1 determines where in the \hat{x} - \hat{y} plane the driving term points.

the spin states $|\uparrow\rangle$ and $|\downarrow\rangle$. Control of these qubits could be achieved through electron spin resonance (ESR), where a large magnetic field B_0 splits $|0\rangle$ and $|1\rangle$, and a small magnetic field perpendicular to B_0 drives rotations in the rotating frame. The two qubit gate came from an exchange interaction brought on by tunneling between quantum dots, which when combined with the single qubit ESR rotations allowed for universal set of one- and two-qubit gates.

Reference [46, 60] demonstrated the single-shot readout of a LD qubit by observing a spin dependent tunnel rate to the leads of the quantum dot [60], and measured the relaxation time $T_1 \sim 0.85$ ms at a field of 8 T. In Ref. [75], a stripline was fabricated on top of a double dot structure, allowing the authors to demonstrate the ESR control of a single LD qubit with a minimum Rabi period of $\tau_R \sim 108$ ns. In a subsequent work, the authors demonstrated a spin echo sequence with a coherence time of $T_2 \sim 500$ ns [78]. References [105], [83], and [118] demonstrated electric dipole spin resonance (EDSR) using electric fields to generate a small magnetic field via the spin orbit interaction ($\tau_R \sim 220$ ns), the Overhauser fields (incoherent), and a magnetic field gradient from a micromagnet

($\tau_R \sim 80$ ns) [107] respectively. This last technique gives each qubit a unique resonance frequency, allowing for qubits to be individually addressed in frequency space. The two-qubit gate and entanglement were demonstrated using single-shot readouts in Ref. [106].

None of the work in this thesis directly pertains to LD qubits, outside of the standard techniques in GaAs spin qubits, but the ESR and EDSR style of control is similar to the work presented in chapter 8. Additionally, Ref. [139] uses a triple quantum dot structure with a micromagnet to lay the groundwork for a three LD qubit device, which is another interesting direction that the triple quantum dot structures make possible.

3.6 Singlet-Triplet Qubits

Singlet-triplet (*ST*) qubits are spin qubits formed from the symmetric, $|T_0\rangle = \frac{1}{\sqrt{2}}(|\uparrow\downarrow\rangle + |\downarrow\uparrow\rangle)$, and anti-symmetric, $|S\rangle = \frac{1}{\sqrt{2}}(|\uparrow\downarrow\rangle - |\downarrow\uparrow\rangle)$, combinations of two electron spin states in individual dots of a double quantum dot system [87, 141]. An exchange splitting created by hybridization with the doubly occupied states, J , drives rotations around the $|S\rangle$ - $|T_0\rangle$ axis of the Bloch sphere while a magnetic field difference between dots, ΔB_z , drives rotations around the $|\uparrow\downarrow\rangle$ - $|\downarrow\uparrow\rangle$ axis [114, 141]. The electron occupation is confined to either the (2,0)-(1,1) or (1,1)-(0,2) regime, where manipulations are performed in the (1,1) region and initialization and readout are performed in the (0,2) or (2,0) regime, depending on which whether the left (2,0) or right (0,2) dot had a better readout.

The qubit is initialized by sitting in the double occupancy regime, which prepares the ground state: a (0,2) singlet.¹³ A tunnel coupling t between the left and right dots allows for the transfer of electrons between dots as a function of the detuning ε between left and right. This tunnel coupling reduces the energy of $|S\rangle$ compared to $|T_0\rangle$, opening up a splitting $J(\varepsilon)$. This splitting takes a vanishingly small value deeply detuned into (1,1), and

¹³For simplicity, we will restrict ourselves to considering the (0,2)-(1,1) regime for the remainder of this section. Everything covered here is applicable to the (2,0) regime as well.

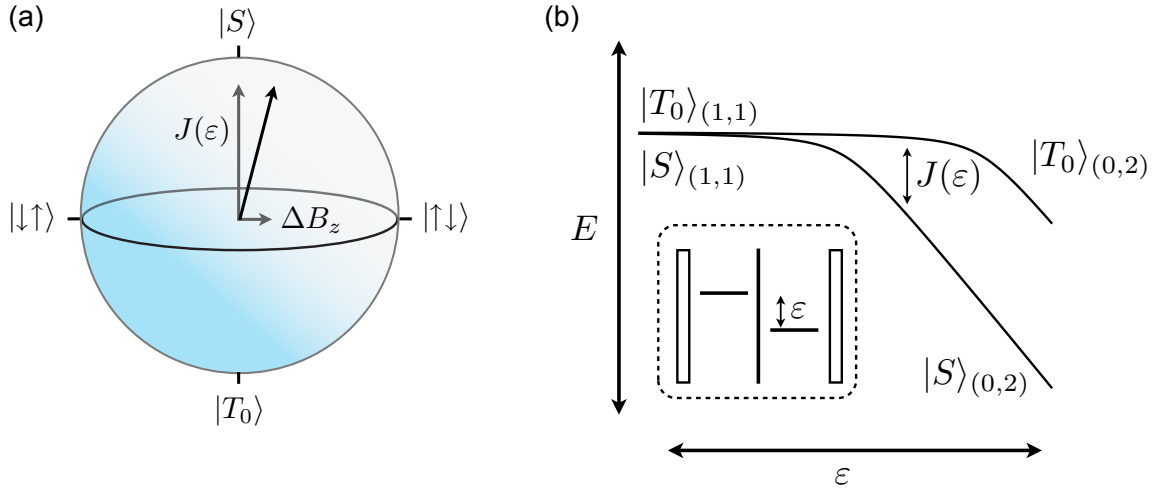


Figure 3.6: (a) The Bloch sphere for an ST qubit in the lab frame. Unlike the LD qubit in Fig. 3.5, there is no easy rotating frame application. Instead, ΔB_z is always on, and $J(\varepsilon)$ is pulsed on and off to drive rotations around an axis given by $\sqrt{J^2 + \Delta B_z^2}$, indicated by the solid black arrow. (b) A model of $J(\varepsilon)$ which includes both the tunnel coupling of the $|S\rangle$ states and the tunnel coupling of the $|T_0\rangle$ states. Experimentally, the curve is not necessarily well fit by this model, as shown in Ref. [41]. (inset) A schematic of the energy levels of the double dot. The parameter ε is the detuning between the $|S\rangle$ state in $(1,1)$ and the $|S\rangle$ state in $(0,2)$.

grows to a maximum of the singlet-triplet splitting in $(0,2)$. The intermediate regime occurs when part of $|S\rangle$ can tunnel into $(0,2)$ while $|T_0\rangle$ remains blocked in $(1,1)$. Measurement is performed by sitting at a detuning where $|S\rangle$ has fully tunneled into $(0,2)$ while $|T_0\rangle$ is trapped in $(1,1)$, and measuring the charge configuration. The work in chapter 4 addresses the effects that large ΔB_z has on this spin-to-charge conversion.

In Ref. [114], the initialization, one axis of control using the exchange interaction $J(\varepsilon)$, spin echo and readout were demonstrated. The rotation period due to the exchange axis was demonstrated to be as small as 700 ps, while the dephasing time was found to be $T_2^* \sim 10$ ns with a coherence time of $T_2 \sim 1.2$ μ s. The limiting factor was the nuclei, which caused a randomly fluctuating Overhauser field gradient between dots, ΔB_z , driving incoherent oscillations between $|S\rangle$ and $|T_0\rangle$.

Several schemes were proposed to remove the effects of nuclear decoherence by controlling the value of the nuclear gradient. The simplest is to work in a system without nuclear spins. A Si/Ge heterostructure recently demonstrated a *ST* spin qubit, and measured a dephasing time of $T_2^* \sim 360$ ns [92]. The cost in this case is that with the low nuclear spin environment, an additional source of magnetic field gradient, such as micromagnet [119, 118, 107], must be included to drive coherent rotations between $|S\rangle$ and $|T_0\rangle$.

If one remains working in GaAs, with its advantages of low effective electron mass¹⁴, the nuclear spins have to be controlled in some fashion. Polarizing the nuclear spins up would reduce the fluctuations in the gradient, and therefore the decoherence, but to achieve even an order of magnitude increase in T_2^* , the polarization would have to be $\sim 99\%$ [24]. The largest reported polarizations so far stand at 60% [18], making this an impractical solution for the time being.

Reference [125] proposed a second method of controlling the dephasing due to nuclei. The authors used a form on dynamical nuclear polarization (DNP) [116], where the $|S\rangle$ was repeatedly transformed into a $|T_+\rangle = |\uparrow\uparrow\rangle$, flipping an electron spin and “flopping” a nuclear one, to build up a small nuclear polarization. Subsequent operation of the qubit revealed a dramatic decrease in oscillations between $|S\rangle$ and $|T_0\rangle$, which the authors attributed to the reduction of ΔB_z and the creation of a “Zamboni” state. In chapter 4, we performed a follow up experiment with a more sensitive readout scheme, and propose an alternate explanation for the effects of DNP.

The third and most successful scheme for limiting the nuclear fluctuations was proposed and implemented in Ref. [15]. Here, the dynamic nuclear pumping scheme was

¹⁴The low effective electron mass allows for large lithographic structures which are easier to control. This fact has been one of the driving forces in GaAs successes to date.

conditional on the current gradient between dots, creating a closed-loop feedback that forced ΔB_z to a narrowed distribution around a known value. This narrowing of ΔB_z resulted in a $T_2^* \sim 94$ ns, approximately an order of magnitude increase in the dephasing time, while turning the incoherent rotation around ΔB_z into a coherent oscillation with a 7 ns period. A more careful treatment of the pulse shapes during the spin echos also resulted in a drastic increase in T_2 in Ref. [16], yielding a coherence time larger than 200 μ s. The latter technique was used in chapters 5 and 6 to study more complex dynamical decoupling techniques.

With these two enhanced techniques, full two-axis control and state tomography of a single *ST* qubit were demonstrated in Ref. [47]. This study then enabled the demonstration of a two qubit gate in Ref. [136]. Here it was noted that the noise in the exchange axis, $J(\varepsilon)$, which drives rotations between $|\uparrow\downarrow\rangle$ and $|\downarrow\uparrow\rangle$, was limiting the two qubit fidelity. In their device, they found that the two qubit interaction strength and the dephasing of each individual qubit were both proportional to $\frac{dJ}{d\varepsilon}$, which meant that the only way to improve the two qubit fidelity was to reduce the noise the qubit felt, either through dynamical decoupling [136] or an improvement in materials and equipment to reduce the total noise.

3.7 Exchange-only Qubits

In both *LD* (section 3.5) and *ST* (section 3.6) qubits in GaAs, a temporally or spatially varying magnetic field was required for two fast coherent rotation axes.¹⁵ In practice, these can be challenging to produce. It would be most convenient, from an experimental standpoint, to control a qubit using only electrical signals, which tend to be easier to generate, and allow for long range coupling through structures such as superconducting cavities [90, 113] and capacitive “dog bones” [144].

¹⁵The spin orbit effect does drive weak EDSR rotations in GaAs [105], but without a micromagnet to augment the field [118], the Rabi period was a sizable fraction of the coherence time [78].

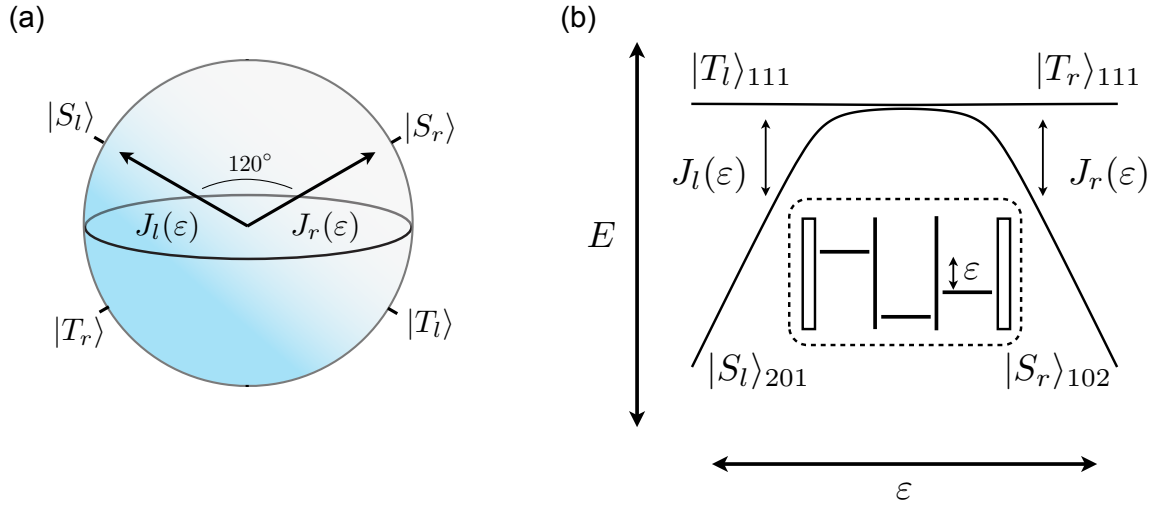


Figure 3.7: (a) The Bloch sphere for an Exchange-Only qubit in the lab frame. Chapter 8 covers a rotating frame application of this qubit. The exchange terms $J_l(\varepsilon)$ and $J_r(\varepsilon)$ are pulsed on and off to drive rotations around axes separated by 120° . (b) A model of $J_l(\varepsilon)$ and $J_r(\varepsilon)$ from the 201 charge region to the 102 charge region. (inset) A schematic of the three dot energy levels. The parameter ε is the detuning between the $|S_l\rangle$ state in 201 and the $|S_r\rangle$ state in 102.

Reference [42] proposed forming a qubit out of three electron spins, with two separate tunnel couplings between nearest neighbors in the three electron chain. These two tunnel couplings allow for two separate exchange interactions which act as rotators on the Bloch sphere separated by 120° . The initialization of a three electron qubit was demonstrated in Ref. [85], as well as the theory behind the exchange control of the specific three electron states. Reference [49] demonstrated the initialization and control of a three electron system that used adiabatic passage through nuclear mediated transitions, similar to work done in the double dot system with an $|S\rangle$ - $|T_+\rangle$ qubit [115]. Chapters 7 and 8 expand on the work of Ref. [85], demonstrating full electrical control and readout of an exchange only spin qubit, as well as tomography and resonant control in the style of NMR experiments. Appendix D covers the supplementary material for chapter 7, including the readout techniques and the detail of the generalized measurements. Appendix F sketches

the dipole moment that could be used to create a two qubit interaction for the qubit demonstrated in chapter 8.

Chapter 4

Singlet-Triplet Relaxation and Readout Visibility in an Overhauser Field Gradient

C. Barthel*, J. Medford*, H. Bluhm, A. Yacoby, C. M. Marcus

Department of Physics, Harvard University, Cambridge, Massachusetts 02138, USA

M. P. Hanson, A. C. Gossard

Materials Department, University of California, Santa Barbara, California 93106, USA

Using single-shot charge detection in a GaAs double quantum dot, we investigate spin relaxation time (T_1) and readout visibility of a two-electron singlet-triplet qubit following single-electron dynamic nuclear polarization (DNP). For magnetic fields up to 2 T, the DNP cycle increases Overhauser field gradients, which in turn decrease T_1 and consequently reduce readout visibility. This effect was previously attributed to a suppression of singlet-triplet dephasing under a similar DNP cycle. A model describing relaxation after singlet-triplet mixing agrees well with experiment. Effects of reduced pulse bandwidth on visibility are also reported¹.

* These authors contributed equally to this work.

¹This chapter is adapted from Ref. [6] with permission, © (2012) by the American Physical Society.

4.1 Introduction

Confined few-electron systems are of interest for investigating spin coherence and controlled entanglement, [27] as probes of mesoscopic nuclear spin environments, [40, 124] and as qubits for quantum information processing. [72, 59] The singlet-triplet basis of two electron spins in a double quantum dot has been investigated as a qubit with immunity to dephasing from uniform fields. [87, 114] An important source of both spin dephasing and relaxation in GaAs devices is hyperfine coupling to nuclear spins in the host material. The slow evolution of Overhauser fields allows echo techniques to recover phase coherence, [126, 124, 114] while even static gradients of Overhauser fields can induce triplet-to-singlet relaxation, [67] which limits the fidelity of readout. [8] It is therefore important to understand how gradients in local Zeeman fields, either from micromagnets [119, 107] or Overhauser fields, [47] affect singlet-triplet qubit relaxation, particularly during readout.

Dynamic nuclear polarization (DNP) using cyclic single-spin transitions can transfer angular momentum from electrons in the double dot (refreshed from reservoirs) into the host nuclei, inducing a net nuclear polarization. [116, 126, 47] In Ref. [125], it was observed that for tens of seconds following the application of the MHz DNP cycle, the probability, P_S , to measure a singlet outcome, after allowing a prepared singlet to evolve in separated dots, remained close to unity. This surprising observation was interpreted as the DNP cycle having reduced the difference in Overhauser fields between the two dots below the normal (thermal) fluctuation level while inducing a net polarization. That interpretation was consistent with some theoretical results, [122, 127, 138] but at odds with subsequent experiment [47] and more recent theory. [57]

In this paper, we show that over a broad range of applied magnetic fields, the DNP pumping cycle investigated in Refs. [116, 126, 125, 47] enhances rather than reduces

the gradient in nuclear polarization, along with inducing an average polarization. Rapidly repeated single-shot readout [8] reveals that the enhanced nuclear gradient leads to a reduction in the visibility of measured qubit precession. We investigate visibility as a function of nuclear field gradient, applied magnetic field, and gate voltage configuration during the measurement (readout) step of a cyclic pulse sequence. Simultaneously, triplet relaxation at the measurement point is measured in the time domain. We find that the dominant reduction in visibility for large nuclear polarizations is due to increased triplet relaxation during measurement, independent of applied magnetic field. We develop a model describing triplet decay via charge relaxation after singlet-triplet mixing driven by a Zeeman field difference between dots, including effects of finite pulse bandwidth. The model is found to be in very good agreement with experimental results.

These results suggest an alternative interpretation of the increased singlet measurement probability following DNP[125], which is that the enhanced nuclear field gradient induced by DNP causes rapid relaxation of the triplet state during measurement, which in turn results in a strongly diminished measurement visibility while the nuclei are out of equilibrium.

The remainder of the paper is organized as follows. Section 4.2 describes the double dot system and the experimental setup. The theory of the two-electron qubit system and nuclear pumping is presented in the first part of section 4.3. The second part of section 4.3 discusses mechanisms of spin relaxation during the measurement and presents our model of these effects, as well as effects of finite pulse bandwidth. Experimental results are presented in section 4.4, beginning with the measurement of nuclear gradients and precession visibilities. Observed connections between visibility, relaxation time and Overhauser field difference are then presented, along with data showing the influence of limited pulse bandwidth. Summary and conclusions are given in section 4.5.

4.2 System

The double quantum dot was formed by Ti/Au depletion gates on a GaAs/Al_{0.3}Ga_{0.7}As heterostructure with a two-dimensional electron gas (2DEG), with density $2 \times 10^{15} \text{ m}^{-2}$, mobility $20 \text{ m}^2/\text{Vs}$, 100 nm below the surface. A magnetic field of magnitude B was applied using a 3-axis magnet. Except where noted, a field of 200 mT was applied in the direction shown in Fig. 1(a).

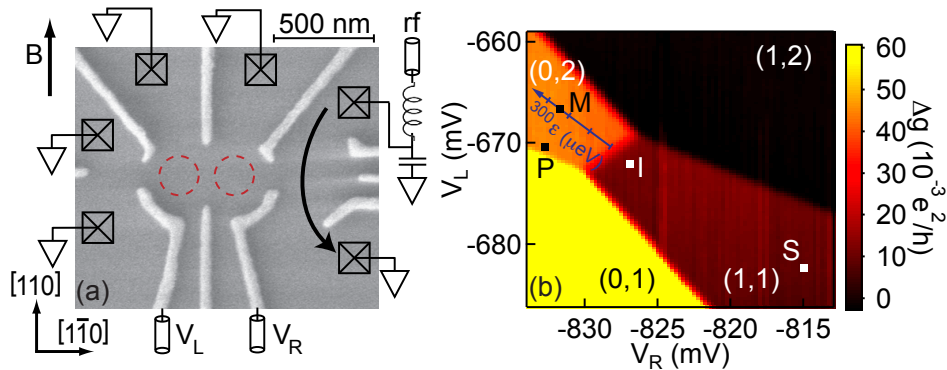


Figure 4.1: (a) (Color online) (a) Micrograph of lithographically identical device. Gate voltages, V_L and V_R , set the electrostatic energy of left and right dot. A sensor quantum dot on the right allows fast measurement of the double dot charge state via rf reflectometry. The direction of magnetic field, B , is indicated, as well as the GaAs crystal axes. (b) Change of sensor dc conductance Δg , with double dot charge state (N_L, N_R), constrained to (1,1), (0,2) in this work. The qubit state is controlled by the (1,1)-(0,2) energy detuning, ϵ , set by gate voltages V_L and V_R along the diagonal axis through the markers S, M. The scaling of detuning is $|\epsilon| = \eta \sqrt{\Delta V_L^2 + \Delta V_R^2}$, with a lever arm $\eta = 40 \mu\text{eV}/\text{mV}$ and voltage detunings, ΔV_L , ΔV_R , from the (1,1)-(0,2) charge degeneracy. Markers indicate gate voltages during pump- and probe-cycles. Singlet preparation at point P. Pump: $S-T_+$ mixing at point I, see text. Probe: Separation of singlet for $S-T_0$ mixing at point S and measurement at point M at variable detuning, $80 \mu\text{eV} < \epsilon_M < 260 \mu\text{eV}$.

A proximal radio-frequency sensor quantum dot (SQD) [Fig. 1(a)] was used to sense the charge state of the double dot.[5, 123] Reflectometry measurement on the SQD provides an output voltage, v_{rf} , with good signal-to-noise on sub- μs time scales.[5] The SQD was energized only during readout and so does not induce dephasing during gate

operations. Gate voltages V_L and V_R , pulsed using a Tektronix AWG5014, controlled charge occupancies N_L and N_R of the left and right dots. The charge state (N_L , N_R) was restricted to (1,1) and (0,2), and was controlled by gate voltages along an axis of energy detuning, ϵ , running between separation (S) and measurement (M) points [Fig. 1(b)]. Detuning scales as $|\epsilon| = \eta \sqrt{\Delta V_L^2 + \Delta V_R^2}$, where ΔV_L and ΔV_R are gate voltages relative to the charge transition point, and $\eta = 40 \mu\text{eV}/\text{mV}$, is the voltage-to-energy lever arm, calibrated via transport through the double dot.[66, 147]² Note that the two gates contribute symmetrically to detuning as observed experimentally. The influence of V_L and V_R on the interdot tunnel coupling is found to be small for the range of voltages used, and is neglected in the model presented below.

4.3 Theory, relaxation model

The dependence of the two-electron energy levels on detuning, ϵ , is shown in Fig. 2(a) in the regime relevant for qubit operation. The two-level system that forms the qubit is the two-electron singlet, S , and the $m = 0$ triplet, T_0 , of the (1,1) charge state. Preparation of the S state is achieved through relaxation into the (0,2) singlet state via electron exchange with the leads at point P [see Figs. 4.1(b) and 4.2(a)]. The (0,2) singlet can be separated into the (1,1) singlet, S , ($+z$ on the qubit Bloch sphere) by following the lower branch of the singlet anticrossing through $\epsilon = 0$ [large anticrossing between black curves in Fig. 2(a).]

Nuclear polarization can be created electrically by cycling ϵ through the anticrossing of the singlet S and the $m = 1$ triplet, T_+ , at point I [inset of Fig. 4.2(a)].[116, 47, 126, 125] First, moving slowly through the anticrossing, an electron spin is flipped and a

²The leverarms for gate voltages V_L and V_R are approximately equal in the measured device

nuclear spin is flopped via hyperfine interaction. The system is then brought quickly to $\epsilon > 0$, without spin flip, and is reset to a singlet state at P via electron exchange with the leads. Ideally, the nuclear pumping cycle flips one nuclear spin per cycle but in practice the efficiency is typically lower.

In an applied magnetic field (whose direction defines the z direction in real space), qubit states at the separation point, S, are split by the difference in the z components of Zeeman fields (including nuclear Overhauser fields), ΔB_z , between left and right dots. This causes a precession between S and T_0 at frequency

$$f_S = \frac{|g| \mu_B \Delta B_z}{h}, \quad (4.1)$$

where h is Planck's constant, μ_B is the Bohr magneton, and $g \sim -0.4$ is the electron g-factor in GaAs. The frequency shift due to residual exchange at the separation point, J_S , ³ can be neglected, as $J_S \sim 10$ neV (~ 0.5 mT) is much smaller than $g\mu_B\Delta B_z$ in the regimes considered in this paper. Including finite J_S , the qubit precesses with reduced visibility

$$V_J = \frac{\Delta B_z^2}{\Delta B_z^2 + (J_S/g^*\mu_B)^2}, \quad (4.2)$$

as shown theoretically [32] and experimentally in previous work. [84] In this work, however, $V_J \sim 1$.

The sensitivity of the qubit at point S to gradients in Overhauser fields is investigated using a probe cycle, executed after many DNP cycles. [124, 8, 47] The probe cycle first prepares a spin singlet in $(0, 2)$, then separates to point S for a time τ_S , and finally returns to the measurement point M. If the separated electrons are in a singlet configuration when the system is pulsed to M, they return to $(0, 2)$; if the two electrons are in a triplet state, they remain in $(1, 1)$. Superpositions are projected to one of the two charge states during

³ J_S , estimated to be $J_S \sim 10$ neV ± 5 neV, from the drop of V_J at the lowest measured field differences, results in a shifted frequency $f_S^* = \sqrt{f_S^2 + (J_S^2/h)^2}$, a negligible correction at the relevant frequencies.

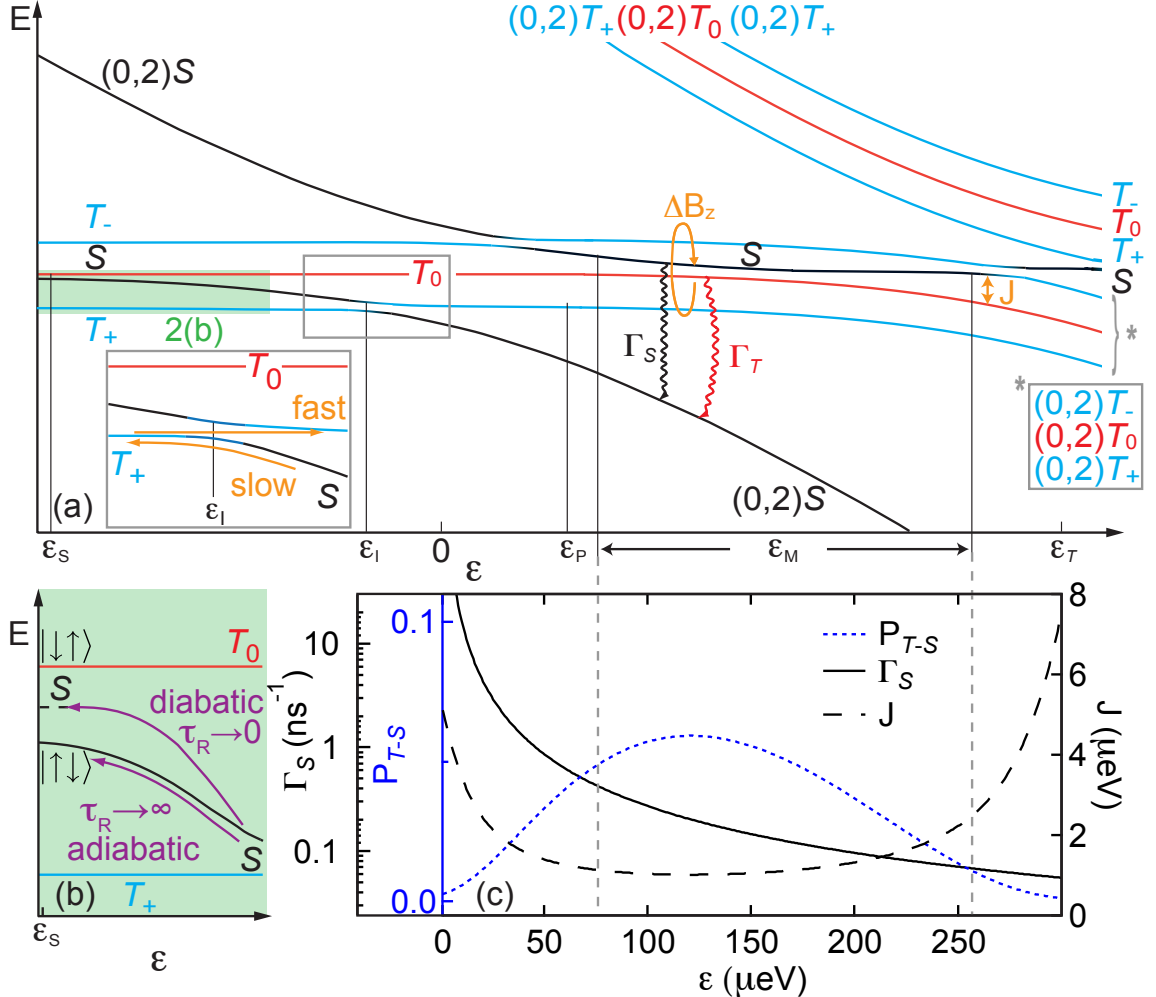


Figure 4.2: (Color online) (a) Energy level diagram as function of detuning, ϵ , charge state is (1,1) unless noted. Pulse-cycle detunings, ϵ_P of singlet preparation, ϵ_I of $S-T_+$ resonance, and ϵ_S of $S-T_0$ precession, are labeled. The relaxation channels of triplet state, T_0 , during measurement at ϵ_M are indicated: Charge relaxation, Γ_S , after $S-T_0$ mixing by nuclear field difference, ΔB_z , and processes not involving ΔB_z , at rate Γ_T . The $S-T_0$ mixing is suppressed by the exchange energy splitting, J , due to two anticrossings, at $\epsilon = 0$ between singlet states of (1,1)-(0,2), and at $\epsilon = \epsilon_T \sim 300 \mu\text{eV}$ between triplet states of (1,1)-(0,2). Inset: Illustration of pump cycle. (b) Ramping the detuning to ϵ_S in finite ramp time, τ_R , for an initial singlet state, S , yields an admixture of the ground state for $J \ll \Delta B_z$, $|\uparrow\downarrow\rangle$. Analogous the fidelity of mapping singlet to (0,2) and triplet to (1,1) during measurement is reduced by finite τ_R . (c) Charge relaxation rate, Γ_S , of metastable (1,1) singlet state, Eq. (4.10), and the singlet admixture, P_{T-S} , Eq. (4.5), of an initial triplet state, mixed by $\Delta B_z = 15 \text{ mT}$, and suppressed by the exchange energy, J , Eq. (4.7), plotted as function of detuning, ϵ . The plots use experimental parameters.

measurement. The qubit state can be detected accurately through this spin-to-charge conversion as long as the measurement time is shorter than the time needed for a triplet to relax to the (0,2) singlet.

The probability of measuring a singlet or a triplet was determined from the accumulating statistics of multiple single-shot measurements.[8] When the single-shot integration time τ_M was much shorter than T_1 , the distribution of outcomes form two separated, noise-broadened gaussians centered at the amplitudes corresponding to singlet (v_{rf}^S) and triplet (v_{rf}^T) states. Measurement visibility can be expressed as $V_M = F_S + F_T(T_1) - 1$, where F_S (F_T) is the singlet (triplet) fidelity, corresponding to the probability that a singlet (triplet) is identified as a triplet (singlet).[8] Depending on the ratio τ_M/T_1 , the metastable triplet may decay into a singlet during the measurement, leading to overcounting of singlets and undercounting of triplets in the output distribution.[8] Specifically—and this is a key point of the analysis—for fixed τ_M , readout visibility V_M decreases with decreasing T_1 . We note that the same reduction in visibility will be observed for continuous (rather than accumulated single-shot) readout, as was used in Refs. [114, 125].

To measure relaxation of triplet states into singlets during measurement, $v_{\text{rf}}(t)$ was measured with fine temporal resolution as a function of time, t , after moving to the measurement point M, then subsequently averaged over many successive pulse cycles. For short times, $t \ll T_1$, the signal corresponds to a mix of singlet and triplet states, $\langle v_{\text{rf}}(t) \rangle \sim (v_{\text{rf}}^S + v_{\text{rf}}^T)/2$, while for $t \gg T_1$ the signal corresponds to the (0,2) charge- and therefore singlet, $\langle v_{\text{rf}}(t) \rangle \sim v_{\text{rf}}^S$. Experimentally, we find that $\langle v_{\text{rf}}(t) \rangle$ is approximately exponential in t , giving a measure of the triplet relaxation time T_1 at the measurement point.

Relaxation pathways of the $m = 0$ triplet at M are shown in the energy diagram in Fig. 2(a). A difference in Zeeman fields, ΔB_z , between the two dots will cause rapid precession between T_0 and the excited (1, 1) singlet S , which can then relax to the (0,2)

singlet with a rate Γ_S via spin-conserving phonon emission. In contrast, direct relaxation of the (1,1) triplet, at a rate Γ_T , involves a change in total spin, mediated, for instance by electron exchange with the leads. This process is much slower.

In a previous measurement of triplet relaxation,[141, 67] exchange splitting J at point M was intentionally set to be small compared to ΔB_z . In this case, a T_0 state brought to M would oscillate between S and T_0 rapidly, giving an average singlet occupation of 1/2, and a decay rate $\Gamma_S/2$, independent of ΔB_z . On the other hand, in the present measurement and in previous T_2^* -type experiments [114, 125, 47], tunnel coupling was much larger, and J was not necessarily small compared to ΔB_z [see Fig. 2(a)]. The effect of significant J at the measurement point is a suppression of mixing between T_0 and S by an amount that depends on the ratio $\Delta B_z/J$. In the case of larger tunneling, the average S occupation at M, and thus triplet decay via fast, spin-conserving processes, increases with increasing ΔB_z .

Triplet decay is modeled by extending Ref. [141] to include nonzero J . Populations of the eigenstates of the Hamiltonian $\mathcal{H} = J(\epsilon_M)(\sigma_z + \mathbb{I})/2 - \Delta B_z \sigma_x/2$, decay with rates $\Gamma^\pm = \Gamma_S(\epsilon_M)|\langle S|E^\pm\rangle|^2 + \Gamma_T|\langle T_0|E^\pm\rangle|^2$.

The eigenstates of \mathcal{H} are given by

$$|E^\pm\rangle = \frac{\Delta B_z|S\rangle + \Omega^\pm|T_0\rangle}{\sqrt{\Delta B_z^2 + (\Omega^\pm)^2}}, \quad (4.3)$$

where $\Omega^\pm = J(\epsilon_M) \pm \sqrt{J(\epsilon_M)^2 + \Delta B_z^2}$.

In principle, this results in a bi-exponential decay of the triplet probability, $P_T(t) = P_T(0)(|\langle T_0|E^+\rangle|^2 e^{-t\Gamma^+} + |\langle T_0|E^-\rangle|^2 e^{-t\Gamma^-})$, but in practice, we expect only a single exponential. This is due to the fact that for $J \gg \Delta B_z$, $|E^-\rangle$ has a large overlap with the singlet, leading to a much larger Γ^- and a correspondingly small overlap with T_0 . For the largest nuclear polarizations $\Delta B_z \sim 35$ mT in this paper, and the smallest exchange split-

tings $J \sim 1 \mu\text{eV}$ in this model, $|E^-\rangle$ accounts for roughly one eighth of the initial triplet, and decays seven times more rapidly than the triplet-like eigenstate, $|E^+\rangle$. Under these conditions, it is appropriate to model $P_T(t)$ as $P_T(0)e^{-t/T_1}$, where

$$T_1 = (\Gamma^+)^{-1} \cong [\Gamma_S(\epsilon_M)P_{T-S} + (1 - P_{T-S})\Gamma_T]^{-1}, \quad (4.4)$$

and P_{T-S} is the fraction of the remaining triplet that overlaps with the (1,1) singlet,

$$P_{T-S} = |\langle S|E^+\rangle|^2 = \frac{1}{2} \left(1 - \frac{J(\epsilon_M)}{\sqrt{\Delta B_z^2 + J(\epsilon_M)^2}} \right). \quad (4.5)$$

In this model, Γ_T is governed by a decay channel that is independent of ΔB_z , such as exchange with the leads. In principle, non-spin-conserving process that generates the triplet relaxation also contribute to Γ_S , but since Γ_T is at least two orders of magnitude smaller than Γ_S for all ϵ_M in the experiment, we ignore such processes. To simplify the modeling further, we assume Γ_T does not depend on ϵ_M .

The dependence of the singlet-triplet splitting, J , on ϵ_M is dominated by the charge-state anticrossings between (1,1) and (0,2) for S and T_0 . We treat the anticrossings as independent and detuned from one another by an energy ϵ_T . The detuning-dependence of the singlet / triplet energy, E_{S/T_0} , is modeled following the treatment of a charge-state anticrossing in Ref. [141]. The energy of the lower branch of the anticrossing is given as $E_U(\epsilon) = \frac{t_c}{2} \tan(\theta(\epsilon))$ by Eq. (16)⁴ in Ref. [141], where

$$\theta(\epsilon) = \arctan \left(\frac{2t_C}{\epsilon - \sqrt{4|t_C|^2 + \epsilon}} \right) \quad (4.6)$$

is the adiabatic angle between (1,1) and (0,2). The tunnel coupling, t_C , may be different for singlet and triplet anticrossings. The energy of the upper branch of the anticrossing, $E_U(\epsilon) = \frac{t_c}{2} \tan(\theta(\epsilon) - \frac{\pi}{2})$, is given by Eq. (17) in Ref. [141].

⁴Equations (16) and (17) of Ref. [141] contain a sign error resulting in the lower branch being positive and the upper branch being negative for all ϵ . We invert the sign in our analysis.

At the measurement point, $0 < \epsilon_M < \epsilon_T$, the (1,1) singlet state corresponds to the upper branch of the singlet anticrossing, while the (1,1) triplet state corresponds to the lower branch of the triplet anticrossing. In the range of parameters that are investigated in this paper, the upper branch of the S anticrossing remains above the lower branch of the T_0 anticrossing for all ϵ_M , as depicted in Figure 2(a). The exchange energy at the measurement point

$$J = E_S(\epsilon_M) - E_{T_0}(\epsilon_M) \quad (4.7)$$

can therefore be expressed in terms of the expressions Eqs. (16,17) in Ref. [141]. The singlet energy is then given by

$$E_S(\epsilon) = E_U(\epsilon) = \frac{t_S^2}{\sqrt{4t_S^2 + \epsilon^2 + \epsilon}}, \quad (4.8)$$

where t_S is the tunnel coupling for the singlet anticrossing at $\epsilon = 0$. The energy of the triplet state is given by

$$E_{T_0}(\epsilon) = E_\cap(\epsilon - \epsilon_T) = \frac{-t_T^2}{\sqrt{4t_T^2 + (\epsilon - \epsilon_T)^2} - (\epsilon - \epsilon_T)}, \quad (4.9)$$

where t_T is the tunnel coupling for the T_0 anticrossing, detuned by ϵ_T from the S anticrossing. Equation (4.7) neglects the change in tunnel couplings due to changes in ϵ via gate voltage pulses, which changes the functional form.[84]

In previous experiments, Γ_S was found to decrease with increased detuning with a dependence falling between ϵ^{-1} and ϵ^{-2} , consistent with expected phonon mechanisms.[48] Specifically, piezoelectric interaction with 3D (2D) phonons, gives $\Gamma_S \propto \epsilon^{-1}$ (ϵ^{-2}).[48] Here, we assume a form

$$\Gamma_S = \alpha\epsilon^{-1} + \beta\epsilon^{-2}. \quad (4.10)$$

Figure 4.2(c) shows the singlet charge relaxation rate, Γ_S , Eq. (4.10), exchange, J , Eq. (4.7), and singlet admixture, P_{T-S} , of an initial triplet state, Eq. (4.5), as functions

of detuning, ϵ , using experimental parameters, discussed in section 4.4

We now discuss the effects of finite pulse rise times. Figure 4.2(b) shows a close-up of the level diagram at large negative detuning, ϵ_S , where S and T_0 are nearly degenerate and split by residual exchange, J_S , smaller than the typical Zeeman splitting between the two eigenstates in the nuclear Overhauser fields, $|\uparrow\downarrow\rangle$ and $|\downarrow\uparrow\rangle$. The arrows in $|\uparrow\downarrow\rangle$ indicate the electron spin in the left (right) dot being parallel (anti-parallel) to the quantization axis, $\Delta B_z > 0$ is assumed without loss of generality. In that notation the triplet/singlet state is $T_0/S = (|\uparrow\downarrow\rangle \pm |\downarrow\uparrow\rangle)/\sqrt{2}$ and in the limit, $J_S/\Delta B_z \rightarrow 0$, the nuclear field eigenstates become the eigenstates of the total Hamiltonian, $|E^\pm\rangle$, as illustrated in Fig. 4.2(b). A singlet, separated infinitely slowly with a ramp time, $\tau_R \rightarrow \infty$, is adiabatically loaded into the ground state of the nuclear field, $|\uparrow\downarrow\rangle$. [114, 141] In the limit of instantaneous separation, with a ramp time, $\tau_R \rightarrow 0$, (but still slow with respect to the interdot tunnel-coupling) a pure singlet state is initialized. For finite ramp- or rise-times, a singlet is initialized with a smaller than one fidelity, with some admixture of the nuclear eigenstates. Similarly, the recombination of the two electrons into one dot, after evolution in point S, only maps the S, T_0 state onto the (0,2), (1,1) charge state with unity fidelity for an instantaneous change of detuning, ϵ . For a finite ramp time, the visibility of singlet and triplet is reduced due to admixture of the nuclear eigenstates, analogous to the separation. In the final part of this paper, the influence of ramp- and rise-time on singlet-triplet precession visibility, V_R , incorporating visibility reduction due to the finite duration of both separation and recombination, is investigated.

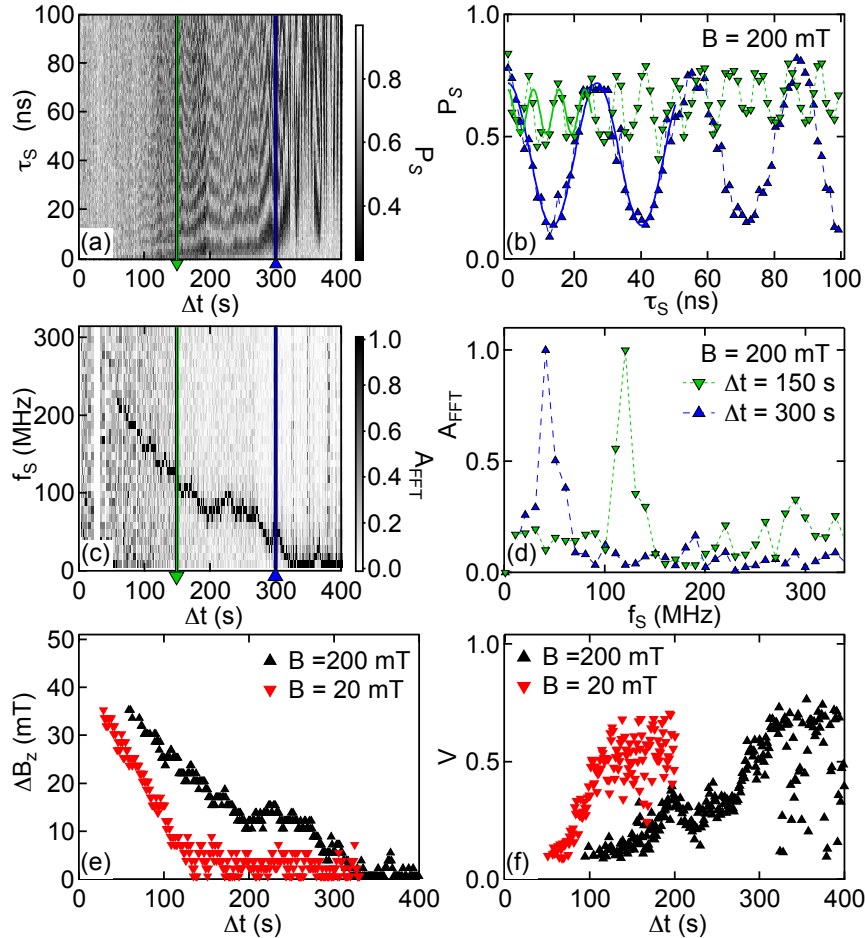


Figure 4.3: (Color online) (a) Probability, P_S , of singlet measurement outcome as function of $S-T_0$ mixing time, τ_S , and time, Δt , after a 60 s, ~ 4 MHz pump cycle; taken at $B = 200$ mT. Note the close to unity singlet measurement probability with low visibility, high frequency oscillations at small Δt . (b) Vertical cuts through (a), showing $P_S(\tau_S)$ curves, from which visibilities, V , and nuclear field differences, ΔB_z , are extracted via cosine fits, Eq. (4.11), for $\Delta t = 150$ s and 300 s. (c) Normalized Fourier-amplitudes, A_{FFT} , of (a), as function of frequency, f_S and time, Δt , after pumping. (d) Vertical cuts through (c), for $\Delta t = 150$ s and 300 s. (e) The nuclear field difference, ΔB_z (black markers), between left and right dot as function of time, Δt after pumping. The gradient, ΔB_z , is extracted from (c,d) by the relation (4.1), yielding $\Delta B_z \sim f_S$ mT/(6.16 MHz). The field difference for equivalent data at applied magnetic field, $B = 20$ mT, is shown as well (red, gray markers). At lower applied field the gradient decays faster, consistent with nuclear spin diffusion. [126, 124] (f) Visibility, V , of measured $S-T_0$ oscillations as function of Δt for data in (a) (black), and equivalent data at $B_{ext} = 20$ mT (red, gray), corresponding to data in (e).

4.4 Experimental Results

To study the nuclear gradients built by the electron-nuclear spin flips, pump-probe experiments are performed. The nuclear state is prepared by a pump cycle, with a ~ 4 MHz repetition rate, ramping through $\sim 10 \mu\text{eV}$ in ϵ around ϵ_I in 100 ns. The pump cycle is repeated ~ 240 million times over 60 s. The waveform generator then immediately performs a sequence of probe-cycles, with varying τ_S , to extract the nuclear field difference from S - T_0 precessions. The singlet measurement probability, P_S , is determined from single-shot measurements, following the procedure described in Ref. [8]. After preparation of $(0, 2)S$ at P, the probe-cycle separates the singlet to point S, see Figs. 4.1(b), 4.2(a), without intentional ramp time, $\tau_R = 0$. The system is held at detuning, $\epsilon_S \sim -700 \mu\text{eV}$, for the separation time, τ_S , and is then brought back to the measurement point M, where the charge signal, v_{rf} , is recorded over the total measurement time, $\tau_M^{\max} \sim 10 \mu\text{s}$. The charge signal, v_{rf} , is then integrated over ~ 300 ns, yielding single-shot measurement outcomes, which are identified as singlets or triplets by comparison to a threshold voltage, as discussed in Ref. [8]. For each separation time, τ_S , 100 single-shot measurements are performed, and the singlet measurement probability, P_S , is calculated as the percentage of singlet outcomes. Figure 4.3(a) shows P_S as function of τ_S and time, Δt , after the pump cycle. The separation time, τ_S , is stepped from 1 ns to 100 ns in 80 steps, for a total of 8000 single-shot measurements before the data is saved and processed. Sets of 8000 cycles, corresponding to a column in Fig. 4.3(a), are acquired every second, and are shown for two values of Δt in Fig. 4.3(b). Measurements immediately after the pump cycle, $\Delta t \lesssim 50$ s, show an almost unity singlet measurement probability, P_S , while after longer times, Δt , high frequency, low visibility oscillations become visible. At long times, $\Delta t \gtrsim 300$ s, close to unity visibility S - T_0 precessions with frequencies corresponding to equilibrium nuclear field

differences, ΔB_z , are observed. Fourier transforms (FFT) of P_S vs τ_S are calculated and the normalized Fourier amplitude A_{FFT} is plotted as function of frequency, f_S , and time after pumping, Δt , in Fig. 4.3(c). The Fourier transforms have clear maxima, as illustrated by two vertical cuts through the data in Fig. 4.3(c) at $\Delta t = 150$ s and $\Delta t = 300$ s, shown in Fig. 4.3(d). The frequency with the maximum FFT component is correlated for two adjacent columns and decreases with time after pumping, Δt , as expected for a decaying nuclear field gradient, ΔB_z . The values of nuclear field difference, ΔB_z , from FFT peak positions are used as starting points for fits of

$$P_S(\tau_S) = P_0 + 1/2 V \cos(2\pi f_S \tau_S) \quad (4.11)$$

to the time domain precession data, as shown in Fig. 4.3(b), with frequency, f_S , given by Eq. (4.1). The nuclear field differences, ΔB_z , extracted from the fits of Eq. (4.1) agree with the values from Fourier transform peak positions within one FFT bin size (~ 1 mT). For the cut at $\Delta t \sim 150$ s the visibility is $V = 0.2$, and the extracted nuclear field difference is $\Delta B_z \sim 20$ mT, while for the cut at $\Delta t \sim 300$ s, $V = 0.6$, and $\Delta B_z \sim 6$ mT.⁵ Figure 4.3(e) shows the nuclear field difference, ΔB_z , corresponding to the frequency, f_S , of maximum Fourier amplitude, A_{FFT} , in Fig. 4.3(c), according to Eq. (4.1). For an identical pump-probe experiment, performed at applied field, $B = 20$ mT, the nuclear field difference, ΔB_z , from FFT peak positions is shown as well. Note that the decay of the field difference with time, Δt , is faster for the 20 mT data, consistent with nuclear spin diffusion. [124, 126] Visibilities, V , extracted from fits to Eq. (4.11), are shown as function of Δt in Fig. 4.3(f).

To investigate the dependence of the visibility on the magnetic field difference and the mechanism reducing the visibility, pump-probe measurements are performed for nine

⁵Other parameters are, $P_0 = 0.6$ for $\Delta t = 150$ s, and $P_0 = 0.4$ for $\Delta t = 300$ s.

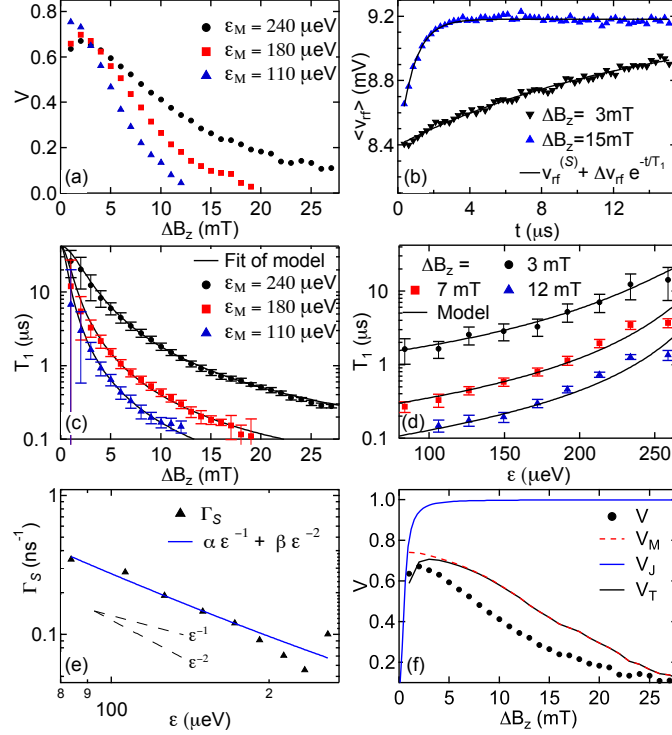


Figure 4.4: (Color online) (a) Measured Visibility, V , of $S-T_0$ precession over measured nuclear field gradient, ΔB_z , for three out of nine measured values of detuning, ϵ_M . (b) Average rf voltage amplitude, $\langle v_{\text{rf}} \rangle$, as function of time, τ_M , spent in the measurement point after $S-T_0$ mixing at point S for 2 different values of nuclear field gradient, ΔB_z . The rf voltage is averaged over 8000 experimental cycles, during which the mixing time, τ_S , is varied from 1 - 100 ns. The triplet relaxation time, T_1 , is extracted via exponential fits with $v_{\text{rf}}^S \sim 9 \text{ mV}$, $\Delta v_{\text{rf}} \sim -1 \text{ mV}$. For $\Delta B_z = 3 \text{ mT}$, $T_1 \sim 13 \mu\text{s}$, while for $\Delta B_z = 15 \text{ mT}$, $T_1 \sim 0.8 \mu\text{s}$. (c) Measured relaxation time, T_1 , of triplet T_0 at point M, as function of ΔB_z . Solid lines are a simultaneous fit of Eq. (4.4) to T_1 data at nine detunings ϵ_M . Fit parameters are $\Gamma_S(\epsilon_M)$, see (e), triplet relaxation rate $\Gamma_T \sim (40 \mu\text{s})^{-1}$, and the T_0 charge tunnel coupling, $t_T = 12 \mu\text{eV}$, which sets $J(\epsilon_M)$, Eq. (4.7). (d) T_1 as function of detuning ϵ_M , for 3 different ΔB_z , with model for T_1 , using the functional form (4.10) of $\Gamma_S(\epsilon_M)$ with parameters from (e), as the fit of $T_1(\Delta B_z)$ is discrete in ϵ_M . (e) Singlet relaxation rate Γ_S , extracted from simultaneous fit of Eq. (4.4) to data in (c,d). The solid line is a fit to Eq. (4.10), with fit parameters $\alpha \sim 11 \mu\text{eV ns}^{-1}$ and $\beta \sim 1600 (\mu\text{eV})^2 \text{ ns}^{-1}$. The functional form is consistent with rate contributions from 3D (α) and 2D (β) piezo-electric phonons, see Ref. [48]. (f) Measured visibility, V , from fits to $S-T_0$ precession data, see Fig. 3(b), for $\epsilon_M = 240 \mu\text{eV}$, with theoretically expected visibility, V_T , Eq. (4.12). The single-shot measurement visibility, V_M , is calculated from the measured T_1 and measurement SNR. The pure singlet precession visibility, V_J , Eq. (4.2), is reduced from unity due to finite exchange, $J_S \sim 10 \text{ neV} \sim 0.5 \text{ mT}$, at point S. [84]

values of measurement point detuning, ϵ_M , after a 60 s, 4 MHz pump cycle. Measured visibilities, V , are shown in Fig. 4.4(a) as function of the simultaneously measured nuclear field difference, ΔB_z , for three of the nine values of ϵ_M . The visibility sharply decreases with increasing magnetic field differences, while the curves for smaller detuning, ϵ_M , fall off with ΔB_z more rapidly. The total S - T_0 precession visibility, V_T , is reduced from unity due to two expected mechanisms,

$$V_T = V_M V_J, \quad (4.12)$$

where the measurement visibility, V_M , captures the imperfect fidelity of the single-shot measurement, as discussed in Ref. [8]. The intrinsic visibility, V_J given in Eq. (4.2), is ~ 1 for all but the smallest nuclear field differences, $\Delta B_z \lesssim 1$ mT. The measurement visibility, V_M , is calculated from the experimental parameters following the analysis in Ref. [8], and depends on the triplet relaxation time, T_1 , at the measurement point. In order to determine the dependence of T_1 on ΔB_z , the relaxation of a triplet state at the measurement point is monitored via the charge signal, v_{rf} , which is recorded with 100 ns time resolution over total time, $\tau_M^{\max} = 4 \mu\text{s}$. After 200 s, the total time spent at M is increased from 4 μs to 15 μs , while the time resolution is changed from 100 ns to 250 ns, in order to measure short and long relaxation times, T_1 , optimally using oscilloscope memory. Figure 4.4(b) shows the rf voltage signal, v_{rf} , averaged over 8000 probe-cycles, with τ_S ranging from 1 to 100 ns, as function of the time, τ_M , spent at the measurement point M. The averaged voltage, $\langle v_{\text{rf}} \rangle$, decays from $v_{\text{rf}}^{(S)} + \Delta v_{\text{rf}} P_T(0)$, corresponding to the initial mixture of charge states (0,2) and (1,1), to $v_{\text{rf}}^{(S)}$, corresponding to the (0,2) charge state. The exponential fit yields a value of $T_1 \sim 13 \mu\text{s}$ for data taken at $\Delta B_z = 3$ mT and a significantly smaller value of $T_1 \sim 0.8 \mu\text{s}$ for the data taken at $\Delta B_z = 15$ mT.

The triplet relaxation time, T_1 , is shown as function of nuclear field gradient,

ΔB_z , in Fig. 4.4(c) for three different values of measurement point detuning, ϵ_M . Like the visibility, T_1 decreases sharply with increasing ΔB_z , and with decreasing ϵ_M as shown in Fig. 4.4(d) for three different values of ΔB_z . To test whether the observed nuclear field dependence agrees with the model, a fit of Eq. (4.4) is performed simultaneously for nine values of ϵ_M , with ΔB_z as the independent variable. The exchange, $J(\epsilon_M)$, at point M is set by Eq. (4.7), and contains one fit parameter, the triplet tunnel coupling, $t_T \sim 12 \mu\text{eV}$. Assuming Eq. 4.7, the singlet tunnel coupling, $t_S \sim 10 \mu\text{eV}$, is estimated from the detuning, ϵ_I , of the $S-T_+$ resonance.⁶ The energy detuning, $\epsilon_T \sim 300 \mu\text{eV}$, of the triplet charge transition is determined from dc transport measurements. [66, 147] The fit, together with the measured parameters, yields the ϵ -dependence of exchange energy, $J(\epsilon_M)$, shown in Fig. 4.2(c). The bare triplet relaxation rate, $\Gamma_T \sim (40 \mu\text{s})^{-1}$, is assumed to be equal for all detunings, an estimation that is justified by the weak dependence of Eq. (4.4) on Γ_T for $\Delta B_z > 1 \text{ mT}$ and because measured values of T_1 agree with each other within the errors at small ΔB_z . For the singlet charge relaxation rate, $\Gamma_S(\epsilon_M)$, one fit parameter is used for each detuning, ϵ_M , yielding the values shown in Fig. 4.4(e). The rate, Γ_S , decreases with increasing detuning, and a fit of Eq. (4.10), yielding $\alpha \sim 11 \mu\text{eV ns}^{-1}$ and $\beta \sim 1600 \mu\text{eV}^2 \text{ns}^{-1}$, shows reasonable agreement with the data. At $\epsilon_M \sim 150 \mu\text{eV}$, the contributions from 2D and 3D phonons are about equal. The charge relaxation rates are consistent with the values measured in Ref. [48], when taking into account the difference in tunnel couplings, t_S . Deviations from the form (4.10) are expected, e.g. due to resonances from finite lengths in the phonon environment. [48] Figure 4.4(d) shows the model, Eq. (4.4), with $\Gamma_S(\epsilon_M)$ from Eq. (4.10), using α and β from the fit in Fig. 4.4(e). Note that the extracted values of α and β are rough estimates, as the functional form of $J(\epsilon_M)$, Eq. (4.7), is only approximate.

⁶At ϵ_I , the exchange energy, J_S , is equal to the Zeeman energy of T_+ . Comparison with $J_S = t_S^2 / (\epsilon_I - \sqrt{4t_S^2 + \epsilon_I^2})$, from Ref. [141], yields an estimate of t_S .

The detuning dependence of Γ_S , assuming Eq. 4.10 and using the obtained fit parameters α and β , is shown in Fig. 4.2(c). Since $\Gamma_S \propto t_S^2$, [48] and roughly $J \propto t_S^2$ (t_T increases with t_S), the first and dominant term in Eq. (4.4) becomes $\propto \Delta B_z^2/t_S^2$ for $\Delta B_z < J$. Contrary to intuition, a more transparent tunnel barrier yields longer triplet relaxation times, which is beneficial for quantum information processing, where large tunnel couplings enable fast operations. [114, 47]

Comparison of the measured visibility, V , shown in Fig. 4.4(f), with the expected total visibility, V_T , from Eq. (4.12), calculated from measured triplet relaxation times, T_1 , shows qualitative agreement. The theory curve, V_T , slightly overestimates the measured visibility except for low values of ΔB_z . We speculate that this deviation is due to imperfect initialization (separation) and recombination of a singlet state, reducing the measured visibility,

$$V = V_T V_R. \quad (4.13)$$

The ramp- and rise- time induced visibility, V_R , captures the reduction in visibility due to an admixture of the nuclear ground state because the separation of the singlet is not completely diabatic, see Fig. 4.2(b), and the analogous reduction because the recombination of the two electrons into one dot is not diabatic either. To test this hypothesis, pump-probe experiments with an intentional ramp time, τ_R , during the probe cycle are performed. As discussed above, a 4 MHz pump cycle is executed for 60 s. During the subsequent probe-cycles, a prepared singlet is separated from the (0,2) charge state at M to the (1,1) charge state at point S over the ramp time, τ_R . After evolution in the nuclear field difference, ΔB_z , the system is ramped back to the point M, over the same ramp time. The singlet measurement probability, P_S , is measured for the same parameters as the data in Fig. 4.4, and the triplet relaxation time, T_1 , is measured as discussed for Fig. 4.4(b). As a control, a pump-probe experiment without intentional ramp is performed under the same conditions.

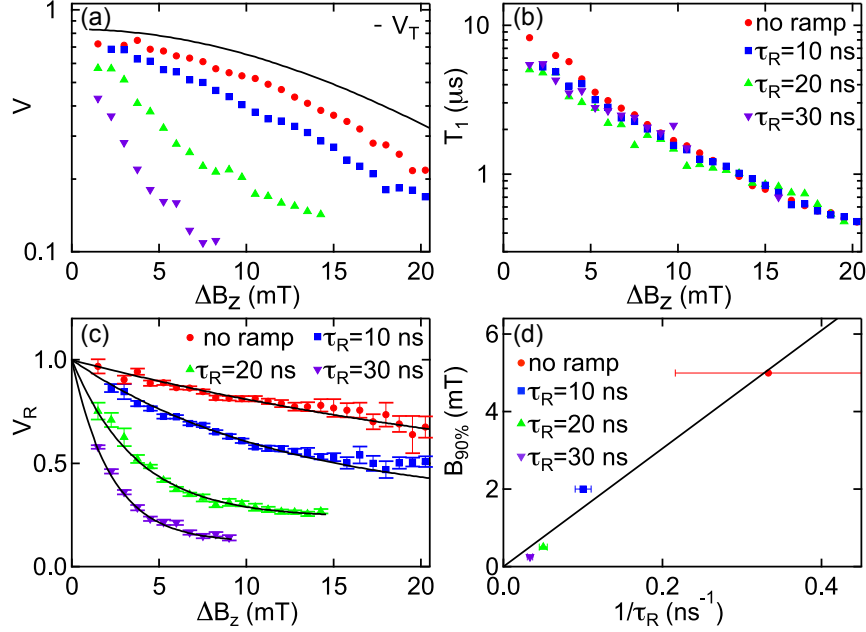


Figure 4.5: (Color online) (a) Measured Visibility, V , of $S-T_0$ precession over field gradient, ΔB_z , for precession experiments, in which the singlet is separated from energy detuning ϵ_M to ϵ_S over different ramp times τ_R . The expected total visibility, V_T , calculated from the measured relaxation time, T_1 (b), as discussed for Fig. 4(f), is shown as a solid line and does not depend on ramp time, τ_R . For $\tau_R = 40$ ns the $S-T_0$ precessions can no longer be clearly distinguished from the noise floor. (b) Singlet relaxation time, T_1 , as function of nuclear field difference, ΔB_z , showing no dependence on ramp time, τ_R . (c) Pulse duration induced visibility, $V_R = V/V_T$, of (1,1) singlet as function of nuclear field gradient for different τ_R , calculated from data in (a). The solid lines are fits, $V_R = e^{-\Delta B_z/B_w} + V_0$, with a phenomenological width, B_w , to extract the initialization range, $B_{90\%}$, the field difference for which the singlet-triplet visibility is down to $V_R = 0.9$. (The saturation values, V_0 , used in fits in Fig. 4.5(c), may be spurious since visibilities are approaching the noise levels. Initialization range, $B_{90\%}$, is used to obtain a width insensitive to errors in low V_R values at high ΔB_z .) (d) Initialization range, $B_{90\%}$, the nuclear field difference, for which $V_R = 0.9$, as function of inverse ramp duration, $1/\tau_R$. Extrapolation of the linear fit (solid line), suggests that V_R is independent of ΔB_z for $\tau_R \rightarrow 0$. The effective ramp due to pulse rise time for the data without intentional ramp is estimated to be $\tau_R \sim 3$ ns \pm 2 ns, and is set by the bandwidth of the coaxial cables.

The measured visibilities, V , are shown in Fig. 4.5(a), together with the expected visibility, V_T , calculated from the measured T_1 , using Eq. (4.12) and following Ref. [8]. The relaxation time, T_1 , does not depend on τ_R as shown in Fig. 4.5(b). The ramp- and rise- time induced

visibility, V_R , shown in Fig. 4.5(c), is calculated as the ratio, $V_R = V/V_T$, of measured and expected visibility. For larger ramp times, V_R falls off with ΔB_z more rapidly. Due to the finite rise time of the pulses, the data without intentional ramp time has an estimated ramp time, $\tau_R \sim 3$ ns, and $V_R < 1$, at finite nuclear field differences. To characterize the decline in visibility with ΔB_z , we define the initialization range, $B_{90\%}$, the maximum nuclear field gradient for which $V_R \geq 0.9$. A phenomenological exponential curve is fitted to the visibilities shown in Fig. 4.5(c) to extract $B_{90\%}$, which increases with increasing ramp rate, $1/\tau_R$, as shown in Fig. 4.5(d). The increase in $B_{90\%}$ is approximately linear in $1/\tau_R$. A linear fit, shown in Fig. 4.5(d) agrees reasonably well with the data. This suggests that the smaller than unity visibility V_R for the probe-cycle without intentional ramp time is due to the finite pulse rise time. For higher bandwidth coaxial cables, a larger singlet initialization fidelity may be obtained, even in the presence of magnetic field gradients.

Pump probe experiments have been performed in six cool-downs of four devices for three different magnetic field directions, along all three crystal axes, indicated in Fig. 4.1(a), and at a wide range of magnetic field magnitudes between 10 mT and 2 T. For data shown in this paper, B is applied along the direction marked in Fig. 4.1(a). At all fields, the same qualitative phenomenology, i.e. a nuclear field gradient and an average nuclear polarization of comparable magnitude, have been observed, while at no field value a suppression of nuclear field fluctuations was found. We speculate that the phenomenology reported in Ref. [125] was the result of a nuclear field gradient, ΔB_z , much larger than the equilibrium field fluctuations, suppressing the measurement visibility. Drifts of the measurement point M result in changes of sensor conductance and measurement visibility that mimic a reduction of P_S for long separation times, as observed and interpreted as a T_2^* envelope in Ref. [125]. The fast, low-visibility precession would not be distinguishable from a sup-

pression of dephasing without the fast measurement techniques that are employed in this paper.

Different applied magnetic fields change the time constant at which nuclear polarizations decay, see Fig. 4.3. However the dependence of visibility, V , and triplet relaxation time, T_1 , on the nuclear field difference, shown in Fig. 4.6(a) and (b), do not change with applied magnetic field, B .

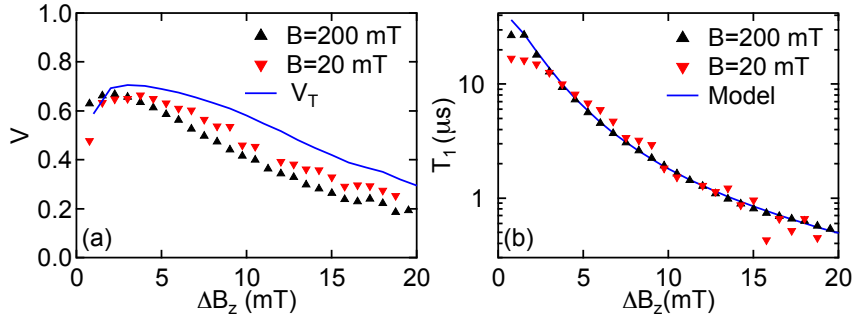


Figure 4.6: (Color online) (a) Parametric plot of measured visibility, V , shown in Fig. 3(f), against measured nuclear field difference, ΔB_z , shown in Fig. 4(e), for two different applied magnetic fields, B . The solid line is the expected total visibility, V_T , from the simultaneously measured relaxation time, T_1 , see Fig. 3(f). (b) Measured triplet relaxation time, T_1 , as function of measured nuclear field difference, ΔB_z , for two different applied magnetic fields, with the model, Eq. (4.4). The corresponding visibility is shown in (a) and the time dependence of polarization and visibility is shown in Fig. 3. The ΔB_z dependence of V and T_1 does not depend on the applied magnetic fields.

4.5 Conclusions

An enhanced nuclear field gradient is always found for an electron-nuclear spin pump cycle. The resulting difference in z components of Overhauser fields, ΔB_z , reduces the relaxation time of a triplet state during the measurement. In the presence of a finite pulse ramp- or rise-time, a gradient appears to furthermore degrade the fidelity of spin to charge conversion, when initializing a (1,1) singlet state by separation of a (0,2) singlet or when mapping spin states onto charge states by recombining a (1,1) charge state into (0,2).

The $S-T_0$ measurement visibility reduction due to field gradients offers an alternative explanation of the experiments discussed in Ref. [125], without requiring new physics or exotic nuclear states. For applications of spin qubits in quantum information processing, where magnetic field gradients are promising tools in the realization of quantum gates, [47, 119] it is desirable to engineer the exchange profile to allow long triplet lifetimes, e.g. by having an (0,2) singlet-triplet splitting slightly larger than the measurement detuning. In the presence of a magnetic field difference, the device should be tuned to a large inter-dot tunnel coupling with a measurement point chosen at large detuning, where exchange protects the triplet and the charge relaxation rate is small. To mitigate errors from finite pulse rise times, an initialization of the qubit via an adiabatic loading of $|\uparrow\downarrow\rangle$, followed by a $\pi/2$ pulse, may be preferable over the diabatic initialization used here and in Refs. [114, 47, 124]. We would like to point out that the results of this paper do not imply a short relaxation time of the qubit while it is operated in the (1, 1) state, where T_1 is much longer and expected to be independent of magnetic field gradients. [3]

Acknowledgments

We acknowledge funding from ARO/iARPA, the Department of Defense. This work was performed in part at the Center for Nanoscale Systems (CNS), a member of the National Nanotechnology Infrastructure Network (NNIN), which is supported by the National Science Foundation under NSF award no. ECS-0335765. We thank D. J. Reilly, J. M. Taylor and S. Foletti for useful discussion.

Chapter 5

Interlaced Dynamical Decoupling and Coherent Operation of a Singlet-Triplet Qubit

C. Barthel*, J. Medford*, C. M. Marcus

Department of Physics, Harvard University, Cambridge, Massachusetts 02138, USA

M. P. Hanson, A. C. Gossard

Materials Department, University of California, Santa Barbara, California 93106, USA

We experimentally demonstrate coherence recovery of singlet-triplet superpositions by interlacing qubit rotations between Carr-Purcell (CP) echo sequences. We then compare performance of Hahn, CP, concatenated dynamical decoupling (CDD) and Uhrig dynamical decoupling (UDD) for singlet recovery. In the present case, where gate noise and drift combined with spatially varying hyperfine coupling contribute significantly to dephasing, and pulses have limited bandwidth, CP and CDD yield comparable results, with $T_2 \sim 80 \mu\text{s}$.

¹

* These authors contributed equally to this work.

¹This chapter is adapted from Ref. [7] with permission, © (2010) by the American Physical Society.

5.1 Introduction

The singlet ($S = (|\uparrow\downarrow\rangle - |\downarrow\uparrow\rangle)/\sqrt{2}$) and $m = 0$ triplet ($T_0 = (|\uparrow\downarrow\rangle + |\downarrow\uparrow\rangle)/\sqrt{2}$) spin states of two electrons in a double quantum dot form a versatile qubit that is inherently protected from collective dephasing [87] and allows sub-nanosecond rotation around one axis via electrical control of the exchange interaction [114]. Rotations around a second axis, needed for universal control, can be induced by a Zeeman field difference between the two quantum dots, created by a proximal micromagnet [107] or controlled Overhauser fields [47]. Fast measurement of a qubit state has been demonstrated for two-electron spin states [98, 8, 5], and also for single electron spin states [46, 3].

Temporal fluctuations of Overhauser fields evolve slowly compared to gate operation times [124], allowing a simple one-pulse Hahn echo [58] to significantly extend qubit coherence [114]. By repeating π -pulses on shorter intervals, Carr-Purcell (CP) sequences [23]² can extend qubit coherence to impressively long times [14]. Theoretical work and experiments in other systems suggests that, depending on the environmental noise spectrum, echo sequences more complex than CP may further increase coherence times [71, 157, 145, 86, 12, 111]. To date, experimental demonstration of decoupling schemes for spin qubits have been limited to recovery of an initially prepared singlet state. For applications in quantum information processing, however, decoupling schemes must preserve an arbitrary qubit state [103].

In this chapter, we demonstrate echo recovery of singlet-triplet superposition amplitude by embedding qubit rotations about two axes of the Bloch sphere between CP sequences. For Overhauser-driven rotations about the x axis of the Bloch sphere, and exchange-driven rotations about the z axis, ensembles of single-shot singlet measurements

²In this context, repeated π -pulses around the z axis can be denoted Carr-Purcell (CP) or Carr-Purcell-Meiboom-Gill (CPMG) [96]. We use CP for brevity

show coherent oscillations for total sequence times (including echoes) of 60 μs . We then compare singlet recovery using Hahn, CP, concatenated dynamical decoupling (CDD) [71, 157], and Uhrig dynamical decoupling (UDD) [145] schemes. We find that for the present setup, a 16-pulse CP sequence and 21-pulse (fifth order) CDD sequence yield comparable performance, both with $T_2 \sim 80 \mu\text{s}$, while a 22-pulse (22nd order) UDD performs less well, possibly due to the limited bandwidth of the pulses.

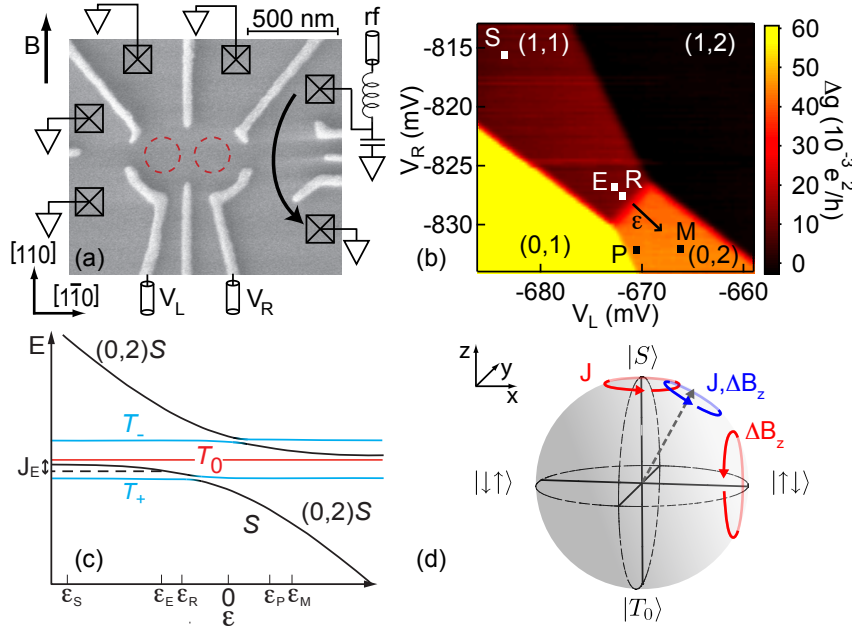


Figure 5.1: (Color online) (a) Micrograph of lithographically identical device with contacts, dot locations, and GaAs crystal axes indicated. Gate voltages, V_L and V_R , set the energy of left and right dot. An rf-coupled sensor dot measures the double dot charge state. (b) dc conductance change, Δg , with double dot charge state. Markers indicate gate voltages during experimental pulse sequences. Detuning, ϵ , is controlled by V_L and V_R along the diagonal through points S and M. (c) Energy level diagram as function of detuning ϵ , indicating locations of ϵ_P where the $(0,2)$ singlet is prepared, ϵ_S of separated electrons for dephasing and x -rotations, ϵ_E of exchange pulse and π -pulses, ϵ_R of mapping ramps, and ϵ_M of the measurement point. Exchange energy, J_E used for π pulses is indicated. (d) Bloch sphere of the singlet-triplet qubit, with mechanisms of rotation indicated, exchange energy, J , and Zeeman field difference along the applied field direction, ΔB_z , drive rotations around the qubit z -axis and x -axis respectively.

5.2 System

The double quantum dot and sensor are defined by Ti/Au depletion gates on a GaAs/Al_{0.3}Ga_{0.7}As heterostructure with a two-dimensional electron gas (density $2 \times 10^{15} \text{ m}^{-2}$, mobility $20 \text{ m}^2/\text{Vs}$) 100 nm below the surface. An in-plane magnetic field, $B = 750 \text{ mT}$, was applied perpendicular to the dot connection axis, as indicated in Fig. 5.1(a). Measurements were carried out in a dilution refrigerator (electron temperature $\sim 150 \text{ mK}$) configured for high-bandwidth gating and rf reflectometry. The state of the double quantum dot was controlled by pulsed gate voltages V_L , V_R [Figs. 5.1(a,b)] using a Tektronix AWG 5014. Except for point P, where the (0,2) singlet is prepared, gate configurations fall on a line between (0,2) and (1,1) charge states, parameterized by the detuning, ϵ [Fig. 5.1(b)]. To reduce effects of voltage drift, average gate voltages were set to the separation point S using a compensation pulse between measurement and preparation [14]. The charge state of the double dot was detected using rf reflectometry [123] of a proximal sensor quantum dot, integrated over $\sim 600 \text{ ns}$ to yield a single-shot measurement, as described previously [8, 5].

All pulse sequences start by allowing two electrons at point P to relax to the (0,2) singlet [Fig. 1(c)]. Fast separation of the electrons to point S initializes the system into the (1,1) singlet, the $+z$ direction on the qubit Bloch sphere [Fig. 1(d)]. Alternatively, fast separation from P to R followed by adiabatic separation from R to S initializes the system into the (1,1) ground state of the Overhauser fields, $|\uparrow\downarrow\rangle$, the $+x$ direction on the Bloch sphere [114]. At point S, exchange splitting, J_S , is negligible but Overhauser gradients are not, and the qubit precesses rapidly around its x axis at frequency $f_S = g^* \mu_B \Delta B_z / h$, where $g^* \sim -0.4$ is the GaAs g-factor and ΔB_z is difference in Zeeman fields (in this case, Overhauser fields) along the direction of applied field. Controlled rotation about the z -axis

of the Bloch sphere is realized by pulsing from S to E, where a large exchange energy, J_E , causes qubit rotation at frequency $f_E = \sqrt{J_E^2 + (g^*\mu_B\Delta B_z)^2}/h$. Frequency f_E includes a small quadrature contribution from ΔB_z that causes inhomogeneous dephasing and alters the rotation axis during the exchange pulse [Fig. 1(d)]. After evolution at S and E, the qubit is measured by pulsing to the measurement point, M. The singlet state can recombine in (0,2) while the triplet state remains in (1,1). The resulting charge state difference is detected by the sensor quantum dot as V_{rf} [8, 5].

5.3 Decoherence and Dynamical Decoupling

Dephasing of the $S-T_0$ qubit can arise from thermally driven evolution of the Overhauser field difference between dots or from electron motion in a spatially varying Overhauser field caused by gate noise or drift. Here, we do not distinguish between decoherence due to quantum entanglement with the environment and dephasing due to a noisy classical environment. Because Overhauser fluctuations are concentrated below 1 Hz [124], apparent dephasing due to precession of the qubit can be readily recovered using dynamical decoupling schemes applied on faster time scales [114, 14]. The simplest such scheme, Hahn echo (HE), uses a single π -pulse, realized in this case by pulsing to E for a time $\pi/(\hbar J_E)$ after a (dephasing) interval $\tau_D/2$ at S, followed by a second (rephasing) interval at S for $\tau_D/2$. Multiple π -pulses applied within a given interval can extend coherence by shortening the interval between dephasing and rephasing, during which the environment may have evolved [23]. The simplest multi-pulse scheme, the CP sequence, inserts several of equally spaced π -pulses surrounded by dephasing and rephasing intervals [23]³.

As a first approach to dynamical decoupling of arbitrary qubit states, we investigate x and z rotations interlaced between two CP sequences. For this purpose, the sequence

³In this context, repeated π -pulses around the z axis can be denoted Carr-Purcell (CP) or Carr-Purcell-Meiboom-Gill (CPMG) [96]. We use CP for brevity.

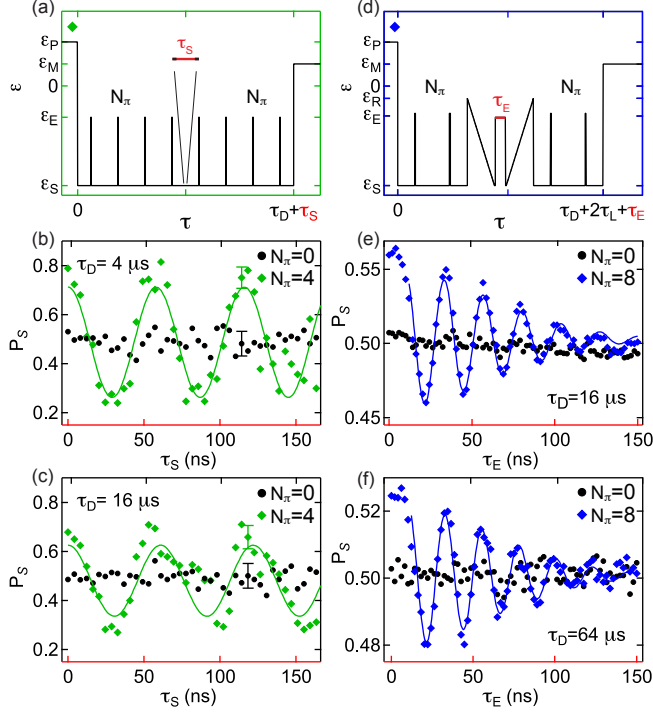


Figure 5.2: (Color online) (a) Pulse sequence for x rotations, cycling through preparation (P), separation (S), exchange-echo (E), and measurement (M) points in gate-voltage space. Evolution at S for time τ_S produces x rotations due to Overhauser gradient. (b) Singlet return probability, P_S , as function of τ_S for $N_\pi = 4$ (green diamonds) and $N_\pi = 0$ (black circles), with $\tau_D = 4 \mu s$, along with cosine fit (curve) to data, post-selected to have a specific period (see text). Without echo pulses ($N_\pi = 0$), no oscillations are seen. Error bar reflects statistics of 100 single-shot measurements per point. (c) Identical to (b) with $\tau_D = 16 \mu s$, showing reduced visibility. (d) Pulse sequence for z rotations: after an initial CP sequence, singlet is mapped to $|\uparrow\downarrow\rangle$ by pulsing to R and ramping to S. Pulsing to E for τ_E induces rotation around z . Pulsing to S then ramping to R then pulsing back to S maps $|\uparrow\downarrow\rangle$ back into the singlet. After a second CP series, pulsing to M yields single-shot measurement. (e) Singlet probability, P_S , as function of τ_S for $N_\pi = 8$ (blue diamonds) and $N_\pi = 0$ (black circles), with $\tau_D = 16 \mu s$, based on an average of 600×100 single-shot measurements, along with cosine fit with gaussian envelope, see text. Error bars from statistics are smaller than markers. (f) Identical to (e) with $\tau_D = 64 \mu s$.

preceding the rotations is not needed, but including it serves to demonstrate general interlacing of qubit operations with dynamical decoupling.

5.4 Interlaced Operations

To interlace x rotations between CP sequences [see Fig. 5.2(a)], the (1,1) singlet was first initialized, followed by a $N_\pi = 4$ CP sequence during an interval $\tau_D/2$. Pausing at S for a time τ_S induced rotation around x axis due to the slowly-varying Overhauser field gradient. This was followed by a second $N_\pi = 4$ CP sequence, and finally a single-shot measurement at point M. For each value of τ_S , this sequence was repeated 100 times, yielding a probability, P_S , of a singlet outcome over these 100 single-shot events. Probabilities for 40 values of τ_S , ranging from 0 to 180 ns, were measured over a total duration of 100 ms. Oscillations of $P_S(\tau_S)$ are well fit by $P_S(\tau_S) = 0.5 (1 + V \cos (\tau_S g^* \mu_B \Delta B_z / \hbar))$, where V is the measurement visibility [Figs. 2(b,c)], the expected form for qubit precession in a fixed Overhauser field difference ΔB_z [8]. Averaging x rotations over the full range of Overhauser fields would wash out oscillations. Instead, $P_S(\tau_S)$ data in Figs. 2(b,c) was selected to cover a narrow range of Overhauser fields around $\Delta B_z \sim 3$ mT. The value of ΔB_z evolves slowly among data sets, observable as a fluctuating oscillation period of $P_S(\tau_S)$.

From the ratio of visibilities for long and short (but otherwise identical) sequences, $V(\tau_D = 16\mu\text{s})/V(\tau_D = 4\mu\text{s}) = 0.88$, we estimate a dephasing time $T_2 \sim 40\mu\text{s}$ for the complete sequence with $N_\pi = 4$ before and after the rotation, assuming a gaussian decay envelope (discussed below) and using the measured normalizations $V_0 \sim 0.70$ with $\tau_D = 0$, $N_\pi = 0$, and $V_0 \sim 0.63$ with $\tau_D = 0$, $N_\pi = 4$. The reduced visibility of S-T₀ precession without the CP sequences can be attributed to limited read-out fidelity, finite exchange at ϵ_S , and imperfect initialization in (1,1). A further $\sim 10\%$ reduction in visibility when including $2N_\pi = 8$ pulses is dominated by tilting of the echo rotation axis away from z by Overhauser field gradients [Fig. 5.1(d)].

Interlaced z rotations between CP sequences were demonstrated using adiabatic

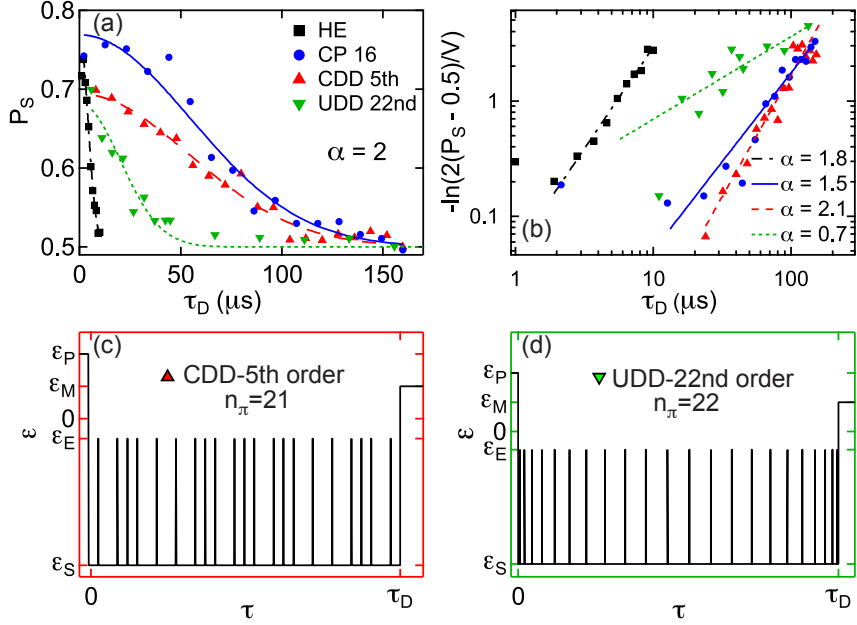


Figure 5.3: (Color online) (a) Singlet recovery amplitude, P_S , as a function of total dephasing time, τ_D , for Hahn, CP, CDD and UDD sequences (see text), with fits of Eq. (5.1) with $\alpha = 2$, yielding $T_2^{\text{HE}} \sim 6 \mu\text{s}$, $T_2^{\text{CDD}} \sim 80 \mu\text{s}$, $T_2^{\text{CP}} \sim 80 \mu\text{s}$, $T_2^{\text{UDD}} \sim 30 \mu\text{s}$. (b) Replotting data in (a) as $-\ln[2(P_S - 1/2)/V]$ allows a fit giving the exponent α in Eq. (1). On a log-log plot, Eq. (1) and data appears linear with slope α . Pulse sequences for (c) 5th order CDD and (d) 22nd order UDD.

ramps that map S and T_0 to $|\uparrow\downarrow\rangle$ and $|\downarrow\uparrow\rangle$ [Fig. 5.2(d)] [114]. Initialization of the (1,1) singlet was followed by a $N_\pi = 8$ CP sequence. The preserved singlet was then mapped to $|\uparrow\downarrow\rangle$ by pulsing from S to R (without passing the $S-T_+$ anticrossing) then ramping slowly to S in a (loading) time $\tau_L \sim 400\text{ns}$. Pulsing to E for a time τ_E induced rotation around z at frequency f_E . Next, pulsing to S, ramping slowly from S to R, then back to S mapped $|\uparrow\downarrow\rangle(|\downarrow\uparrow\rangle)$ to $S(T_0)$. The resulting superposition amplitude was preserved over a time $\tau_D/2$ by a second $N_\pi = 8$ CP sequence. Finally, the superposition amplitude was measured by pulsing to M. 600 singlet probabilities, each based on 100 single-shot measurements, were averaged over fluctuating Overhauser fields for each τ_E . Oscillations in $P_S(\tau_E)$ do survive averaging over Overhauser fields, since for $J_E \gg \Delta B_z$ the oscillation frequency f_E depends

only weakly on ΔB_z . However, this averaging does contribute to the decay envelope seen in Figs. 2(e,f). Note that mapping between z and x axes accurately preserves the angle of the superposition from the corresponding axis (amplitude), with some loss of azimuthal angle (phase) information due to environment dynamics on the time scale of the 400 ns ramp. State tomography [47] requires fast rotations compared to environment dynamics [124].

Singlet return probability $P_S(\tau_E)$, averaged over fluctuating Overhauser fields, for $\tau_D = 16 \mu\text{s}$ [Fig. 2(e)] and $\tau_D = 64 \mu\text{s}$ [Fig. 2(f)] using $N_\pi = 8$ CP sequences show damped oscillations a function of the exchange time τ_E . Fits to $P_S = 1/2 + (V/2) \cos(\tau_E J_E/\hbar) \exp[-(\tau_E/T_2^*)^2]$, the expected form for a qubit precessing in exchange splitting, J_E , with inhomogenous dephasing due to both fluctuating Overhauser fields and electrical noise, yield $J_E \sim 0.2 \mu\text{eV}$ and $T_2^* \sim 100 \text{ ns}$ from the decay envelope⁴. Visibilities $V \sim 0.09(0.06)$ for $\tau_D = 16(64) \mu\text{s}$, along with $V \sim 0.3$ measured without CP sequences (not shown), yield a coherence time $T_2 \sim 80 \mu\text{s}$. Besides finite coherence time (T_2), other contributions that reduce visibility include nonzero ΔB_z during exchange pulses, nonzero exchange at the separation point, J_S , and gate noise during π -pulses.

Next, we consider alternative dynamical decoupling schemes for recovery of a prepared singlet without interlaced rotations. A prepared (1,1) singlet at point S was given n_π π -pulses, spaced in time according to the particular decoupling scheme, over a total interval τ_D . For each value of τ_D , an Overhauser-averaged singlet return probability P_S was found by averaging $\sim 10^4$ single-shot measurements, normalized by reflectometer output voltages of singlet and triplet outcomes via single-shot histograms [8]. For all decoupling schemes, $P_S(\tau_D)$ data are well described by the functional form

$$P_S(\tau_D) = 1/2 + (V/2) e^{-(\tau_D/T_2)^\alpha}. \quad (5.1)$$

⁴An offset of $\sim 10 \text{ ns}$ due to finite pulse-rise time is taken into account for the fit.

We either set $\alpha = 2$ [Fig. 3(a)] or leave α as a fit parameter [Fig. 3(b)]. Allowing α to vary can give insight into the dominant dephasing mechanism, depending on the decoupling scheme [156, 159]. For instance, for simple Hahn echo, a white-noise environment is expected to give exponential decay, $\alpha = 1$. In contrast, the enhanced low-frequency content of an Overhauser-field-dominated environment is expected to yield $\alpha \sim 4$ for Hahn echo [156, 159], as observed experimentally [14].

Experimental $P_S(\tau_D)$, for several decoupling schemes along with fits of Eq. (5.1) with fixed $\alpha = 2$ yields values for T_2 [Fig. 3(a)]. For a single-pulse Hahn echo, $T_2^{\text{HE}} \sim 6 \mu\text{s}$, while $T_2^{\text{CP}} \sim 80 \mu\text{s}$ for a CP sequence with 16 π -pulses⁵. A comparison of CP sequences with different N_π are shown in Fig. 3(b). Best-fit values for α are extracted by taking the logarithm of Eq. (1), as shown in Fig. 5.3(c). For Hahn echo, the best fit value is $\alpha^{\text{HE}} = 1.8$, suggesting that electrical (gate) noise and drift, combined with spatially varying Overhauser fields, are likely the dominant source of dephasing, rather than time dependence of the Overhauser fields themselves. For the CP sequence, the best fit exponent is $\alpha^{\text{CP}} \sim 1.5$.

Alternative decoupling sequences may outperform CP, depending on the decohering environment [157, 145, 86]. A favorable scheme for spin qubits coupled to nuclear environments is CDD whose n th order sequence is created from two sequences of $(n - 1)$ th order with an additional π -pulse between them for odd n [157]: first-order CDD is Hahn echo; second-order CDD is CP with two π -pulses; fifth-order CDD, with 21 π -pulses, is shown in Fig. 5.3(c). Another pulse scheme optimized for spin-bath environments is UDD, which has n_π π -pulses (indexed by j) at times $\delta\tau = \tau_D \sin^2[j\pi/(2n + 2)]$. The 22nd-order UDD ($n_\pi = 22$) is shown in Fig 5.3(d). Singlet probabilities $P_S(\tau_D)$ for the 5th-order CDD and 22nd-order UDD sequence is shown in Fig. 5.3(a) along with Hahn and CP, and yield

⁵Other parameters in Fig. 5.3(a): $V^{\text{HE}} \sim 0.6$, $V^{\text{CP}} \sim 0.6$, $V^{\text{CDD}} \sim 0.4$, $V^{\text{UDD}} \sim 0.4$. In Fig. 5.3(b): $V^{\text{HE}} \sim 0.6$, $T_2^{\text{HE}} \sim 5 \mu\text{s}$; $V^{\text{CP}} \sim 0.6$, $T_2^{\text{CP}} \sim 70 \mu\text{s}$; $V^{\text{CDD}} \sim 0.4$, $T_2^{\text{CDD}} \sim 80 \mu\text{s}$; $V^{\text{UDD}} \sim 0.4$, $T_2^{\text{UDD}} \sim 17 \mu\text{s}$

$T_2^{\text{CDD}} \sim 80 \mu\text{s}$ and $T_2^{\text{UDD}} \sim 30 \mu\text{s}$ ⁶. We note that (i) all multi-pulse sequences significantly outperform Hahn echo; (ii) the fifth-order CDD sequence ($n_\pi = 21$) has no better performance than the $n_\pi = 16$ CP sequence, and (iii) the T_2 achieved for UDD is considerably shorter than for comparable CDD and CP sequences. This presumably results from experimental artifacts such as pulse bandwidth limitations, but could also reflect the non-optimality of UDD for an environment with a $1/f^2$ high-frequency tail [124]. For a dephasing power spectrum closer to the experiment the optimal spin echo pulse sequence has been predicted to be very similar to a simple CP sequence [111], while in Ref. [86] it was predicted that UDD is optimal for hyperfine-induced dephasing in GaAs quantum dots. Optimizing pulse sequences with contributions from gate noise and drift combine with spatially and temporally varying Overhauser fields remains an outstanding problem experimentally and theoretically.

Acknowledgments

CB and JM contributed equally to this work. We acknowledge funding from iARPA/ARO and the Department of Defense. We thank Hendrik Bluhm, Sandra Foletti, Daniel Loss, David Reilly, and Wayne Witzel for useful discussion.

⁶Other parameters in Fig. 5.3(a): $V^{\text{HE}} \sim 0.6$, $V^{\text{CP}} \sim 0.6$, $V^{\text{CDD}} \sim 0.4$, $V^{\text{UDD}} \sim 0.4$. In Fig. 5.3(b): $V^{\text{HE}} \sim 0.6$, $T_2^{\text{HE}} \sim 5 \mu\text{s}$; $V^{\text{CP}} \sim 0.6$, $T_2^{\text{CP}} \sim 70 \mu\text{s}$; $V^{\text{CDD}} \sim 0.4$, $T_2^{\text{CDD}} \sim 80 \mu\text{s}$; $V^{\text{UDD}} \sim 0.4$, $T_2^{\text{UDD}} \sim 17 \mu\text{s}$

Chapter 6

Scaling of Dynamical Decoupling for Spin Qubits

J. Medford, C. Barthel, C. M. Marcus

Department of Physics, Harvard University, Cambridge, Massachusetts 02138, USA

L. Cywiński

Institute of Physics, Polish Academy of Sciences, Al. Lotników 32/46, PL 02-668 Warszawa, Poland

M. P. Hanson, A. C. Gossard

Materials Department, University of California, Santa Barbara, California 93106, USA

We investigate scaling of coherence time, T_2 , with the number of π -pulses, n_π , in a singlet-triplet spin qubit using Carr-Purcell-Meiboom-Gill (CPMG) and concatenated dynamical decoupling (CDD) pulse sequences. For an even numbers of CPMG pulses, we find a power law, $T_2 \propto (n_\pi)^{\gamma_e}$, with $\gamma_e = 0.72 \pm 0.01$, essentially independent of the envelope function used to extract T_2 . From this surprisingly robust value, a power-law model of the noise spectrum of the environment, $S(\omega) \sim \omega^{-\beta}$, yields $\beta = \gamma_e/(1 - \gamma_e) = 2.6 \pm 0.1$. Model values for $T_2(n_\pi)$ using $\beta = 2.6$ for CPMG with both even and odd n_π up to 32 and CDD orders 3 through 6 compare very well with experiment¹.

¹This chapter is adapted from Ref. [94] with permission, © (2012) by the American Physical Society.

6.1 Introduction

A variety of solid state systems are emerging as effective platforms for studying decoherence and entanglement in controlled quantum systems [16, 7, 22, 39]. Among them, quantum-dot-based spin qubits have recently achieved sufficient control and long coherence times [16, 7] that new information about the noise environment of the qubit can be extracted, complementing related work in nitrogen-vacancy centers in diamond [39], superconducting qubits [22], trapped ions [12], and neutral atoms [130].

Dynamical decoupling in the form of a sequence of π -pulses [152, 145, 71, 70] functions as a high-pass filter, thus providing information about the spectral content of environmental noise [40, 36, 12, 39, 10, 22, 9, 2, 160]. For spin qubits, the effectiveness of various decoupling schemes at mitigating dephasing due to nuclear bath dynamics has been well studied theoretically [159, 156, 158, 37, 102]. Much less is known about mitigating the effects of charge noise, which couples to the qubit via gate dependent exchange interaction and through spatially varying Overhauser fields [16]. When the decoherence time, T_2 , is short compared to the energy relaxation time, T_1 ,—which is the case in this study—both the envelope of the coherence decay as well as the dependence of T_2 on the number of π -pulses, n_π , depend on the spectral density of the environment, $S(\omega)$. Knowledge of $S(\omega)$ inferred from such measurements can in turn be used to design optimal decoupling sequences [36, 53, 12, 110, 1].

In this chapter, we investigate scaling of T_2 with the number of π -pulses for Carr-Purcell-Meiboom-Gill (CPMG) and concatenated dynamical decoupling (CDD) sequences in a GaAs two-electron singlet-triplet qubit [Fig. 1(a)]. The coherence envelope is reasonably well described by the form $\exp(-(\tau_D/T_2)^\alpha)$, where τ_D is the time during which π -pulses are applied [Fig. 2(b)]. It is difficult, however, to accurately determine α by directly fitting to

this form. In contrast, we find that the scaling relation $T_2 \sim (n_\pi)^\gamma$ very accurately describes the data irrespective of the value of α used to extract T_2 . The resulting γ can then be related to α and other quantities of interest within specific noise models. For CPMG with even n_π , the scaling relation $T_2 \propto (n_\pi)^{\gamma_e}$ yields $\gamma_e = 0.72 \pm 0.01$, using T_2 values extracted using any α in the range 2 to 5. A model of dephasing due to a power-law spectrum of classical noise, $S(\omega) \sim \omega^{-\beta}$, leads to a scaling relation in the number of π -pulses, with the exponent of the power law, β , related to the scaling exponent by the simple relation $\beta = \gamma_e / (1 - \gamma_e)$. For the present experiment, $\gamma_e = 0.72$ thus yields $\beta = 2.6$. Further support for a power-law form for $S(\omega)$ is found by comparing experimental and theoretical dependences $T_2(n_\pi)$ for CPMG with both even and odd n_π as well as CDD pulse sequences. This model also gives the simple relation $\alpha = \beta + 1$ connecting the noise spectrum and the decoherence envelope exponent. The resulting value, $\alpha = 3.6 \pm 0.1$ is thus determined with considerably greater accuracy than can be obtained from direct fits to the coherence envelope data.

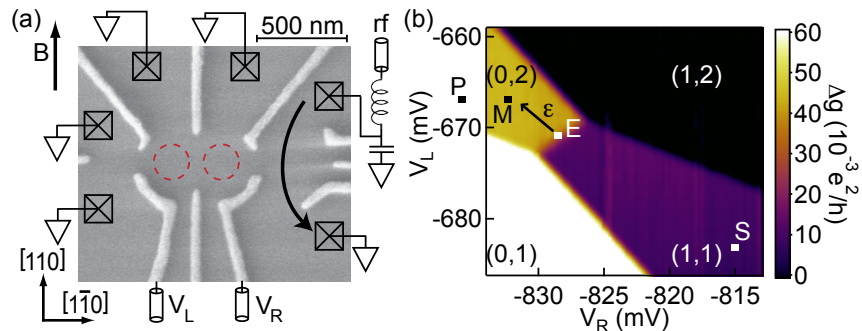


Figure 6.1: (Color online) (a) Micrograph of lithographically identical device with dot locations depicted. Gate voltages, $V_{R(L)}$, set the charge occupancy of right (left) dot as well as the detuning of the qubit. An rf-sensor quantum dot is indicated on the right. (b) Double dot charge state mapped onto dc conductance change, Δg , with lettered pulse sequence gate voltages. Detuning axis is orthogonal to the (0,2)-(1,1) charge degeneracy through points E, S, and M.

6.2 Device and Qubit System

The lateral double quantum dot investigated was defined by Ti/Au depletion gates patterned using electron beam lithography on a GaAs/Al_{0.3}Ga_{0.7}As heterostructure with a two dimensional electron gas (density $2 \times 10^{15} \text{ m}^{-2}$, mobility $20 \text{ m}^2/\text{V s}$) 100 nm below the surface. Measurements were performed in a dilution refrigerator with an electron temperature $T_e \sim 150 \text{ mK}$. The double quantum dot is operated as a spin qubit by first depleting the quantum dots to the last two electrons, then manipulating the charge occupancy of the two dots with high bandwidth plunger gates V_L and V_R along a detuning axis ϵ [Fig. 1(b)]. In this work, the charge occupancy was manipulated between states (0,2) and (1,1), where (N_L, N_R) represent the charge in the left and right dots. Charge occupancy was determined by the conductance change, Δg , through a proximal sensor quantum dot, which in turn modulated the reflection coefficient of the radio-frequency (rf) readout circuit [123, 5].

The logical spin qubit subspace is spanned by the singlet ($S = (|\uparrow\downarrow\rangle - |\downarrow\uparrow\rangle)/\sqrt{2}$) and the $m = 0$ triplet ($T_0 = (|\uparrow\downarrow\rangle + |\downarrow\uparrow\rangle)/\sqrt{2}$) states of two electrons. The $m = \pm 1$ triplet states were split off by a 750 mT magnetic field applied in the plane of the electron gas, perpendicular to the dot connection axis. A (0,2) singlet was prepared at point P, off the detuning axis, through rapid relaxation to the ground state, then moved to the separation point S in (1,1). Uncorrelated Overhauser fields in the two dots create an evolving Zeeman gradient, ΔB_z , that drives transitions between S and T_0 . Single-shot readout was performed by moving to point M, where S can tunnel to (0,2) while T_0 remains in (1,1). The reflectometer signal was integrated for 600 ns per shot, averaged over 10^4 shots, and compared to voltage values corresponding to S and T_0 outcomes [8], yielding $P_S(\tau_D)$, the probability of singlet return.

6.3 Dynamical Decoupling

Coherence lost due to (thermally driven) evolution of ΔB_z can be partially restored using a Hahn echo by pulsing at time $\tau_D/2$ to point E, where the exchange splitting between S and T_0 drives a π -rotation about the \hat{x} axis, changing the sign of the acquired phase. Returning to S for an equal time $\tau_D/2$ cancels the phase acquired due to the low-frequency ($\omega < 2/\tau_D$) end of the spectrum of fluctuations of ΔB_z [40, 36]. Dynamical decoupling using a series of π -pulses allows efficient removal of more of the low-frequency end of the noise spectrum [40, 36]. The CPMG sequence [149], for example, uses evenly spaced gate pulses from point S to point E with a half interval before the first and after the last π -pulse [Figs. 6.2(b,c)]. Concatenated dynamical decoupling [71, 7, 112] (CDD) uses nonuniformly spaced pulses to point E, where the k -th order sequence is determined recursively from the lower order one, with an additional π -pulse in the center of odd orders [Fig. 6.2(d)].

6.4 CPMG scalings as Noise Spectrometer

Singlet return probabilities $P_S(\tau_D)$ were measured for CPMG sequences with $n_\pi = 1, 2, 3, 4, 8, 16$, and 32. Fits to $P_S = 0.5 + V/2 \exp[-(\tau_D/T_2)^\alpha]$, with visibility V and T_2 as fit parameters, were equally good for fixed values of α between 2 and 4, as seen in Fig. 3(a). For this reason, though $S(\omega)$ is related to α , these fits give little information about the spectrum of the environment. Figure 3(b), showing the fitted value of T_2 as a function of the fixed α and n_π for an even number of CPMG pulses, shows two remarkable features. First, values of T_2 do not depend on the value of α used in the fits to $P_S(\tau_D)$. Second, T_2 shows a power-law scaling $T_2 = T_2^0(n_\pi)^\gamma$ whose power, γ , also does not depend on the value of α used in the fits.

To model these observations, we consider Gaussian noise affecting the energy split-

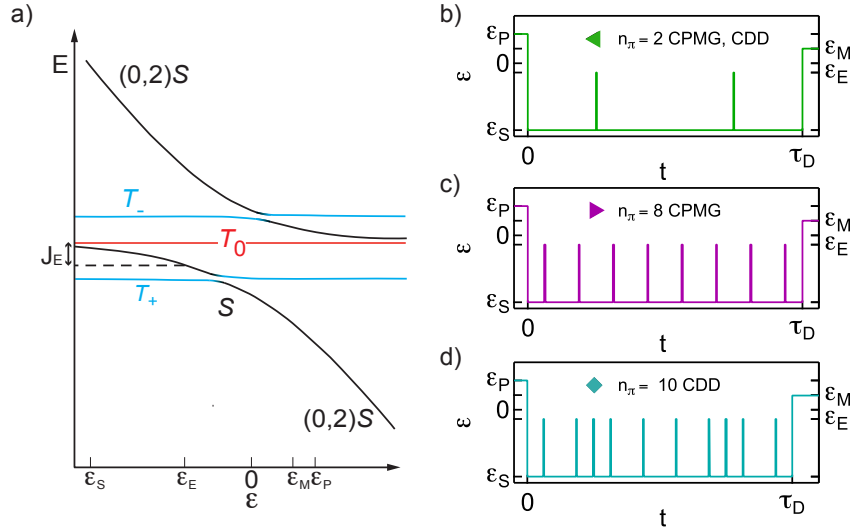


Figure 6.2: (Color online) (a) Energy level diagram along the detuning axis ϵ . The $(0,2)$ singlet was prepared at ϵ_P , followed by separation to ϵ_S . π -pulses are performed at ϵ_E , allowing for subsequent rephasing at ϵ_S . Single-shot readout at ϵ_M using a proximal sensor dot. The exchange energy, J_E , that drives the π -pulses at ϵ_E is indicated with a dashed line. (b-d) Schematics of detunings during CPMG and CDD pulse sequences with detuning points on the vertical axis.

ting of the qubit, which leads to the off-diagonal (in the basis of $|\uparrow\downarrow\rangle$ and $|\downarrow\uparrow\rangle$) elements of the qubit density matrix decaying as $\exp[-\chi(\tau_D)]$, where

$$\chi(\tau_D) = \int_0^\infty \frac{d\omega}{\pi} S(\omega) \frac{F(\omega\tau_D)}{\omega^2}, \quad (6.1)$$

with $F(\omega\tau_D)$ being the filter function determined by the sequence of π -pulses driving the qubit. For CPMG sequence $F(z) < (z/2n_\pi)^4$ for $z < 2n_\pi$, i.e. $F(z)$ strongly suppresses the low-frequency noise, while for large z and n_π the filter function can be approximated [36] by a periodic train (with period $z_p = 2\pi n_\pi$) of square peaks of height $h \approx 2n_\pi^2$ and width $\Delta z \approx z_p^2/\pi h \ll z_p$.

We find that the value of γ_e and the presence of an even-odd effect (EOE) in n_π (i.e. $\gamma_e \neq \gamma_o$) act as discriminators for several classes of $S(\omega)$: (i) The case of $0 < \gamma_e \leq 2/3$ and absent EOE is compatible with a model of $S(\omega) \sim \omega^{-\beta}$ (over a range of ω roughly

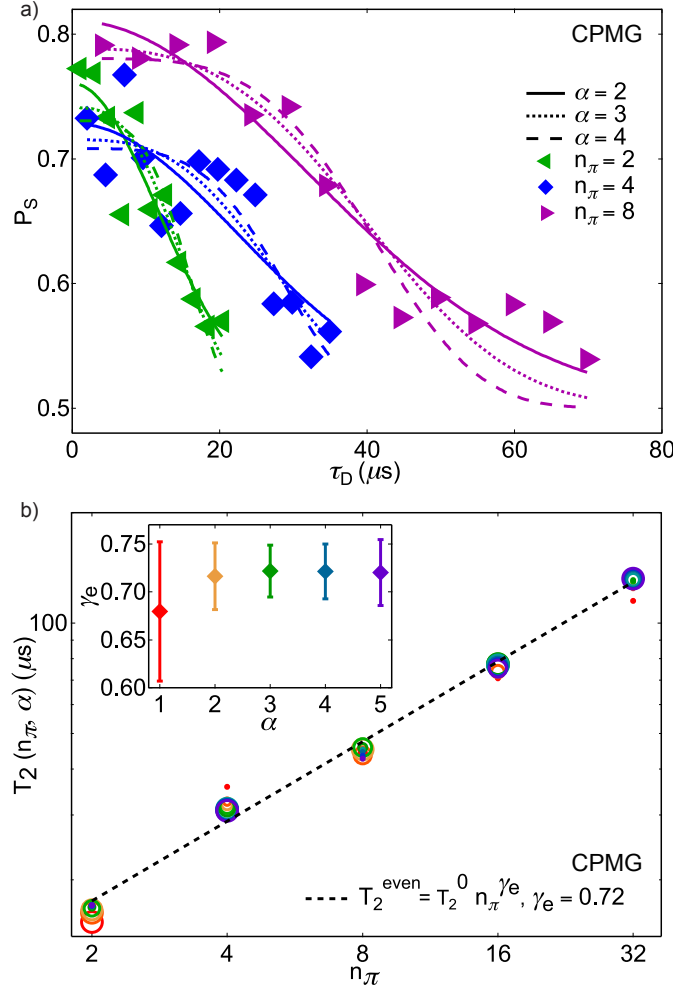


Figure 6.3: (Color online) (a) Experimental singlet return probabilities as a function of time for CPMG with $n_\pi = 2, 4, 8$. Fits to $P_S(\tau_D) = 0.5 + V/2 \exp(-(\tau_D/T_2)^\alpha)$, with α constrained to 2 (solid curves), 3 (dotted curves) and 4 (dashed curves). CPMG visibilities for $\alpha = 2$ are: $n_\pi = 2, V = 0.52 \pm 0.02$; $n_\pi = 4, V = 0.46 \pm 0.04$; $n_\pi = 8, V = 0.62 \pm 0.02$. Visibilities for $\alpha = 3$ are: $n_\pi = 2, V = 0.48 \pm 0.03$; $n_\pi = 4, V = 0.43 \pm 0.02$; $n_\pi = 8, V = 0.58 \pm 0.03$. Visibilities for $\alpha = 4$ are: $n_\pi = 2, V = 0.46 \pm 0.03$; $n_\pi = 4, V = 0.42 \pm 0.02$; $n_\pi = 8, V = 0.56 \pm 0.03$. It is difficult to determine α from these fits. (b) Extracted T_2 for even- n_π CPMG sequences for α constrained to 1, 2, 3, 4, and 5. Circle size proportional to χ^2 goodness of fit of $P_S(\tau_D)$ in (a). A power-law fit to the form $\ln(T_2^{\text{even}}(\alpha)) = \ln(T_2^0) + \gamma_e \ln(n_\pi)$, shown for $\alpha=3$ (dashed line) gives $\gamma_e = 0.72$. The fit value γ_e depends only weakly on α in the range 2 – 5 (inset). The weighted average over $\alpha = 2 - 5$ yields $\gamma_e = 0.72 \pm 0.01$.

bounded by the minimal and maximal values of n_π/τ_D , with $0 < \beta \leq 2$. In this case $\gamma_e = \beta/(1+\beta)$ and $\alpha = \beta+1$. This can be derived by realizing that the contribution to $\chi(\tau_D)$

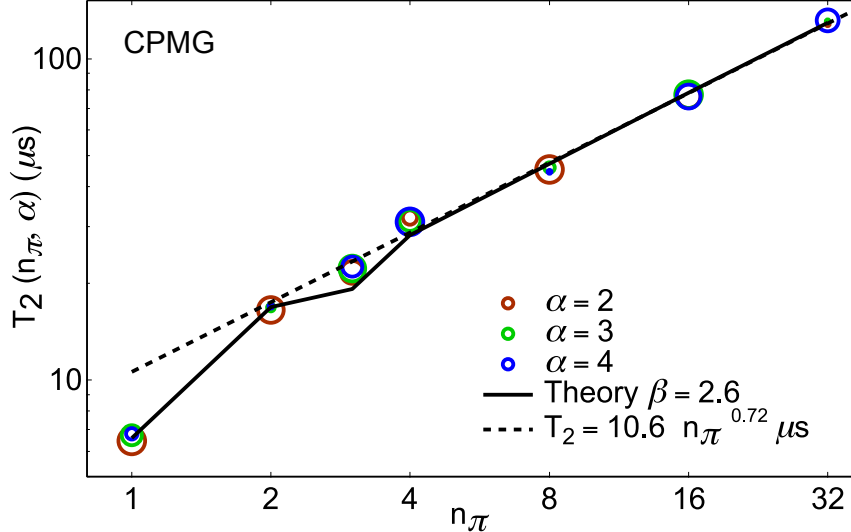


Figure 6.4: (Color online) T_2 for all measured n_π for CPMG, extracted using $\alpha = 2, 3$, and 4 (circles). Circle size for each α proportional to χ^2 goodness of fit. Theory (black solid curve) for integration of Eq. (6.1) with the CPMG filter functions and $\beta = \gamma_e/(1-\gamma_e) = 2.6$. Note that Eq. (6.2) captures the even/odd effect quantitatively for small n_π . Black dashed line is the power-law fit to the even n_π points.

for CPMG is dominated by a narrow peak of height $2n_\pi^2$ at $\omega\tau_D \approx \pi n_\pi$ in the $F(\omega\tau_D)$ filter [36, 22, 2, 160]. One example is the case of Ornstein-Uhlenbeck noise [43] (having Lorentzian $S(\omega)$ with ω^{-2} tail typically dominating the decoherence under dynamical decoupling), where $\gamma = 2/3$ was confirmed by experiments on the NV center [39]. (ii) When an EOE is present, $\gamma_e = 2/3$ suggests a hard cutoff in $S(\omega)$ at $\omega_c < 2/T_2$, in which case $\gamma_o = 1$. (iii) For $\omega_c > 2/T_2$, i.e. for larger ω_c or larger n_π (leading to longer T_2), the EOE disappears and γ tends to 1 [9]. (iv) Finally, the presence of the EOE and $2/3 < \gamma_e < 1$ indicate $S(\omega) \sim \omega^{-\beta}$, with $\beta > 2$.

Experimentally, we find $\gamma_e = 0.72$ for even number of CPMG pulses, and $n_\pi = 1$ not along the scaling line, indicating an EOE. We conclude that scenario (iv) applies, namely $S(\omega) = A^{\beta+1}/\omega^\beta$ with $2 < \beta < 3$. Using Eq. (6.1) and the CPMG filter function gives in the

large- n_π limit

$$\chi(t) \approx (A\tau_D)^{1+\beta} \left(\frac{a}{n_\pi^\beta} + \frac{b_{e/o}}{n_\pi^4} \right), \quad (6.2)$$

with $a \approx \Sigma_{2+\beta}/\pi^2(2\pi)^\beta$, where $\Sigma_\delta = \sum_{k=1}^{\infty} (k - \frac{1}{2})^{-\delta}$, and for odd (even) n_π we have $b_o \approx [32\pi(3 - \beta)]^{-1}$ ($b_e \approx [128\pi(5 - \beta)]^{-1} \approx b_o/10$), i.e., the b/n_π^4 term is negligible for even n_π , while it gives a significant correction for small, odd n_π . The EOE comes from the difference in the low- z behavior of the CPMG filter functions, which for $z < 1$ behave as $F(z) \sim z^4/2^5 n_\pi^4$ ($z^6/2^7 n_\pi^4$) for odd (even) n_π . For $\beta > 2$ this leads to different contributions of very low ω to the integral in Eq. (6.1). For even n_π , we find that $\chi(\tau_D)$ approximately reduces to $(A\tau_D)^{1+\beta} a/n_\pi^\beta$, from which we obtain the $\beta \leq 2$ result of $\gamma_e = \beta/(1 + \beta)$ in this case as well. Note that in Fig. 3b we fit a parameter $T_2^0 = [Aa^{1/(1+\beta)}]^{-1}$, which corresponds to a hypothetical echo decay time in the absence of very low- ω noise (i.e. putting $F(z) = 0$ for $z < 1$).

Assuming this form of $S(\omega)$, fits to the even n_π [Fig. 3(b)] yield $\beta = 2.6$ and $A^{-1} = 3.6 \mu\text{s}$. Using these two parameters we calculate odd- n_π values for T_2 by numerically integrating Eq. (6.1). As shown in Fig. 6.4, the obtained value of T_2 is in good agreement with the measured value for $n_\pi = 1$ (Hahn echo). We note that the large n_π scaling of $T_2 \sim n_\pi^\gamma$ is due to the behavior of $S(\omega)$ at $\omega \geq \pi n_\pi/T_2$, which is $\sim 0.3(n_\pi)^{0.28} \mu\text{s}^{-1}$ here, while the EOE at small n_π is due to behavior at $\omega < 1/T_2$, which is $\sim 0.15 \mu\text{s}^{-1}$. The consistency between small- and large- n_π data indicates that $S(\omega) \sim \omega^{-2.6}$ over this range of frequencies (i.e., $\omega/2\pi \sim 10 - 100 \text{ kHz}$). The EOE behavior at low n_π can be fit within scenario (ii) using $S(\omega) = A^3/\omega^2$ with $A^{-1} \sim 1 \mu\text{s}$ and $\omega_c \sim 0.08 \mu\text{s}^{-1}$. However, this scenario crosses over to (iii) for $n_\pi > 5$, where γ tends to 1. The resulting large- n_π behavior, $T_2 \sim n_\pi \times 7 \mu\text{s}$, departs significantly from the $n_\pi \geq 8$ data in Fig. 4.

6.5 CDD sequences

Using $S(\omega) = A^{\beta+1}/\omega^\beta$ with parameters A and β fixed from the even- n_π CPMG fit, we can calculate the expected dependence of $T_2(n_\pi)$ for the CDD pulse sequence using the known filter functions [36]. For $n_\pi = 5, 10$, and 21 we get good agreement between the calculated and measured T_2 [Fig. 5]. For $n_\pi = 42$, the experimental T_2 is shorter than predicted by theory, possibly reflecting an accumulation of errors for such a large number of pulses. Note that CDD was shown to be robust to pulse errors [154] only in the case of two-axis control (i.e. when the π -pulses are about x and y axes alternately) and for a quasi-static bath.

Let us note that $S(\omega)$ of a very similar form ($\sim 1/\omega^{2.5}$) was recently inferred in Ref. [129] from the transport data taken from Ref. [76]. The strong low-frequency noise was tentatively ascribed to electron current shot noise generating much slower Overhauser field dynamics.

6.6 Conclusions

Summarizing, the measurements of qubit decoherence under dynamical decoupling with the CPMG pulse sequence have been used to reconstruct the crucial features of the spectral density of noise dephasing the qubit. Using the data for even n_π of CPMG we have been able to estimate the magnitude of noise and its functional form. The reconstructed spectral density of noise allows us to calculate the expected decoherence signal for other pulse sequences, and this calculation agrees with the CDD sequence measurements for n_π as well as the odd- n_π CPMG data. We have shown that instead of fitting the exact functional form of the coherence decay function, an analysis of the scaling of the measured T_2 time with the number of applied pulses allows for a clearer understanding of the system. We cannot

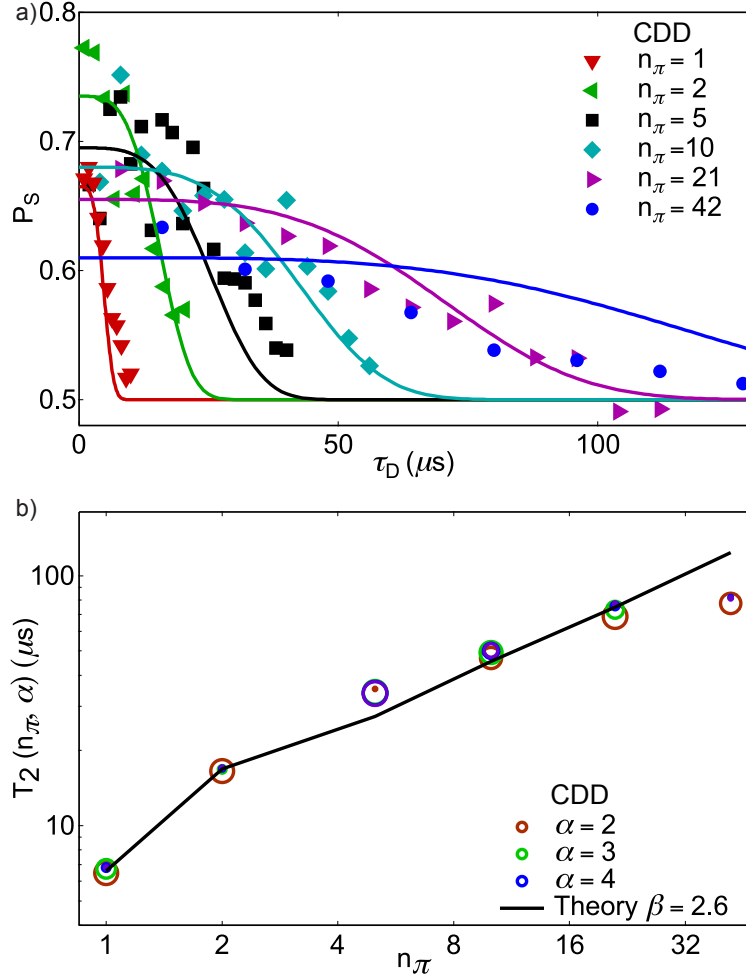


Figure 6.5: (Color online) (a) Experimental singlet return probabilities for orders 1 through 6 CDD (symbols) along with fits to $P_S(\tau_D) = 0.5 + V/2 \exp(-(\tau_D/T_2)^\alpha)$ using $\beta = \gamma_e/(1 - \gamma_e) = 2.6$ (solid curves). (b) Extracted T_2 for using different values of α (circle size proportional to χ^2 measure of goodness of fit). Theory (solid curve) based on $\beta = \gamma_e/(1 - \gamma_e) = 2.6$ and integration of Eq. (6.1) with appropriate CDD filter function [36].

say at this point whether the observed value $\gamma_e = 0.72$ is characteristic of Overhauser-dominated dephasing in general, or just our particular combination of noise sources.

Acknowledgments

We acknowledge funding from IARPA under the MQCO program, from NSF under the Materials World Network program, and from the Homing Programme of the Foundation for Polish Science supported by the EEA Financial Mechanism (LC). We thank M. Biercuk and V. Dobrovitski for useful discussions.

Chapter 7

Self-Consistent Measurement and State Tomography of an Exchange-Only Spin Qubit

J. Medford¹, J. Beil^{1,2}, J. M. Taylor³, S. D. Bartlett⁴, A. C. Doherty⁴, E. I. Rashba¹, D. P. DiVincenzo^{5,6}, H. Lu⁷, A. C. Gossard⁷, and C. M. Marcus^{1,2}

¹*Department of Physics, Harvard University, Cambridge, Massachusetts 02138, USA*

²*Center for Quantum Devices, Niels Bohr Institute, University of Copenhagen,
Universitetsparken 5, DK-2100 Copenhagen, Denmark*

³*Joint Quantum Institute/NIST, College Park, MD, USA*

⁴*Centre for Engineered Quantum Systems, School of Physics, The University of Sydney,
Sydney, NSW 2006, Australia*

⁵*Institute for Quantum Information, RWTH Aachen University, 52056 Aachen, Germany*

⁶*Dept. Theoretical Nanoelectronics, PGI, Forschungszentrum Juelich, 52425 Juelich,
Germany*

⁷*Materials Department, University of California, Santa Barbara, California 93106, USA*

We report initialization, complete electrical control, and single-shot readout of an exchange-only spin qubit. Full control via the exchange interaction is fast, yielding a demonstrated 75 qubit rotations in under 2 ns. Measurement and state tomography are performed using a maximum-likelihood estimator method, allowing decoherence, leakage out of the qubit state space, and measurement fidelity to be quantified. The methods developed here are generally applicable to systems with state leakage, noisy measurements, and non-orthogonal control axes¹.

¹This chapter is adapted from Ref. [93], submitted to Nature Nanotech.

7.1 Introduction

Nanoelectronics show great promise as a quantum information platform, in particular as superconducting qubits [101, 26, 91, 74, 97] and spin qubits in semiconductors [114, 75, 105, 49]. One or two electron spin qubits use, respectively, oscillating magnetic [75] or electric fields [105, 100], or quasi-static Zeeman field gradients [83, 118, 47, 115], to achieve full qubit control. Adding a third spin provides exchange-driven qubit rotations along two axes, hence full control of spin information via electrostatic gating only [42, 85, 49, 62, 95, 155].

The three-electron exchange-only spin qubit has a more complicated level structure than its one- and two-electron counterparts [85, 62, 95], providing, for example, multiple initialization states, but also allowing leakage out of the qubit state space. Here, we characterize the performance of the three-electron spin qubit by performing measurement and state tomography [89, 19, 97]. Measurement tomography allows accurate state tomography in the presence of noisy measurements and leakage.

7.2 Device and System

A three-electron linear triple quantum dot was formed by Ti/Au electrostatic gates patterned on a GaAs/AlGaAs heterostructure with the two-dimensional electron gas 110 nm below the surface (see Fig. 6.1(a)). Left and right plunger voltages, V_l and V_r , controlled electron occupation of each dot. All manipulations kept a three electron total, with the arrangement, $(N_l \ N_m \ N_r)$, set by the detuning parameter, $\varepsilon = (V_r - V_r^0)/2 - (V_l - V_l^0)/2$, where $\varepsilon = 0$ is defined as the center of 111 (see Fig. 7.2(a)).

Three electrons have eight possible spin states, four with total spin $S = 3/2$, and four with $S = 1/2$ [20, 85]. An external magnetic field splits the eight states into four subspaces with spin projection, $m_S = \pm 3/2, \pm 1/2$. The linear geometry allows two

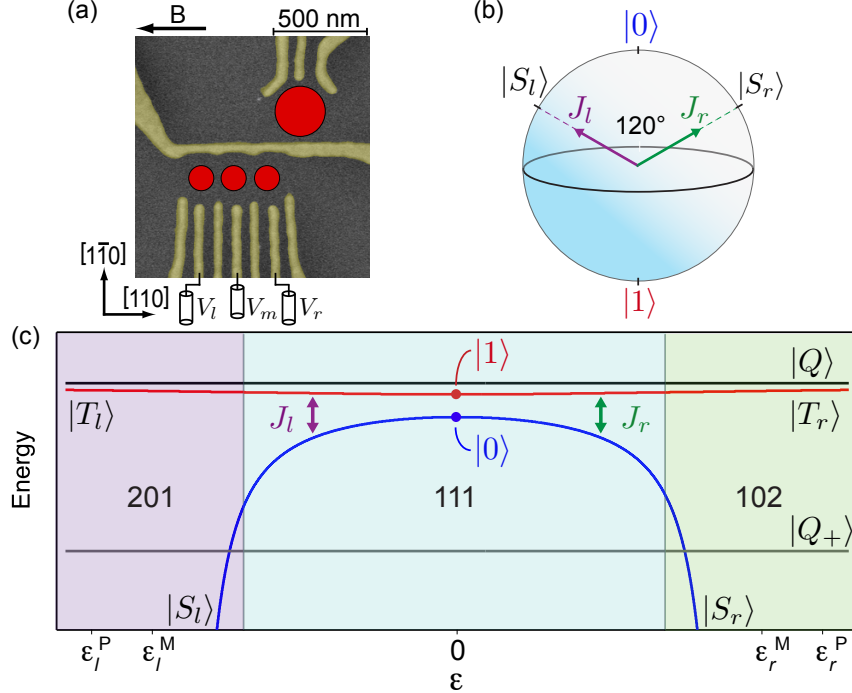


Figure 7.1: (a) False color micrograph of lithographically identical device with locations of triple dot (smaller red circles) and sensor dot (larger red circle). Gate voltages V_l and V_r set the charge occupancy of left and right dot as well as the detuning, ε of the qubit. (b) A Bloch sphere representation of the qubit with control axes J_l and J_r indicated, as well as two initialization states, $|S_l\rangle$ and $|S_r\rangle$. (c) Energy levels as a function of detuning for the lowest energy states [85]. The red and blue levels form the logical subspace inside 111, with the logical states $|0\rangle$ and $|1\rangle$ denoted at the detuning at which they are the eigenstates of the system. Each state has a spin-split partner state with opposite spin projection, not shown. Values of ϵ for preparation (P) and measurement (M) in 201 and 102 are indicated.

exchange interactions, which lower the energy of singlet-like pairs within the $S = 1/2$, $m_S = \pm 1/2$ subspaces. In particular, tunneling between the left and middle dots opens a splitting, $J_l(\varepsilon)$, between the left singlet-like² state $|S_l\rangle = \frac{1}{\sqrt{2}}(|\uparrow\uparrow\downarrow\rangle - |\downarrow\uparrow\uparrow\rangle)$ and the left triplet-like state $|T_l\rangle = \frac{1}{\sqrt{6}}(|\downarrow\uparrow\uparrow\rangle + |\uparrow\downarrow\uparrow\rangle - 2|\uparrow\uparrow\downarrow\rangle)$. $J_l(\varepsilon)$ increases as the detuning is shifted towards the 201 charge state. Tunneling between right and middle dots similarly opens a splitting $J_r(\varepsilon)$ between $|S_r\rangle = \frac{1}{\sqrt{2}}(|\uparrow\uparrow\downarrow\rangle - |\uparrow\downarrow\uparrow\rangle)$ and $|T_r\rangle = \frac{1}{\sqrt{6}}(|\uparrow\uparrow\downarrow\rangle + |\uparrow\downarrow\uparrow\rangle - 2|\downarrow\uparrow\uparrow\rangle)$

²We refer to states as singlet-like because two of the three electron spins form a spin singlet. A similar logic applies to the triplet-like states.

which increases as ε is shifted towards 102.

The logical qubit space is chosen to be in the $S = 1/2, m_S = +1/2$ subspace³, where gate voltages control the energy spectrum. The logical qubit states, $|0\rangle = \frac{1}{\sqrt{6}}(|\uparrow\uparrow\downarrow\rangle + |\downarrow\uparrow\uparrow\rangle - 2|\uparrow\downarrow\uparrow\rangle)$ and $|1\rangle = \frac{1}{\sqrt{2}}(|\uparrow\uparrow\downarrow\rangle - |\downarrow\uparrow\uparrow\rangle)$, are eigenstates in the center of 111, with $J_l(\varepsilon) = J_r(\varepsilon)$. Two states with $S = 3/2$ couple into the logical subspace through Zeeman field gradients. Longitudinal gradients couple the qubit space to the $S = 3/2, m_S = 1/2$ state, $|Q\rangle = \frac{1}{\sqrt{3}}(|\uparrow\uparrow\downarrow\rangle + |\uparrow\downarrow\uparrow\rangle + |\downarrow\uparrow\uparrow\rangle)$. The state $|Q\rangle$ is a spin symmetric state, being triplet-like for both left-middle and middle-right pairs of spins, and is the dominant leakage state for this qubit. Leakage into the $S = 3/2, m_S = 3/2$ state, $|Q_+\rangle = |\uparrow\uparrow\uparrow\rangle$, is suppressed by a large Zeeman field except at two anticrossings. By traversing these anticrossings diabatically—unlike in previously triple-dot experiments [85, 49]—leakage into $|Q_+\rangle$ can be made negligible.

7.3 Two Exchange Interactions

The left singlet-like state, $|S_l\rangle$, is prepared by moving to ε_l^P in 201, and briefly moving near the 201-101 charge transition border to promote rapid relaxation to the ground state. The right singlet-like state, $|S_r\rangle$, is similarly prepared by moving to ε_r^P in 102 and pulsing near the charge border. The excursions to these charge borders during initialization are the only departures from $\delta = 0$, where $\delta = (V_r - V_r^0)/2 + (V_l - V_l^0)/2$ defines the center line of 111 (see Fig. 7.2(a)).

Arbitrary qubit states are determined by projection onto $|S_l\rangle$ or $|S_r\rangle$. Projection onto $|S_l\rangle$ is accomplished by moving to the left measurement point, ε_l^M , where $|S_l\rangle$ can move to 201 while $|T_l\rangle$ and $|Q\rangle$ remain trapped in 111 [85]. During the measurement, an rf exci-

³At the external magnetic field and electron temperature in this work, the $m_S = -1/2$ states are also loaded at times. These states behave identically to the $m_S = +1/2$ states in the regime presented in this work and states of different spin projections do not interact with one another. We have chosen therefore to ignore this added degree of freedom in the remainder of this work to reduce confusion.

tation is applied across the sensor quantum dot. The reflected signal is demodulated using homodyne detection [123] and integrated for $\tau_M = 50 \mu s$, resulting in a signal corresponding to either the 201 or 111 charge state. Projection of the qubit state onto $|S_r\rangle$ is carried out in a similar way at measurement point ε_r^M in 102.

Effects of exchange interactions, $J_l(\varepsilon)$ and $J_r(\varepsilon)$, on qubit dynamics are modeled by an effective Hamiltonian

$$H_J(\varepsilon) = J_l(\varepsilon)\sigma_l + J_r(\varepsilon)\sigma_r, \quad (7.1)$$

where $\sigma_l \equiv (\sqrt{3}\sigma_x - \sigma_z)/4$, $\sigma_r \equiv (-\sqrt{3}\sigma_x - \sigma_z)/4$, and σ_x and σ_z are Pauli matrices in the logical basis $\{|0\rangle, |1\rangle\}$. As illustrated in Fig. 6.1(b), $J_l(\varepsilon)$ and $J_r(\varepsilon)$ drive rotations about axes that are 120° apart on the Bloch sphere. In what follows, we use the terms J_l and J_r rotations and axes in the spirit of this model.

7.4 Coherent Rotations

To demonstrate two-axis control and readout, as well as to test the applicability of the simple model, Eq. (1), we first initialize the system in the $|S_l\rangle$ state and separate the electrons into 111 at a detuning ε^S for a time τ_S , where the qubit evolves under $H_J(\varepsilon^S)$ [Fig. 7.2(b)]. The qubit is then pulsed to ε_l^M to measure the projection of the evolved state onto $|S_l\rangle$, which we determine by measuring the singlet return probability on the left, P_1 , over an ensemble of repeated experiments. Pulsing instead to ε_r^M allows for a measurement of the projection onto $|S_r\rangle$, which when averaged over an ensemble gives the singlet return probability on the right, P_2 .

Figure 7.2(b) shows that for states initialized in $|S_l\rangle$, there is a rapid oscillation of the measured P_1 as a function of τ_S at positive detunings ε^S , $J_l(\varepsilon^S) \ll J_r(\varepsilon^S)$, and a roughly constant $P_1 \sim 1$ at negative detunings, $J_l(\varepsilon^S) \gg J_r(\varepsilon^S)$. The reverse is true for states prepared as $|S_r\rangle$ in Fig. 7.2(c): $P_2 \sim 1$ at positive detunings while P_2 exhibits rapid

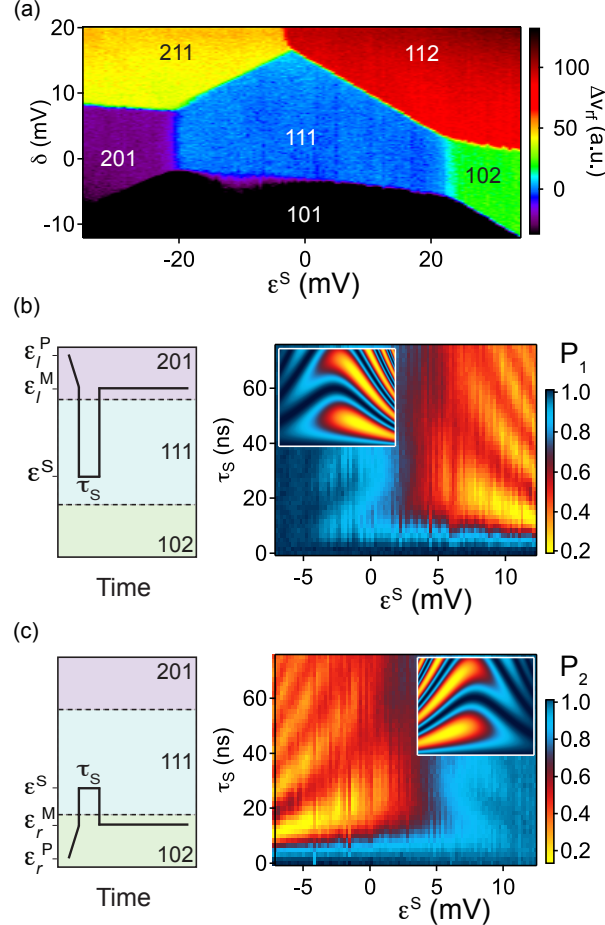


Figure 7.2: (a) Triple dot charge occupancy N_l, N_m, N_r as a function of V_l and V_r in and near the 111 regime; $\varepsilon = (V_r - V_r^0)/2 - (V_l - V_l^0)/2$, $\delta = (V_r - V_r^0)/2 + (V_l - V_l^0)/2^5$. The charge occupancy is measured using the change in the reflected rf signal, Δv_{rf} , incident on the proximal sensor. (b) Schematic of a pulse sequence that prepares $|S_l\rangle$ in 201, and transfers that state to 111, by moving along ε at $\delta = 0$. The sequence then waits at ε^S for a time τ_s , and returns to 201 for measurement. The probability, P_1 , of remaining in the initial state, $|S_l\rangle$, is plotted as a function of pulse position and wait time. Positive ε brings the state closer to 102, while negative ε brings the state closer to 201. (c) Schematic of a pulse sequence, along with a plot of the probability of remaining in $|S_r\rangle$ for an excursion to the separation point ε^S for a time τ_s . (insets) Model of qubit evolution as a function of exchange. No noise has been included.

oscillations as a function of τ_s at negative detunings.

The insets of Fig. 7.2 show model calculations of $P_1 = |\langle S_l | e^{-iH_J(\varepsilon^S)\tau_s/\hbar} | S_l \rangle|^2$ and $P_2 = |\langle S_r | e^{-iH_J(\varepsilon^S)\tau_s/\hbar} | S_r \rangle|^2$, which agree well with experiment. These calculations

neglect noise in $J_l(\varepsilon^S)$ and $J_r(\varepsilon^S)$ as well as fluctuations in local hyperfine fields. These contributions are considered in detail below.

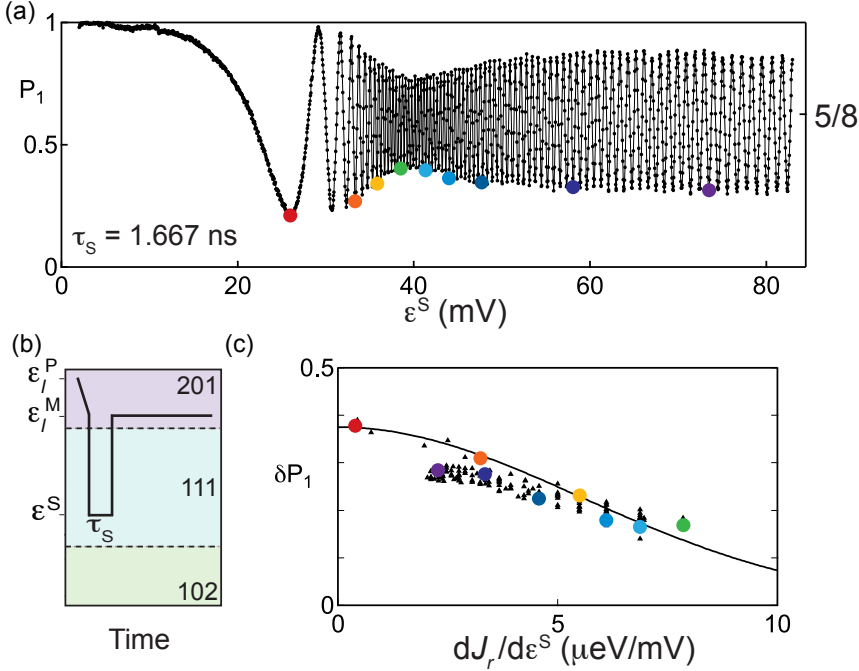


Figure 7.3: (a) Qubit precession as a function of detuning at the separation point, ε^S for fixed pulse duration, $\tau_s = 1.667 \text{ ns}$. This pulse width is less than the rise time of both the coax and the pulse generator, leading to a significant pulse attenuation at the sample. (b) One cycle of the pulse sequence schematic used to generate rotation about the J_r axis. (c) Amplitude of oscillation, δP_1 , as a function of $dJ_r/d\varepsilon^S$, measured from the period of oscillations in (a). Theoretical form $\delta P_1 = \frac{3}{8} e^{-\alpha^2(dJ_r/d\varepsilon^S)^2}$, where $\alpha = \tau_s \sigma_\varepsilon / \sqrt{2}$ [36] with single parameter, $\sigma_\varepsilon = 450 \mu\text{V}$, fit over the first 29 oscillations, to the left of the green point (4th from the left) dot in (a).

7.5 Exchange Noise

An exchange pulse can generate rapid qubit evolution on nanosecond time scales, faster than dynamics induced by other sources such as spin-orbit or hyperfine coupling. The short-pulse regime thus allows exchange and its noise to be examined in isolation from other sources of qubit dynamics. Figure 3(a) shows P_1 for a short exchange pulse, $\tau_s = 1.667 \text{ ns}$, as a function of pulse amplitude, $J_r(\varepsilon^S)$, over a range of phase $\phi = \tau_s J_r(\varepsilon^S)/\hbar$ from 0 to

$\sim 158\pi$, corresponding to a 47.4 GHz rotation.

At large positive ε^S , where $J_r(\varepsilon^S) \gg J_l(\varepsilon^S)$, the noiseless model predicts $P_1 = 5/8 + 3/8 \cos(\tau_S J_r(\varepsilon^S)/\hbar)$ for initial state $|S_l\rangle$ ⁶. Experimental data agrees well with the 5/8 average [see Fig. 3(a)], but the observed oscillation amplitude, δP_1 , is notably less than 3/8, with a distinct dip where phase varies most rapidly with ε^S , i.e., where $dJ_r/d\varepsilon^S$ is largest. The reduced amplitude can be understood quantitatively as the result of averaging over exchange noise arising from noise in ε , yielding $\delta P_1 = \frac{3}{8} e^{-\alpha^2(dJ_r/d\varepsilon^S)^2}$, where $\alpha = \tau_S \sigma_\varepsilon / \sqrt{2}$ [36]. The period of oscillations in Fig. 3(a) gives a direct measurement of $dJ_r/d\varepsilon^S$, leaving a single fit parameter, σ_ε , the effective standard deviation of noise in ε . Experiment and theory are in excellent agreement [Fig. 7.3(c)]. The fit value, $\sigma_\varepsilon = 450 \mu\text{V}$, is only nominal, as it includes effects of finite coax bandwidth, making it larger than the actual ε noise in the system.

In Fig 7.4, the free induction decay measured at longer separation times, τ_S , and at fixed detuning, ε^S , reveals the combined effects of exchange noise, which causes dephasing, discussed above, and Zeeman field gradients, which cause both dephasing and leakage out of the qubit space.

Quasi-static longitudinal (effective) field differences between dots, $\Delta B_l = B_l^z - B_m^z$ and $\Delta B_r = B_m^z - B_r^z$, drive coherent evolution between $|0\rangle$ and $|1\rangle$. Gradients due to hyperfine fields appear static on the time scale of a single sequence of measurements, but execute a thermal random walk over an ensemble of measurements. In addition, Zeeman differences $g\mu_B\Delta B_l$ and $g\mu_B\Delta B_r$ comparable in magnitude to $J_l(\varepsilon)$ or $J_r(\varepsilon)$ will drive evolution into $|Q\rangle$, the leakage state. Here μ_B is the Bohr magneton and $g \sim -0.4$ is the

⁶The values 5/8 and 3/8 only hold for pulses that are adiabatic with respect to the interdot tunnel couplings, but diabatic with respect to $J_l(0) + J_r(0)$, the total exchange in the center of 111. This allows pulses to be modeled as instantaneous changes of the Hamiltonian, giving $P_1 = |\langle S_l | e^{-iH_J(\varepsilon^S)\tau_S/\hbar} | S_l \rangle|^2 = 5/8 + 3/8 \cos(\tau_S J_r(\varepsilon^S)/\hbar)$

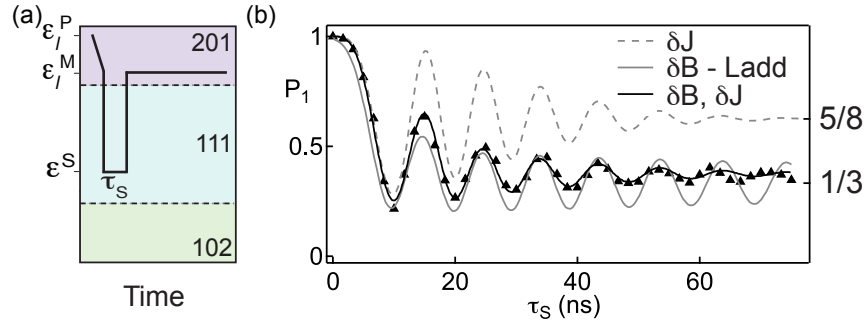


Figure 7.4: (a) A schematic of the pulses for a rotation about the J_r axis. (b) Free induction decay (FID) as a function of τ_S . The dashed gray curve is a theory model of a rotation around the J_r axis ($J_l = 0$) in the presence of dephasing, the solid gray curve is a model of Ref. [81], that accounts for the same rotation in the presence of dephasing and leakage due solely to nuclear magnetic field gradients. The solid black curve is fit to a numerical integration of the qubit evolution for a rotation around J_r , in the presence of quasistatic Gaussian distributions of nuclear gradients ΔB_l and ΔB_r , as well as quasistatic noise in J_r . J_l was also allowed to be nonzero in the fit. Noise is evaluated as quasistatic, rather than incorporating unknown spectral densities. Here, $J_l = 20 \pm 8$ neV, $J_r = 388 \pm 2$ neV, and standard deviations $\sigma_B = 2.0 \pm 0.1$ mT, $\sigma_J = 19 \pm 2$ neV, with a turn-on of the exchange modeled as an exponential with time constant $\tau = 12.6 \pm 0.2$ ns.

electron g factor. Averaging over the entire nuclear ensemble during repeated measurements results in a damped oscillation towards the triplet outcome as the qubit dephases and leaks into $|Q\rangle$. By examining in detail the τ_S dependence of P_1 at a fixed ε^S in Fig. 7.4, and comparing it with theoretical models for low frequency exchange and Overhauser [81] noise, we conclude that nuclear fluctuations are the predominant source of noise in this system, with a standard deviation of 2.0 mT.

7.6 Dynamical Decoupling

Low-frequency hyperfine noise [124, 77] can be compensated using dynamical decoupling [16, 94]. Unlike the situation in double quantum dots, however, a single-pulse echo cannot undo the effects of two hyperfine field gradients in the three-dot system[155]. Nevertheless, a single π -pulse can undo a *portion* of the dephasing due both to nuclei and low-frequency exchange noise.

Single-pulse partial echo is demonstrated by preparing $|S_l\rangle$ in 201, separating to 111 where the state rotates for a time τ_1 around J_r , followed by a π -pulse around J_l , followed by further rotation around J_r for a time τ_2 . The sequence is illustrated in Fig. 7.5(a). P_1 shows robust oscillations as a function of both sum and difference of the dephasing times τ_1 and τ_2 , similar to a Ramsey measurement with a refocusing pulse in the middle. The decay envelope in $\tau_1 + \tau_2$ at $\tau_1 = \tau_2$ in Fig. 7.5(b) gives a lower bound on the coherence time, $T_2 \sim 100$ ns, while the decay envelope in $\tau_1 - \tau_2$ shown in Fig. 7.5(c) gives a dephasing time, $T_2^* \sim 25$ ns. The dephasing time in $\tau_1 - \tau_2$ is consistent with FID times [Fig. 7.4(b)], while decay as a function of $\tau_1 + \tau_2$ is extended by a factor of ~ 4 for the echo condition $\tau_1 = \tau_2$. This modest enhancement is consistent with decoupling a portion of the noise from the environment. A model of classical, slowly fluctuating hyperfine field gradients [Fig. 7.5(d)], yields a value for the standard deviation of ΔB_l and ΔB_r of 3.4 mT, and indicates these gradients to be the dominant noise source for this pulse sequence.

7.7 Tomographic Characterization of the System

Qubit performance is commonly assessed by state and process tomography. These techniques require a well-characterized set of measurements that give enough information to reconstruct all the matrix elements of the density matrix of the system. It is important to recognize, however, that measurements themselves are subject to noise, relaxation, and systematic errors, and may not be well described by idealized projective measurements. To accommodate both state preparation and measurement errors we implement a self-consistent approach that combines measurement data and models of system dynamics within a maximum likelihood estimation routine. Self-consistent tomography along similar lines has been carried out recently for superconducting qubits in Ref. [97].

Consider single-shot measurement in the singlet-triplet basis, for the moment ig-

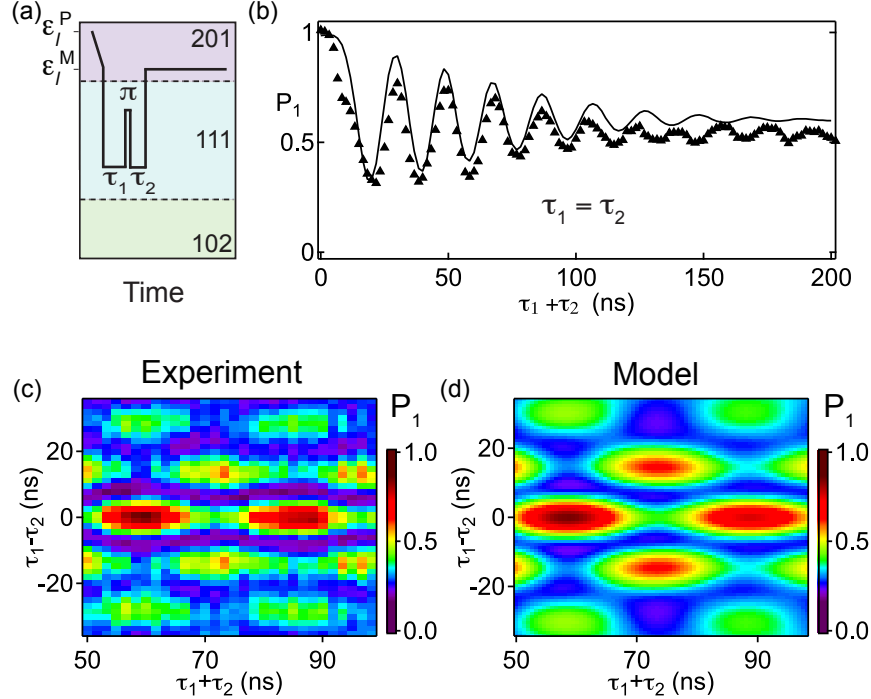


Figure 7.5: (a) A schematic for a three pulse sequence demonstrating an echo, where a prepared $|S_l\rangle$ precesses around J_r for a time τ_1 , performs a π -pulse around J_l , and then precesses again around J_r for a time τ_2 before being measured in 201. (b) Probability P_1 of measuring $|S_l\rangle$ for the pulse sequence depicted in (a), for the case $\tau_1 = \tau_2$. The solid black curve is a model with noise from J_r , ΔB_l , and ΔB_r during the dephasing times τ_1 and τ_2 , and noise due to J_l , ΔB_l , and ΔB_r during the π -pulse using parameters extracted from FID data in Fig. 7.4(b). (c) The results of a three pulse echo sequence, illustrated in (a), that maps the probability of remaining $|S_l\rangle$ as a function of the total dephasing time ($\tau_1 + \tau_2$), and the difference in time between the first free induction decay, τ_1 , and the second, τ_2 . (d) A model plot for (c) that averages over thermal distributions of nuclear gradients. See Appendix D for details of the calculation.

noring leakage into state $|Q\rangle$. The singlet measurement fidelity F_S is the probability that the measurement correctly registers the singlet outcome when measuring a system prepared in the singlet state; similarly, F_T is the probability that system prepared in the triplet state yields the triplet outcome for the measurement [8]. Given that the measurement is defined to be along the $|S_l\rangle$ - $|T_l\rangle$ or $|S_r\rangle$ - $|T_r\rangle$ axis of the Bloch sphere, these two numbers completely characterize an imperfect two-outcome measurement on a qubit. On the other hand, measurements along other directions require rotations which are themselves imper-

fect as well. This, then, requires a general description of a noisy measurement that includes errors in measurement *direction* as well as reduced fidelities. Such a description is provided by the formalism of Positive Operator-Valued Measure (POVM) elements. As all our measurements have two outcomes, the POVM describing each measurement basis choice i is given by a single positive Hermitian matrix E_i associated with the “singlet” outcome. (The corresponding “triplet” outcome is associated with the matrix $(\mathbb{I} - E_i)$.) The eigenvectors of E_i determine the axis of the Bloch sphere along which the measurement is made. The eigenvalues are bounded between zero and one, with the larger eigenvalue of E_i equal to F_S while the smaller eigenvalue is $1 - F_T$. Using the POVM formalism, the probability that a system described by a density matrix ρ will yield the singlet outcome when the measurement of basis i is performed is

$$P_i(\rho) = \text{Tr}[E_i \rho]. \quad (7.2)$$

The POVM formalism can be applied to the three-state system of qubit states plus leakage state $|Q\rangle$, in which case the E_i are 3×3 Hermitian matrices. As our measurements are insensitive to coherence between the leakage and qubit states, which in any case is expected to be small, we restrict E_i to be incoherent with the $|Q\rangle$ space (i.e., each E_i has support on the reduced qubit subspace together with a population in $|Q\rangle$). We note that the $|Q\rangle$ state will, with an idealized spin-to-charge measurement, always yield the triplet outcome. As such, the $|Q\rangle$ -population of E_i quantifies the error-induced probability that a system prepared in the $|Q\rangle$ state will instead yield the singlet outcome.

7.8 Measurement Tomography

Measurement of the four matrices, E_i , $i=1-4$, is required for state tomography, additionally yielding the population of the leakage state. Each of the four E_i has five parameters associated with the qubit state and the leakage population, for a total of 20

unknown quantities⁷. Measurement tomography therefore requires measurement outcome statistics on five well-characterized input states, ρ_j , using each of the four generalized measurements to yield 20 independent observed probabilities, P_{ij} . We then solve $P_{ij} = \text{Tr}[E_i \rho_j]$ self-consistently for E_i , subject to the constraints on the eigenvalues of E_i to lie between 0 and 1. Details of this procedure are given in the Methods section, as well as in Appendix D.

Using the reconstructed E_i , we extract the measurement bases and fidelities from the eigenvalues and eigenvectors as discussed above. The singlet outcome fidelity is indicated by the length of the E_i arrow in Figs. 7.6(e,f). The smaller eigenvalue in the qubit space relates to the fidelity of the triplet outcome, $F_{Ti} = 1 - \lambda_{i2}$, while the eigenvalue in the leakage subspace relates to the probability that $|Q\rangle$ will have a triplet outcome, $F_{Qi} = 1 - \lambda_{i3}$. Finally, the measurement visibility in the qubit subspace is found as $V_i = F_{Si} + F_{Ti} - 1 = \lambda_{i1} - \lambda_{i2}$. The average singlet fidelity over all four generalized measurements was found to be 69%, while the average triplet fidelity was 80%, giving an overall average measurement fidelity in the qubit subspace of 75% with an average measurement visibility of 49%.

7.9 State Tomography

We can now perform state tomography on arbitrary states of our system using our set of tomographically characterized generalized measurements despite the fact that these measurements are inherently noisy. As a demonstration, we generated sets of unknown states by performing a simple rotation around J_l in the presence of dephasing for multiple fresh input states. In Fig. 7.6, two separate input states, ρ_1 (red) and ρ_2 (blue), are prepared and then pulsed to a negative detuning where $J_l \gg J_r$, followed by a generalized measurement (the markers in Fig. 7.6(a-d)). Using our descriptions of E_i , we are able to

⁷The four unknowns of E_i containing the qubit state-leakage state coherence are set to zero because without a coherent, stable magnetic field gradient, they are impossible to reliably measure and are negligibly small

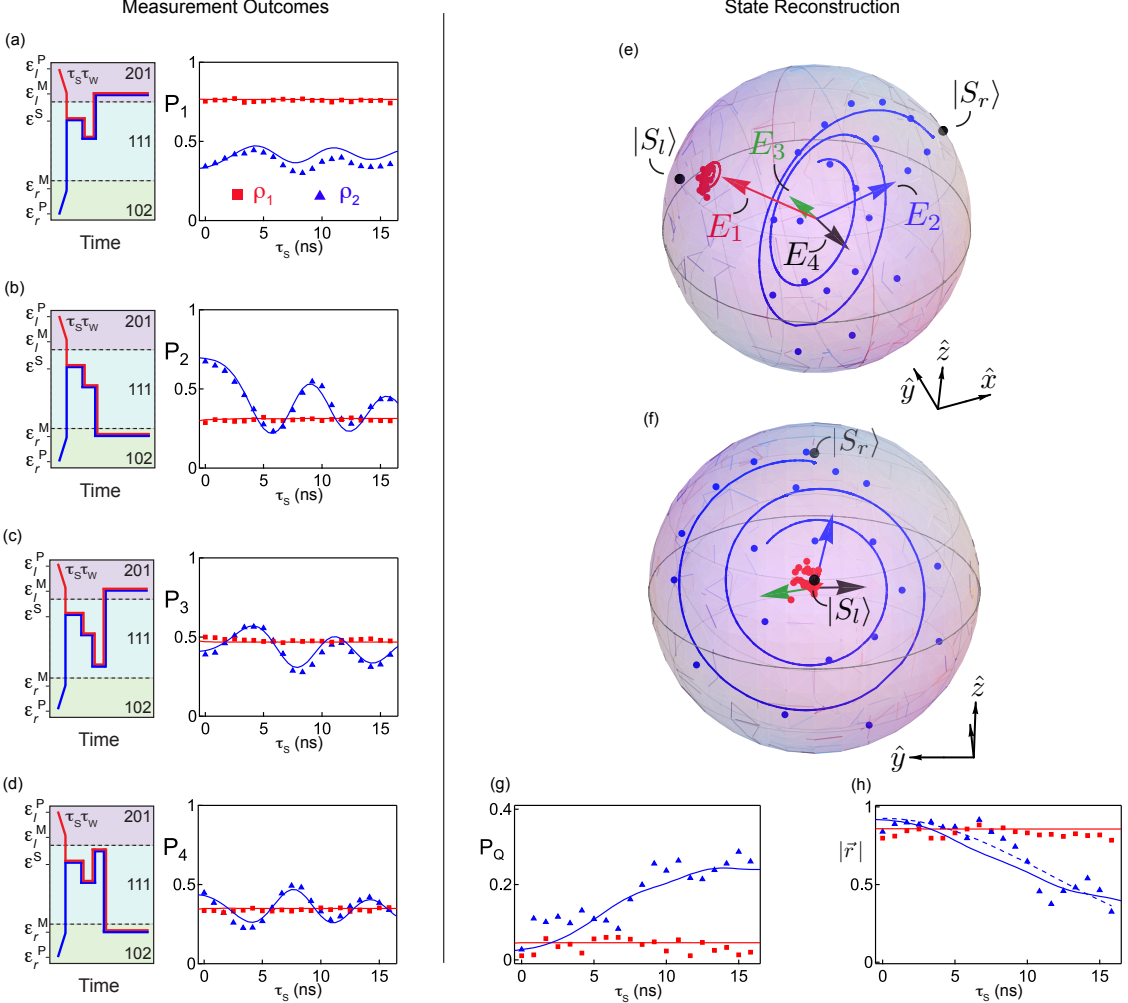


Figure 7.6: State tomography of the qubit during evolution around J_l . Measurement outcome probabilities for four measurement bases for initial states ρ_1 (red) and ρ_2 (blue), pulsed towards ε^S near the 201-111 charge transition, producing rotation mostly around J_l . The solid curves in (a-d) are a fit to the model (see Appendix D). Solid curves in (g) and (h) are generated from the model in (a-d). (a) Schematic and measurements of $P_1(\rho_1)$ (red) and $P_1(\rho_2)$ (blue); (b) $P_2(\rho_1)$ (red) and $P_2(\rho_2)$ (blue); (c) $P_3(\rho_1)$ (red) and $P_3(\rho_2)$ (blue); (d) $P_4(\rho_1)$ (red) and $P_4(\rho_2)$ (blue). (e-f) Views of Bloch sphere with measurement axes. Graphical representation of the qubit portion of E_1 (red), E_2 (blue), E_3 (green) and E_4 (black). (g) Population of the leakage state as a function of separation time. (h) The length of the Bloch vector as a function of separation time data (blue triangles), model (blue curve), and gaussian fit [width 16.4 ± 0.9 ns] (dashed blue curve).

reconstruct the state at a set of time intervals during the evolution by solving equation (7.2) again for ρ (the markers in Fig. 7.6(e,f)). The theory curves overlaid on top of the data

in Fig. 7.6(a-h) are fits to the Liouville-von Neumann equation, accounting for the finite bandwidth of the coax and a theoretical model of the exchange profile, in the presence of the nuclear noise determined from the calibration procedure.

As expected, pulsing towards a negative detuning yields an outcome that depends on the input state. For the states prepared as $\rho_1 = |S_l\rangle\langle S_l|$, the red markers and curves in Fig. 7.6(e,f), sitting at a position of large J_l only imparts a trivial phase. At this detuning, $|S_l\rangle$ is split off energetically from $|Q\rangle$, suppressing leakage out of the qubit space. This is observed on the Bloch sphere as a collection of points near the idealized $|S_l\rangle$ state.

The state that is prepared as $\rho_2 = |S_r\rangle\langle S_r|$, the blue markers and curves in Fig. 7.6(e,f), has a very different response. Since it is an eigenstate of J_r , at this detuning it is a superposition of the ground and excited qubit states. As a result, it precesses around the J_l axis in the presence of dephasing, which causes the state to spiral inwards towards the rotation axis.

At this detuning a fraction of ρ_2 is in the excited qubit state, which is energetically close to the $|Q\rangle$ state, allowing the Overhauser gradients to rotate that fraction out of the qubit space. This leakage into the $|Q\rangle$ state occurs on a 10 ns timescale in both the data and the theory, which increases the decay of the Bloch vector \vec{r} towards the center of the Bloch sphere in Figs 7.6(e,f,h) as the probability exits the qubit subspace. The leakage is seen clearly in the rise of the $|Q\rangle$ population, P_Q , in Fig. 7.6(g). The qubit state vector length in Fig. 7.6(h) acts as a measure of qubit coherence and population, and it decays with a $T_2^* \sim 16$ ns, which is consistent with previous measurements.

In conclusion, we have demonstrated the initialization, complete fast electrical control, and state reconstruction of an exchange-only spin qubit. The method of tomographic calibration we developed can be applied directly to other qubit systems to quantify measurement errors. Future work will include investigating regimes where J_l and J_r are

simultaneously much larger than the nuclear gradient Zeeman energy, which would suppress leakage into $|Q\rangle$, and structures comprising of six dots that implement a fast two-qubit gate [42].

7.10 Methods

Measurement tomography requires a choice of five input states, ρ_j , which span the qubit subspace. The initialization states $|S_l\rangle$ and $|S_r\rangle$ provide ρ_1 and ρ_2 respectively. We create two additional states ρ_3 and ρ_4 by rotating $|S_l\rangle$ around J_r at ε_3^S and $|S_r\rangle$ around J_l at ε_4^S respectively. These four input states span the qubit space. The rotated states are subject to rotation errors, dephasing, and leakage, which we need to characterize using a phenomenological model for the dynamics and fit the parameters of this model using experimental data.

To facilitate this, we use a series of states for ρ_3 and ρ_4 . The noisy evolution of ρ_3 and ρ_4 is then modeled with a generalization of $H_J(\varepsilon)$ to the larger manifold of $|0\rangle$, $|1\rangle$, and $|Q\rangle$, including the effects of ΔB_l and ΔB_r (see Appendix D for details). During the calibration of the E_i 's, we compare the model of this evolution to the series of states $\rho_3(\tau_3)$ created by initializing $|S_l\rangle$ and rotating around J_r at ε_3^S for a set of times τ_3 before measuring. The series of states $\rho_4(\tau_4)$ was produced in a similar fashion by preparing $|S_r\rangle$ and rotating for a set of times τ_4 about J_l at ε_4^S . These series of states contain enough information to determine the strength of the nuclear dephasing and the exchange axes at ε_3^S and ε_4^S .

The final input state, ρ_5 , is chosen to be a completely mixed state with no coherences remaining and a significant weight in the leakage state. This choice allows for accurate measurements of the $|Q\rangle\langle Q|$ parameter in each E_i . The ensemble of ρ_5 was prepared by performing repeated pulses to dephase around J_l and J_r over a distribution of ΔB_l and

ΔB_r .

With the observed statistics P_{ij} for five known input states j using four measurements i , we determine E_i by fitting the calibration probabilities from all of our input states to our model of the noisy evolution to produce a Maximum Likelihood Estimate (MLE) for E_1-E_4 as well as the nuclear noise and exchange during the calibration⁸. For the data in Fig. 7.6, the standard deviations of ΔB_l and ΔB_r were ~ 2.5 mT, which is consistent with the earlier estimations extracted from the FID and echo data.

Acknowledgements

We gratefully acknowledge support from IARPA through the MQCO program, the Danish National Research Foundation, and the Villum Foundation. S.B. and A.D. acknowledge support from the ARC via the Centre of Excellence in Engineered Quantum Systems (EQuS), project number CE110001013. We thank Oliver Dial, Bert Halperin, Ferdinand Kuemmeth, Thaddeus Ladd, and Amir Yacoby for useful discussions. We thank Brandon Armstrong for technical contributions.

⁸Noise on J_l and J_r was neglected, as ε_3^S and ε_4^S were in a region where exchange noise was not the dominant source of dephasing.

Chapter 8

Resonant Microwave Control of a Symmetric Exchange-Only Spin Qubit

J. Medford

Department of Physics, Harvard University, Cambridge, Massachusetts 02138, USA

J. Beil, C. M. Marcus

Department of Physics, Harvard University, Cambridge, Massachusetts 02138, USA

*Center for Quantum Devices, Niels Bohr Institute, University of Copenhagen,
Universitetsparken 5, DK-2100 Copenhagen, Denmark*

J. M. Taylor

Joint Quantum Institute/NIST, College Park, MD, USA

H. Lu, A. C. Gossard

Materials Department, University of California, Santa Barbara, California 93106, USA

We use a triple quantum dot in a GaAs heterostructure configured in a regime protected from charge noise and state leakage as a new electrically controlled spin qubit. This symmetric exchange-only (SEO) spin qubit acts as an artificial spin-1/2 particle that responds to oscillating electric fields in an analogous fashion to a real spin-1/2 particle in an oscillating magnetic field. We study the spectroscopy, nutation, two-axis manipulation, lifetime and dynamical decoupling of this new spin qubit. We find that the nutation sensitivity is as high as 5.1 GHz/mV for resonant excitations, with a $T_1 \sim 40 \mu\text{s}$ and a $T_2 \sim 20 \mu\text{s}$ for a CPMG-64 sequence. Finally, we extract a noise power spectral density of $S(\omega) \sim \omega^{-5}$, which suggests that further gains may be made with more advanced dynamical decoupling sequences.

8.1 Introduction

The improvement of qubit fidelity has been a major goal in quantum information processing, either through decoupling the qubit from the environment via spin echo techniques [11, 111, 14, 7, 10, 22, 146] or through optimized qubit architectures [74, 132, 61, 15, 109] or materials [92]. In the semiconductor spin qubit community, charge noise has been shown to be the limiting factor in fidelity of two-qubit operations in double quantum dots [14, 136, 41], which introduces decoherence to each qubit proportional to the two-qubit interaction. This sensitivity to charge noise comes from the exchange interaction between neighboring spins, which has a strong dependence on the local electrical environment in the two quantum dot system. Here, we demonstrate a semiconductor spin qubit formed from a triple quantum dot [42, 51, 50, 85, 49, 93] which is operated at a “sweet spot” with respect to charge noise, which should enable it to achieve high fidelity single- and two-qubit operations.

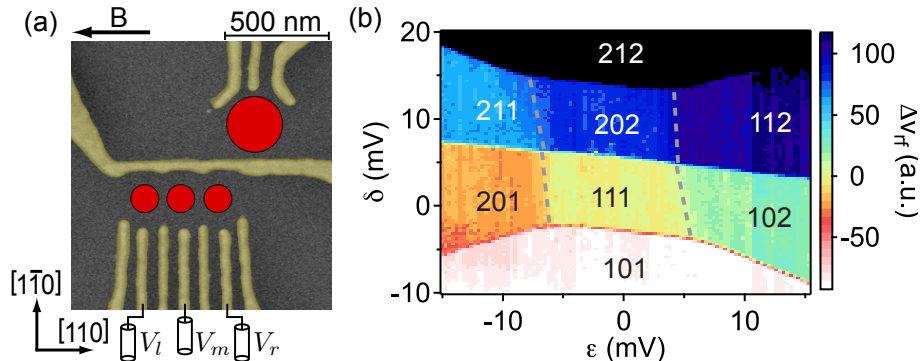


Figure 8.1: (a) False color micrograph of lithographically identical device with dot locations depicted; gates are marked in yellow. Gate voltages, V_l and V_r , set the charge occupancy of left and right dot as well as the detuning, ε of the qubit. A neighboring sensor quantum dot is indicated with a larger circle. (b) Triple dot charge occupancy N_l N_m N_r as a function of V_l and V_r in and near the 111 regime; $\varepsilon = (V_r - V_r^0)/2 - (V_l - V_l^0)/2$, $\delta = (V_r - V_r^0)/2 + (V_l - V_l^0)/2 + 3(V_m - V_m^0)$.

In this chapter, we characterize an optimized, all electrically controlled, spin qubit

for potential quantum information processing architectures. We find that spectroscopy of the system supports our simple model of available energy states and couplings and reveals a g-factor for this device of -0.34 ± 0.01 , allowing for a quantitative study of the qubit dynamics. The qubit responds to oscillating electric fields with a Rabi frequency, ω_R , that depends linearly on the applied voltage as $\omega_R = \alpha V$, with an α that depends on the splitting between qubit states, ω_{01} . We find that for $\omega_{01}/2\pi = 1.98$ GHz, $\alpha \sim 2\pi \times 5$ GHz/mV. The T_1 of the qubit is also dependent on ω_{01} , and is in excess of $40\ \mu\text{s}$ at a splitting of ~ 0.34 GHz, but decreases to as little as 98 ns for a splitting as large as 1.98 GHz. The coherence time is measured to be $T_2 = 19 \pm 2\ \mu\text{s}$ for a 64 π -pulse Carr Purcell Meiboom Gill (CPMG-64) at 0.2 GHz splitting. The dependence of the coherence time T_2 on the even numbers of pulses indicates that despite working at relatively large exchanges, the noise power spectrum is not dominated by charge noise, confirming that this qubit is largely insensitive to electrical noise.

8.2 Device and System

The qubit was formed from the spin states of three electrons trapped a triple quantum dot in a GaAs/Al_{0.3}Ga_{0.7}As heterostructure. Metal surface gates were used to deplete the two dimensional electron gas (density $2.6 \times 10^{15}\ \text{m}^{-2}$, mobility $43\ \text{m}^2/\text{V s}$) 110 nm below the surface, and isolate one electron in each well (see Fig. 8.1). High bandwidth gates V_l and V_r were used to control the detuning, $\varepsilon = (V_r - V_r^0)/2 - (V_l - V_l^0)/2$, while the high bandwidth gate V_m controlled the size of the 111 charge region¹. The conductance channel directly adjacent to the triple quantum dot is used as an rf-charge sensor for rapid state detection [123, 5].

Inter-dot tunneling between the left and middle and the middle and right dots

¹ $(V_l^0, V_m^0, V_r^0) = (-588\ \text{mV}, -452\ \text{mV}, -145\ \text{mV})$.

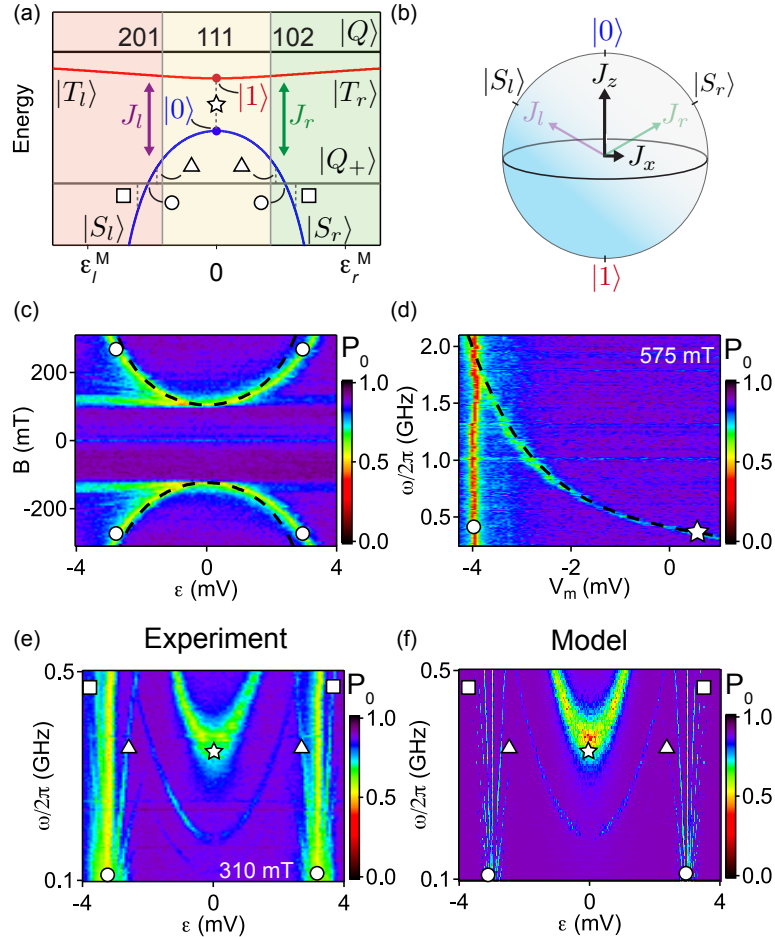


Figure 8.2: (a) Energy level diagram for a constant δ . Charge transitions are marked with circles (qubit- $|Q_+\rangle$), triangles (qubit- $|Q_+\rangle$, photon), squares (qubit- $|Q_+\rangle$, photon), and a star ($|0\rangle$ - $|1\rangle$) transitions. (b) Schematic of the effects of J_l and J_r on the qubit Bloch sphere (c) The qubit- $|Q_+\rangle$ anti-crossing is mapped out in magnetic field and detuning without an excitation. Dashed line is a model of the exchange splitting for equal tunnel couplings. (d) A sweep of the middle plunger gate at $\varepsilon = 0$ mV and fixed field of 575 mT, demonstrating control of the main qubit transition. The dashed curve is a model of $J_l + J_r$ as a function of $\varepsilon_0 = (V_m - V_m^0)/2$. The theory curve is a plot of $\omega_{01} = \left(-\alpha(V_m - V_m^0)/2 + \sqrt{4t^2 + \alpha^2(V_m - V_m^0)^2}/4 \right)/4\hbar$, where $\alpha = 40 \mu\text{eV}/\text{mV}$, $t = 16.9 \mu\text{eV}$, and $V_m^0 = -4.05 \text{ mV}$. A constant tunnel coupling was used here rather than a Gaussian dependent tunnel coupling, because V_l and V_r were constant. (e) At a fixed field of 310 mT, detuning and microwave burst frequency are swept to trace out the spectroscopy of the qubit. (f) A model of qubit evolution in the presence of a microwave excitation and magnetic field gradients between dots in the longitudinal and transverse directions.

gives rise to two ε -dependent exchange terms depicted in Fig. 8.2(a), $J_l(\varepsilon) = -(\varepsilon_0 + \varepsilon)/2 + \sqrt{t^2 + (\varepsilon_0 + \varepsilon)^2/4}$ and $J_r(\varepsilon) = -(\varepsilon_0 - \varepsilon)/2 + \sqrt{t^2 + (\varepsilon_0 - \varepsilon)^2/4}$, where t is the tunnel coupling and $\pm\varepsilon^0$ are the detunings of the charge transitions [85]. These exchanges adiabatically map the lower energy level of the qubit, $|0\rangle = \frac{1}{\sqrt{6}}(|\uparrow\uparrow\downarrow\rangle + |\downarrow\uparrow\uparrow\rangle - 2|\uparrow\downarrow\uparrow\rangle)$, onto the singlet-like ground states in 201, $|S_l\rangle = \frac{1}{\sqrt{2}}(|\uparrow\downarrow\uparrow\rangle - |\downarrow\uparrow\uparrow\rangle)$, and 102, $|S_r\rangle = \frac{1}{\sqrt{2}}(|\uparrow\uparrow\downarrow\rangle - |\uparrow\downarrow\uparrow\rangle)$, as shown in Fig. 8.2(a). The excited qubit state, $|1\rangle = \frac{1}{\sqrt{2}}(|\uparrow\uparrow\downarrow\rangle - |\downarrow\uparrow\uparrow\rangle)$, is adiabatically mapped onto triplet states which do not tunnel into 201 or 102, allowing for qubit state detection using the charge sensor [123, 5]. A third state, $|Q_+\rangle = |\uparrow\uparrow\uparrow\rangle$, intersects the lower qubit energy level at two anti-crossings, which are fixed by the in-plane external magnetic field. By sweeping the magnetic field, the lower qubit energy level can be mapped out in detuning, as shown in Fig. 8.2(a,c). Unlike in Ref. [93], the fourth state in Fig. 8.2(a), $|Q\rangle = \frac{1}{\sqrt{3}}(|\uparrow\uparrow\downarrow\rangle + |\uparrow\downarrow\uparrow\rangle + |\downarrow\uparrow\uparrow\rangle)$, is gapped from the qubit by the presence of both J_l and J_r throughout 111, preventing the qubit state from leaking into it.

8.3 Spectroscopy

By applying a small oscillating voltage to V_l , we change J_l and J_r , creating a small perturbation that when resonant with energy level splittings drive transitions between accessible states. This microwave spectroscopy allows us to map out the qubit energy spectrum of states that do no intersect with $|Q_+\rangle$. As we see in Fig. 8.2(e), at a fixed external magnetic field there is a bright U-shaped transition line in the center of the 111 region corresponding to the $|0\rangle$ - $|1\rangle$ transition. A model of J_l and J_r where the tunnel coupling has a Gaussian dependence on ε [93], as well as fluctuating longitudinal and transverse nuclear polarizations is shown in Fig. 8.2(f), and demonstrates that the transitions observed in (e) are reasonably well explained by this model.

By comparing the $|0\rangle$ - $|1\rangle$ transition marked with a (\star) in Fig. 8.2(e) to the $|0\rangle$ -

$|Q_+\rangle$ splitting mapped out in Fig. 8.2(c), which is 1.5 times large, we are able to extract a g-factor for this system of -0.34 ± 0.01 . We are also able to controllably tune the frequency of the $|0\rangle$ - $|1\rangle$ transition, ω_{01} , by adjusting V_m ² which controls the separation of the charge transitions. We find that we are able to move $\omega_{01}/2\pi$ from ~ 100 MHz to ~ 2 GHz on nanosecond timescales, as illustrated in Fig. 8.2(d). The dashed line in Fig. 8.2(d) is a plot of J_l+J_r as a function of the middle plunger gate, which controls ε_0 , for the tunnel coupling in Fig. 8.2(f)³.

Following Refs. [85, 93], we model the qubit Hamiltonian as

$$\mathcal{H}(\varepsilon) = J_z \sigma_z + J_x \sigma_x, \quad (8.1)$$

where $J_z = -\frac{1}{4}(J_l(\varepsilon) + J_r(\varepsilon))$, and $J_x = \frac{\sqrt{3}}{4}(J_l(\varepsilon) - J_r(\varepsilon))$ as depicted in Fig. 8.2(b). We can see that at $\varepsilon = 0$, $\frac{dJ_z}{d\varepsilon} = 0$, while $\frac{dJ_x}{d\varepsilon} = -\frac{\sqrt{3}}{4}(1 - \varepsilon_0/\sqrt{4t^2 + \varepsilon_0^2})$. For small ε , J_z is constant and $J_x \sim \varepsilon$, making this system analogous to a free spin-1/2 in a large static field B_0 with a small applied transverse field B_1 . If J_x oscillates at a frequency commensurate with J_z , we can drive nutations in the same fashion as with the spin-1/2 particle. Noise can affect J_z through V_m , as demonstrated in Fig. 8.2(d), but as this gate does not carry an excitation, the bandwidth can be reduced to diminish the incident noise.

8.4 Rabi Oscillations

In Fig. 8.3, we prepare a $|S_r\rangle$ in 102 and adiabatically transition it to $|0\rangle$, moving rapidly through the $|Q_+\rangle$ anti-crossing to $\varepsilon = 0$. We then apply a burst of microwaves to V_l of frequency ω , applying power for a time τ_B , before returning to 102 for measurement. By

²The gates V_l and V_r were also adjusted with V_m to keep δ constant, ie keep the qubit in the 111 charge region.

³The theory curve is a plot of $\omega_{01} = \left(-\beta(V_m - V_m^0) + \sqrt{4t^2 + \beta^2(V_m - V_m^0)^2}\right)/4\hbar$, where $\beta = 20$ $\mu\text{eV}/\text{mV}$, $t = 16.9$ μeV , and $V_m^0 = -4.05$ mV. A constant tunnel coupling was used here rather than a Gaussian dependent tunnel coupling, because V_l and V_r were constant. See appendix E for further details.

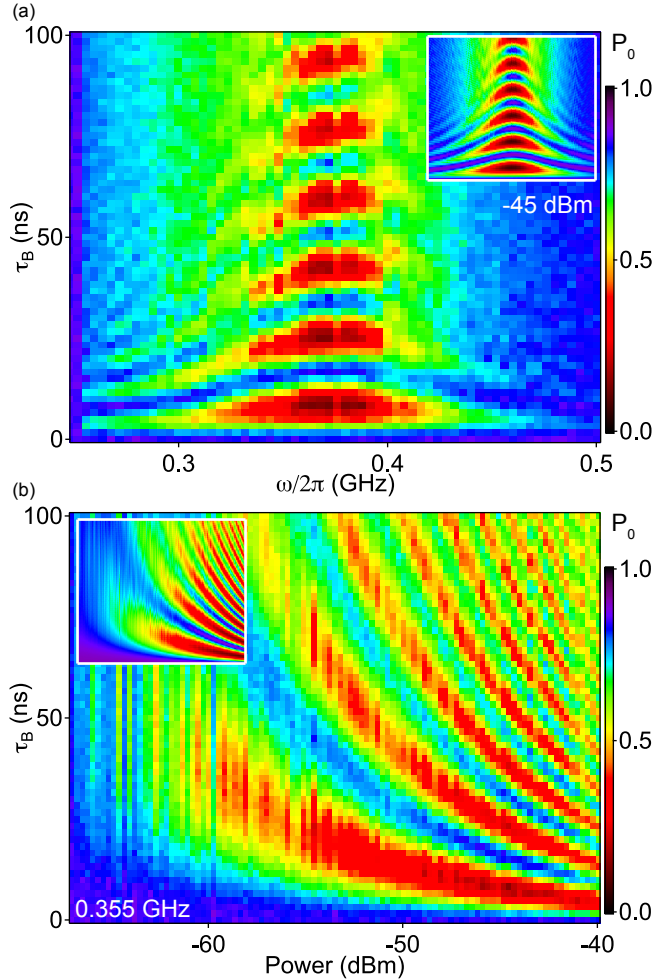


Figure 8.3: (a) A Rabi nutation for a -45 dBm excitation on the left plunger gate with the detuning biased to the center of the transition. (inset) A model of this nutation using the exchange profile from 8.2(f) and fluctuating longitudinal magnetic field gradients. (b) A Rabi nutation with a 0.355 GHz excitation on the left plunger gate with the detuning biased to the center of the transition. (inset) An identical model to (a).

sweeping ω and power, we see patterns characteristic of Rabi nutations which are subject to low frequency noise in ω_{01} . This is consistent with our model of nuclear noise, which directly affects ω_{01} . In the rotating frame, the amplitude of the oscillation gives the strength of the \S rotation, while the frequency detuning, $\Omega = \omega - \omega_{01}$, gives the strength of the \ddagger rotation. As seen in Fig. 8.3(b), as the power increases, the effects of small Ω errors due to nuclei decrease. At $\omega_{01}/2\pi = 0.355$ GHz, the nutation frequency scales with voltage as

$\omega_R \sim 2\pi \times 70$ MHz/mV. This scaling increases with $\frac{dJ_x}{d\varepsilon}$, which grows as the 111 region is shrunk ($\varepsilon_0 \rightarrow 0$) to increase ω_{01} . At $\omega_{01}/2\pi = 1.98$ GHz, this scaling was measured to be $\sim 2\pi \times 5$ GHz/mV, demonstrating a way to increase coupling to external voltages, such as those from a superconducting cavity.

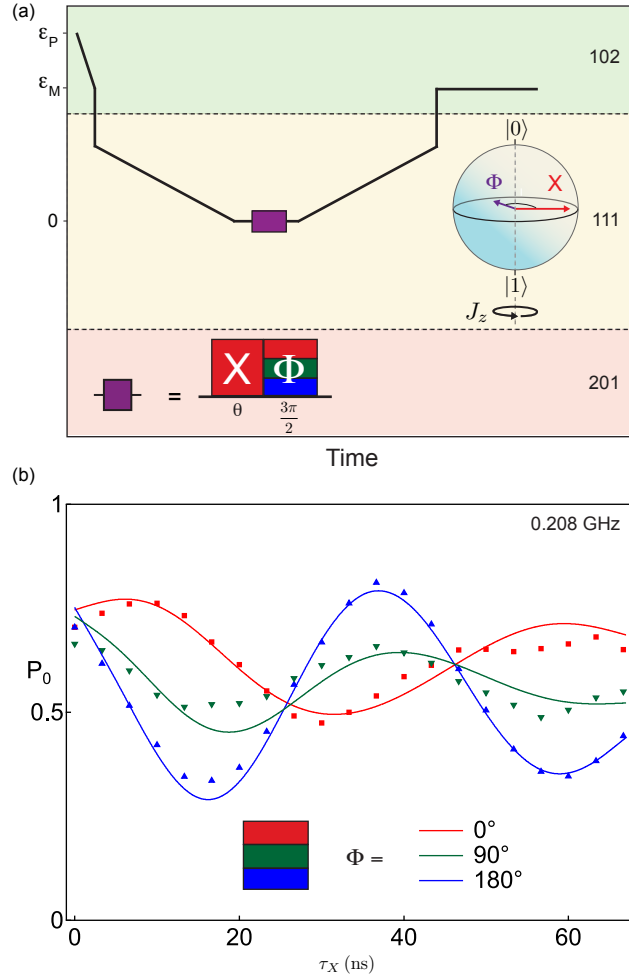


Figure 8.4: (a) A schematic of the detuning during a two-pulse sequence, where the first pulse is an X rotation and the second pulse is a rotation around an angle set by the relative phase of the carrier, Φ , as depicted on the Bloch sphere. (b) The qubit readout for a rotation about X , followed by a $\frac{3\pi}{2}$ rotation about an axis Φ , for three different Φ 's. The solid lines are fits to the model in Fig. 8.2(c,d,f) and the insets of Fig. 8.3.

Even though the rotating frame approximation is poor in this particular regime, with $\omega_R \sim \omega_{01}/6$, we can still observe a carrier phase dependent response, which is the

main tool for two-axis manipulation. On resonance in the rotating frame, the Hamilton takes the form $\mathcal{H}_{\text{rf}} = \cos(\Phi)\sigma_x + \sin(\Phi)\sigma_y$, where Φ is the relative phase of the carrier wave with respect to the first pulse incident on the qubit. To test the qubit response, we prepare a $|0\rangle$ and drive a rotation on resonance for a time τ_x similar to Fig. 8.3, and then apply a second pulse that drives a $3\pi/2$ rotation with a carrier phase shift of Φ , as demonstrated in Fig. 8.4(a).

By looking at $\Phi = 0^\circ, 90^\circ$, and 180° in Fig. 8.4(b), we can see a clear dependence the phase of the carrier, which is well described by the model. In order to gain an intuition for how these pulses are affecting the qubit, we plot the model outcomes on a Bloch sphere in the rotating frame, and observe their dynamics there. We see that for $\Phi = 0^\circ$ and 180° , the qubit stayed in the y - z plane as desired, while for $\Phi = 90^\circ$, the qubit deviated towards the x - y plane as desired. The model shows that the second pulse was slightly over $3\pi/2$, and that the nuclei further prevented the second rotation from placing the qubit state in the x - y plane through Ω shifts. Stronger pulses and a larger ω_{01} would have brought this result much closer to the desired rotating frame approximation outcome.

8.5 Dynamical Decoupling

This rough phase control was still sufficient to implement a CPMG dynamical decoupling sequence, where π -pulses are applied along the \dagger axis in the rotating frame, as shown in the lower half of Fig. 8.5, which provides some protection against rotation errors [149]. We studied a series of CPMG sequences up to CPMG-64, with 64 π -pulses, which resulted in a $T_2 = 19 \pm 2 \mu\text{s}$. For $n = 2$ -16 pulses, we observed that the coherence time was well described by the model $T_2 = A(n_\pi)^\gamma$, where $\gamma = 0.84 \pm 0.05$. As shown in Ref. [36, 94], this implies a power spectral density of $S(\omega) \sim \omega^{-\beta}$ with a $\beta = 5 \pm 1$. This is similar to previous work in double quantum dots [17, 94] in a nuclear noise dominated

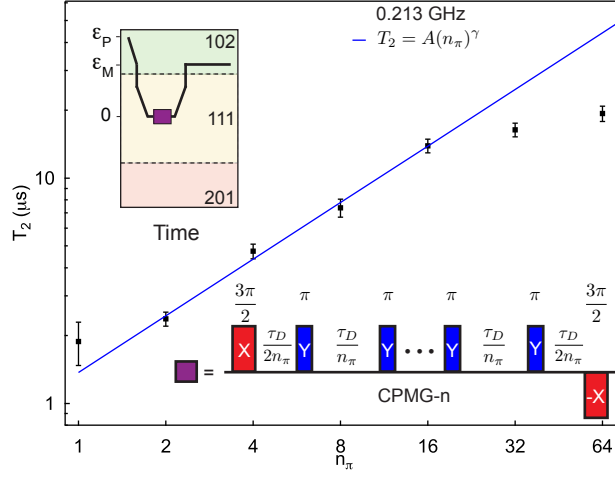


Figure 8.5: (a) T_2 for various orders of CPMG- n , where each sequence contains $n \pi$ rotations about y , as depicted in the lower inset. The upper inset depicts the detuning sequence for this experiment. We found that up to $n = 16$, the even number of pulses was well described by $T_2 = A(n_\pi)^\gamma$, where $\gamma = 0.84 \pm 0.05$. This translates to a power spectral density of $S(\omega) \sim \omega^{-\beta}$, where $\beta = 5 \pm 1$.

regime, and at odds with the charge noise dominated regime where $\beta \sim 0.7$ [41]. This is a further indication that by operating in a location where $\frac{dJ_z}{d\varepsilon} = 0$ the qubit has a very low sensitivity to charge noise.

For large numbers of pulses, T_2 departs sharply from the model, saturating near $20 \mu\text{s}$. The reason for this is not well understood. The measured T_1 for a splitting $\omega_{01}/2\pi = 0.33 \text{ GHz}$ was $\sim 40 \mu\text{s}$, and decreased monotonically with increasing ω_{01} , suggesting that T_1 was not limiting T_2 in this case, at $\omega_{01}/2\pi = 0.2 \text{ GHz}$. Pulse errors, especially in this regime where the rotating wave approximation is not really applicable, are a more likely cause of error, suggesting that there is an optimum ω_{01} for control where pulse fidelity and T_1 are maximized.

Understanding the mechanisms of the qubit relaxation process as well as improving the control fidelity are two significant avenues of exploration in this field. Additionally, the ability of this qubit to respond to electric fields suggests the possibility of interesting

couplings between the qubit and a superconducting cavity, creating a hybrid qubit that combines circuit QED with spin physics. Finally, a nuclear feedback scheme [14] or a transition to a nuclear free system such as silicon [92] could significantly enhance the dephasing times in this system, as it currently appears to be limited by nuclear fluctuations.

Acknowledgements

We gratefully acknowledge support from IARPA through the MQCO program, the Danish National Research Foundation, and the Villum Foundation. We thank Bert Halperin, Ferdinand Kuemmeth, Thaddeus Ladd, and Emmanuel Rashba for useful discussions.

Appendix A

Triple Dot Fabrication Recipe

Here is the recipe used to fabricate JM19-2b. I will give an overview of the entire process in section A.1, followed by a slightly more detailed look at each step in sections A.3-A.11. Many steps in this process are repeated multiple times, including the “3 solvent clean” and the “coverslip chip glue”, so I cover them once in section A.2.

A.1 Overview

1. Cleave Chip
 - (a) Scribe xtal orientation on back
 - (b) Record chip in wafer booklet
 - (c) Cleave junk chip as well
2. Mesa Pattern → Junk and real chip (sec A.3)
3. Mesa Etch → Junk and real chip (sec A.4)
4. Ohmics Pattern → Junk and real chip (sec A.5)
5. Ohmics Deposit → Junk and real chip (sec A.6)
6. Anneal using Modified Barthel Recipe (sec A.7)
7. **Optional:** Cleave sample using Scriber¹ into four smaller wafers for multiple e-beam attempts

¹LSD-100 Scriber/Cleaver from Loomis.

8. Fine Gates Pattern → real chip (sec A.8)
9. Fine Gates Deposit → real chip (sec A.9)
10. Outer Connection Layer Pattern → real chip (sec A.10)
11. Outer Connection Layer Deposit → real chip (sec A.11)
12. Bond, cooldown, measure, publish, graduate!

A.2 Repeated actions

A.2.1 The 3 Solvent Clean

This is the basic clean we use at each step to strip off unwanted junk. Contrary to the experience of some others, I have found that it isn't actually sufficient when removing a failed photoresist pattern, so don't rely on it to be a cure-all. Also, this clean should use sonication only **before** the fine gates are placed down. Afterward the fine gates are down, the chip should be allowed to rest quietly in each solvent. The 3 solvent clean is as follows:

1. Sonicate Trichloroethylene (TCE) for 5 mins
2. Sonicate Acetone for 5 mins
3. Sonicate Isopropyl Alcohol (IPA) for 5 mins
4. Blow dry with N₂ gas.

A.2.2 Gluing a chip to a coverslip

This is an operation that can make handling small chips easier and reduces the edge beads that form during the spin. It is only really necessary for the outer connection layer pattern, section A.10, but can be used during all photolithography steps. NOTE: do not attempt to use it for e-beam patterning. This process creates an insulating layer between chip and stage, which would create significant problems during e-beam writing.

1. Singe 4+ minutes @ 200° C
2. Cool 60 s on a single cleanroom wipe resting on metal surface
3. Place 1 drop of S1818 on a glass coverslip, off center
4. Place chip at edge of droplet, let S1818 wet under the chip without touching the top surface of the chip. If it touches the top surface, stop immediately and perform a 3 solvent clean, and start over.
5. Bake 15 mins @ 115° C

If you chose not to glue the chip to a glass coverslip, you need to singe the chip instead

1. Singe 2+ min @ 200° C
2. Cool 60 s on a single cleanroom wipe resting on metal surface

A.3 Mesa Patterning

Devices on the same chip are kept electrically isolated from one another by etching away the 2deg in between them. This is done in a two part process, where first the mesas, or islands of 2deg the devices live on, are patterned with photoresist. In section A.4, we etch away the donor layer that helps form the 2deg (see chapter 3 for more details on 2degs), completing the isolation. In practice, we often etch right down to the GaAs-Al_{0.3}Ga_{0.7}As interface, just to ensure the isolation.

Mesa Pattern → Junk and real chip.

1. 3 Solvent Clean, N₂ dry (sec A.2.1)
2. Singe/glue chip to coverslip (sec A.2.2)

3. Spin S1813:

- (a) 5 s, 500 rpm, 500 rpm/s
- (b) 60 s, 4 krpm, 4 krpm/s
- (c) Bake 2 mins @ 115° C

4. **Record orientation of xtal with respect to mask.** After the etch step, the scribe mark will be gone.

5. Expose in Mask Aligner, time determined by dose testing

6. Develop:

- (a) 60 s CD-26
- (b) 20 s DI rinse
- (c) N₂ dry

7. O₂ plasma clean, 5s 110 W, 40 sccm

A.4 Mesa Etch

After patterning both a junk chip and a real chip, you etch the wafer to isolate the devices. Every etch bath that you create has a slightly different etch rate, so it is best to test this etch rate out in advance. Stirring the bath thoroughly is a must, and avoiding the use of old hydrogen peroxide can help ensure more consistent results. There are two philosophies on how to best etch the device. The first is that you use the junk chip to roughly determine the etch rate, and then you etch the real device in steps, monitoring the growth of the step from the top of the resist to the bare etched wafer at each step. In practice, I've found this to be an unreliable method, due to variations in coating thickness that exceeded my etch depth.

The second method of determining the etch rate is to simply place the junk chip in the etch bath for 60 seconds, calculate the etch rate, and then etch the real chip for a calculated time. Since the junk chip is pure GaAs, while the upper portion of the real chip is mostly $\text{Al}_{0.3}\text{Ga}_{0.7}\text{As}$, the etch rates can be somewhat different. That said, I've had better results with this single etch method. As long as the donors at least are etched away, the devices should be isolated, leaving more leeway to over etch rather than under etch².

Mesa Etch → Junk and real chip

1. Prepared etch bath $\text{H}_2\text{SO}_4:\text{H}_2\text{O}_2:\text{H}_2\text{O}$ in a ratio of (2:16:480 mL). **Stir thoroughly.**
2. Determine etch rate (do this for each etch bath):
 - (a) Etch junk chip for 60 s
 - (b) Sonicate junk chip in acetone 5 mins
 - (c) Sonicate in IPA 2 mins, N_2 dry
 - (d) Determine etch rate with profilometer
3. Etch real chip using calculated etch rate
4. Sonicate real chip in acetone 5 mins
5. Sonicate in IPA 2 mins
6. N_2 dry
7. Clean in 55° C acetone 2+ hours. **Approach this step carefully. Do only in a hood, and only if it is allowed in your facility. The risk of igniting the acetone is small, but potentially non-zero.**

²The height of the mesa determines the thickness of the outer connection layer in sec. A.11. As long as this thickness is kept reasonably small, ~ 200 nm or less, the liftoff should succeed. This places the bound on what constitutes and over etch.

8. Squirt IPA, N₂ dry

A.5 Ohmic Pattern

We use a thick stack of metal to create the ohmic connection to the 2deg, which makes the liftoff a little more challenging. Our solution was to use a thicker photoresist layer, and to submerge the chip in chlorobenzene prior to development. The chlorobenzene makes the surface more resilient to the developer, facilitating the formation of an undercut which helps with the liftoff process.

Ohmics Pattern → Junk and real chip

1. 3 Solvent Clean, N₂ dry
2. Singe/glue chip to coverslip (sec A.2.2)
3. Spin S1818:
 - (a) 5 s, 500 rpm, 500 rpm/s
 - (b) 60 s, 4 krpm, 4 krpm/s
 - (c) Bake 2 mins @ 115° C
4. Expose in Mask Aligner, time determined by dose testing
5. Bake 1 min @ 115° C
6. Dip 4 mins in Chlorobenzene. This creates a more firm surface on the resist, forming an undercut when developing.
7. Develop:
 - (a) 60 s CD-26
 - (b) 20 s DI rinse

(c) N₂ dry

8. O₂ plasma clean, 5s 110 W, 40 sccm

A.6 Ohmic Deposition

In order to create a good ohmic contact to the 2deg, it is necessary to remove the native oxide on the surface of the wafer directly before depositing the metal. It is best to prepare the deposition chamber in advance, and perform the etch as close as reasonably possible to the chamber, to prevent any chance of oxide reformation or the accumulation of other unwanted substances on the bare surface. The sample was under vacuum less than two minutes after the end of the etch, though no direct correlation was noticed between ohmic contact success rate or resistance and the time it took to load the sample into the chamber.

Following the deposition it is important to strip the remaining resist off completely. Though a chip may look clean, any residue that remains on the surface will leave raised black patterns on the chip following the anneal. To avoid this, I implemented the clean in 60° C acetone. Use caution while doing this, and always perform this clean in a well ventilated hood with the sash down.

Ohmics Deposit → Junk and real chip

1. Prep Thermal (E-beam if necessary) Evaporator, loading Ni, Au, Ge. Following etch, want to be able to place sample directly into vacuum.

2. Remove native oxide under ohmics:

(a) Dip in Ammonium Hydroxide (NH₄OH) etch 3 s (this time is adjustable, but keep small, or it will eat under the resist and strip the oxide off of the entire surface of the chip.)

- (b) DI rinse 30 s
 - (c) **Optional:** Extremely fast observation under UV filtered microscope
 - (d) Rush to evaporator, load and pump down
3. Pump to < 1 E-6 torr, Degas metals
 4. Degas metals
 5. Deposit Ni/Ge/Au/Ni/Au (60/400/800/200/1000) (Å). These thicknesses are for a 110 nm deep 2deg. The general rule of thumb is, the Ge+Au \sim 2deg depth, but always test with new wafers.
 6. Liftoff **carefully** in 60° C Acetone for multiple hours
 7. Squirt and wet observe Acetone. Sonication ok at this step, if necessary.
 8. Squirt IPA, N₂ dry

A.7 Anneal Recipe

The anneal recipe is a slight modification of Christian Barthel's. This recipe is run once with the junk chip, to confirm that the temperatures are tracking properly, and then a second time with the real chip. Do not remove the chip until the chamber has cooled below 80° C. On the rapid thermal annealer that was used in the Harvard Cleanroom³, there was the additional input of “control factors” that affected the temperature controller. Christian's original recipe used the factors (1.1, 0.15, 1.4, 1.6, 0.65) while the current recipe used the factors (0.55, 0.3, 2.0, 1.6, 0.7). The only thing that really matters is that the actual temperature reasonably tracks the desired one.

³Rapid Thermal Processor RTP-600xp, from Modular Process Technology

#	Function	Time (s)	Temp (° C)	N ₂ (sccm)	N ₂ /H ₂ (sccm)
1	Idle	20	0	10,000	0
2	Idle	30	0	0	2,000
3	Idle	20	0	0	1,000
4	Ramp	20	120	0	1,000
5	Hold	50	120	0	1,000
6	Ramp	20	220	0	1,000
7	Hold	20	220	0	1,000
8	Ramp	10	300	0	1,000
9	Ramp	10	370	0	1,000
10	Hold	20	370	0	1,000
11	Ramp	15	500	0	1,000
12	Hold	1	500	0	1,000
13	Ramp	5	510	0	1,000
14	Hold	100	510	0	1,000
15	Idle	120	0	0	2,000
16	Idle	700	0	10,000	0
17	Stop				

A.8 Fine Gates Pattern

This is where the actual device is created. The gates that are defined with the e-beam writer set the size and shape of the confining potentials. The writing is broken into two consecutive steps. The first is the writing of the inner most 75 μm region, followed by a more course writing of a 300 μm region. Both of these writes are performed on the same resist, during the same write session, without venting the chamber or removing the chip.

To reduce sensitivity to stage drift, the inner $75 \mu\text{m}$ region is itself carefully divided. Each gate is divided into two separate polygons, the first being within $\sim 5 \mu\text{m}$ of the device center, and the second outside that region. The write order of the polygons is then set such that the inner most polygons are written first. This ensures that the gates that define the potentials are all written within a few milliseconds of each other, keeping the pattern immune to most small stage drifts.

Fine Gates Pattern → real chip

1. 3 Solvent Clean, N_2 dry
2. Spin PMMA A4:
 - (a) Bake 2+ min @ 180°C
 - (b) Rest on wipe 15 s
 - (c) 5 s, 500 rpm, 100 rpm/s
 - (d) 60 s, 4 krpm, 4 krpm/s
 - (e) Bake 5 mins @ 180°C
3. Load into Elionix
4. Burn 3 spots to determine planar tilt, determine position and height of each mesa
5. Write fine features @ 100 pA, 100 keV, $75 \mu\text{m}$, 20 kpts, adjusting height for each mesa
6. Write connection layer @ 2 nA, 100 keV, $300 \mu\text{m}$, 20 kpts, using mean height for all
7. Cold develop:
 - (a) Chill developer MIBK:IPA 1:3 in a beaker placed in an ice bath (crushed Ice + water) for 15 mins

(b) 90 s in cold MIBK:IPA

(c) 30 s in room temp IPA

(d) N₂ dry

A.9 Fine Gates Deposit

Fine Gates Deposit → real chip

1. Prep Thermal Evaporator, Ti, Au
2. Load in chip
3. Pump to < 1 E-6 torr, degas metals
4. Deposit Ti/Au (50/150) (Å)
5. Liftoff 30+ minutes in Acetone, sonicate 10 s
6. Squirt and wet observe Acetone
7. Squirt IPA, N₂ dry

A.10 Outer Connection Layer Pattern

Now comes the somewhat nerve-wracking part of the fab process; the final patterning of the almost finished device. If the chip was cleaved into smaller sections after the anneal, it is highly recommended that you use the chip gluing method to reduce edge beads during this process. Also, remember to avoid sonication from here on out.

Outer Connection Layer Pattern → real chip

1. 3 Solvent Clean, **NO Sonication**, N₂ dry
2. Singe/glue chip to coverslip (sec A.2.2)

3. Spin S1818:

- (a) 5 s, 500 rpm, 500 rpm/s
- (b) 60 s, 4 krpm, 4 krpm/s
- (c) Bake 2 mins @ 115° C

4. Expose in Mask Aligner, time determined by dose testing

5. Bake 1 min @ 115° C

6. Dip 4 mins in Chlorobenzene. This creates a more firm surface on the resist, forming an undercut when developing.

7. Develop:

- (a) 60 s CD-26
- (b) 20 s DI rinse
- (c) N₂ dry

8. O₂ plasma clean, 5s 110 W, 40 sccm

A.11 Outer Connection Layer Deposit

Outer Connection Layer Deposit → real chip

- 1. Prep Thermal Evaporator, Ti, Au
- 2. Load in chip
- 3. Pump to < 1 E-6 torr, degas metals
- 4. Deposit Ti/Au (100/~/1.2x) (Å), where x is the mesa height measured in sec A.4

5. Liftoff ~ 12 hours in Acetone, NO sonication
6. Squirt and wet observe Acetone
7. Squirt IPA, N₂ dry

Appendix B

Catalogue of Devices and Design Tips

Here is a list of devices and wafers studied while coming to the current triple dot design configuration. Most of the design iteration was accomplished by testing in a He³ system, which cooled down to ~ 300 mK. This system had a rapid turn around time, where it was possible to bond a device, cool it down to base temperature, search for Coulomb blockade, and warm it back to room temperature in a single day if needed. I combined this rapid turn around with a practice of creating 16 blank devices¹, scribing them into sub-chips of four devices each, and e-beam writing new gate patterns on four devices at a time. These two techniques allowed for the testing of devices with identical mesas and ohmics, but modified gate patterns every few days.

The rapid design iteration allowed for the testing of a few design ideas. The first major breakthrough was the completely linear geometry seen in Fig. 7.1(a), where the connection to the leads is along the dot axis. By making every exchange coupling between dots or between dots and the leads along the same line, we remove a degree of freedom in the dot position. Devices of the style in shown in Fig. 3.2 and 4.1(a) have dots that are free to move in two dimensions, which drastically increases the parameter space while tuning, increasing the time it takes to evaluate and configure a device.

The downside to having less parameter space is that the device may not be tunable into a regime that the experimenter is interested in. In order to have coupling between

¹Devices which were processed through sec. A.7 of the recipe, including the mesa etch and the annealed ohmics.

Name	Grower	d (nm)	ρ (10^{11} cm $^{-2}$)	μ (10^5 cm 2 /V·s)	doping (10^{12} cm $^{-2}$)
G050329A	M. Hanson	110	2.00	2.00	
G080721A	H. Lu	110	2.30	3.35	4.00
G080721B	H. Lu	110	2.40	4.30	4.00
G090402A	H. Lu	57	5.22	3.20	4.00
G090402B	H. Lu	57	2.79	1.88	2.00
G090402D	H. Lu	57	4.14	3.70	8.00
G110523C	H. Lu	30	1.18	5.70	8.00

Table B.1: These are the wafers grown for us by Art Gossard, Micah Hanson, and Hong Lu of UC Santa Barbara. ρ is the electron density in the 2DEG and μ is the mobility, determined by our growers with quantum hall measurements at ~ 20 K. The depth of the 2DEG below the surface is given by d , while doping is the nominal density of Si atoms in the donor layer.

neighboring dots in a linear triple dot, it is necessary to squeeze the lithographic structure horizontally, placing the dots closer to one another and to the leads. At the same time, the distance between the vertical gates on the bottom and the horizontal gate that forms the top wall of the structure has to be kept large enough to allow a quantum dot to form. For the devices I studied, this increased the coupling strength, and made it possible to observe simultaneously coupling between the left and middle and the middle and right dots.

The placement of the sensor in the device shown in Fig. 7.1(a) turned out to be very convenient. By placing the dots between the sensor and the fast gates we were able to significantly reduce the coupling between gates and sensor. This allowed us to avoid having to adjust the sensor as we swept over the charge region, as was necessary in Fig. 4.1(b). The fact that there was no metal gap between dots and sensor may have been balanced by the fact that the sensor can sit much closer to the dot than in previous double dot designs, resulting in single-shot times that were comparable².

²Unpublished results from a new cooldown of the device show that single-shot integration times of a few μ s are achievable in this device, which is consistent with an average cooldown of the device in chapters 4, 5, and 6.

Date	Chip	Wafer	d (nm)	Docs	Temp	ALD	PB (mV)	<i>I</i> (nA)	Noisy?
	CB7	G050329A	110		30	N			N
7/22/10	JM7	G080721B	110	V1, pg 1	4000	N	N/A	N/A	N/A
9/16/10	JM8	G090402D	57	V1, pg 54	30	N	300	35	N
10/26/10	JM8	G090402D	57	V1, pg 148	30	N	250	5	N
1/3/11	JM2	G080702A	110	V2, pg 93	30	Y	250;350	0.4	N
2/21/11	JM10 H	G090402A	57	V3, pg 91	30	N	50	0.22	Y
2/23/11	JM10 L	G090402A	57	V3, pg 99	30	N	75	0.4	Y
3/3/11	JM10 L	G090402A	57	V3, pg 105	286	N	300	14	Y
3/9/11	JM10 J	G090402A	57	V3, pg 114	286	Y	250	1.4	N
4/14/11	JM11-1A	G090402D	57	V3, pg 126	317	N	200	68	Y
4/18/11	JM11-1C	G090402D	57	V3, pg 134	306	N	0	0	Y
4/19/11	JM11-1C	G090402D	57	V3, pg 138	307	N	250	9	Y
5/17/11	JM11-2D	G090402D	57	V3, pg 146	293	Y	200	0.5	N
5/18/11	JM11-2D	G090402D	57	V3, pg 149	294	Y	600	1	N
5/23/11	JM11-2D	G090402D	57	V3, pg 151	301	Y	600;1000	1.1	N
5/31/11	JM13-1b-f	G110523C	30	V4, pg 10	4000	Y	N/A	N/A	N/A
6/2/11	JM12-1d	G080721A	110	V4, pg 11	293	N	300	8	Y
6/13/11	JM12-1a	G080721A	110	V4, pg 17	303	N	0	0	Y
6/17/11	JM12-2c	G080721A	110	V4, pg 21	303	N	0	0	Y
6/17/11	JM12-2c	G080721A	110	V4, pg 21	320	N	300	4.7	~
6/20/11	JM12-3c	G080721A	110	V4, pg 28	294	Y	250	1.4	Y
6/28/11	JM12-3d	G080721A	110	V4, pg 36	310	Y	200	0.4	Y
7/13/11	JM15-3a	G080721A	110	V4, pg 40	48	N	200	1	N
8/19/11	JM19-2b	G080721A	110	V4, pg 120	49	N	100	2	N

Table B.2: A list of cool downs of triple dot devices investigated. Docs lists the notebook where the cooldown is recorded, Temp is the temperature in mK that the device was tested at, ALD lists whether or not a thin layer (~ 5 nm) of Al_2O_3 was deposited through Atomic Layer Deposition, PB lists the positive bias used during cooldown while I lists the maximum current measured during cool down. Noisy refers to massive noise in the device transport that was seen in some devices. Fig. B.1(b) is an example of some of the most severe noise I saw during the testing. Fig. B.1(c) demonstrates the effect of placing ALD directly under the gates. Section 3.1 covers some of the details of positive biasing a quantum dot structure.

The testing also revealed a form of charge noise that affected some devices, often those further from the center of the wafer. The symptom was massive amounts of noise in the DC transport through the device, which I attributed to leakage from the gates. As seen in Fig. B.1(b,c), virtually identical devices³ that differ only in a thin layer of Al₂O₃ under the gates can show significantly different transport properties. I did not determine if this noise was process related or wafer related, though the recipe in Appendix A produced the most quiet results. The trick of placing Al₂O₃ was not convenient for qubit work, as it made the gates hysteretic, and prone to more sudden jumps in the electrostatic environment.

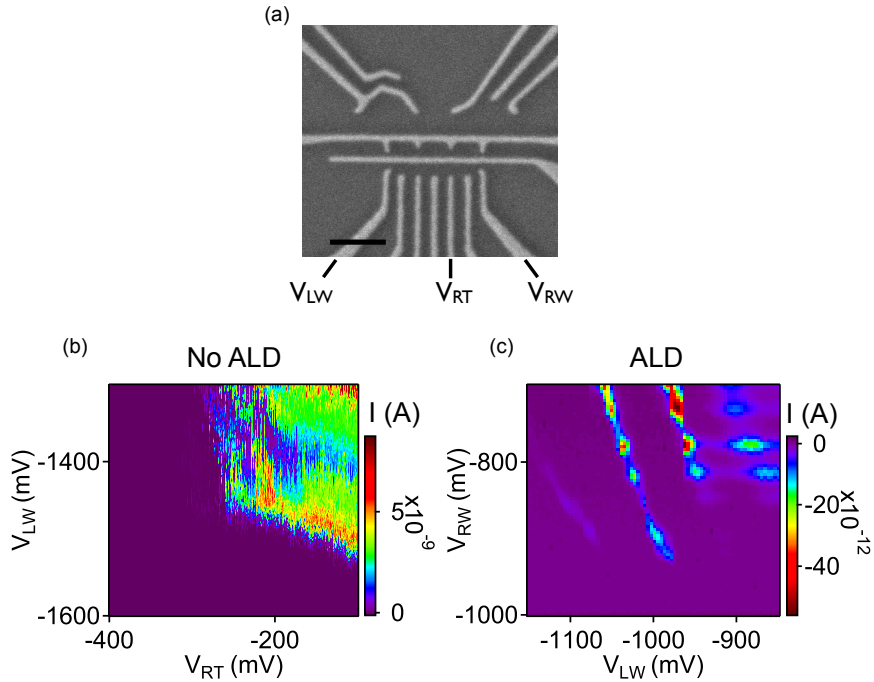


Figure B.1: (a) A micrograph of a lithographically identical device to the ones measured in (b) and (c). The gate that runs horizontally through the center of the device where the dots would sit was kept at ground or slight positive voltages. The scale bar is 300 nm in length. (b) A wall plot that measures current passing through the device JM10 L, for a device that did not have ALD under the gates. (c) A wall plot from device JM10 J that is identical in every way to the device in (b), located a few millimeters away on the same wafer, but with a thin (~ 5 nm) layer of ALD under the gates.

³The mesas and ohmics were made simultaneously, after which the chip was scribed to e-beam write JM10 L (Fig. B.1(b)) first.

Appendix C

Cryogenic Measurement

Spin qubit measurement can be thought of as a balance between control bandwidth and thermal loads/electrical noise. The control of a spin qubit requires precise voltage manipulation between DC and ~ 1 GHz; the same pathways that transmit the high bandwidth voltages provide an easy conduit for noise and heat to enter the experiment, limiting the coherence of the device.

The large bandwidth is only needed on a few of the control and readout lines, allowing us to divide this bandwidth up into two regimes. The first is the DC end of the spectrum which every gate and Ohmic connection needs to define the electrostatic confining potential¹. In practice, the bandwidth of these lines is limited inside the fridge to be $\sim 0 - 300$ Hz, allowing for heavy attenuation of most broadband noise. The control and reflectometry lines require higher bandwidths, which we supply with bulkier coaxial cables. Large bandwidth coaxial cables are generally better thermal conductors than the DC lines, so their use is limited to lines that absolutely need it or fridges with lots of cooling power.

The experimental setup used in chapters 7 and 8 was initially constructed by Edward Laird. I made only a few changes, which I will document here along with a description of the fridge wiring. The original wiring scheme is detailed nicely in Ref. [82]. The setup used in chapters 4, 5, and 6 were created by Christian Barthel and David Reilly, and are detailed in Ref. [4].

¹This also prevents the charging, or “floating”, that affects regions without a DC connection.

C.1 Configuration of DC lines

The DC lines need to be stable to the 0.01% – 0.1% level on long timescales, ideally at least the month range. In practice this is a very challenging requirement to meet, though with the DecaDac² waveform generators we approach these levels³. The voltages from the DecaDacs are then divided down by a filter/divider, which provides a division of 5:1 and time constant of 24 ms, and filtered again by a BLP-1.9+, a ~ 1 MHz lowpass from MiniCircuits. From there, the lines are connected to the breakout box, which breaks the twisted pair loom inside the fridge out into individual bnc connections. The signals then travel through a shielded dsub connection to a Fisher connector at the top of the fridge.

Inside the fridge the signals travel down twisted pair constantine loom, which is GE varnished to various copper spools at each stage of the fridge. At the mixing chamber we replaced the resistor bank with a modified “Ferdie Filter”⁴. Our modified versions included 1.2 k Ω of resistance from surface mount resistors and 80 MHz surface mount low pass filters from MiniCircuits⁵ in a copper enclosure that we bolted to the cold finger of the fridge. The modification is the removal of the capacitor bank from the filters. We moved these capacitors to sample pc board, so that we could control which lines had a capacitative load on it. From there the signals traveled to a 51 pin nano-dsub connector and onto the sample pc board, where lines that were not coupled to high bandwidth bond pads had 5 nF capacitors to ground (see figure C.5(b,d)). The lines that were coupled to the pulse

²Supplied to us by Jim MacArthur of the Harvard Physics/SEAS Electronics shop.

³The devices exhibit small (equivalent to \sim mV on a gate) shifts in electrostatic environment on the day to week timescales, obscuring drifts in the control devices. While ideally we could measure the drift of a DecaDac itself on the timescale of months, I am not aware of any thorough study undertaken to that effect. The DecaDac's appear stable on at least the 1% level on the timescale of months without question.

⁴Developed by Ferdinand Kuemmeth, who prefers to call them Harvard PC Board Filters. I prefer “Ferdie Filter”.

⁵Part number LFCN-80.

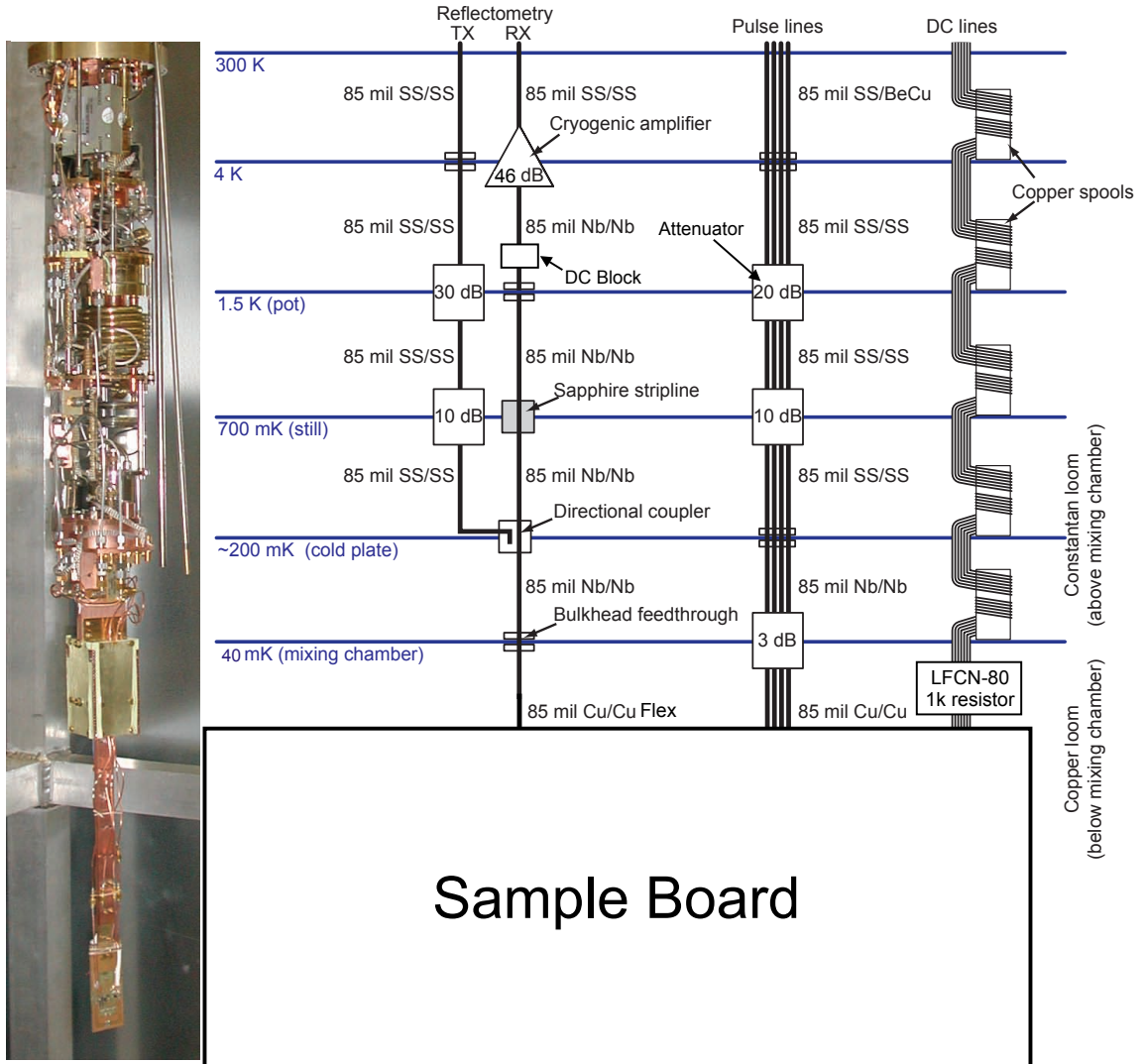


Figure C.1: A schematic of the wiring in the dilution refrigerator used in chapters 7 and 8. Adapted with permission from reference [82]. The contents of the sample board are shown in figure C.5.

gates were coupled to a 50Ω stripline by a bias tee made of a $100 \text{ k}\Omega$ resistor and a 33 nF capacitor.⁶ The lines that were coupled to the reflectometry circuit were coupled by a bias tee made of a $5 \text{ k}\Omega$ resistor and a 100 pF capacitor (see Fig. C.5(e)).

⁶The long resulting highpass time constant for the pulse line allowed for easy highpass correction of the pulses, enabling long steady pulses and cleaner single-shot integrations.

C.2 Configuration of High Bandwidth Lines

There are two types of high bandwidth lines used in this experiment, pulse lines and reflectometry lines. The pulse lines are attached to the handful of gates that we want to manipulate on nanosecond timescales. We place attenuators at each stage of the fridge in order to thermalize the inner conductor, which is insulated by a sheath of plastic from the outer conductor. The attenuators have a resistance of a few hundred ohms between the inner and outer conductor, allowing for the flow of heat as well as electrons. The outer conductors were tied via copper wire to the stages of the fridge, ensuring that the outer was properly thermalized as well. Since attenuators also dissipate heat, we made sure that every signal was AC-coupled, preventing a constant voltage across the attenuator from heating the fridge. We also placed the majority of the 33 dB of attenuation at the highest stages to dump the majority of the dissipation where we had the greatest cooling power.

The reflectometry line is a little more challenging to thermalize. While attenuation can be used on the input up to the directional coupler, attenuation can not be used between the directional coupler and the sample or between the directional coupler and the top of the fridge. The reason for this is that attenuators in those places reduce the signal we are trying to receive from the sample, and there is never enough signal to waste on an attenuator. The attenuation in the directional coupler is used to thermalize the inner and outer conductors of the readout line, and below the directional couple we often use superconducting coax such as Nb or NbTi to minimize the heat transfer and maximize the signal.⁷ On the return path we employ a DC block⁸ between the directional coupler and the cold amplifier⁹, breaking

⁷We purchase specialty coax like these from Coax Company Ltd.

⁸We avoid the use of a circulator here because all models we have seen would severely restrict the available bandwidth. That said, there is potentially some gains to be made by better isolating the cold amp from the device.

⁹A Weinreb Amplifier CITLF1, a Cryogenic SiGe Low Noise Amplifier, with a bandwidth from 0.001 -

the inner conductor with an insulator which inhibits heat transmission.

C.3 High Frequency Control Circuits

In chapter 8 we used a vector source generator¹⁰ in conjunction with a wide bandwidth Arbitrary Waveform Generator(AWG)¹¹ and a low bandwidth AWG¹² that provided background ramps through multiple charge states. The slow ramps were combined with the AWG using the “add input” terminal in the back. This allowed signals smaller than 2 Vpp to be added onto the output of the AWG. It had the added benefit of being controlled by an electronic switch inside of the AWG, allowing us to turn off the switch and electrically isolate the ramp from the setup, which was useful during diagnostics. Because the ramp was traveling down the coax, the waveform was distorted from the standard saw tooth ramp by a highpass correction to pass through the bias tee on the sample board. We were able to run ramps between 47 Hz and 951 Hz, which allowed for rapid charge scans. The vector source was added through a resistive splitter and an attenuator, which helped preserve the shape of the AWG waveform.

C.4 Reflectometry

As discussed in references [131, 123, 5], the large resistances of our charge sensing channels ($\sim 100 \text{ k}\Omega$) combined with the parasitic capacitances in a twisted pair loom ($\sim 1 \text{ nF}$), combine to give lowpass characteristic frequencies of $f_{3dB} = \frac{1}{2\pi RC} \sim 1 \text{ kHz}$. This low passing effect prevents us from using standard loom to observe fast charge dynamics. In

1.5 GHz, 46 dB of gain, and a noise temperature $T_N \sim 3.5K$. Shielding and high frequency filtering of the power supply lines is critical to noise performance.

¹⁰The vector source was a Rhode & Schwarz SMBV100A.

¹¹The high bandwidth AWG was a Tektronix AWG5014C, with a 1.2 GSPS sample rate and a bandwidth of $\sim 300 \text{ MHz}$ in the mode we used.

¹²The low bandwidth AWG was an Agilent 33250A.

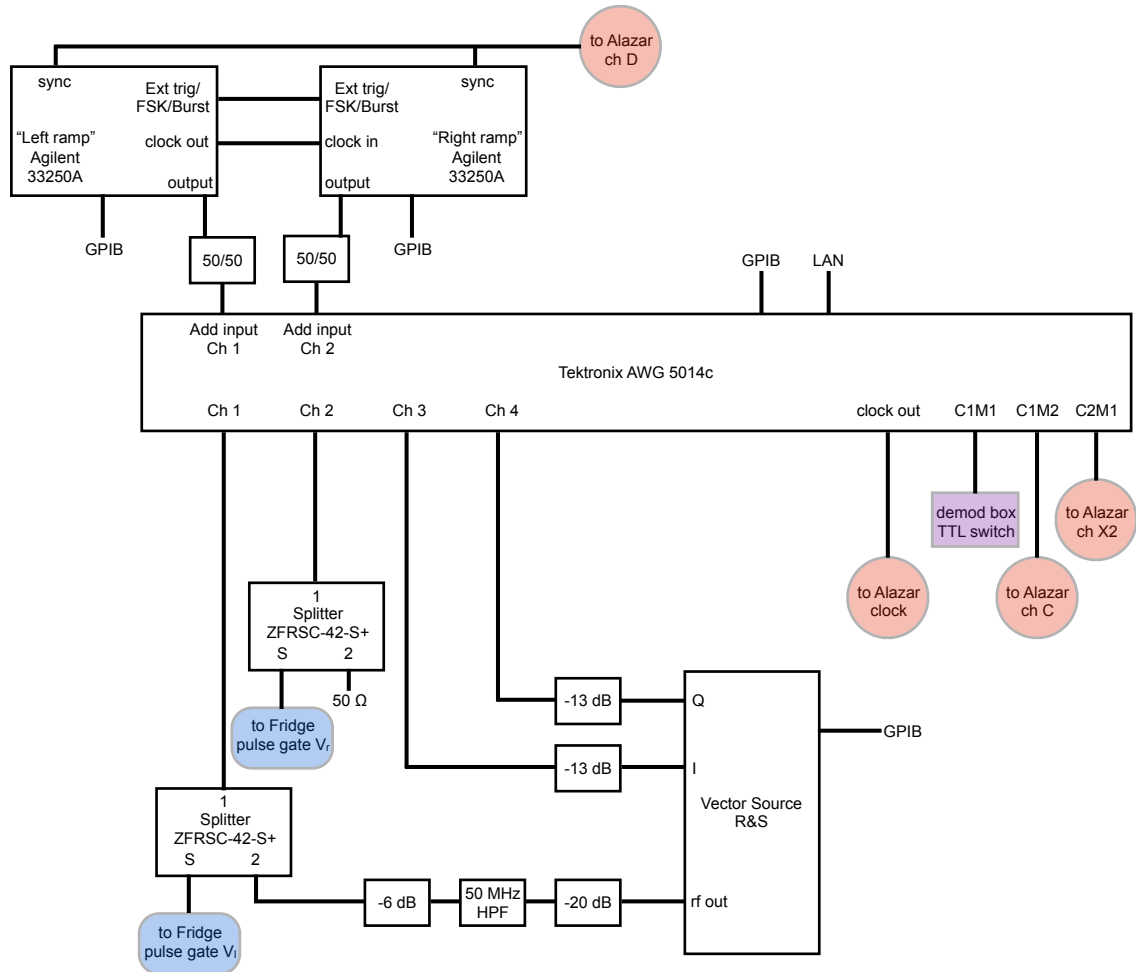


Figure C.2: A schematic of the dynamic control system used to manipulate the qubit in 8. The Agilent 33250 function generators were used to create highpass corrected saw tooth ramps, which were used to scan over large charge regimes such as Figure 8.1b. The Tektronix AWG was used to create the high frequency shifts in detuning that initialized, measured, and reset the qubit, while the Rhode & Schwarz (R&S) SMBV100A vector signal generator provided the resonant excitations that drove the qubit. Various triggers and clocks were sent to the AlazarTech PCI card (AlazarTech ATS9400 PCI express digitizer), which was used to record the output of the reflectometry circuit described in section C.4. The multiple triggers are to facilitate three separate types of events: the start of a ramp in a charge scan (Alazar Ch D), the start of a single-shot measurement (Alazar Ch C), and the start of a sequence of single-shot measurements (Alazar X2, which can also act as an output in the future).

order to get around this limitation, we utilize the methods pioneered in refs [131, 123], namely reflectometry, to transform our high resistances into low impedances that we can observe rapidly. A description of how these signals were processed and turned into state probabilities is discussed in detail in appendix D.

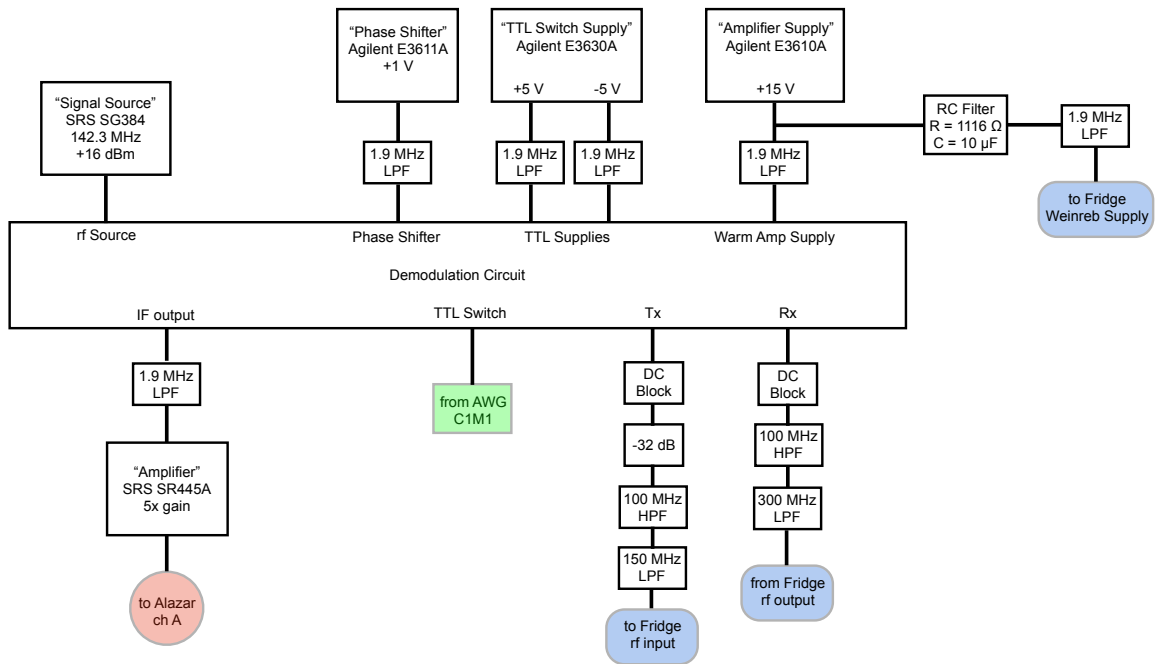


Figure C.3: A schematic of the reflectometry wiring outside the dilution refrigerator used in chapters 7 and 8. The contents of the demodulation circuit are displayed in figure C.4.

The signal that is being observed via the reflectometry is the voltage reflected off of the rf-tank circuit attached to the sensor ohmic on the device, as demonstrated in Ref. [123]. The circuit has a reflection coefficient, Γ , that is sensitive to the large resistance of the QPC or sensor dot it is attached to, effectively transforming the $100 \text{ k}\Omega$ load into something near 50Ω .

The standard model for the operation of the rf-charge readout assumes a perfect ohmic contact to the two dimensional electron gas (2DEG). In general we have round it

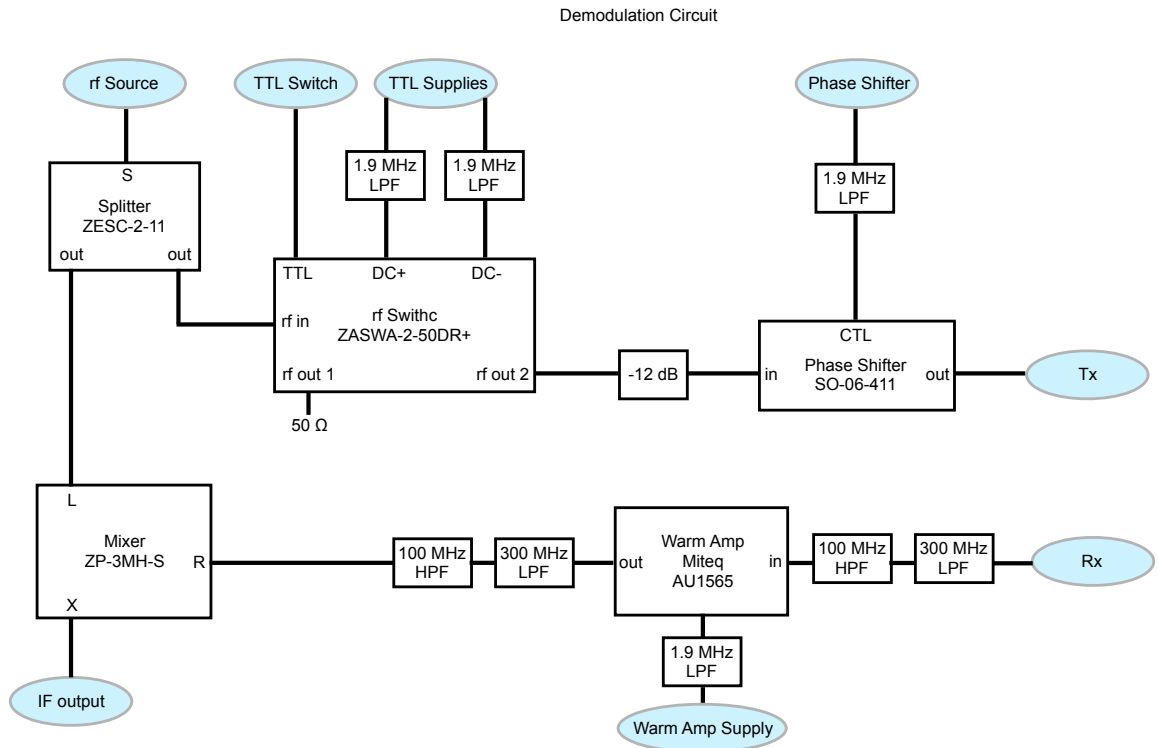


Figure C.4: A schematic of the reflectometry demodulation circuit used in chapters 7 and 8. The demodulation circuit is attached to the experiment through the wiring in figure C.4.

to be qualitatively correct in most circumstances, but only occasionally quantitative in its predictions of matching resistance. At the end of this section I will briefly cover possible reasons for discrepancies between model and reality.

In this basic model shown in Fig. C.5(c), we write the impedance of the circuit as

$$z(\omega) = i\omega L + \frac{R}{1 + i\omega RC} \quad (\text{C.1})$$

where L is the inductor value, C is the stray capacitance due to bond wires, surface mount casings, and 2DEG that the bond wires pass over, and R is the resistance of the device. The reflected power is proportional to $|\Gamma|^2$, where

$$\Gamma(\omega) = \frac{z(\omega) - z_0}{z(\omega) + z_0}, \quad (\text{C.2})$$

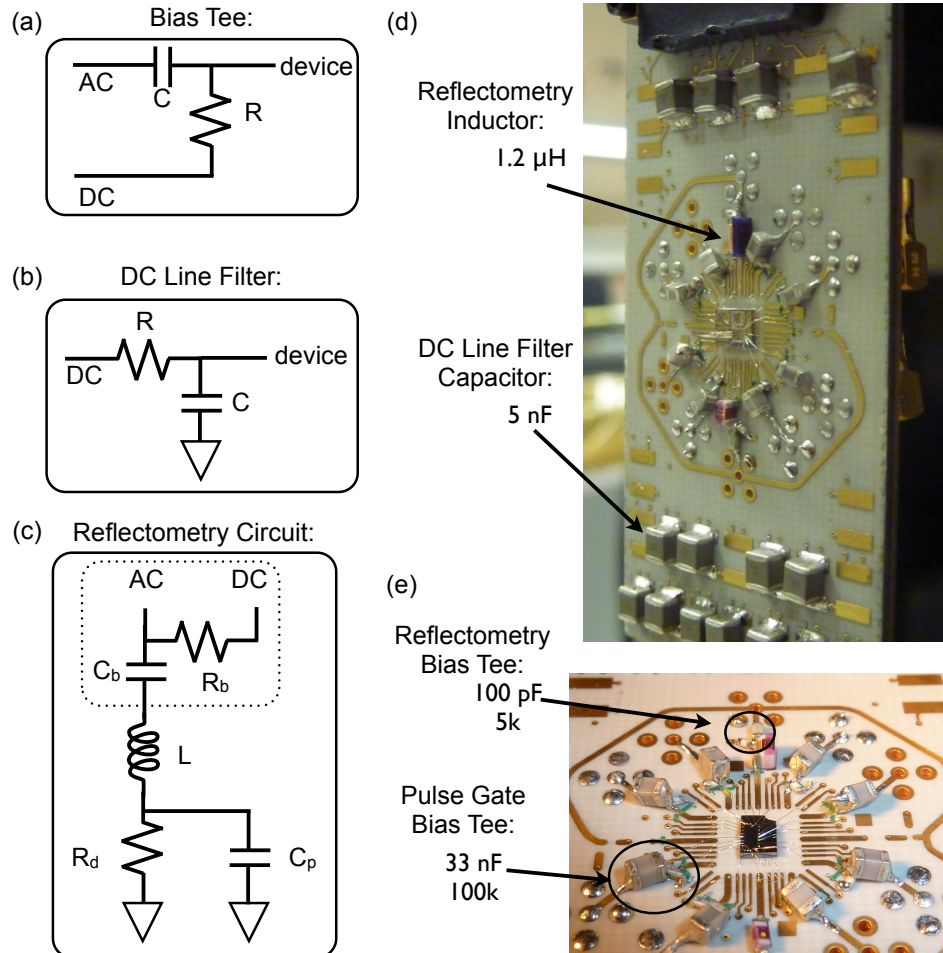


Figure C.5: A schematic of the PC board sample package used in chapters 7 and 8. (a) A circuit diagram of a bias tee. (b) A circuit diagram of a lowpass filter found on the PC board. The resistor is not on board, but in the “Ferdie Filter” mounted to the cold finger for PC board space reasons. (c) A circuit diagram for the reflectometry circuit. The inductor L , along with the device resistance R_d and parasitic capacitance C_p for a tank circuit to reflect incoming power. The dashed box encloses the bias tee that allows for transport measurements in addition to high frequency reflectometry measurements. (d) A picture of the PC board with the sample glued and bonded in. The inductor and filtering capacitors are highlighted. (e) A close up of the high frequency bias tees surrounding the device. These boards were designed by Jim MacArthur, with help from Hugh Churchill, Andrew Higginbotham, Peter Nissen, and myself. The idea behind these boards was to reduce the complexity of device bonding by providing DC and AC lines evenly throughout the perimeter of the sample area, minimizing the number of bonds which crossed.

and $z_0 = 50 \Omega$. With this, we can express the reflected power as

$$|\Gamma|^2 = 1 - \frac{200R}{(50+R)^2 - \omega^2[L^2 - 2CR(L-1250C)] + C^2L^2R^2\omega^4} \quad (\text{C.3})$$

which we can rewrite as

$$|\Gamma|^2 = 1 - \frac{200R}{(R+50)^2 - L^2C^2R^2\omega_{\text{res}}^4 + (\omega^2 - \omega_{\text{res}}^2)^2} \quad (\text{C.4})$$

$$|\Gamma|^2 = 1 - \frac{4GG_m}{(G+G_m)^2[1 - \frac{L}{4C}(G-G_m)^2] + L^2C^2(\omega^2 - \omega_{\text{res}}^2)^2} \quad (\text{C.5})$$

where the matching resistance and frequency are $R_m = \frac{L}{50C}$ and $\omega_{\text{res}} = \frac{1}{\sqrt{LC}}\sqrt{1 - \frac{L}{2C}(G^2 + G_m^2)}$, and $G \equiv \frac{1}{R}$ and $G_m \equiv \frac{1}{R_m}$ are the conductances associated with the device and matching resistances respectively.

When the tank circuit is excited on resonance, $\omega = \omega_{\text{res}} \approx (LC)^{-1/2}$, the reflection coefficient is very sensitive to changes in conductance around the matching conductance $G_m = \frac{50C}{L}$. If we Taylor expand about the matching conductance, we see

$$|\Gamma|^2 \simeq \frac{1}{4} \left(\frac{1}{G_m^2} - \frac{50}{G_m} \right) (G - G_m)^2 + O(G - G_m)^3, \quad (\text{C.6})$$

meaning that exactly on the matching condition we are actually relatively insensitive to changes in conductance. Since the pre-factor scales¹³ as $\frac{1}{G_m^2} = R_m^2$, we can get a sharper response away from matching by working with a circuit tuned to a high matching resistance/low matching conductance.

As mentioned earlier, the model does not always predict the matching resistance R_m very well. In particular, real circuits sometimes exhibit a phenomenon where the resonance deepens monotonically with increasing device resistance, but from a range of $G \sim 0 - 1e^2/h$ is almost completely insensitive. The resonance is often less than 10 dB deep in these cases, in contrast to the “good” case where the resonance is modulated by 30 dB

¹³Our devices are usually sensitive in a regime between 10 kΩ and 100 kΩ, making $R_m^2 \gg R_m$.

or more. We refer to this as “matching at pinch off”, and it renders the circuit useless for sensing.

A simple explanation for this is that if there is a large ohmic resistance, higher than $\sim 1-2\text{ k}\Omega$, it is no longer correct to think of the impedance of the device set entirely by the real resistance of the sensing channel, with all stray capacitances in the device simply adding to C . With a high ohmic resistance, one should instead talk about the complex impedance of the device, where the sensing channel resistance is in parallel with many capacitive paths to ground, such as the gates and other 2DEG regions. When the sensing channel resistance becomes very large, in the region where the resonance stops agreeing with the model, the device impedance becomes dominated by the capacitive paths to ground, leaving the reflection coefficient unchanged by the sensing channel. Good ohmic contacts and low resonance frequencies limit these effects.

The model also breaks down in an identical way the presence of long, looping bond wires. Re-bonding with a shorter path between circuit board and ohmic seems to restore the circuit to its ideal resonator behavior. As demonstrated in Ref. [28] among other places, fabricating superconducting spiral inductors directly next to the ohmic pads may remove this uncertainty entirely.

Appendix D

Supplemental Material for Self-Consistent Measurement and State Tomography of an Exchange-Only Spin Qubit

This supporting document describes further details of the fabrication, state readout, noise modeling, and measurement tomography techniques. The measurement tomography section details the pulse sequences and fitting routines used to extract the POVM elements, as well as the effects of finite bandwidth limitations on the state reconstruction.

D.1 Device

The three-electron system was confined in a lateral triple quantum dot formed in the two-dimensional electron gas (2DEG) at the GaAs/Al_{0.3}Ga_{0.7}As interface 110 nm below the surface of the heterostructure. The GaAs/Al_{0.3}Ga_{0.7}As heterostructure was grown on a solid-source Varian Gen II molecular beam epitaxy (MBE) system equipped with an arsenic valved cracker source to provided As² for the growth. The heterostructure was grown on a semi-insulating (100) GaAs substrate with a growth rate of 1 $\mu\text{m}/\text{hr}$. The 2DEG is formed by a Si modulation doping (δ -doping) of $\sim 4 \times 10^{16} \text{ m}^{-2}$ (40 nm away from the 2DEG

interface). Hall effect measurement done at 20K gives a 2DEG density of $\sim 2.6 \times 10^{15} \text{ m}^{-2}$ and a mobility of $\sim 43 \text{ m}^2/\text{V s}$.

High bandwidth coaxial lines were attached to the left, middle, and right plunger gates of the triple quantum dot, and a radio-frequency (rf) reflectometry circuit was connected to a neighboring quantum dot for fast state readout [123, 8]. The experiment was performed in a dilution refrigerator equipped with a cryogenic amplifier (noise temperature $T_N \sim 3 \text{ K}$), with an electron temperature of $\sim 120 \text{ mK}$. An in-plane external magnetic field of 300 mT was applied along the dot connection axis [see Fig. 1(a) in main text].

D.2 Measurement and Normalization

D.2.1 Normalizations Based on Single-Shot Outcomes

A uniform normalization procedure was used for all data in Figs. 2-5 to convert the measured reflectometry signals into output probabilities. For a given set of pulse parameters (ε^S , τ_S , $\tau_1+\tau_2$, $\tau_1-\tau_2$, etc.), the qubit was measured using four preparation and measurement routines. In the first two routines, the state $|S_l\rangle$ was prepared in 201 then measured either in 201 ($|S_l\rangle$ projection, yielding P_1) or in 102 ($|S_r\rangle$ projection, yielding P_2). In the other two routines, the state $|S_r\rangle$ was prepared in 102 then measured either in 201 ($|S_l\rangle$ projection) or in 102 ($|S_r\rangle$ projection). Each measurement consisted of sitting at the measurement point— ε_l^M (ε_r^M) for $|S_l\rangle$ ($|S_r\rangle$) readout—and integrating the demodulated rf signal reflected from the impedance transforming circuit [123] attached to the rf-sensor quantum dot for $\tau_M = 50 \mu\text{s}$ to yield v_{rf} .

This process was then repeated while stepping one of the pulse parameters (ε^S , τ_S , $\tau_1+\tau_2$, $\tau_1-\tau_2$, etc.). Each sequence was then repeated 2^{13} or 2^{14} times to obtain measurement statistics. The resulting data was then histogrammed, following the procedure in Ref. [8], and fit to a function of the form,

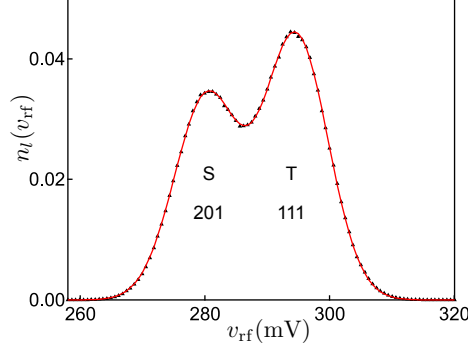


Figure D.1: A histogram of outcomes for Fig. 7.3(a). Red solid curve is a fit to equation (E.1).

$$n_l(v_{\text{rf}}) = \frac{P_1}{\sqrt{2\pi\sigma^2}} \exp\left[-\frac{(v_{\text{rf}} - v_{\text{rf}}^{201})^2}{2\sigma^2}\right] + e^{-\tau_M/T_1} \frac{(1 - P_1)}{\sqrt{2\pi\sigma^2}} \exp\left[-\frac{(v_{\text{rf}} - v_{\text{rf}}^{111})^2}{2\sigma^2}\right] + \int_{v_{\text{rf}}^{201}}^{v_{\text{rf}}^{111}} \frac{dV}{\sqrt{2\pi\sigma^2}} \frac{\tau_M}{T_1} \frac{(1 - P_1)}{\Delta v_{\text{rf}}} \exp\left[-\frac{\tau_M}{T_1} \frac{V - v_{\text{rf}}^{201}}{\Delta v_{\text{rf}}} - \frac{(v_{\text{rf}} - V)^2}{2\sigma^2}\right], \quad (\text{D.1})$$

where $n_l(v_{\text{rf}})$ is the fraction of histogram events with outcomes v_{rf} for a measurement in 201, v_{rf}^{201} is the reflected voltage corresponding to double occupancy in the left dot, v_{rf}^{111} is the reflected voltage corresponding to single charge occupancy in the all three dots, $\Delta v_{\text{rf}} \equiv v_{\text{rf}}^{111} - v_{\text{rf}}^{201}$, P_1 is the fraction of 201 outcomes in the data set, T_1 is the relaxation time at ε_l^M , τ_M is the measurement time, and σ is the standard deviation of the histogram peaks due to noise in the rf equipment and shot noise intrinsic to the rf sensor dot. For measurements in the right dot, n_r has an identical form, with all 201 notations replaced with 102 and P_1 replaced with P_2 .

The extracted parameters v_{rf}^{201} and v_{rf}^{111} are then used to normalize the return probabilities on the left side,

$$P_1^0(\varepsilon^S, \tau_S) = \frac{\langle v_{\text{rf}}(\varepsilon^S, \tau_S) \rangle - v_{\text{rf}}^{111}}{v_{\text{rf}}^{201} - v_{\text{rf}}^{111}}, \quad (\text{D.2})$$

where $\langle v_{\text{rf}}(\varepsilon^S, \tau_S) \rangle$ is the average voltage over all repetitions of the measurement sequence for a specific ε^S and τ_S . P_2^0 is normalized similarly, with v_{rf}^{201} replaced by v_{rf}^{102} .

Equation (E.2) converts v_{rf} into a probability, but it does not account for relaxation during the measurement time τ_M , where a 111 state relaxes to a 201 state for $|S_l\rangle$ projections or a 102 state for $|S_r\rangle$ projections. Relaxation during the measurement was accounted for using a two step process. The histogram shape is only weakly dependent on the precise value of T_1 , but failing to allow for relaxation of the 111 charge state would underestimate the separation between histogram peaks. T_1 decay was therefore included in equation (E.1) to determine the peak positions v_{rf}^{201} and v_{rf}^{111} accurately, but the T_1 fit parameter is not itself an accurate measurement of the relaxation time in the data. In order to more accurately correct for relaxation, we project a state prepared as $|S_r\rangle$ in 102 against $|S_l\rangle$ in 201, and record the probability as P_1^{cal} , at the beginning of each sequence and compare it with the theoretical value $|\langle S_r | S_l \rangle|^2 = 0.25$; we confirm the theoretical value by measuring relaxation as a function of measurement time τ_M , as described in Sec. B.2. Traces were then corrected as

$$P_1 = 1 - (1 - P_1^0) \frac{1 - 0.25}{1 - P_1^{\text{cal}}} \quad (\text{D.3})$$

A measurement of a state prepared as $|S_l\rangle$ and measured in 102 is similarly used to correct for T_1 decay in P_2 .

D.2.2 T_1 Relaxation During Measurement

The relaxation time was extracted from measurements of the dependence of the uncorrected singlet probabilities P_1^0 and P_2^0 as functions of the integration time τ_M for $|S_l\rangle$ measured in 102 and $|S_r\rangle$ measured in 201. The observed dependence was well described

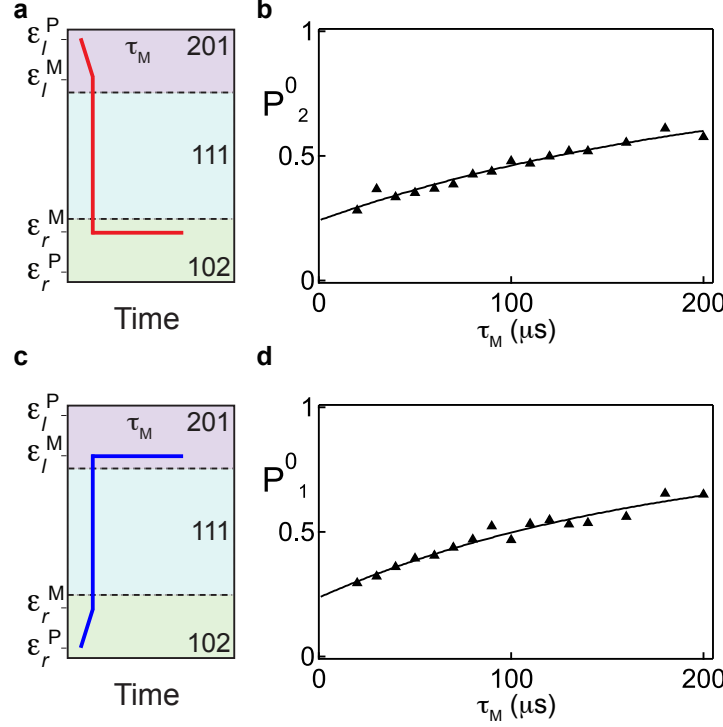


Figure D.2: (a) Schematic for preparing $|S_l\rangle$ and projecting it onto $|S_r\rangle$. (b) Experiment (triangles) and numerics (solid curve) for the probability of measuring a singlet in 102 if the state was prepared as $|S_l\rangle$ in 201, as a function of measurement time τ_M . The numerical results are uncorrected for relaxation during the measurement. Numerical result is a fit to the function (D.4) with fit parameters $T_1 = 137 \pm 9 \mu\text{s}$ and $|\langle S_r | S_l \rangle|^2 = 0.24 \pm 0.01$ at $\tau_M = 0$. (c) Schematic for preparing $|S_r\rangle$ and projecting it onto $|S_l\rangle$. Experiment (triangles) and numerics (solid curve) for the probability of measuring a singlet in 201 if the state was prepared as $|S_r\rangle$ in 102, as a function of measurement time τ_M , uncorrected for relaxation during the measurement. Numerical result is a fit to the function (D.4) with fit parameters $T_1 = 110 \pm 8 \mu\text{s}$ and $|\langle S_r | S_l \rangle|^2 = 0.24 \pm 0.02$ at $\tau_M = 0$.

by exponential relaxation of triplets integrated over the measurement time,

$$1 - P_1^0 = \frac{1}{\tau_M} \int_0^{\tau_M} dt (1 - A) e^{-t/T_1}$$

$$P_1^0 = 1 - \frac{(1 - A)T_1}{\tau_M} (1 - e^{-\tau_M/T_1}), \quad (\text{D.4})$$

where A is the fraction of singlets present at $\tau_M = 0$, and corresponds to $|\langle S_r | S_l \rangle|^2$ in the absence of any evolution when pulsing the prepared state to the measurement position. The expression for P_2^0 is identical, with T_1 referring to the measurement relaxation on the right

rather than the left. In the data shown in Fig. D.2, extrapolation to zero measurement time yields $A = 0.24 \pm 0.02$ for both P_1^0 and P_2^0 . This allows us to correct for relaxation by normalizing the data with the theoretical singlet probability.

D.3 Figure 4b Theory Curves

D.3.1 Pure Electrical Dephasing

We model exchange rotation in the presence of low-frequency detuning noise as:

$$P_1(\tau_S) = \frac{5}{8} \left\{ 1 - \cos[\tau_S J(\tau_S)] \exp \left[- \left(\frac{\tau_S}{T_2^*} \right)^2 \right] \right\}, \quad (\text{D.5})$$

where T_2^* is a characteristic time for dephasing due to electrical noise. Rise-time effects, due for instance to bandwidth limits of the coaxial cable, are modeled as an exponential rise in the exchange,

$$J(t) = J_0 \left[1 - \exp \left(-\frac{t}{\tau_R} \right) \right]. \quad (\text{D.6})$$

The dashed gray curve in Fig. 4b of the main text used the parameters $J_0 = 391$ neV, $T_2^* = 25$ ns, and $\tau_R = 13$ ns.

D.3.2 Dephasing due to Nuclei - Ladd Curve

Following Ref. [81], Eqs. 9, 14-16, we model the effect of nuclear fluctuations on the qubit as

$$P_1(\tau_S) = \frac{1}{2} + \frac{1}{4} \left\{ -I_1(\tau_S) + \exp \left[-\frac{3}{2} (\sigma_{\Delta B} \tau_S)^2 \right] I_2(\tau_S) \right\}, \quad (\text{D.7})$$

where

$$I_1(t) = \frac{\sqrt{\pi} J(t)}{4\sigma_{\Delta B}} \exp \left[\frac{J(t)^2}{8\sigma_{\Delta B}^2} \right] \operatorname{erfc} \left[\frac{J(t)}{2\sqrt{2}\sigma_{\Delta B}} \right] \times \\ \left\{ 1 - \sqrt{A(t, J, 0)} \cos \left[tJ(t) + \frac{1}{2} \cos^{-1} \left(A(t, J, 0) \right) \right] \right\} \quad (\text{D.8a})$$

$$I_2(t) = \sqrt{A(t, 2J, 0)} \left\{ \cos[tJ(t)] + \cos \left[tJ(t) + \frac{1}{2} \cos^{-1} \left(A(t, 2J, 0) \right) \right] \right\} \quad (\text{D.8b})$$

$$A(t, \xi, \omega) = \frac{1}{\sqrt{1 + \left[\frac{4\sigma_{\Delta B}^2 t}{\xi} (1 + 2\omega) \right]^2}} \quad (\text{D.8c})$$

$$J(t) = J_0 \left[1 - \exp \left(-\frac{t}{\tau_R} \right) \right] \quad (\text{D.8d})$$

Here, we take the standard deviation of the nuclear fluctuations to be the same in each dot, which simplifies the expressions in Ref. [81]. The solid gray curve in Fig. 4b of the main text uses fit parameters $J_0 = 386 \pm 2$ neV, $\sigma_{\Delta B} = 1.9 \pm 0.2$ mT, and $\tau_R = 13$ ns.

D.3.3 Numerical Model: Electrical and Nuclear dephasing

In order to incorporate both electrical and magnetic sources of noise, we used a numerical model for the time evolution of an initial $|S_l\rangle$ in the presence of both exchange interactions J_l and J_r , as well as longitudinal field gradients ΔB_l and ΔB_r . The finite bandwidth of the coax and function generator are accounted for with an exponential turn-on as described in Sec. C.1. We take J_r to be Gaussian distributed, appropriate for small amplitude fluctuations in ε^S over a range where J_r varies approximately linearly with ε^S , that is, $\delta J \approx (\Delta J_r / \Delta \varepsilon^S) \delta \varepsilon^S$. In the region of detuning where $dJ_r/d\varepsilon^S \gg dJ_l/d\varepsilon^S$, only fluctuations in J_r were taken into account. Since the left exchange was decreasing while the right exchange was increasing, they were approximated as:

$$J_l = J_l^0 e^{-t/\tau_R} \quad (\text{D.9})$$

$$J_r = J_r^0 (1 - e^{-t/\tau_R}) + \delta J \quad (\text{D.10})$$

The effects of the slowly fluctuating nuclear bath were incorporated by taking an ensemble average over Gaussian distributions of nuclear gradients between the left and middle (ΔB_l) and middle and right (ΔB_r) dots. Limiting this model to detuning regions away from the $|Q_+\rangle$ - $|S_l\rangle$ and $|Q_+\rangle$ - $|S_r\rangle$ anti-crossings, transverse components of the hyperfine field can be safely neglected, leaving only gradients between longitudinal components. This model assumes a Gaussian distribution of classical nuclear gradients, with no back-action on the nuclei from the qubit.

Explicitly, P_1 was evaluated numerically using a uniform step size,

$$P_1(\tau_S) = \int \frac{d\Delta B_l d\Delta B_r d\delta J}{(2\pi)^{3/2} \sigma_B^2 \sigma_J} \left| \langle S_l | e^{-i\mathcal{H}_1 \tau_S / \hbar} | S_l \rangle \right|^2 e^{-(\Delta B_l^2 + \Delta B_r^2)/(2\sigma_B^2) - (\delta J)^2/(2\sigma_J^2)} \quad (\text{D.11})$$

$$\approx \sum \frac{(\Delta B_{max} - \Delta B_{min})^2 (J_{max} - J_{min})}{(2\pi)^{3/2} \sigma_B^2 \sigma_J N_{step}^3} \left| \langle S_l | e^{-i\mathcal{H}_1 \tau_S / \hbar} | S_l \rangle \right|^2 \\ \times e^{-(\Delta B_l^2 + \Delta B_r^2)/(2\sigma_B^2) - (J_r - J_r^0)^2/(2\sigma_J^2)}, \quad (\text{D.12})$$

where τ_S is the time spent during the rotation, σ_B is the standard deviation of the Gaussian distribution of classical values that each nuclear gradient could achieve, σ_J is the standard deviation of the Gaussian distribution of J_r values, N_{step} is the number of discrete values sampled for each Gaussian, ΔB_{max} and ΔB_{min} are the limits of ΔB_l and ΔB_r values sampled, J_{max} and J_{min} are the limits of δJ values sampled, τ_R is the turn-on time for the exchange, \mathcal{H}_1 is the Hamiltonian at the dephasing position. The Hamiltonian consisted of two parts, the model laid out in Ref. [85], and a nuclear Hamiltonian; $\mathcal{H}(\varepsilon^1) = \mathcal{H}_J(J_l, J_r) + \gamma \mathcal{H}_B(\Delta B_l, \Delta B_r)$, where $\gamma = g\mu_B = -25.4 \text{ neV/mT}$.

We can write the exchange Hamiltonian in the basis of $(|0\rangle, |1\rangle, |Q\rangle)$ as:

$$\mathcal{H}_J = \begin{pmatrix} -\frac{3}{4}(J_l + J_r) & \frac{\sqrt{3}}{4}(J_l - J_r) & 0 \\ \frac{\sqrt{3}}{4}(J_l - J_r) & -\frac{1}{4}(J_l + J_r) & 0 \\ 0 & 0 & 0 \end{pmatrix} \quad (\text{D.13})$$

Here, the zero energy state has been shifted relative to $H_J(\varepsilon)$ in the main text to make the energy of the $|Q\rangle$ state zero at zero detuning. This brings our notation into agreement with Ref. [85].

The longitudinal nuclear terms in this basis are:

$$\mathcal{H}_B = \begin{pmatrix} \frac{1}{6}(\Delta B_l - \Delta B_r) & \frac{1}{2\sqrt{3}}(\Delta B_l + \Delta B_r) & -\frac{1}{3\sqrt{2}}(\Delta B_l - \Delta B_r) \\ \frac{1}{2\sqrt{3}}(\Delta B_l + \Delta B_r) & -\frac{1}{6}(\Delta B_l - \Delta B_r) & \sqrt{\frac{1}{6}}(\Delta B_l + \Delta B_r) \\ -\frac{1}{3\sqrt{2}}(\Delta B_l - \Delta B_r) & \sqrt{\frac{1}{6}}(\Delta B_l + \Delta B_r) & 0 \end{pmatrix} \quad (\text{D.14})$$

where $\Delta B_l = (B_1^z - B_2^z)$ and $\Delta B_r = (B_2^z - B_3^z)$ are the differences in local magnetic field along the \hat{z} direction. Terms that only contribute a global phase in this basis have been dropped for clarity.

A fit to this model yields: $J_l^0 = 21 \pm 8$ neV, $J_r^0 = 388 \pm 2$ neV, $\sigma_B = 2.0 \pm 0.1$ mT, $\sigma_J = 19 \pm 2$ neV, $\tau_R = 12.6 \pm 0.2$ ns. The distributions were each sampled evenly 12 times (N_{step}) each for a total of $12^3 = 1728$ samples between $3\sigma_B$ and $-3\sigma_B$ for the nuclei and between $3\sigma_J$ and $-3\sigma_J$ for δJ . This gives the solid black curve in Fig. 4b.

D.4 Figure 5d Echo with Hyperfine Dephasing and Leakage, without Electrical Noise

The partial echo (Fig. 5 in the main text) was analyzed using a model similar to the one used in Figure 4c. The timescales involved in the echo are much longer than the rise time τ_R , so the phenomenological exponential turn on of the exchange is removed for simplicity. In addition, since the dephasing was dominated by nuclei in Figure 4 the noise on J_r is omitted.

The model includes the evolution of an initial $|S_l\rangle$ under the action of the three exchange pulse sequence in the limit of instantaneous rise times in the qubit environment of 111. The pulses are evaluated in a piecewise-static manner, ignoring the weak adiabatic

effects associated with pulsing from one detuning position to the other. Explicitly, P_1 was evaluated numerically using a uniform step size as:

$$P_1(\tau_1, \tau_2) = \int \frac{d\Delta B_l d\Delta B_r}{2\pi\sigma_B^2} \left| \langle S_l | e^{-i\mathcal{H}(\varepsilon^1)\tau_2/\hbar} e^{-i\mathcal{H}(\varepsilon^2)\tau_\pi/\hbar} e^{-i\mathcal{H}(\varepsilon^1)\tau_1/\hbar} | S_l \rangle \right|^2 e^{-(\Delta B_l^2 + \Delta B_r^2)/(2\sigma_B^2)} \quad (\text{D.15})$$

$$\approx \sum \frac{(\Delta B_{max} - \Delta B_{min})^2}{2\pi\sigma_B^2 N_{step}^2} \times \left| \langle S_l | e^{-i\mathcal{H}(\varepsilon^1)\tau_2/\hbar} e^{-i\mathcal{H}(\varepsilon^2)\tau_\pi/\hbar} e^{-i\mathcal{H}(\varepsilon^1)\tau_1/\hbar} | S_l \rangle \right|^2 e^{-(\Delta B_l^2 + \Delta B_r^2)/(2\sigma_B^2)}, \quad (\text{D.16})$$

where $\tau_{1(2)}$ is the time before (after) the π pulse, σ_B is the standard deviation of the Gaussian distribution of nuclear gradients, N_{step} is the number of discrete values sampled for each gradient, ΔB_{min} and ΔB_{max} are the limits of ΔB_l and ΔB_r values sampled, $\mathcal{H}(\varepsilon^1)$ is the Hamiltonian at the dephasing position, including nuclei, and $\mathcal{H}(\varepsilon^2)$ is the Hamiltonian for the π pulse. The Hamiltonians were of the same form as equations (D.13) and (D.14), with $\mathcal{H}(\varepsilon^1) = \mathcal{H}_J(0, J_r) + \gamma\mathcal{H}_B(\Delta B_l, \Delta B_r)$, $\mathcal{H}(\varepsilon^2) = \mathcal{H}_J(J_l, 0) + \gamma\mathcal{H}_B(\Delta B_l, \Delta B_r)$. The values used in the model were $\gamma = g\mu_B = -25.4 \text{ neV/mT}$, $\sigma_B = 1.7 \text{ mT}$, $J_r = 276 \text{ neV}$, $J_l = 824 \text{ neV}$. The magnetic field gradients were each sampled uniformly between $3\sigma_B$ and $-3\sigma_B$, with $N_{step} = 40$.

D.5 Measurement Tomography for the Exchange Only Qubit

D.5.1 Measurements and Measurement Operators

In order to determine the populations ($|0\rangle\langle 0|$, $|1\rangle\langle 1|$) and coherences ($\text{Re}[|0\rangle\langle 1|]$, $\text{Im}[|0\rangle\langle 1|]$) in the qubit subspace (four unknowns), as well the population of the leakage state ($|Q\rangle\langle Q| \equiv 1 - |0\rangle\langle 0| - |1\rangle\langle 1|$), we need to perform four measurements. The measurement

probabilities can be expressed in the following fashion:

$$P_1(\rho) = \text{Tr}[E_1\rho] \quad (\text{D.17a})$$

$$P_2(\rho) = \text{Tr}[E_2\rho] \quad (\text{D.17b})$$

$$P_3(\rho) = \text{Tr}[E_3\rho] \quad (\text{D.17c})$$

$$P_4(\rho) = \text{Tr}[E_4\rho] \quad (\text{D.17d})$$

where ρ denotes an unknown input state and E_i is a measurement operator that describes the fidelity of a singlet outcome for a measurement in the i^{th} basis. If we have a set of five (or more) known input states, ρ_j , one can use those states to measure the E_1 , E_2 , E_3 , and E_4 by solving the set of equations (D.17). Once the E_i are determined, we can reconstruct any unknown state ρ from the four probabilities, P_1 , P_2 , P_3 , and P_4 .

Our measurement tomography approach uses known input states to characterize the measurement operators E_i . Of the five required input states, three are relatively easy to prepare. These are the two initialization states, $|S_l\rangle$ and $|S_r\rangle$, and the completely mixed state. Their density matrices in the $|0\rangle$ - $|1\rangle$ - $|Q\rangle$ basis can be written as:

$$\rho_1 = |S_l\rangle\langle S_l| = \begin{pmatrix} \frac{3}{4} & -\frac{\sqrt{3}}{4} & 0 \\ -\frac{\sqrt{3}}{4} & \frac{1}{4} & 0 \\ 0 & 0 & 0 \end{pmatrix} \quad (\text{D.18})$$

$$\rho_2 = |S_r\rangle\langle S_r| = \begin{pmatrix} \frac{3}{4} & \frac{\sqrt{3}}{4} & 0 \\ \frac{\sqrt{3}}{4} & \frac{1}{4} & 0 \\ 0 & 0 & 0 \end{pmatrix} \quad (\text{D.19})$$

$$\rho_5 = |mixed\rangle\langle mixed| = \begin{pmatrix} \frac{1}{3} & 0 & 0 \\ 0 & \frac{1}{3} & 0 \\ 0 & 0 & \frac{1}{3} \end{pmatrix} \quad (\text{D.20})$$

We create ρ_5 by pulsing to regions of large J_l and J_r repeatedly, allowing the state to dephase around both rotation axes as well as the nuclear gradients. The preparation of the dephased state is confirmed by comparing measurements of the dephased state that was initially prepared as $|S_l\rangle$ with the state initially prepared as $|S_r\rangle$. The only way that these two outcomes will be identical is if they are both completely dephased in the qubit space. The length of the sequence is many times larger than $T_{2,nuc}^*$, which when combined with the pulses yields a completely mixed state with $|Q\rangle$ as well¹. This state allows for the characterization of the $|Q\rangle$ fidelity in each measurements, which is not necessarily identical to the qubit triplet-like ($|T_l\rangle$ and $|T_r\rangle$) fidelity.

Those three states are entirely real by construction. It is more challenging to prepare high fidelity states with $\text{Im}[|0\rangle\langle 1|] \neq 0$, which are needed to fully characterize the system. These superposition states allow us to characterize the complex quantities of our measurement operators, and in turn allow us to measure any superposition of states in the qubit subspace. Since we do not have access to initialization states with $\text{Im}[|0\rangle\langle 1|] \neq 0$, we need to create these states through evolutions under control pulses. These pulses themselves contain noise. The extent to which we correctly account for the dephasing and leakage that occurs during the preparation of these states determines our ability to characterize the two rotated input states, $\rho_3 = |\hat{R}_r S_l \rangle\langle S_l \hat{R}_r|$ and $\rho_4 = |\hat{R}_l S_r \rangle\langle S_r \hat{R}_l|$, and therefore E_3 and E_4 . We incorporate the details of the evolution, including noise, into the estimation of our input states using MLE techniques, which results in a more accurate state reconstruction.

The final algorithm we use simultaneously estimates the evolution of ρ_3 and ρ_4 as well as the POVM elements $E_1 - E_4$ by using a Levenberg-Marquardt least-squares method to minimize the difference between the output of the model and the measured probabilities

¹The $|Q\rangle$ mixing is confirmed by allowing for preparation infidelity in the MLE routine, and finding that the most likely population of the leakage state is 0.336, as opposed to the ideal 0.333. The ideal value is used in the data presented.

associated with $\rho_1 - \rho_5$. This gives us our Maximum Likelihood Estimate for $E_1 - E_4$.

D.5.2 Creation and Determination of the Known Input States

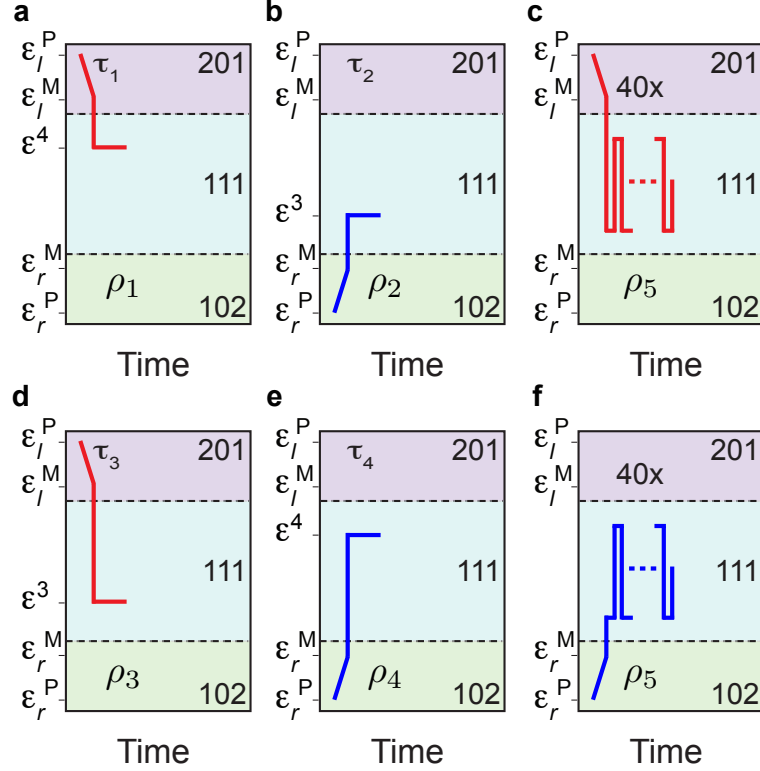


Figure D.3: Schematics for pulse sequences that create the five input states. (a) Input state ρ_1 . (b) Input state ρ_2 . (c) Input state ρ_5 prepared from an initial $|S_l\rangle$. (d) Input state ρ_3 . (e) Input state ρ_4 . (f) Input state ρ_5 prepared from an initial $|S_r\rangle$.

One way to minimize the error in estimating ρ_3 and ρ_4 is to spread ρ_3 and ρ_4 out into a set of input states that evolved under a common axis of rotation for a range of rotation times τ_3 and τ_4 . In other words, ρ_3 becomes a set of states $\rho_3(\tau_3)$ evolving at ε^3 and ρ_4 becomes a set of states $\rho_4(\tau_4)$ evolving at ε^4 . With these sets of rotation times, we can accurately estimate axis of the rotations and the frequency of the rotation at the fixed detunings ε^3 and ε^4 , and therefore each state in the series $\rho_3(\tau_3)$ and $\rho_4(\tau_4)$. In this manner we can prepare a set of reasonably high fidelity input states that are superpositions of our

measurement basis states with complex coefficients.

Explicitly, we take the effective Hamiltonian for this system, equations (D.13) and (D.14), and evolve the initial density matrix in time. We then average that evolution over a distribution of ΔB 's, calculate the probabilities using equations (D.17) and compare it to the data. The fitting procedure, if started from good initial guesses (which we generate iteratively through incremental fits, and incremental relaxation of constraints), can generate the MLE for the Hamiltonian parameters and every element of E_1 , E_2 , E_3 , and E_4 .

The fit is performed by calculating the theoretical Hamiltonian of the system, using the same techniques that were employed for the FID and the partial echo. Assuming time independent Hamiltonians, $\rho_3(\tau_3)$ and $\rho_4(\tau_4)$ can be written as

$$\rho_3(\tau_3) = \int \frac{d\Delta B_l d\Delta B_r}{2\pi\sigma_B^2} e^{-i\mathcal{H}(\varepsilon^3)\tau_3} \rho_1 e^{i\mathcal{H}(\varepsilon^3)\tau_3} e^{-(\Delta B_l^2 + \Delta B_r^2)/(2\sigma_B^2)} \quad (\text{D.21})$$

$$\rho_4(\tau_4) = \int \frac{d\Delta B_l d\Delta B_r}{2\pi\sigma_B^2} e^{-i\mathcal{H}(\varepsilon^4)\tau_4} \rho_2 e^{i\mathcal{H}(\varepsilon^4)\tau_4} e^{-(\Delta B_l^2 + \Delta B_r^2)/(2\sigma_B^2)}, \quad (\text{D.22})$$

where $\mathcal{H}(\varepsilon^3) = \mathcal{H}_J(J_l(\varepsilon^3), J_r(\varepsilon^3)) + \gamma \mathcal{H}_B(\Delta B_l, \Delta B_r)$, $\mathcal{H}(\varepsilon^4) = \mathcal{H}_J(J_l(\varepsilon^4), J_r(\varepsilon^4)) + \gamma \mathcal{H}_B(\Delta B_l, \Delta B_r)$, and σ_B is the standard deviation of the Gaussian distribution of nuclear gradients. We then generate the probabilities for each measurement using Eqs. (D.17). The Levenberg-Marquardt least-squares algorithm subsequently optimizes the parameters of $\mathcal{H}(\varepsilon^3)$, $\mathcal{H}(\varepsilon^4)$, and σ_B to minimize the difference between measured and calculated probabilities. The estimates that the fitting function produce come with error bars, which may be useful indications of the reliability of the MLE output.

There is a further improvement that we can make to this scheme. $\rho_3(\tau_S)$ and $\rho_4(\tau_S)$ are formed by pulsing to a region of high exchange, and then pulsing to the settle point, while ρ_1 and ρ_2 are formed by pulsing from 201 and 102 respectively. This can increase the lowpass effects that the settle point is trying to mitigate. To improve the situation, and to have ρ_1 , ρ_2 , and ρ_5 have equal weight with $\rho_3(\tau_S)$ and $\rho_4(\tau_S)$, we can evolve ρ_1 and ρ_2

under the same Hamiltonians as $\rho_4(\tau_S)$ and $\rho_3(\tau_S)$ respectively, where ρ_1 is approximately an eigenstate of the Hamiltonian that evolved $\rho_4(\tau_S)$, and ρ_2 is approximately an eigenstate of the Hamiltonian that evolved $\rho_3(\tau_S)$.

A few further improvements were made to the calibration routine to mitigate the low-pass effects of the coaxial lines:

- A voltage overshoot was added to the first 833 ps of the pulse to ε^S for $\rho_3(\tau_3)$ and $\rho_4(\tau_4)$. This makes the pulse shapes closer to the ideal square pulse, which is easier to evaluate in our fitting routine.
- The calibration routine records the evolution of $\rho_3(\tau_3)$ and $\rho_4(\tau_4)$ for $\tau_3, \tau_4 > 4$ ns, which further reduces the effects of transients at the beginning of the pulses.
- The settle point employed directly before measurement is a tradeoff between decoupling the rotation pulses from the measurement pulses, which improves with settle time τ_W , and the dephasing brought on by nuclei, which gets worse with increasing τ_W . The settle time needed increases with the amplitude of the pulse directly before the settle point. In order to keep τ_W to a minimum, ρ_1 is placed at ε^4 for $\tau_1 = 5$ ns, the evolution point for $\rho_4(\tau_4)$, where it is approximately an eigenstate. This prevents the need to pulse all the way from 201 to the settle point, which is a significantly larger amplitude pulse. ρ_2 is similarly placed at ε^3 for $\tau_2 = 5$ ns to reduce the amplitude necessary to bring it to the settle point as well. The time spent at ε^3 and ε^4 is then incorporated into the fitting routine as well, making $\rho_1(\tau_1 = 5\text{ ns})$ and $\rho_2(\tau_2 = 5\text{ ns})$.
- $\rho_1(\tau_1 = 5\text{ ns})$, $\rho_2(\tau_2 = 5\text{ ns})$, ρ_5 are then repeated to give them the same weight in the fitting routine as $\rho_3(\tau_3)$ and $\rho_4(\tau_4)$.

As the last refinement, we allow for small preparation infidelities, which are included as incoherent mixtures of $|T_l\rangle + |Q\rangle$ and $|T_r\rangle + |Q\rangle$ into $\rho_1(\tau_1 = 5\text{ ns})$ and $\rho_2(\tau_2 = 5\text{ ns})$

respectively. This adds two more free parameters.

There are 27 unknowns in this problem: five unique quantities for each of the four measurement operators, two unknown exchange terms at ε^3 and two at ε^4 , one unknown for the standard deviation of the nuclear gradients, and two unknowns for the preparation infidelities. These 27 parameters were optimized over the entire data set, resulting in the best estimate of the POVM elements and the Hamiltonians at the calibration positions.

Once the system is fully characterized, we invert equation (D.17), this time using known E_i 's, to solve for the unknown ρ . This solution is then used to create the MLE output using the techniques described in Ref. [137].

D.5.3 Normalization of Single-Shot Data in Figure 6

Unlike the charge sensor normalization procedure used for the data in Figs. 2-5, which was covered in Sec. D.2, the data in Figure 6 was not normalized by extracting v_{rf}^{201} and v_{rf}^{111} and normalizing the average voltage. Instead, we used a single-shot threshold voltage, v_{rf}^T , which was chosen to separate 201 and 111 outcomes, as was done in Ref. [8]. This allowed us to make a clean comparison to previous single-shot measurements, including the definitions of measurement fidelity. The downside of this method is that it reduces the visibility of the oscillations, which is part of the reason for the reduced amplitude in figure 6. P_i is then defined as the fraction of outcomes whose v_{rf} is on the 201 (for P_1 and P_3) or 102 (for P_2 and P_4) side of v_{rf}^T .

Figure D.4 shows the example data for the calibration routines which determine E_1 - E_4 . The markers are the measurements of the known input states ρ_1 - ρ_5 , while the solid curves are the outputs of the MLE routine that extracts the Hamiltonian parameters and the POVM elements. The calibration for ρ_1 , ρ_2 , and ρ_5 are repeated to provide an equal weighting with ρ_3 and ρ_4 in the MLE routine. The Hamiltonian parameters are: for $\rho_3(\tau_3)$:

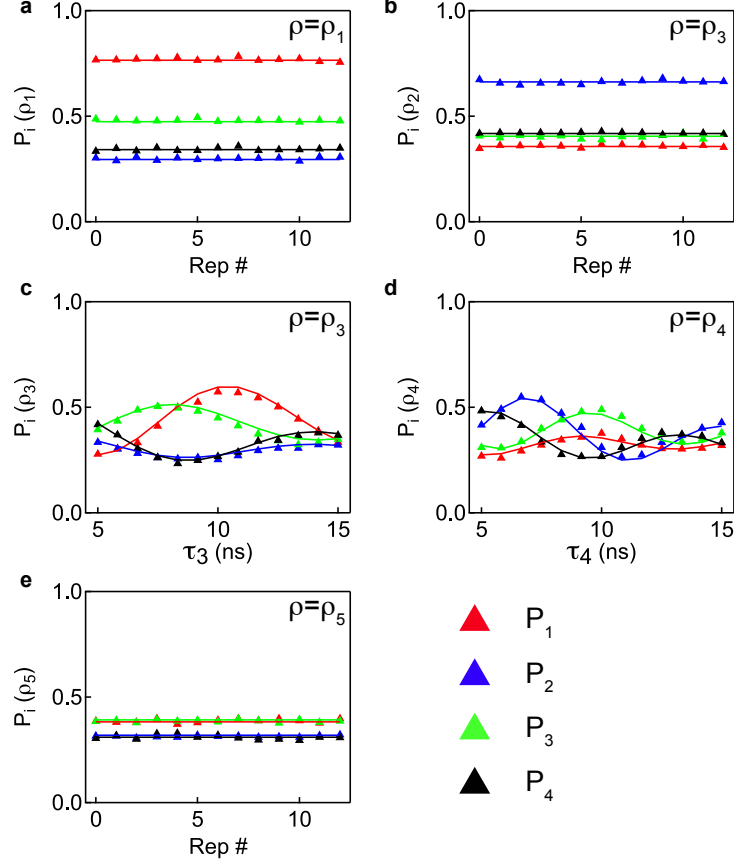


Figure D.4: The calibration curves and their fits. (a) ρ_1 (b) ρ_2 (c) ρ_3 (d) ρ_4 (e) ρ_5

$J_l(\varepsilon^3) = 33 \pm 8$ neV, $J_r(\varepsilon^3) = 380 \pm 4$ neV, for $\rho_4(\tau_4)$: $J_l(\varepsilon^4) = 530 \pm 8$ neV, $J_r(\varepsilon^4) = 4 \pm 10$ neV, $\sigma_B = 2.8 \pm 0.1$ mT. These parameters define four measurement axes, which when inverted yield the data in Figure 6.

D.6 Theory Curves in All Panels of Figure 6

In the presence of sharp (instantaneous) pulses, the theory curve for the $|S_r\rangle$ initial state stays close to the plane that cuts through $|S_r\rangle$ and the origin, perpendicular to J_l . This is because the pulses move rapidly through the center of 111, where J_l and J_r are both active. If that region is traversed slowly, the net rotation pulls the state towards $|S_l\rangle$,

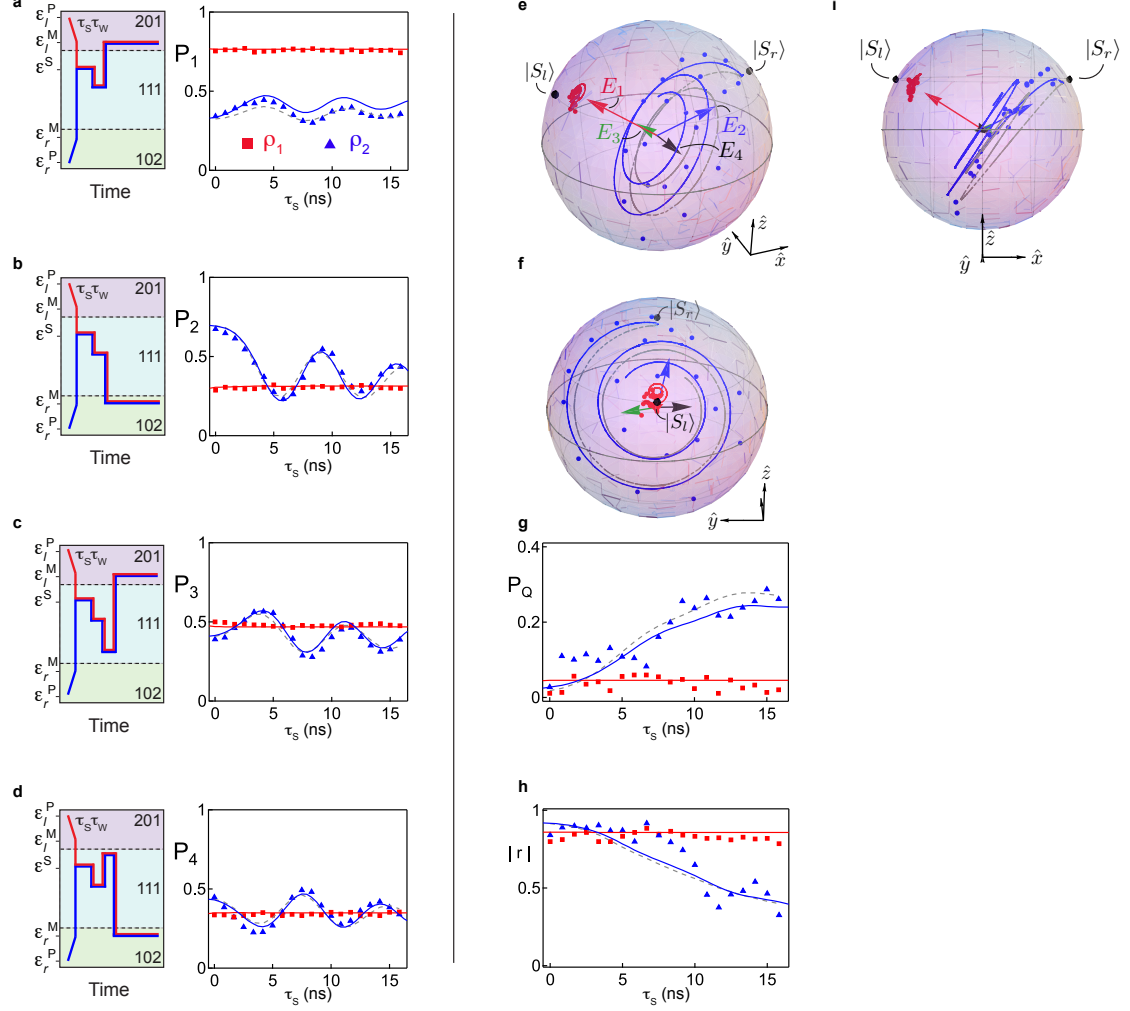


Figure D.5: Same data as Fig. 6 of the main paper, here showing a comparison of models using instantaneous pulses (dashed gray), and bandwidth limited pulses (blue).

with the end result being that subsequent rotations around J_l trace out a larger circle on the Bloch sphere as it approaches a great circle. To correct for this increased circumference, the full bandwidth limited pulse shape is needed.

The theory curves in Fig. 6 of the main paper were generated by solving the Liouville-von Neumann equation, $i\hbar\dot{\rho} = [\mathcal{H}(\varepsilon), \rho]$, where $\mathcal{H}(\varepsilon)$ is a function of the time-dependent pulse detuning, as well as the nuclear gradients, ΔB_l and ΔB_r . J_l and J_r are modeled following Ref. [85], with the modification that the tunnel couplings are themselves

a Gaussian function of the detuning. This modification was necessary to explain the data in Figs. 3 and 6.

$$J_l(t) = \frac{\alpha}{2}[-\varepsilon^C - \varepsilon(t)] + \sqrt{\left\{t \exp\left[-\left(\frac{\varepsilon^C + \varepsilon(t)}{W_t}\right)^2\right]\right\}^2 + \frac{\alpha^2}{4}[\varepsilon^C + \varepsilon(t)]^2} \quad (\text{D.23})$$

$$J_r(t) = \frac{\alpha}{2}[-\varepsilon^C + \varepsilon(t)] + \sqrt{\left\{t \exp\left[-\left(\frac{\varepsilon^C - \varepsilon(t)}{W_t}\right)^2\right]\right\}^2 + \frac{\alpha^2}{4}[\varepsilon^C - \varepsilon(t)]^2} \quad (\text{D.24})$$

Here, the tunnel coupling width $W_t = \varepsilon_0/0.55$ mV, the charge transition detuning $\varepsilon^C = 18$ mV, the lever arm $\alpha = 40 \mu\text{eV}/\text{mV}$, and the tunnel coupling $t = 22 \mu\text{eV}$.

To model the system accurately, the ordinary differential equation (ODE) was solved up to the end of the rotation at ε^S for each value of τ_S . Those solutions were then used as the initial values in a second solution, where the system was pulsed to the settle point for a time τ_W before pulsing the measurement point. The pulses were modeled as the low passed output of the intended piecewise functions,

$$\varepsilon_A(t) = \begin{cases} \varepsilon^0 + (\varepsilon^1 - \varepsilon^0)[1 - \exp(-\frac{t-t_0}{\tau_R})] & \text{if } t_0 \leq t < t_1 \\ \left(\varepsilon^0 + (\varepsilon^1 - \varepsilon^0)[1 - \exp(-\frac{t_1-t_0}{\tau_R})]\right) \exp(-\frac{t-t_1}{\tau_R}) \\ + \varepsilon^2[1 - \exp(-\frac{t-t_1}{\tau_R})] & \text{if } t_1 \leq t < \tau_S, \end{cases} \quad (\text{D.25})$$

where ε^0 is the measurement point, ε^1 is a resting point at large exchange prior to the rotation, and ε^2 is the rotation point ε^S . The time spent at the resting point starts at $t_0 = -2.5$ ns, while the time at the rotation point starts at $t_1 = 0$ ns. The set of pulses used in the second ODE were

$$\varepsilon_B(t) = \begin{cases} \varepsilon_A(\tau_S) \exp(-\frac{t-\tau_S}{\tau_R}) & \text{if } \tau_S \leq t < \tau_S + \tau_W, \end{cases} \quad (\text{D.26})$$

which accounted for the approach to the settle point. After this, the POVM elements take effect, describing the rest of the measurement.

The time evolution is calculated for each configuration of ΔB_l and ΔB_r , and averaged over a Gaussian weighting for each gradient, the standard deviation of which was extracted in the POVM characterization routines described above. No exchange noise was included in this model. The measurement probabilities associated with the averaged solution of the Liouville-von Neumann equation were then extracted using equations (D.17). The population of the $|Q\rangle$ state was extracted as $P_Q = |Q\rangle\langle Q|$. The Bloch sphere vector length is extracted from the qubit subspace of the density matrix as $|\vec{r}| = \sqrt{(\rho_x^*)^2 + (\rho_y^*)^2 + (\rho_z^*)^2}$, where

$$\rho^* = \begin{pmatrix} |0\rangle\langle 0| & |0\rangle\langle 1| \\ |1\rangle\langle 0| & |1\rangle\langle 1| \end{pmatrix} \quad (\text{D.27})$$

is the density matrix of the qubit subspace. Here, $\rho_x^* = \text{Tr}[\rho^*\sigma_x] = 2\text{Re}[|0\rangle\langle 1|]$, $\rho_y^* = \text{Tr}[\rho^*\sigma_y] = -2\text{Im}[|0\rangle\langle 1|]$, and $\rho_z^* = \text{Tr}[\rho^*\sigma_z] = |0\rangle\langle 0| - |1\rangle\langle 1|$.

Appendix E

Supplementary Information for Resonant Microwave Control of a Symmetric Exchange-Only Spin Qubit

E.1 Measurement and Normalization

A single normalization procedure was used for all data in chapter 8 to convert the measured reflectometry signals into output probabilities. It is similar to the normalization procedure described in section D.2, except that the normalize of the T_1 decay does not depend on measuring the overlap between $|S_r\rangle$ and $|S_l\rangle$. A measurement of the overlap $|\langle S_r | S_l \rangle|^2$ requires a diabatic passage through the center of the 111 region. In our current setup, the large gap in the center region forces our state to adiabatically follow the lower branch. Normalization of T_1 is done through a separate independent measurement of T_1 for each figure, as described below.

As in section D.2, the measurements of a given parameter (ε , ω , burst power, etc.) was repeated 2^{13} or 2^{14} times to obtain measurement statistics and then histogrammed, following the procedure in Ref. [8]. The resulting histogram, shown in Fig. D.1, is fit to a

function of the form,

$$n(v_{\text{rf}}) = \frac{P}{\sqrt{2\pi}\sigma^2} \exp\left[-\frac{(v_{\text{rf}} - v_{\text{rf}}^{102})^2}{2\sigma^2}\right] + e^{-\tau_M/T_1} \frac{(1-P)}{\sqrt{2\pi}\sigma^2} \exp\left[-\frac{(v_{\text{rf}} - v_{\text{rf}}^{111})^2}{2\sigma^2}\right] + \int_{v_{\text{rf}}^{102}}^{v_{\text{rf}}^{111}} \frac{dV}{\sqrt{2\pi}\sigma^2} \frac{\tau_M}{T_1} \frac{(1-P)}{\Delta v_{\text{rf}}} \exp\left[-\frac{\tau_M}{T_1} \frac{V - v_{\text{rf}}^{102}}{\Delta v_{\text{rf}}} - \frac{(v_{\text{rf}} - V)^2}{2\sigma^2}\right], \quad (\text{E.1})$$

where $n(v_{\text{rf}})$ is the fraction of histogram events with outcomes v_{rf} for a measurement in 102, v_{rf}^{102} is the reflected voltage corresponding to double occupancy in the right dot, v_{rf}^{111} is the reflected voltage corresponding to single charge occupancy in the all three dots, $\Delta v_{\text{rf}} \equiv v_{\text{rf}}^{111} - v_{\text{rf}}^{102}$, P is the fraction of 102 outcomes in the data set, T_1 is the relaxation time at ε_M , τ_M is the measurement time, and σ is the standard deviation of the histogram peaks due to noise in the rf equipment and shot noise intrinsic to the rf sensor dot.

The extracted parameters v_{rf}^{102} and v_{rf}^{111} are then used to normalize the return probabilities P as

$$P = \frac{\langle v_{\text{rf}} \rangle - v_{\text{rf}}^{111}}{v_{\text{rf}}^{102} - v_{\text{rf}}^{111}}, \quad (\text{E.2})$$

where $\langle v_{\text{rf}} \rangle$ is the average voltage for a particular parameter (ε , ω , burst power, etc.) over all repetitions of the measurement sequence.

Equation (E.2) converts v_{rf} into a probability, but it does not account for relaxation during the measurement time τ_M , where a 111 state relaxes to a 102 state. As described in Ref. [67], P is related to the actual probability P^0 through

$$P^0 = \frac{1}{\tau_M} \int_0^{\tau_M} dt P \exp\left(-\frac{t}{T_1}\right) = P \frac{T_1}{\tau_M} \left[1 - \exp\left(-\frac{\tau_M}{T_1}\right)\right]. \quad (\text{E.3})$$

By knowing τ_M and T_1 , we can correct for measurement relaxation. A measurement of the relaxation time at ε_M is acquired for each section of data in chapter 8, by fitting the average probability as a function of τ_M , as shown in Fig. D.2.

E.2 Model of the exchange interactions

We find that the exchange interactions J_l and J_r are well described by the model laid out in section D.6 as

$$J_l = \frac{\alpha}{2}(-\varepsilon_0 - \varepsilon) + \sqrt{\left\{ t \exp \left[- \left(\frac{\varepsilon_0 + \varepsilon}{W_t \varepsilon_0} \right)^2 \right] \right\}^2 + \frac{\alpha^2}{4}(\varepsilon_0 + \varepsilon)^2} \quad (\text{E.4})$$

$$J_r = \frac{\alpha}{2}(-\varepsilon_0 + \varepsilon) + \sqrt{\left\{ t \exp \left[- \left(\frac{\varepsilon_0 - \varepsilon}{W_t \varepsilon_0} \right)^2 \right] \right\}^2 + \frac{\alpha^2}{4}(\varepsilon_0 - \varepsilon)^2}, \quad (\text{E.5})$$

where α is the lever arm between ε and energy, W_t is a phenomenological suppression of the tunnel coupling with ε , and $\pm\varepsilon_0$ is the detuning of the 111-102 and 111-201 charge transitions, or half the width of the 111 region. We can then write $J_z = -\frac{1}{4}(J_l(\varepsilon) + J_r(\varepsilon))$ as

$$\begin{aligned} J_z = & \frac{1}{4} \left(\alpha \varepsilon_0 - \sqrt{\left\{ t \exp \left[- \left(\frac{\varepsilon_0 + \varepsilon}{W_t \varepsilon_0} \right)^2 \right] \right\}^2 + \frac{\alpha^2}{4}(\varepsilon_0 + \varepsilon)^2} \right. \\ & \left. - \sqrt{\left\{ t \exp \left[- \left(\frac{\varepsilon_0 - \varepsilon}{W_t \varepsilon_0} \right)^2 \right] \right\}^2 + \frac{\alpha^2}{4}(\varepsilon_0 - \varepsilon)^2} \right). \end{aligned} \quad (\text{E.6})$$

At $\varepsilon = 0$, eq (E.6) simplifies to

$$J_z = \alpha \frac{V_m - V_m^0}{8} - \frac{1}{2} \sqrt{\left\{ t \exp \left[- \left(\frac{1}{W_t} \right)^2 \right] \right\}^2 + \frac{\alpha^2}{16}(V_m - V_m^0)^2}, \quad (\text{E.7})$$

where we have replaced ε_0 with $(V_m - V_m^0)/2$. Experimentally, we see that the width of the 111 region, $2\varepsilon_0$, is linear in $V_m - V_m^0$, with the same lever arm as the other gates. Equation (E.7) is used in Fig. 8.2(d) to map the resonance as a function of V_m ¹. In Fig. 8.2(d),

¹In Fig. 8.2(d), the tunnel coupling was simplified back to just t , with no exponential dependence. The physical reason for this is not well understood, but the model clearly fits the data if this is true, and drastically disagrees if the full form is used.

$t = 16.9 \mu\text{eV}$, W_t was taken to be very large, such that the exponential was ignored, V_m^0 was taken to be -4.05 mV on this plot².

The transverse exchange, $J_x = \frac{\sqrt{3}}{4} (J_l(\varepsilon) - J_r(\varepsilon))$, can be written as

$$J_x = -\frac{\sqrt{3}}{4} \left(\alpha\varepsilon - \sqrt{\left\{ t \exp \left[-\left(\frac{\varepsilon_0 + \varepsilon}{W_t \varepsilon_0} \right)^2 \right] \right\}^2 + \frac{\alpha^2}{4} (\varepsilon_0 + \varepsilon)^2} \right. \\ \left. + \sqrt{\left\{ t \exp \left[-\left(\frac{\varepsilon_0 - \varepsilon}{W_t \varepsilon_0} \right)^2 \right] \right\}^2 + \frac{\alpha^2}{4} (\varepsilon_0 - \varepsilon)^2} \right). \quad (\text{E.8})$$

E.3 Model in Figure 8.2(c)

Reference [85] gives the separation between the lower branch of the qubit state, which they refer to as $|\Delta'\rangle$, and the $|Q\rangle$ state as

$$E_{\Delta'Q} = -\frac{1}{2} \left(J_l + J_r + \sqrt{J_l^2 + J_r^2 - J_l J_r} \right), \quad (\text{E.9})$$

which is the lowest eigenvalues of equation (D.13). The separation between $|Q\rangle$ and $|Q_+\rangle$, E_{QQ+} is $g^* \mu B_{\text{ext}}$. In Fig. 8.2(c) we plot the intersection of these two curves, $B_{\text{ext}}(\varepsilon) = B_0 + E_{\Delta'Q}(\varepsilon)/\hbar g^* \mu$, where B_0 is an experimentally determined offset in the field due to remnant fields from ferromagnetic components in the cryostat. We find that an offset of $B_0 = -9.3 \text{ mT}$ and an effective g-factor of $g^* = -0.34$ describe our data well in the center of 111. The tunnel coupling t was $16.9 \mu\text{eV}$, $\varepsilon_0 = 3.7 \text{ mV}$, $\alpha = 40 \mu\text{eV}/\text{mV}$, $W_t = 3$.

E.4 Model and Power Broadening in Figure 8.2(d)

The model in Fig. 8.2(d) is a plot of eq. (E.7), where $\delta = (V_l - V_l^0) + (V_r - V_r^0) + \gamma(V_m - V_m^0)$ was held constant, with an experimentally determined $\gamma = 3$. In Fig. E.1(b), the resonance ω_{01} was extracted along with its width in frequency space by fitting it to a

²An overall background to V_m of -452 mV was already removed, leaving just the amount that was pulsed using the AWG.

Gaussian at each value of V_m . We find in Fig. E.1(d) that the resonance width, shown in Fig. E.1(c), is proportional to $d\omega_{01}/dV_m$, which could suggest that the resonance widens with electrical noise. $d\omega_{01}/dV_m$ is also proportional to $dJ_x/d\varepsilon$, which sets the strength of the Rabi oscillation. From this, we cannot determine whether the resonance is broadened due to fluctuations in V_m , or due to power broadening from an increased $dJ_x/d\varepsilon$.

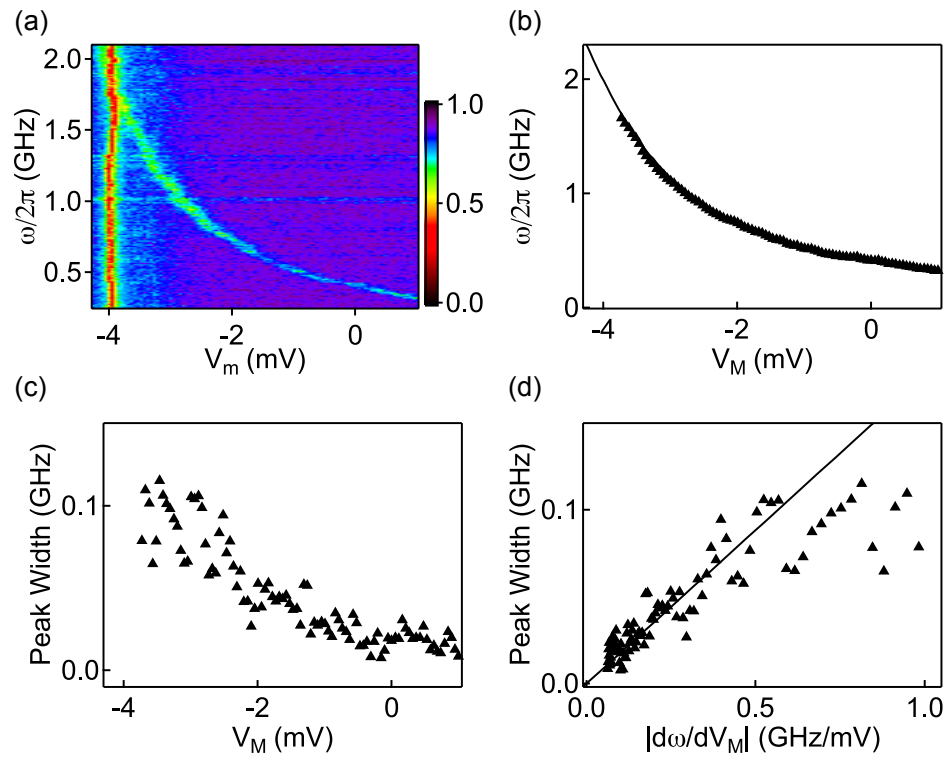


Figure E.1: (a) The data in Fig. 8.2(d) without the theory overlay. (b) The resonance center value extracted from Gaussian fits, along with the plot of eq. (E.7). (c) The widths of the resonance extracted from the Gaussian fits. (d) The widths of the resonance plotted against the analytic derivative of eq. (E.7). The analytic derivative was chosen to remove the noise from the numerical derivative of the data in panel (b).

E.5 Model in Figure 8.2(f)

The model in Figure 8.2(f) used seven of the eight spin states available to the three electron system to reproduce the dynamics of the spectroscopy.

$$|Q_+\rangle \equiv \left|Q_{\frac{3}{2}}\right\rangle_+ = |\uparrow\uparrow\uparrow\rangle \quad (\text{E.10})$$

$$|0\rangle \equiv |0\rangle_+ = \frac{1}{\sqrt{6}} (|\uparrow\uparrow\downarrow\rangle + |\downarrow\uparrow\uparrow\rangle - 2|\uparrow\downarrow\uparrow\rangle) \quad (\text{E.11})$$

$$|1\rangle \equiv |1\rangle_+ = \frac{1}{\sqrt{2}} (|\uparrow\uparrow\downarrow\rangle - |\downarrow\uparrow\uparrow\rangle) \quad (\text{E.12})$$

$$|Q\rangle \equiv |Q\rangle_+ = \frac{1}{\sqrt{3}} (\lvert \uparrow\uparrow\downarrow \rangle + \lvert \downarrow\uparrow\uparrow \rangle + \lvert \uparrow\downarrow\uparrow \rangle) \quad (\text{E.13})$$

$$|0\rangle_- = \frac{1}{\sqrt{6}} (|\downarrow\downarrow\uparrow\rangle + |\uparrow\downarrow\downarrow\rangle - 2|\downarrow\uparrow\downarrow\rangle) \quad (\text{E.14})$$

$$|1\rangle_- = \frac{1}{\sqrt{2}} (|\downarrow\downarrow\uparrow\rangle - |\uparrow\downarrow\downarrow\rangle) \quad (\text{E.15})$$

$$|Q\rangle_- = \frac{1}{\sqrt{3}} (|\downarrow\downarrow\uparrow\rangle + |\uparrow\downarrow\downarrow\rangle + |\downarrow\uparrow\downarrow\rangle) \quad (\text{E.16})$$

The eight level, $|Q_{\frac{3}{2}}\rangle_- = |\downarrow\downarrow\downarrow\rangle$, is separated from all other levels by the external magnetic field, and is therefore ignored in order to speed up computation. The simulation described the qubit evolution in the presence of exchange interactions, longitudinal and transverse nuclei, whose Hamiltonians can be written in the basis of

$$\left\{ \left| Q_{\frac{3}{2}} \right\rangle_+, |0\rangle_+, |1\rangle_+, |Q\rangle_+, |0\rangle_-, |1\rangle_-, |Q\rangle_- \right\} \text{ as:}$$

$$\mathcal{H}_{Bz} = \begin{pmatrix} \frac{b_1+b_2+b_3}{2} & 0 & 0 & 0 & 0 & 0 & 0 \\ 0 & \frac{2b_1-b_2+2b_3}{6} & \frac{b_1-b_3}{2\sqrt{3}} & -\frac{b_1-2b_2+b_3}{3\sqrt{2}} & 0 & 0 & 0 \\ 0 & \frac{b_1-b_3}{2\sqrt{3}} & \frac{b_2}{2} & \frac{b_1-b_3}{\sqrt{6}} & 0 & 0 & 0 \\ 0 & -\frac{b_1-2b_2+b_3}{3\sqrt{2}} & \frac{b_1-b_3}{\sqrt{6}} & \frac{b_1+b_2+b_3}{6} & 0 & 0 & 0 \\ 0 & 0 & 0 & 0 & \frac{-2b_1+b_2-2b_3}{6} & \frac{-b_1+b_3}{2\sqrt{3}} & \frac{b_1-2b_2+b_3}{3\sqrt{2}} \\ 0 & 0 & 0 & 0 & \frac{-b_1+b_3}{2\sqrt{3}} & -\frac{b_2}{2} & \frac{-b_1+b_3}{\sqrt{6}} \\ 0 & 0 & 0 & 0 & \frac{b_1-2b_2+b_3}{3\sqrt{2}} & \frac{-b_1+b_3}{\sqrt{6}} & \frac{-b_1-2b_2-b_3}{6} \end{pmatrix}, \quad (\text{E.18})$$

$$\mathcal{H}_{Bx} = \begin{pmatrix} 0 & \frac{b_1-2b_2+b_3}{2\sqrt{6}} & \frac{-b_1+b_3}{2\sqrt{2}} & \frac{b_1+b_2+b_3}{2\sqrt{3}} & 0 & 0 & 0 \\ \frac{b_1-2b_2+b_3}{2\sqrt{6}} & 0 & 0 & 0 & \frac{-2b_1+b_2-2b_3}{6} & \frac{-b_1+b_3}{2\sqrt{3}} & \frac{b_1-2b_2+b_3}{6\sqrt{2}} \\ \frac{-b_1+b_3}{2\sqrt{2}} & 0 & 0 & 0 & \frac{-b_1+b_3}{2\sqrt{3}} & -\frac{b_2}{2} & \frac{b_1-b_3}{2\sqrt{6}} \\ \frac{b_1+b_2+b_3}{2\sqrt{3}} & 0 & 0 & 0 & \frac{-b_1-2b_2+b_3}{6\sqrt{2}} & \frac{b_1-b_3}{2\sqrt{6}} & \frac{b_1+b_2+b_3}{3} \\ 0 & \frac{-2b_1+b_2-2b_3}{6} & \frac{-b_1+b_3}{2\sqrt{3}} & \frac{-b_1-2b_2+b_3}{6\sqrt{2}} & 0 & 0 & 0 \\ 0 & \frac{-b_1+b_3}{2\sqrt{3}} & -\frac{b_2}{2} & \frac{b_1-b_3}{2\sqrt{6}} & 0 & 0 & 0 \\ 0 & \frac{-b_1-2b_2+b_3}{6\sqrt{2}} & \frac{b_1-b_3}{2\sqrt{6}} & \frac{b_1+b_2+b_3}{3} & 0 & 0 & 0 \end{pmatrix}, \quad (\text{E.19})$$

and $\mathcal{H}_{By} =$

$$\begin{pmatrix} 0 & -\frac{i(b_1-2b_2+b_3)}{2\sqrt{6}} & \frac{i(b_1-b_3)}{2\sqrt{2}} & -\frac{i(b_1+b_2+b_3)}{2\sqrt{3}} & 0 & 0 & 0 \\ \frac{i(b_1-2b_2+b_3)}{2\sqrt{6}} & 0 & 0 & 0 & \frac{i(2b_1-b_2+2b_3)}{6} & \frac{i(b_1-b_3)}{2\sqrt{3}} & \frac{i(b_1-2b_2+b_3)}{6\sqrt{2}} \\ -\frac{i(b_1-b_3)}{2\sqrt{2}} & 0 & 0 & 0 & \frac{i(b_1-b_3)}{2\sqrt{3}} & \frac{ib_2}{2} & -\frac{i(b_1-b_3)}{2\sqrt{6}} \\ \frac{i(b_1+b_2+b_3)}{2\sqrt{3}} & 0 & 0 & 0 & \frac{i(b_1-2b_2+b_3)}{6\sqrt{2}} & -\frac{i(b_1-b_3)}{2\sqrt{6}} & -\frac{i(b_1+b_2+b_3)}{3} \\ 0 & -\frac{i(2b_1-b_2+2b_3)}{6} & -\frac{i(b_1-b_3)}{2\sqrt{3}} & -\frac{i(b_1-2b_2+b_3)}{6\sqrt{2}} & 0 & 0 & 0 \\ 0 & -\frac{i(b_1-b_3)}{2\sqrt{3}} & -\frac{ib_2}{2} & \frac{i(b_1-b_3)}{2\sqrt{6}} & 0 & 0 & 0 \\ 0 & -\frac{i(b_1-2b_2+b_3)}{6\sqrt{2}} & \frac{i(b_1-b_3)}{2\sqrt{6}} & \frac{i(b_1+b_2+b_3)}{3} & 0 & 0 & 0 \end{pmatrix}. \quad (\text{E.20})$$

The magnetic field terms b_i in equations (E.19), (E.20), and (E.18) are the magnetic fields in dot i , where $i = 1$ corresponds to the left, along the direction listed in the Hamiltonian, ie the \hat{z} direction for eq. (E.18). The exchange terms J_l and J_r in eq. (E.17) are the ε -dependent terms from eqs. (E.4) and (E.5).

The model was created in the following way. At a given ε and ω , nine random variables were drawn from a normal distribution to take the nine nuclear field components, B_x , B_y , and B_z in each of the three dots. From there, eigenstates of the full Hamiltonian, $\mathcal{H} = \mathcal{H}_J + \mathcal{H}_{Bx} + \mathcal{H}_{By} + \mathcal{H}_{Bz}$, were calculated, and an initial state density matrix was chosen as a mixture of 90% of the eigenstate with the largest overlap with $|0\rangle_+$, and 5% of the eigenstates with the largest overlaps with $|1\rangle_+$ and $|Q\rangle_+$. The initial state was then

time evolved according to the Louisville-von Neumann equation,

$$i\hbar \frac{d\rho}{dt} = [\mathcal{H}, \rho], \quad (\text{E.21})$$

for 300 ns in the presence of an oscillatory ε . The final density matrix was then transformed into eigenstates of only the exchange interactions and the external magnetic field, and the population of the lower qubit eigenstate was recorded³. This process is then repeated 25 times with new random values for all of the nuclear fields, and the average return probability is recorded in the model⁴.

In the model, the amplitude was a 0.225 mV oscillation in detuning, equivalent to a 0.45 mV oscillation in V_l , or -51 dBm. The standard deviation of nuclear gradients was 3.9 mT with a $g^* = -0.34$. The tunnel coupling t was $16.9 \mu\text{eV}$, $\varepsilon_0 = 3.7 \text{ mV}$, $\alpha = 40 \mu\text{eV}/\text{mV}$, $W_t = 3$.

The simulation used seven levels to enable us to check if whether we loaded in states with $|0\rangle_-$, $|1\rangle_-$, and $|Q\rangle_-$ components. Figure E.2(a) shows a close up of the region near the $|Q_{\frac{3}{2}}\rangle_+$ anti-crossing from Fig. 8.2(f). Panel (b) shows that same region with a mixture of $|0\rangle_-$, $|1\rangle_-$, and $|Q\rangle_-$ components also loaded into the initial state, approximating the density matrix in the case that we load into the other Zeeman manifold approximately half the time. The presence of these extra states causes a doubling of the transition lines near this anti-crossing, a phenomenon that we do not see reproduced in the data. From this we determine that we are only loading in the $|0\rangle_+$, $|1\rangle_+$, and $|Q\rangle_+$ states, which is consistent with the fact that our initialization procedure does not involve relaxation via the leads in

³The eigenstates of the Hamiltonian with the nuclei were used for the initialization because the slow ramp in to this state allows the system to adiabatically enter the anti-crossing with $|Q_{\frac{3}{2}}\rangle_+$. The pulse to measurement position is a much more rapid, meaning that the qubit left that region diabatically. The difference in eigenstates allows us to capture this effect reasonably well without considering the full time dynamics of the problem.

⁴In order to speed up computation, the repetitions were truncated at 5 samples if the average return probability was $> 86\%$. This saw a drastic improvement in speed with little qualitative change to the plots.

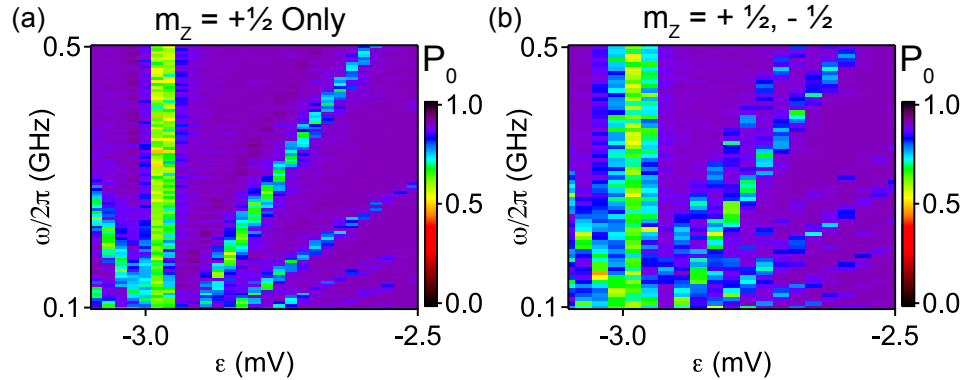


Figure E.2: (a) A seven level simulation where the initial states were a mixture of $|0\rangle_+$, $|1\rangle_+$, and $|Q\rangle_+$. (b) A seven level simulation where the initial states were a mixture of $|0\rangle_+$, $|1\rangle_+$, $|Q\rangle_+$, $|0\rangle_-$, $|1\rangle_-$, and $|Q\rangle_-$. Panel (b) was sampled more sparsely because it was a test run of the larger initialization space. Since it did not accurately represent the data, it did not receive a follow up calculation at higher sampling, as panel (a) did.

this work.

E.6 Model in Figure 8.3 insets

Having shown in section E.5 that we are only in the space of $|0\rangle$, $|1\rangle$, and $|Q\rangle$ states, we now restrict ourselves to only the 3×3 Hamiltonians of equations (D.13) and (D.14), which is valid when we are far away from the $|Q_+\rangle$ anti-crossings as we are in Fig. 8.3. For the insets, we create an initialization state that is 90% $|0\rangle$, and 10% $|1\rangle$ and $|Q\rangle$, and time evolve it using equation (E.21) for 100 ns in the presence of an oscillatory ε and static longitudinal nuclear field gradients ΔB_l and ΔB_r . The $|0\rangle\langle 0|$ term is extracted at multiple times during the evolution, and recorded. This process is repeated with a new set of ΔB_l and ΔB_r drawn from a random normal distribution, and averaged with the previous set. Unlike the simulation in 8.2(f), the nuclei are presumed to be static over the course of a single column, which provides the flickering effect seen in the model and the data. The data was acquired more rapidly in this set, justifying the modification to the model.

In the model in Fig. 8.3(a), the amplitude was a 0.45 mV oscillation in detuning,

equivalent to a 0.89 mV oscillation in V_l , or -45 dBm. The standard deviation of nuclear gradients was 3.9 mT with a $g^* = -0.34$. The tunnel coupling t was $16.9 \mu\text{eV}$, $\varepsilon_0 = 3.7 \text{ mV}$, $\alpha = 40 \mu\text{eV}/\text{mV}$, $W_t = 3$.

E.7 Model in Figure 8.4

The theory curves in Fig. 8.4 are based on a similar model to the insets in Fig. 8.3, with the complication that we perform a second time evolution which takes the final state of the first evolution as its input. In the second time evolution, the ε oscillation at a phase Φ with respect to the oscillation in the first time evolution. The preparation was 90% $|0\rangle$ and 10% $|1\rangle$ and $|Q\rangle$.

In the model curves in Fig. 8.4(b), the amplitude was a 0.30 mV oscillation in detuning, equivalent to a 0.60 mV oscillation in V_l , or ~ -55 dBm. The standard deviation of nuclear gradients was 5.2 mT with a $g^* = -0.34$. The tunnel coupling t was $12.4 \mu\text{eV}$, $\varepsilon_0 = 3.7 \text{ mV}$, $\alpha = 40 \mu\text{eV}/\text{mV}$, $W_t = 3$.

Appendix F

Dipole Moment of the Symmetric Exchange Only Qubit

F.1 Static Dipole Moment of a Bloch Sphere State

The dipole moment of the symmetric exchange only qubit may be useful for coupling two qubits through an ac capacitive interaction. In order to estimate the strength of the dipole moment, we want to make the charge nature of each qubit state explicit. The basis states of this qubit are:

$$|0\rangle = \frac{1}{\sqrt{6}} (|\uparrow\uparrow\downarrow\rangle + |\downarrow\uparrow\uparrow\rangle - 2|\uparrow\downarrow\uparrow\rangle) \quad (\text{F.1})$$

$$|1\rangle = \frac{1}{\sqrt{2}} (|\uparrow\uparrow\downarrow\rangle - |\downarrow\uparrow\uparrow\rangle). \quad (\text{F.2})$$

which we would like to express in terms of the states related to different charge distributions,

$$|S_l\rangle = \frac{1}{\sqrt{2}} (|\uparrow\downarrow\uparrow\rangle - |\downarrow\uparrow\uparrow\rangle) \quad (\text{F.3})$$

$$|S_r\rangle = \frac{1}{\sqrt{2}} (|\uparrow\uparrow\downarrow\rangle - |\uparrow\downarrow\uparrow\rangle), \quad (\text{F.4})$$

which we recognize are non-orthogonal; $\langle S_l | S_r \rangle = -\frac{1}{2}$. The state $|S_l\rangle$ has an admixture of 201 charge in it, while the state $|S_r\rangle$ has an admixture of 102 charge in it. Both states are primarily 111 in charge nature. We project a state onto this non-orthogonal basis as¹

$$|\psi\rangle = \frac{(\langle S_l | \psi \rangle - \langle S_l | S_r \rangle \langle S_r | \psi \rangle) |S_l\rangle + (\langle S_r | \psi \rangle - \langle S_l | S_r \rangle \langle S_l | \psi \rangle) |S_r\rangle}{1 - |\langle S_l | S_r \rangle|^2}. \quad (\text{F.5})$$

¹A special thanks to Emmanuel Rashba for correcting the form of this in a private communication.

Writing an arbitrary qubit state $|\psi\rangle$ in terms of the Bloch sphere angles (θ, ϕ) in Fig. 2.1

$$|\psi\rangle = \cos\left(\frac{\theta}{2}\right)|0\rangle + e^{i\phi}\sin\left(\frac{\theta}{2}\right)|1\rangle, \quad (\text{F.6})$$

we can re-express this as:

$$|\psi\rangle = \left[-\frac{\cos\left(\frac{\theta}{2}\right)}{\sqrt{3}} + e^{i\phi}\sin\left(\frac{\theta}{2}\right)\right]|S_l\rangle + \left[\frac{\cos\left(\frac{\theta}{2}\right)}{\sqrt{3}} + e^{i\phi}\sin\left(\frac{\theta}{2}\right)\right]|S_r\rangle. \quad (\text{F.7})$$

Now we are interested in calculating the *static* charge dipole moment, which we will define as $\hat{P} = e\langle\psi|\hat{x}|\psi\rangle$, where the dipole oscillates along the dot connection axis, e is the electron charge and x is the position along the dot connection axis with the average position in the center of the 111 region defined as $x = 0$. In order to evaluate this, we note that:

$$\langle S_l | \hat{x} | S_l \rangle = x_- \quad (\text{F.8})$$

$$\langle S_r | \hat{x} | S_r \rangle = x_+ \quad (\text{F.9})$$

$$\langle S_l | \hat{x} | S_r \rangle = 0 \quad (\text{F.10})$$

$$\langle S_r | \hat{x} | S_l \rangle = 0, \quad (\text{F.11})$$

where x_- is the average position of a $|S_l\rangle$ state and x_+ is the average position of a $|S_r\rangle$ state. To determine x_+ and x_- , we adopt the adiabatic formalism from the double dot literature [141] and say that

$$|S_r\rangle = \cos(\gamma_r)|S_{111,r}\rangle + \sin(\gamma_r)|S_{102,r}\rangle \quad (\text{F.12})$$

$$|S_l\rangle = \cos(\gamma_l)|S_{111,l}\rangle + \sin(\gamma_l)|S_{102,l}\rangle, \quad (\text{F.13})$$

where γ_l and γ_r are the adiabatic angles associated with the left and right charge transitions

respectively. We write these adiabatic angles as

$$\gamma_l = \tan^{-1} \left(\frac{2t_l}{(-\varepsilon - \varepsilon_l) - \sqrt{4t_l^2 + (\varepsilon + \varepsilon_l)^2}} \right) \quad (\text{F.14})$$

$$\gamma_r = \tan^{-1} \left(\frac{2t_r}{(\varepsilon - \varepsilon_r) - \sqrt{4t_l^2 + (\varepsilon - \varepsilon_r)^2}} \right), \quad (\text{F.15})$$

where $t_{l(r)}$ is the left (right) tunnel coupling and $\varepsilon_{l(r)}$ is the detuning of the left (right) charge transition. We can then say that $x_+ = \sin(\gamma_r)^2 x_0$ while $x_- = -\sin(\gamma_l)^2 x_0$, assuming that the center of the left and right dot distributions are $\pm x_0$ away from $x = 0$. In a completely symmetric device, $\varepsilon_l = \varepsilon_r = \varepsilon_0$, $t_l = t_r = t$, and $\gamma_l = \gamma_r$ at the center of the 111 region ($\varepsilon = 0$). In this case, we can write

$$\sin^2(\gamma) = \frac{1}{2} \left(1 - \frac{\varepsilon_0}{\sqrt{4t^2 + \varepsilon_0^2}} \right). \quad (\text{F.16})$$

It is worth noting here that $\sin^2(\gamma) = \frac{dJ_r}{d\varepsilon}|_{\varepsilon=0} = -\frac{dJ_l}{d\varepsilon}|_{\varepsilon=0}$.

With this we can evaluate the dipole element for an arbitrary state $|\psi\rangle = \alpha|S_l\rangle + \beta|S_r\rangle$ as

$$\begin{aligned} \hat{P} &= e\langle\psi|\hat{x}|\psi\rangle \\ \hat{P} &= e(\alpha^*\langle S_l | + \beta^*\langle S_r |)\hat{x}(\alpha|S_l\rangle + \beta|S_r\rangle) \\ \hat{P} &= e x_0 \sin^2(\gamma) (|\beta|^2 - |\alpha|^2). \end{aligned} \quad (\text{F.17})$$

Reverting to the logical basis again, we write $|\psi\rangle = \cos\left(\frac{\theta}{2}\right)|0\rangle + e^{i\phi}\sin\left(\frac{\theta}{2}\right)|1\rangle$, and

$$\hat{P} = \frac{2e x_0 \sin^2(\gamma) \sin(\theta)}{\sqrt{3}} \cos(\phi) \quad (\text{F.18})$$

$$\hat{P} = \frac{e x_0 \sin(\theta)}{\sqrt{3}} \left(1 - \frac{\varepsilon_0}{\sqrt{4t^2 + \varepsilon_0^2}} \right) \cos(\phi_0 + \omega_{01}t), \quad (\text{F.19})$$

where ω_{01} is the resonant frequency of the qubit.² If the qubit is not driven, the system evolves according to $\phi = \phi_0 + \omega_{01}t$, where ϕ_0 is the initial phase of the qubit, which is

²This result agrees with a separate calculation E. I. Rashba performed, detailed in a private memo, to within a numerical pre-factor.

equivalent to the precession of a free spin in an external magnetic field. Here, $\omega_{01}/2\pi = J_l + J_r$. This makes the electric field that qubit A radiates a constant term in the rotating frame of qubit B, if both qubits are brought into resonance.

For comparison, in our previous device, $\varepsilon_0 \sim 200 \mu\text{eV}$ while $t \sim 20 \mu\text{eV}$, yielding a prefactor of $1 - \frac{\varepsilon_0}{\sqrt{4t^2 + \varepsilon_0^2}} \sim 0.01$ in the regime where $\omega_{01}/2\pi = 0.355 \text{ GHz}$, and the 111 region is $\sim 10 \text{ mV}$ wide. In this regime, we observed a Rabi oscillation frequency of 70 MHz/mV . The average position of the oscillating charge, x_0 is a little harder to put a number on. It has to be larger than the width of the middle dot, $\sim 190 \text{ nm}$, and less than the distance between the centers of the lithographical left and right dots, $\sim 380 \text{ nm}$. For an $x_0 = 285 \text{ nm}$, halfway between the minimum and maximum value, we find a maximum $\hat{P} \sim 16 ea_0$, where a_0 is the Bohr radius. The maximum dipole moment that we could have observed with an interdot distance of 285 nm would have been $\sim 6000 ea_0$, in the limit that the full charge was allowed to move between dots.

F.2 Dipole Transition Matrix Element

We are also interested in potentially coupling this system to a superconducting cavity, as in Ref. [90]. This coupling depends on the dipole transition element between $|0\rangle$ and $|1\rangle$, $\langle 1|e\hat{x}|0\rangle$. We can estimate this element using the same set of assumptions as in the previous section as

$$|0\rangle = \frac{|S_r\rangle - |S_l\rangle}{\sqrt{3}} \quad (\text{F.20})$$

$$|1\rangle = |S_r\rangle + |S_l\rangle \quad (\text{F.21})$$

$$\langle 1|e\hat{x}|0\rangle = \frac{e}{\sqrt{3}} (\langle S_r | \hat{x} | S_r \rangle - \langle S_l | \hat{x} | S_l \rangle) \quad (\text{F.22})$$

$$\langle 1|e\hat{x}|0\rangle = \frac{2ex_0 \sin^2(\gamma)}{\sqrt{3}} \quad (\text{F.23})$$

The dipole transition matrix element then scales with tunnel coupling as

$$\langle 1 | e \hat{x} | 0 \rangle = \frac{ex_0}{\sqrt{3}} \left(1 - \frac{\varepsilon_0}{\sqrt{4t^2 + \varepsilon_0^2}} \right) \quad (\text{F.24})$$

Bibliography

- [1] A. Ajoy, G. A. Álvarez, and D. Suter. Optimal pulse spacing for dynamical decoupling in the presence of a purely dephasing spin bath. *Phys. Rev. A*, 83(3):032303, 2011. [66]
- [2] G. A. Álvarez and D. Suter. Measuring the spectrum of colored noise by dynamical decoupling. *Phys. Rev. Lett.*, 107:230501, Nov 2011. [66, 72]
- [3] S. Amasha, K. MacLean, I. P. Radu, D. M. Zumbühl, M. A. Kastner, M. P. Hanson, and A. C. Gossard. Electrical control of spin relaxation in a quantum dot. *Phys. Rev. Lett.*, 100(4):46803, 2008. [53, 55]
- [4] C. Barthel. *Control and fast Measurement of Spin Qubits*. PhD thesis, Harvard University Cambridge, Massachusetts, 2010. [15, 16, 122]
- [5] C. Barthel, M. Kjærgaard, J. Medford, M. Stopa, C. M. Marcus, M. P. Hanson, and A. C. Gossard. Fast sensing of double-dot charge arrangement and spin state with a radio-frequency sensor quantum dot. *Phys. Rev. B*, 81(16):161308(R), 2010. [17, 34, 55, 57, 58, 68, 96, 98, 126]
- [6] C. Barthel, J. Medford, H. Bluhm, A. Yacoby, C. M. Marcus, M. P. Hanson, and A. C. Gossard. Relaxation and readout visibility of a singlet-triplet qubit in an overhauser field gradient. *Phys. Rev. B*, 85:035306, 2010. [31]
- [7] C. Barthel, J. Medford, C. M. Marcus, M. P. Hanson, and A. C. Gossard. Interlaced dynamical decoupling and coherent operation of a singlet-triplet qubit. *Phys. Rev. Lett.*, 105:266808, 2010. [54, 66, 69, 95]

- [8] C. Barthel, D. J. Reilly, C. M. Marcus, M. P. Hanson, and A. C. Gossard. Rapid single-shot measurement of a singlet-triplet qubit. *Phys. Rev. Lett.*, 103:160503, 2009. [22, 32, 33, 36, 38, 44, 47, 50, 55, 57, 58, 60, 62, 68, 87, 134, 148, 153]
- [9] M. J. Biercuk and H. Bluhm. Phenomenological study of decoherence in solid-state spin qubits due to nuclear spin diffusion. *Phys. Rev. B*, 83(23):235316, Jun 2011. [66, 72]
- [10] M. J. Biercuk, A. C. Doherty, and H. Uys. Dynamical decoupling sequence construction as a filter-design problem. *J. Phys. B: At. Mol. Opt. Phys.*, 44(15):154002, 2011. [66, 95]
- [11] M. J. Biercuk, H. Uys, A. P. VanDevender, N. Shiga, W. M. Itano, and J. J. Bollinger. Experimental uhrig dynamical decoupling using trapped ions. *Phys. Rev. A*, 79(6):062324, 2009. [95]
- [12] M. J. Biercuk, H. Uys, A. P. VanDevender, N. Shiga, W. M. Itano, and J. J. Bollinger. Optimized dynamical decoupling in a model quantum memory. *Nature*, 458:996, 2009. [55, 66]
- [13] F. Bloch. Nuclear induction. *Phys. Rev.*, 70:460–474, Oct 1946. [7]
- [14] H. Bluhm, S. Foletti, D. Mahalu, V. Umansky, and A. Yacoby. Enhancing the coherence of a spin qubit by operating it as a feedback loop that controls its nuclear spin bath. *Phys. Rev. Lett.*, 105:216803, 2010. [22, 55, 57, 58, 63, 95, 104]
- [15] H. Bluhm, S. Foletti, D. Mahalu, V. Umansky, and A. Yacoby. Enhancing the coherence of a spin qubit by operating it as a feedback loop that controls its nuclear spin bath. *Phys. Rev. Lett.*, 105:216803, Nov 2010. [27, 95]

- [16] H. Bluhm, S. Foletti, I. Neder, M. Rudner, D. Mahalu, V. Umansky, and A. Yacoby. Dephasing time of gaas electron-spin qubits coupled to a nuclear bath exceeding 200 μ s. *Nature Phys.*, 7(2):109–113, 2010. [22, 28, 66, 85]
- [17] H. Bluhm, S. Foletti, I. Neder, M. Rudner, D. Mahalu, V. Umansky, and A. Yacoby. Long coherence of electron spins coupled to a nuclear spin bath. *Nature Phys.*, 7:109, 2011. [102]
- [18] A. S. Bracker, E. A. Stinaff, D. Gammon, M. E. Ware, J. G. Tischler, A. Shabaev, A. L. Efros, D. Park, D. Gershoni, V. L. Korenev, and I. A. Merkulov. Optical pumping of the electronic and nuclear spin of single charge-tunable quantum dots. *Phys. Rev. Lett.*, 94(4):47402, 2005. [27]
- [19] G. Brida, L. Ciavarella, I. P. Degiovanni, M. Genovese, L. Lolli, M. G. Mingolla, F. Piacentini, M. Rajteri, E. Taralli, and M. G. A. Paris. Quantum characterization of superconducting photon counters. *New J. Phys.*, 14(8):085001, 2012. [78]
- [20] A. L. Buchachenko and V. L. Berdinsky. Electron spin catalysis. *Chem. Rev.*, 102(3):603–612, 2002. [78]
- [21] C. Buizert, F. H. L. Koppens, M. Pioro-Ladrière, H.-P. Tranitz, I. T. Vink, S. Tarucha, W. Wegscheider, and L. M. K. Vandersypen. *insitu* reduction of charge noise in GaAs/ al_xga_{1-x} As schottky-gated devices. *Phys. Rev. Lett.*, 101:226603, Nov 2008. [17]
- [22] J. Bylander, S. Gustavsson, F. Yan, F. Yoshihara, K. Harrabi, G. Fitch, D. G. Cory, Y. Nakamura, J.-S. Tsai, and W. D. Oliver. Dynamical decoupling and noise spectroscopy with a superconducting flux qubit. *Nature Phys.*, 7:565, 2011. [66, 72, 95]

- [23] H. Y. Carr and E. M. Purcell. Effects of diffusion on free precession in nuclear magnetic resonance experiments. *Phys. Rev.*, 94:640, 1954. [55, 58]
- [24] V. Cerletti, W. A. Coish, O. Gywat, and D. Loss. Recipes for spin-based quantum computing. *Nanotechnology*, 16(4):R27, 2005. [27]
- [25] E. A. Chekhovich, A. B. Krysa, M. S. Skolnick, and A. I. Tartakovskii. Direct measurement of the hole-nuclear spin interaction in single InP/GaInP quantum dots using photoluminescence spectroscopy. *Phys. Rev. Lett.*, 106:027402, Jan 2011. [20]
- [26] I. Chiorescu, Y. Nakamura, C. J. P. M. Harmans, and J. E. Mooij. Coherent quantum dynamics of a superconducting flux qubit. *Science*, 299(5614):1869–1871, 2003. [1, 78]
- [27] L. Chirolli and G. Burkard. Decoherence in solid-state qubits. *Adv. Phys.*, 57(3):225–285, 2008. [32]
- [28] H. O. H. Churchill. *Quantum Dots in Gated Nanowires and Nanotubes*. PhD thesis, Harvard University Cambridge, Massachusetts, 2012. [132]
- [29] M. Ciorga, A. S. Sachrajda, P. Hawrylak, C. Gould, P. Zawadzki, S. Jullian, Y. Feng, and Z. Wasilewski. Addition spectrum of a lateral dot from coulomb and spin-blockade spectroscopy. *Phys. Rev. B*, 61:R16315–R16318, Jun 2000. [14]
- [30] J. I. Cirac and P. Zoller. Quantum computations with cold trapped ions. *Phys. Rev. Lett.*, 74:4091–4094, May 1995. [1]
- [31] C. Cohen-Tannoudji, B. Diu, and F. Laloë. *Quantum Mechanics Volumes 1 and 2*. Hermann, 1977. [9]

- [32] W. A. Coish and D. Loss. Singlet-triplet decoherence due to nuclear spins in a double quantum dot. *Phys. Rev. B*, 72:125337, 2005. [36]
- [33] D. G. Cory, A. F. Fahmy, and T. F. Havel. Ensemble quantum computing by nmr spectroscopy. *Proc. Nat. Acad. Sci.*, 94(5):1634–1639, 1997. [1]
- [34] D. G. Cory, A. F. Fahmyz, and T. F. Havelz. An experimentally accessible paradigm for quantum computing. In *Proceedings of the Fourth Workshop on Physics and Computation*. New England Complex Systems Institute, Citeseer, 1996. [1]
- [35] D. G. Cory, M. D. Price, and T. F. Havel. Nuclear magnetic resonance spectroscopy: an experimentally accessible paradigm for quantum computing. *Physica D: Nonlinear Phenomena*, 120(1):82–101, 1998. [1]
- [36] L. Cywiński, R. M. Lutchyn, C. P. Nave, and S. Das Sarma. How to enhance dephasing time in superconducting qubits. *Phys. Rev. B*, 77:174509, 2008. [13, 66, 69, 70, 72, 74, 75, 83, 84, 102]
- [37] L. Cywiński, W. M. Witzel, and S. Das Sarma. Pure quantum dephasing of a solid-state electron spin qubit in a large nuclear spin bath coupled by long-range hyperfine-mediated interaction. *Phys. Rev. B*, 79:245314, 2009. [66]
- [38] J. H. Davies. *The physics of low-dimensional semiconductors: an introduction*. Cambridge university press, 1997. [14, 15, 20, 21]
- [39] G. de Lange, Z. H. Wang, D. Ristè, V. V. Dobrovitski, and R. Hanson. Universal dynamical decoupling of a single solid-state spin from a spin bath. *Science*, 330:60, 2010. [66, 72]
- [40] R. de Sousa. Electron spin as a spectrometer of nuclear-spin noise and other fluctuations. *Top. Appl. Phys.*, 115:183, 2009. [32, 66, 69]

- [41] O. E. Dial, M. D. Shulman, S. P. Harvey, H. Bluhm, V. Umansky, and A. Yacoby. Electrometry using coherent exchange oscillations in a singlet-triplet-qubit. *arXiv preprint arXiv:1208.2023*, 2012. [26, 95, 103]
- [42] D. P. DiVincenzo, D. Bacon, J. Kempe, K. B. Whaley, and G. Burkard. Universal quantum computation with the exchange interaction. *Nature*, 408(6810):339–342, 2000. [29, 78, 92, 95]
- [43] V. V. Dobrovitski, A. E. Feiguin, R. Hanson, and D. D. Awschalom. Decay of rabi oscillations by dipolar-coupled dynamical spin environments. *Phys. Rev. Lett.*, 102:237601, 2009. [72]
- [44] T. J. Drummond, W. T. Masselink, and H. Morkoc. Modulation-doped gaas/(al, ga) as heterojunction field-effect transistors: Modfets. *Proceedings of the IEEE*, 74(6):773–822, 1986. [14]
- [45] A. I. Ekimov and A. A. Onushchenko. Quantum size effect in three-dimensional microscopic semiconductor crystals. *JEPT Letters*, 34:345, September 1981. [18]
- [46] J. M. Elzerman, R. Hanson, L. H. Willems van Bereven, B. Witkamp, L. M. K. Vandersypen, and L. P. Kouwenhoven. Single-shot read-out of an individual electron spin in a quantum dot. *Nature*, 430:431, 2004. [24, 55]
- [47] S. Foletti, H. Bluhm, D. Mahalu, V. Umansky, and A. Yacoby. Universal quantum control of two-electron spin quantum bits using dynamic nuclear polarization. *Nature Phys.*, 5:903, 2009. [22, 28, 32, 35, 36, 39, 49, 53, 55, 62, 78]
- [48] T. Fujisawa, T. H. Oosterkamp, W. G. van der Wiel, B. W. Broer, R. Aguado, S. Tarucha, and L. P. Kouwenhoven. Spontaneous emission spectrum in double quantum dot devices. *Science*, 282(5390):932–935, 1998. [23, 41, 46, 48, 49]

- [49] L. Gaudreau, G. Granger, A. Kam, G. C. Aers, S. A. Studenikin, P. Zawadzki, M. Pioro-Ladrière, Z. R. Wasilewski, and A. S. Sachrajda. Coherent control of three-spin states in a triple quantum dot. *Nature Phys.*, 8(1):54–58, 2011. [29, 78, 80, 95]
- [50] L. Gaudreau, A. Kam, G. Granger, S. A. Studenikin, P. Zawadzki, and A. S. Sachrajda. A tunable few electron triple quantum dot. *Appl. Phys. Lett.*, 95(19):193101–193101–3, nov 2009. [95]
- [51] L. Gaudreau, S. A. Studenikin, A. S. Sachrajda, P. Zawadzki, A. Kam, J. Lapointe, M. Korkusinski, and P. Hawrylak. Stability diagram of a few-electron triple dot. *Phys. Rev. Lett.*, 97:036807, Jul 2006. [95]
- [52] N. A. Gershenfeld and I. L. Chuang. Bulk spin-resonance quantum computation. *Science*, 275(5298):350–356, 1997. [1]
- [53] G. Gordon, G. Kurizki, and D. A. Lidar. Optimal dynamical decoherence control of a qubit. *Phys. Rev. Lett.*, 101:010403, 2008. [66]
- [54] D. M. Grant and R. K. Harris. *Encyclopedia of Nuclear Magnetic Resonance, 8 Volume Set*. Encyclopedia of Nuclear Magnetic Resonance. John Wiley & Sons, 1996. [20]
- [55] L. K. Grover. A fast quantum mechanical algorithm for database search. In *Proceedings of the twenty-eighth annual ACM symposium on Theory of computing*, pages 212–219. ACM, 1996. [3]
- [56] L. K. Grover. Quantum mechanics helps in searching for a needle in a haystack. *Phys. Rev. Lett.*, 79(2):325–328, 1997. [3]

- [57] M. Gullans, J. J. Krich, J. M. Taylor, H. Bluhm, B. I. Halperin, C. M. Marcus, M. Stopa, A. Yacoby, and M. D. Lukin. Dynamic nuclear polarization in double quantum dots. *Phys. Rev. Lett.*, 104(22):226807, 2010. [32]
- [58] E. L. Hahn. Spin echoes. *Phys. Rev.*, 80:580, 1950. [7, 12, 55]
- [59] R. Hanson, L. P. Kouwenhoven, J. R. Petta, S. Tarucha, and L. M. K. Vandersypen. Spins in few-electron quantum dots. *Rev. Mod. Phys.*, 79:1217, 2007. [19, 32]
- [60] R. Hanson, L. H. W. van Beveren, I. T. Vink, J. M. Elzerman, W. J. M. Naber, F. H. L. Koppens, L. P. Kouwenhoven, and L. M. K. Vandersypen. Single-shot readout of electron spin states in a quantum dot using spin-dependent tunnel rates. *Phys. Rev. Lett.*, 94(19):196802, 2005. [24]
- [61] A. A. Houck, J. Koch, M. H. Devoret, S. M. Girvin, and R. J. Schoelkopf. Life after charge noise: recent results with transmon qubits. *Quantum Information Processing*, 8(2):105–115, 2009. [95]
- [62] C. Y. Hsieh, Y. P. Shim, M. Korkusinski, and P. Hawrylak. Physics of lateral triple quantum-dot molecules with controlled electron numbers. *Rep. Prog. Phys.*, 75(11):114501, 2012. [78]
- [63] Z. Hu and H. J. Kimble. Observation of a single atom in a magneto-optical trap. *Opt. Lett.*, 19(22):1888–1890, 1994. [14]
- [64] F. Jelezko, T. Gaebel, I. Popa, M. Domhan, A. Gruber, and J. Wrachtrup. Observation of coherent oscillation of a single nuclear spin and realization of a two-qubit conditional quantum gate. *Phys. Rev. Lett.*, 93:130501, Sep 2004. [1]
- [65] A. C. Johnson. *Charge sensing and spin dynamics in GaAs quantum dots*. PhD thesis, Harvard University Cambridge, Massachusetts, 2005. [15]

- [66] A. C. Johnson, J. R. Petta, C. M. Marcus, M. P. Hanson, and A. C. Gossard. Singlet-triplet spin blockade and charge sensing in a few-electron double quantum dot. *Phys. Rev. B*, 72(16):165308, 2005. [35, 48]
- [67] A. C. Johnson, J. R. Petta, J. M. Taylor, A. Yacoby, M. D. Lukin, C. M. Marcus, M. P. Hanson, and A. C. Gossard. Triplet-singlet spin relaxation via nuclei in a double quantum dot. *Nature*, 435:925, 2005. [32, 39, 154]
- [68] T. A. Kennedy, F. T. Charnock, J. S. Colton, J. E. Butler, R. C. Linares, and P. J. Doering. Single-qubit operations with the nitrogen-vacancy center in diamond. *Physica Status Solidi (b)*, 233(3):416–426, 2002. [1]
- [69] A. V. Khaetskii, D. Loss, and L. Glazman. Electron spin decoherence in quantum dots due to interaction with nuclei. *Phys. Rev. Lett.*, 88(18):186802, 2002. [20]
- [70] K. Khodjasteh, T. Erdélyi, and L. Viola. Limits on preserving quantum coherence using multipulse control. *Phys. Rev. A*, 83:020305, 2011. [66]
- [71] K. Khodjasteh and D. A. Lidar. Performance of deterministic dynamical decoupling schemes: Concatenated and periodic pulse sequences. *Phys. Rev. A*, 75:062310, 2007. [55, 56, 66, 69]
- [72] D. Klauser, W. Coish, and D. Loss. Quantum-dot spin qubit and hyperfine interaction. *Advances in Solid State Physics*, pages 17–29, 2007. [32]
- [73] D. L. Klein, P. L. McEuen, J. E. B. Katari, R. Roth, and A. P. Alivisatos. An approach to electrical studies of single nanocrystals. *Applied Physics Letters*, 68(18):2574–2576, 1996. [18]
- [74] J. Koch, T. M. Yu, J. Gambetta, A. A. Houck, D. I. Schuster, J. Majer, A. Blais,

- M. H. Devoret, S. M. Girvin, and R. J. Schoelkopf. Charge-insensitive qubit design derived from the cooper pair box. *Phys. Rev. A*, 76:042319, 2007. [1, 78, 95]
- [75] F. H. L. Koppens, C. Buizert, K. J. Tielrooij, I. T. Vink, K. C. Nowack, T. Meunier, L. P. Kouwenhoven, and L. M. K. Vandersypen. Driven coherent oscillations of a single electron spin in a quantum dot. *Nature*, 442(7104):766–771, 2006. [1, 24, 78]
- [76] F. H. L. Koppens, J. A. Folk, J. M. Elzerman, R. Hanson, L. H. Willems van Beveren, I. T. Vink, H. P. Tranitz, W. Wegscheider, L. P. Kouwenhoven, and L. M. K. Vandersypen. Control and detection of singlet-triplet mixing in a random nuclear field. *Science*, 309(5739):1346–1350, 2005. [74]
- [77] F. H. L. Koppens, D. Klauser, W. A. Coish, K. C. Nowack, L. P. Kouwenhoven, D. Loss, and L. M. K. Vandersypen. Universal phase shift and nonexponential decay of driven single-spin oscillations. *Phys. Rev. Lett.*, 99:106803, 2007. [85]
- [78] F. H. L. Koppens, K. C. Nowack, and L. M. K. Vandersypen. Spin echo of a single electron spin in a quantum dot. *Phys. Rev. Lett.*, 100:236802, 2008. [24, 28]
- [79] L. P. Kouwenhoven, D. G. Austing, and S. Tarucha. Few-electron quantum dots. *Rep. Prog. Phys.*, 64(6):701, 2001. [18]
- [80] L. P. Kouwenhoven, C. M. Markus, P. L. McEuen, S. Tarucha, R. M. Westervelt, and N. S. Wingreen. Electron transport in quantum dots. *NATO ASI Series E Applied Sciences-Advanced Study Institute*, 345:105–214, 1997. [18]
- [81] T. D. Ladd. Hyperfine-induced decay in triple quantum dots. *Phys. Rev. B*, 86:125408, Sep 2012. [85, 138, 139]
- [82] E. A. Laird. *Electrical control of quantum dot spin qubits*. PhD thesis, Harvard University Cambridge, Massachusetts, 2009. [122, 124]

- [83] E. A. Laird, C. Barthel, E. I. Rashba, C. M. Marcus, M. P. Hanson, and A. C. Gossard. Hyperfine-mediated gate-driven electron spin resonance. *Phys. Rev. Lett.*, 99(24):246601, 2007. [24, 78]
- [84] E. A. Laird, J. R. Petta, A. C. Johnson, C. M. Marcus, A. Yacoby, M. P. Hanson, and A. C. Gossard. Effect of exchange interaction on spin dephasing in a double quantum dot. *Phys. Rev. Lett.*, 97(5):56801, 2006. [36, 41, 46]
- [85] E. A. Laird, J. M. Taylor, D. P. DiVincenzo, C. M. Marcus, M. P. Hanson, and A. C. Gossard. Coherent spin manipulation in an exchange-only qubit. *Phys. Rev. B*, 82:075403, Aug 2010. [29, 78, 79, 80, 95, 98, 99, 140, 141, 150, 156]
- [86] B. Lee, W. M. Witzel, and S. Das Sarma. Universal pulse sequence to minimize spin dephasing in the central spin decoherence problem. *Phys. Rev. Lett.*, 100:160505, 2008. [55, 63, 64]
- [87] J. Levy. Universal quantum computation with spin-1/2 pairs and heisenberg exchange. *Phys. Rev. Lett.*, 89(14):147902, 2002. [25, 32, 55]
- [88] D. Loss and D. P. DiVincenzo. Quantum computation with quantum dots. *Phys. Rev. A*, 57:120, 1998. [1, 23]
- [89] J. S Lundein, A. Feito, H. Coldenstrodt-Ronge, K. L. Pregnell, C. Silberhorn, T. C. Ralph, J. Eisert, M. B. Plenio, and I. A. Walmsley. Tomography of quantum detectors. *Nature Phys.*, 5(1):27–30, 2008. [78]
- [90] J. Majer, J. M. Chow, J. M. Gambetta, J. Koch, B. R. Johnson, J. A Schreier, L. Frunzio, D. I. Schuster, A. A. Houck, A. Wallraff, A. Blais, M. H. Devoret, S. M. Girvin, and R. J. Schoelkopf. Coupling superconducting qubits via a cavity bus. *Nature*, 449(7161):443–447, 2007. [28, 166]

- [91] J. M. Martinis, S. Nam, J. Aumentado, and C. Urbina. Rabi oscillations in a large josephson-junction qubit. *Phys. Rev. Lett.*, 89:117901, 2002. [1, 78]
- [92] B. M. Maune, M. G. Borselli, B. Huang, T. D. Ladd, P. W. Deelman, K. S. Holabird, A. A. Kiselev, I. Alvarado-Rodriguez, R. S. Ross, A. E. Schmitz, M. Sokolich, C. A. Watson, M. F. Gyure, and A. T. Hunter. Coherent singlet-triplet oscillations in a silicon-based double quantum dot. *Nature*, 481(7381):344–347, 2012. [27, 95, 104]
- [93] J. Medford, J. Beil, J. M. Taylor, S. D. Bartlett, A. C. Doherty, E. I. Rashba, D. P. DiVincenzo, H. Lu, A. C. Gossard, and C. M. Marcus. Self-consistent measurement and state tomography of an exchange-only spin qubit. *arXiv:1302.1933[cond-mat.mes-hall]*, 2013. [77, 95, 98, 99]
- [94] J. Medford, Ł. Cywiński, C. Barthel, C. M. Marcus, M. P. Hanson, and A. C. Gossard. Scaling of dynamical decoupling for spin qubits. *Phys. Rev. Lett.*, 108:086802, Feb 2012. [65, 85, 102]
- [95] S. Mehl and D. P. DiVincenzo. Noise analysis of qubits implemented in triple quantum dot systems in a davies master equation approach. *arXiv:1211.0417[cond-mat.mes-hall]*, 2012. [78]
- [96] S. Meiboom and D. Gill. Modified spin-echo method for measuring nuclear relaxation times. *Rev. Sci. Instrum.*, 29:688, 1958. [55, 58]
- [97] S. T. Merkel, J. M. Gambetta, J. A. Smolin, S. Poletto, A. D. Córcoles, B. R. Johnson, C. A. Ryan, and M. Steffen. Self-consistent quantum process tomography. *arXiv preprint arXiv:1211.0322*, 2012. [78, 86]
- [98] T. Meunier, I. T. Vink, L. H. W. van Beveren, F. H. L. Koppens, H. P. Tranitz, W. Wegscheider, L. P. Kouwenhoven, and L. M. K. Vandersypen. Nondestructive

- measurement of electron spins in a quantum dot. *Phys. Rev. B*, 74(19):195303, 2006. [55]
- [99] T. Meunier, I. T. Vink, L. H. W. van Beveren, K. J. Tielrooij, R. Hanson, F. H. L. Koppens, H. P. Tranitz, W. Wegscheider, L. P. Kouwenhoven, and L. M. K. Vandersypen. Experimental signature of phonon-mediated spin relaxation in a two-electron quantum dot. *Phys. Rev. Lett.*, 98(12):126601, 2007. [23]
- [100] S. Nadj-Perge, S. M. Frolov, E. Bakkers, and L. P. Kouwenhoven. Spin-orbit qubit in a semiconductor nanowire. *Nature*, 468(7327):1084–1087, 2010. [78]
- [101] Y. Nakamura, Yu. A. Pashkin, and J. S. Tsai. Coherent control of macroscopic quantum states in a single-cooper-pair box. *Nature*, 398:786, 1999. [1, 78]
- [102] I. Neder, M. S. Rudner, H. Bluhm, S. Foletti, B. I. Halperin, and A. Yacoby. Semi-classical model for the dephasing of a two-electron spin qubit coupled to a coherently evolving nuclear spin bath. *Phys. Rev. B*, 72:052113, 2011. [22, 66]
- [103] H. K. Ng, D. A. Lidar, and J. Preskill. Combining dynamical decoupling with fault-tolerant quantum computation. *Phys. Rev. A*, 84(1):012305, 2011. [55]
- [104] M. A. Nielsen and I. L. Chuang. *Quantum Computation and Quantum Information*. Cambridge University Press, Cambridge, England, 2000. [3, 4, 10]
- [105] K. C. Nowack, F. H. L. Koppens, Yu. V. Nazarov, and L. M. K. Vandersypen. Coherent control of a single electron spin with electric fields. *Science*, 318:1430, 2007. [24, 28, 78]
- [106] K. C. Nowack, M. Shafiei, M. Laforest, G. Prawiroatmodjo, L. R. Schreiber, C. Reichl, W. Wegscheider, and L. M. K. Vandersypen. Single-shot correlations and two-qubit gate of solid-state spins. *Science*, 333(6047):1269–1272, 2011. [25]

- [107] T. Obata, M. Pioro-Ladrière, Y. Tokura, Y. S. Shin, T. Kubo, K. Yoshida, T. Taniyama, and S. Tarucha. Coherent manipulation of individual electron spin in a double quantum dot integrated with a micromagnet. *Phys. Rev. B*, 81(8):085317, 2010. [25, 27, 32, 55]
- [108] D. Paget, G. Lampel, B. Sapoval, and V. I. Safarov. Low field electron-nuclear spin coupling in gallium arsenide under optical pumping conditions. *Phys. Rev. B*, 15:5780, 1977. [20]
- [109] H. Paik, D. I. Schuster, L. S. Bishop, G. Kirchmair, G. Catelani, A. P. Sears, B. R. Johnson, M. J. Reagor, L. Frunzio, L. I. Glazman, S. M. Girvin, M. H. Devoret, and R. J. Schoelkopf. Observation of high coherence in josephson junction qubits measured in a three-dimensional circuit qed architecture. *Phys. Rev. Lett.*, 107(24):240501, 2011. [95]
- [110] Y. Pan, Z.-R. Xi, and W. Cui. Optimal dynamical decoupling sequence for the ohmic spectrum. *Phys. Rev. A*, 81(2):022309, 2010. [66]
- [111] S. Pasini and G. S. Uhrig. Optimized dynamical decoupling for power-law noise spectra. *Phys. Rev. A*, 81(1):012309, 2010. [55, 64, 95]
- [112] X. Peng, D. Suter, and D. A. Lidar. High fidelity quantum memory via dynamical decoupling: theory and experiment. *J. Phys. B*, 44:154003, 2011. [69]
- [113] K. D. Petersson, L. W. McFaul, M. D. Schroer, M. Jung, J. M. Taylor, A. A. Houck, and J. R. Petta. Circuit quantum electrodynamics with a spin qubit. *Nature*, 490:380–383, 2012. [28]
- [114] J. R. Petta, A. C. Johnson, J. M. Taylor, E. A. Laird, A. Yacoby, M. D. Lukin, C. M. Marcus, M. P. Hanson, and A. C. Gossard. Coherent Manipulation of Coupled

- Electron Spins in Semiconductor Quantum Dots. *Science*, 309(5744):2180–2184, 2005.
[1, 21, 25, 26, 32, 38, 39, 42, 49, 53, 55, 57, 58, 61, 78]
- [115] J. R. Petta, H. Lu, and A. C. Gossard. A coherent beam splitter for electronic spin states. *Science*, 327(5966):669–672, 2010. [29, 78]
- [116] J. R. Petta, J. M. Taylor, A. C. Johnson, A. Yacoby, M. D. Lukin, C. M. Marcus, M. P. Hanson, and A. C. Gossard. Dynamic nuclear polarization with single electron spins. *Phys. Rev. Lett.*, 100:067601, 2008. [22, 27, 32, 35]
- [117] M. Pioro-Ladrière, J. H. Davies, A. R. Long, A. S. Sachrajda, L. Gaudreau, P. Zwadzki, J. Lapointe, J. Gupta, Z. Wasilewski, and S. Studenikin. Origin of switching noise in GaAs/Al_xGa_{1-x}As lateral gated devices. *Phys. Rev. B*, 72:115331, Sep 2005.
[17]
- [118] M. Pioro-Ladrière, T. Obata, Y. Tokura, Y.-S. Shin, T. Kubo, K. Yoshida, T. Taniyama, and S. Tarucha. Electrically driven single-electron spin resonance in a slanting zeeman field. *Nat. Phys.*, 4:776, 2008. [24, 27, 28, 78]
- [119] M. Pioro-Ladrière, Y. Tokura, T. Obata, T. Kubo, and S. Tarucha. Micromagnets for coherent control of spin-charge qubit in lateral quantum dots. *Appl. Phys. Lett.*, 90(2):024105–024105, 2007. [27, 32, 53]
- [120] I. I. Rabi, J. R. Zacharias, S. Millman, and P. Kusch. A new method of measuring nuclear magnetic moment. *Phys. Rev.*, 53:318–318, Feb 1938. [7]
- [121] D. C. Ralph, C. T. Black, and M. Tinkham. Spectroscopic measurements of discrete electronic states in single metal particles. *Phys. Rev. Lett.*, 74:3241–3244, Apr 1995.
[18]

- [122] G. Ramon and X. Hu. Dynamical nuclear spin polarization and the zamboni effect in gated double quantum dots. *Phys. Rev. B*, 75:161301(R), 2007. [32]
- [123] D. J. Reilly, C. M. Marcus, M. P. Hanson, and A. C. Gossard. Fast single-charge sensing with a rf quantum point contact. *Appl. Phys. Lett.*, 91:162101, 2007. [34, 57, 68, 81, 96, 98, 126, 128, 134]
- [124] D. J. Reilly, J. M. Taylor, E. A. Laird, J. R. Petta, C. M. Marcus, M. P. Hanson, and A. C. Gossard. Measurement of temporal correlations of the overhauser field in a double quantum dot. *Phys. Rev. Lett.*, 101:236803, 2008. [32, 36, 43, 45, 53, 55, 58, 62, 64, 85]
- [125] D. J. Reilly, J. M. Taylor, J. R. Petta, C. M. Marcus, M. P. Hanson, and A. C. Gossard. Suppressing spin qubit dephasing by nuclear state preparation. *Science*, 321:817, 2008. [2, 22, 27, 32, 33, 35, 38, 39, 51, 53]
- [126] D. J. Reilly, J. M. Taylor, J. R. Petta, C. M. Marcus, M. P. Hanson, and A. C. Gossard. Exchange control of nuclear spin diffusion in a double quantum dot. *Phys. Rev. Lett.*, 104:236802, 2010. [32, 35, 43, 45]
- [127] H. Ribeiro and G. Burkard. Nuclear state preparation via landau-zener-stückelberg transitions in double quantum dots. *Phys. Rev. Lett.*, 102(21):216802, 2009. [32]
- [128] Ch. Roos, Th. Zeiger, H. Rohde, H. C. Nägerl, J. Eschner, D. Leibfried, F. Schmidt-Kaler, and R. Blatt. Quantum state engineering on an optical transition and decoherence in a paul trap. *Phys. Rev. Lett.*, 83:4713–4716, Dec 1999. [1]
- [129] M. S. Rudner, F. H. L. Koppens, J. A. Folk, L. M. K. Vandersypen, and L. S. Levitov. Nuclear spin dynamics in double quantum dots: Fixed points, transients, and intermittency. *Phys. Rev. B*, 84:075339, 2011. [74]

- [130] Y. Sagi, I. Almog, and N. Davidson. Process tomography of dynamical decoupling in a dense cold atomic ensemble. *Phys. Rev. Lett.*, 105:053201, Jul 2010. [66]
- [131] R. J. Schoelkopf, P. Wahlgren, A. A. Kozhevnikov, P. Delsing, and D. E. Prober. The radio-frequency single-electron transistor (rf-set): a fast and ultrasensitive electrometer. *Science*, 280(5367):1238–1242, 1998. [126, 128]
- [132] J. A. Schreier, A. A. Houck, J. Koch, D. I. Schuster, B. R. Johnson, J. M. Chow, J. M. Gambetta, J. Majer, L. Frunzio, M. H. Devoret, S. M. Girvin, and R. J. Schoelkopf. Suppressing charge noise decoherence in superconducting charge qubits. *Phys. Rev. B*, 77:180502, 2008. [95]
- [133] D. Schröer, A. D. Greentree, L. Gaudreau, K. Eberl, L. C. L. Hollenberg, J. P. Kotthaus, and S. Ludwig. Electrostatically defined serial triple quantum dot charged with few electrons. *Phys. Rev. B*, 76:075306, Aug 2007. [19]
- [134] B. Schumacher. Quantum coding. *Phys. Rev. A*, 51:2738–2747, Apr 1995. [1]
- [135] P. W. Shor. Algorithms for quantum computation: discrete logarithms and factoring. In *Foundations of Computer Science, 1994 Proceedings., 35th Annual Symposium on*, pages 124–134. IEEE, 1994. [3]
- [136] M. D. Shulman, O. E. Dial, S. P. Harvey, H. Bluhm, V. Umansky, and A. Yacoby. Demonstration of entanglement of electrostatically coupled singlet-triplet qubits. *science*, 336(6078):202–205, 2012. [28, 95]
- [137] John A. Smolin, Jay M. Gambetta, and Graeme Smith. Efficient method for computing the maximum-likelihood quantum state from measurements with additive gaussian noise. *Phys. Rev. Lett.*, 108:070502, Feb 2012. [148]

- [138] M. Stopa, J. J. Krich, and A. Yacoby. Inhomogeneous nuclear spin flips: Feedback mechanism between electronic states in a double quantum dot and the underlying nuclear spin bath. *Phys. Rev. B*, 81(4):041304, 2010. [32]
- [139] T. Takakura, M. Pioro-Ladrière, T. Obata, Y. S. Shin, R. Brunner, K. Yoshida, T. Taniyama, and S. Tarucha. Triple quantum dot device designed for three spin qubits. *Appl. Phys. Lett.*, 97(21):212104–212104, 2010. [25]
- [140] J. M. Taylor and M. D. Lukin. Dephasing of quantum bits by a quasi-static mesoscopic environment. *Quant. Info. Process.*, 5:503, 2006. [8]
- [141] J. M. Taylor, J. R. Petta, A. C. Johnson, A. Yacoby, C. M. Marcus, and M. D. Lukin. Relaxation, dephasing, and quantum control of electron spins in double quantum dots. *Phys. Rev. B*, 76:035315, 2007. [20, 21, 22, 25, 39, 40, 41, 42, 48, 164]
- [142] C. Testelin, F. Bernardot, B. Eble, and M. Chamarro. Hole-spin dephasing time associated with hyperfine interaction in quantum dots. *Phys. Rev. B*, 79:195440, May 2009. [20]
- [143] J. S. Townsend. *A modern approach to quantum mechanics*. Univ Science Books, 2000. [5]
- [144] L. Trifunovic, O. Dial, M. Trif, J. R. Wootton, R. Abebe, A. Yacoby, and D. Loss. Long-distance spin-spin coupling via floating gates. *Physical Review X*, 2(1):011006, 2012. [28]
- [145] G. S. Uhrig. Keeping a quantum bit alive by optimized pi-pulse sequences. *Phys. Rev. Lett.*, 98:100504, 2007. [55, 56, 63, 66]
- [146] T. van der Sar, Z. H. Wang, M. S. Blok, H. Bernien, T. H. Taminiau, D. M. Toyli, D. A. Lidar, D. D. Awschalom, R. Hanson, and V. V. Dobrovitski. Decoherence-protected

- quantum gates for a hybrid solid-state spin register. *Nature*, 484(7392):82–86, 2012. [95]
- [147] W. G. van der Wiel, S. De Franceschi, J. M. Elzerman, T. Fujisawa, S. Tarucha, and L. P. Kouwenhoven. Electron transport through double quantum dots. *Rev. Mod. Phys.*, 75(1):1, 2002. [19, 35, 48]
- [148] H. van Houten, C. W. J. Beenakker, and A. A. M. Staring. Coulomb-blockade oscillations in semiconductor nanostructures. In H. Grabert and M. H. Devoret, editors, *Single Charge Tunneling*. Plenum, New York, 1992. Also available at: arXiv:cond-mat/0508454v1. [18]
- [149] L. M. K. Vandersypen and I. L. Chuang. Nmr techniques for quantum control and computation. *Rev. Mod. Phys.*, 76:1037–1069, 2005. [69, 102]
- [150] A. Vidan, R. M. Westervelt, M. Stopa, M. P. Hanson, and A. C. Gossard. Charging and spin effects in triple dot artificial molecules. *J. Supercond.*, 18:223–227, 2005. [19]
- [151] I. T. Vink, K. C. Nowack, F. H. L. Koppens, J. Danon, Y. V. Nazarov, and L. M. K. Vandersypen. Locking electron spins into magnetic resonance by electron–nuclear feedback. *Nature Phys.*, 5(10):764–768, 2009. [22]
- [152] L. Viola and S. Lloyd. Dynamical suppression of decoherence in two-state quantum systems. *Phys. Rev. A*, 58(4):2733, 1998. [66]
- [153] X. Wang, S. Yang, and S. Das Sarma. Quantum theory of the charge-stability diagram of semiconductor double-quantum-dot systems. *Phys. Rev. B*, 84:115301, Sep 2011. [19]
- [154] Z.-H. Wang, W. Zhang, A. M. Tyryshkin, S. A. Lyon, J. W. Ager, E. E. Haller, and

- V. V. Dobrovitski. Effect of pulse error accumulation on dynamical decoupling of the electron spins of phosphorus donors in silicon. *arXiv:1011.6417*, 2010. [74]
- [155] J. R. West and B. H. Fong. Exchange-only dynamical decoupling in the three-qubit decoherence free subsystem. *New J. Phys.*, 14(8):083002, 2012. [78, 85]
- [156] W. M. Witzel and S. Das Sarma. Quantum theory for electron spin decoherence induced by nuclear spin dynamics in semiconductor quantum computer architectures: Spectral diffusion of localized electron spins in the nuclear solid-state environment. *Phys. Rev. B*, 74:035322, 2006. [63, 66]
- [157] W. M. Witzel and S. Das Sarma. Concatenated dynamical decoupling in a solid-state spin bath. *Phys. Rev. B*, 76:241303(R), 2007. [55, 56, 63]
- [158] W. M. Witzel and S. Das Sarma. Multiple-pulse coherence enhancement of solid state spin qubits. *Phys. Rev. Lett.*, 98:077601, 2007. [66]
- [159] W. Yao, R.-B. Liu, and L. J. Sham. Theory of electron spin decoherence by interacting nuclear spins in a quantum dot. *Phys. Rev. B*, 74:195301, 2006. [63, 66]
- [160] T. Yuge, S. Sasaki, and Y. Hirayama. Measurement of the noise spectrum using a multiple-pulse sequence. *Phys. Rev. Lett.*, 107:170504, 2011. [66, 72]